Università degli studi di Roma "Sapienza"
Facoltà di Scienze Matematiche, Fisiche e Naturali
PhD in Physics - XXXIV Cycle

Search for the X(17) particle in the ^{7}Li$(p, e^+e^-)^8$Be reaction with the MEG II detector

PhD Thesis

Advisor
Prof. Gianluca Cavoto
Co-Advisor
Dr. Francesco Renga

Candidate
Manuel Meucci

XXXIV PhD cycle - Academic Year 2021/2022

Contents

Introduction

The main topic of this PhD thesis is to show the capability of the MEG II experiment to perform the measurement of the Internal Pair Creation in the $^{7}\text{Li}(p, e^{+}e^{-})^{8}\text{Be}$ nuclear reaction. This reaction is of particular interest because a recent measurement of its decay products performed at the Atomki laboratory in Hungary showed an unexpected excess in their angular distribution. The significance of the observed bump is ~ 7 standard deviations, and following measurements of the same reaction but with an upgraded experimental apparatus showed analogous results. Moreover, a measurement of the $^{3}\text{H}(p, e^{+}e^{-})^{4}\text{He}$ reaction showed another significant excess at a different angle. Both these observations can be explained by the creation of a new physics boson with a 17 MeV/c^2 mass called X(17). The MEG II experiment was designed to search for Charged Lepton Flavor Violation in the $\mu^{+} \rightarrow e^{+}\gamma$ decay, but its detectors are able to measure the $^{7}\text{Li}(p, e^{+}e^{-})^{8}\text{Be}$ reaction as well. The experiment is in fact equipped with a photon detector and a magnetic spectrometer, and has access to a Cockcroft-Walton accelerator for the photon detector calibrations. The accelerator can be used to generate the necessary proton beam, and the magnetic spectrometer can be used to measure the decay products of the reaction. An independent measurement with an experiment that guarantees a better invariant mass resolution and a larger angular acceptance can confirm that the anomaly observed at Atomki is not an artifact of the detector geometry, but a real anomaly not explained by any known nuclear physics effect.

My contribution is focused around the signal and background simulations of the X(17) measurement at MEG II, the participation in the commissioning of the drift chamber of the magnetic spectrometer and the participation in the preliminary data taking. The target region used for the photon detector calibration is not compatible with the X(17) measurement because its material increases the multiple scattering, spoiling the tracking performance of the drift chamber. A redesign was then necessary, and I implemented the signal and background models in the MEG II simulation to study the expected resolution and efficiency. This was done for different configurations to find an optimal solution for the new target region design. I also participated in the commissioning of the drift chamber from 2018 to 2021, both during the data taking and the hardware operations periods. Finally, I participated in the data taking with a preliminary setup for the X(17) measurement, built and installed during 2021. This setup is not the optimal one, whose construction is underway, but it was used to take some preliminary data used for some test before the final measurement, which is foreseen in the first months of 2022.

In chapter 1 I will introduce the nuclear reaction investigated at Atomki. I will give some information about the IPC models existing before the measurements and the development that followed. After that I will show the results obtained at Atomki for every measurement they performed, and finally I will describe some of the interpretations given by the scientific community to these results. In chapter 2 I will report on the X(17) searches in different channels, and introduce some of the experiments that are planning to study the IPC in nuclear reactions in the near future. In chapter 3 I will focus on MEG II, for which I will show some details of its experimental apparatus. In chapter 4 I will focus on the MEG II drift chamber, describing its design, construction and commissioning. I will also report the results obtained from the data collected in the 4 pre-engineering runs of the last years. In chapter 5 I will show the simulations of the signal and background of the X(17) measurement at MEG II and the optimization of the new target region design. I will report the expected performance in terms of resolution and efficiency. In chapter 6 I will report the results of the studies on the significance and data taking time needed for a successful measurement. Finally, in chapter 7 I will describe the different configurations used in the data taking of 2021 with the preliminary setup. I will also show a first attempt at the analysis of such data.

Chapter 1

Anomaly in the Internal Pair Creation

In 2016 an experimental group working in the Atomki laboratory (Debrecen, Hungary) observed an excess in the angular distribution of the Internal Pair Creation (IPC) in the nuclear reaction ^{7}Li$(p, e^+e^-)^8$Be. The most fascinating interpretation of this observation is based on the creation of a new physics boson mediator of a fifth fundamental force that describes the interaction between dark matter and ordinary matter. This particle is now called X(17) boson, because of its measured 17 MeV$/c^2$ mass.

This anomaly puzzled the Atomki collaboration, that decided to deepen the knowledge of this phenomenon with new experiments. They repeated the measurement with an improved experimental apparatus in 2017, improved the analysis in 2018 and repeated the experiment with ^{4}He excited states in 2019. They always obtained results consistent with the X(17) boson production hypothesis. This means that the X(17) search is a promising path to follow to find new physics.

The possible implications of this anomaly captured the attention of the scientific community. Several collaborations around the world plan to repeat this measurement or search for this particle in other channels, and many theories are being investigated to solve this puzzle. In this chapter I will introduce the first nuclear reaction investigated at the Atomki laboratory and report the knowledge on the IPC theory at the time of the anomaly observation. I will then summarize the experimental results obtained in the past years, along with the many interpretations given to this interesting observation, both in the nuclear and particle physics fields. I will focus on the improvements in the IPC model for ^{8}Be, result of the studies triggered by the Atomki measurements, and on the interpretation of the anomaly as the creation of a new physics light boson.

1.1 ^{7}Li$(p,\gamma)^8$Be reaction

The ^{7}Li$(p,\gamma)^8$Be nuclear reaction is obtained from a proton beam impinging on a Li target, that leads to the creation of ^{8}Be excited states through proton capture. Figure 1.1 shows the cross section of this reaction as a function of the proton kinetic energy. Two resonances emerge from this plot, one at $E_p = 0.441$ MeV and one at $E_p = 1.03$ MeV. The ^{8}Be states populated in these resonances are called ^{8}Be* and ^{8}Be*' respectively. Figure 1.2 shows the energy levels of the ^{8}Be states. The energies of the two resonant states are 17.6 MeV and 18.15 MeV for the lower and the higher energy resonance respectively. I will use the notation used in [1] and refer to these states as Mostly IsoVector (MIV) and Mostly IsoScalar (MIS) resonance.

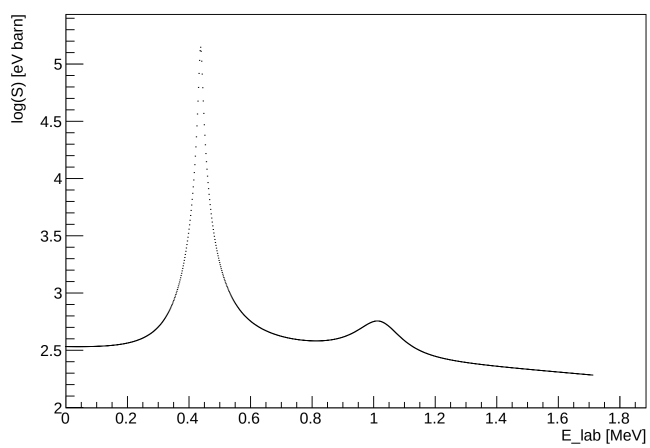

Figure 1.1: ^{7}Li$(p,\gamma)^8$Be cross section as a function of the proton energy in the lab frame. It is calculated from a theoretical model published in [1].

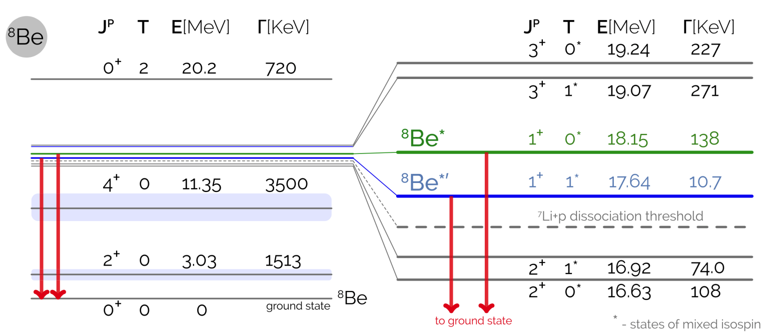

Figure 1.2: Relevant ^{8}Be states and energy levels. The two states inspected at Atomki are ^{8}Be* at 18.15 MeV (MIS) and ^{8}Be*' at 17.64 MeV (MIV). Image from [2].

The $^7\mathrm{Li}(p,\gamma)^8\mathrm{Be}$ reaction can give as final product an electron-positron pair, that can be created by the particle produced in the de-excitation of the $^8\mathrm{Be}^*$. This particle is usually a photon γ, that can convert into a pair inside the nuclear reaction: in this case we talk about IPC, as explained in section 1.1.2. The anomalous excess observation that will be described in section 1.2 can be a hint of the presence of another particle that decays into the e^+e^- pair in place of the photon: the X(17) boson. Figure 1.3 shows the possible reaction in which the X(17) boson can be produced.

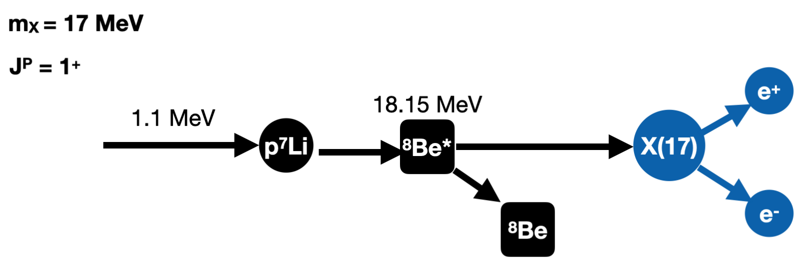

Figure 1.3: Schematisation of the X(17) boson production from the $^7\mathrm{Li}(p,e^+e^-)^8\mathrm{Be}$ nuclear reaction.

1.1.1 Multipolarity of nuclear transitions

Nuclear transitions are characterized by energy emission, since in a nucleus the ground state has lower energy with respect to the excited states. This energy variation between different states is compensated by the emission of photons. The transitions can be therefore classified by the multipolarity of the emitted radiation, i.e. by the order of the multipole expansion of the electric and magnetic field [3]. Electric and magnetic multipole radiations are indicated with EL and ML respectively, where L is the order of the multipole expansion (e.g. a dipole has order L=1, which corresponds to $2^{\mathrm{L}} = 2$ poles, while a quadrupole has order 2). Notice that there is no magnetic monopole, so M0 does not exist. In this text I will refer to the transition in which an electric/magnetic multipole radiation is emitted as "electric/magnetic transitions" or simply "EL/ML transitions".

Nuclear states are defined by their energy and spin-parity J^P. Here J is the total angular momentum, that can be integer or half integer, and P is the parity, that can be positive or negative. Electric and magnetic multipole radiations of the same order L carry the same angular momentum L and have different parity. Selection rules stem from the angular momentum conservation, defining the possible radiations that can be emitted in a nuclear transitions:

- in EL transitions the parity changes for odd L;
- in ML transitions the parity changes for even L.

The ^{8}Be* and ^{8}Be*' transitions to the ground state ^{8}Be are both M1 transitions, since the angular momentum transferred is 1 and the parity remains unchanged. Figure 1.4 shows the energy level and spin-parity of these states, together with the ^{7}Li+p threshold at 17.26 MeV. Other nuclear transitions in ^{8}Be can have any multipolarity, but E0 is an exception. This kind of transitions are characterized from the absence of single photon emission, which is forbidden because of quantum numbers: E0 transitions are $0^+ \rightarrow 0^+$ (no angular momentum is transferred), but the photon emission carries at least one unit of angular momentum.

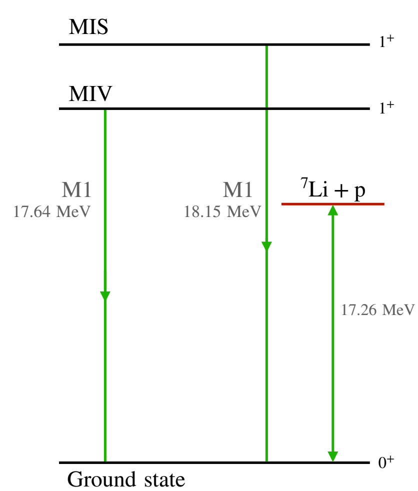

Figure 1.4: M1 transitions between MIS and MIV state of ^{8}Be to the ground state. The red line indicates the ^{7}Li+p threshold.

1.1.2 Internal Pair Creation

Electron-positron pairs can be produced in nuclear reactions from the internal conversion of a photon coming from the transition of an excited nucleus to its ground state. This phenomenon is called Internal Pair Creation (IPC). IPC is an alternative decay mode for an excited nucleus, in contrast with the photon emission and the Internal Conversion (IC), which is the emission of an orbital electron of the atom. IPC is characterized by the e^+e^- opening angle distribution and the conversion coefficient, i.e. the number of IPC events per photon emitted in the nuclear reaction. Rose measured the Z dependence of the IPC and IC coefficient in 1949-51, and reported his results in [4] and [5]. He found out that the IPC coefficient increases with increasing photon energy and is almost independent of Z, in contrast with the IC coefficient, that decreases with increasing photon energy and decreasing Z.

Figure 1.5 shows the Feynman diagrams for M1, E1 and E2 transitions in the $^7\text{Li}(p,\gamma)^8\text{Be}$ reaction. The diagrams for IPC are obtained by attaching the lepton line to the virtual photon line. This reaction is called proton capture, since the proton from the beam is captured by the target nucleus and a heavier nucleus is created. In case of M1 transitions we talk about resonant proton capture, while for E1 and E2 we talk about direct proton capture: they happen respectively in resonant ^{8}Be states and off resonance. In the resonant proton capture an excited state, e.g. $^8\text{Be}^*$ or $^8\text{Be}^{*\prime}$, is created before the photon emission, as represented in figure 1.5 with the symbol Ψ.

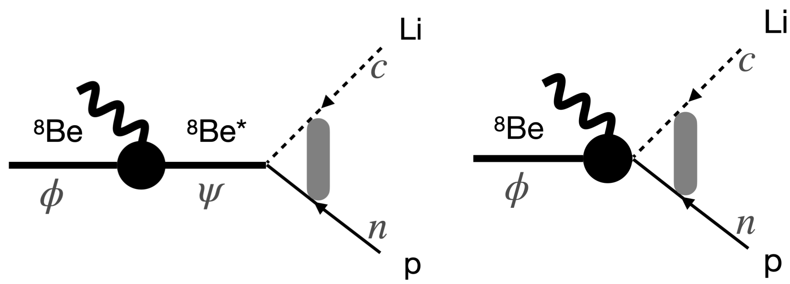

(a) (b)

Figure 1.5: Feynman diagrams of resonant M1 (a) and non-resonant E1, E2, M2 (b) proton capture. For IPC diagrams the lepton line must be attached to the virtual photon line. Here c, n, ϕ, ψ are the fields of ^{7}Li, proton, ^{8}Be Ground State (GS) and ^{8}Be 1^+ excited states. In this diagram I use the notation used in [1].

Early IPC model

Rose carried out a study of the IPC properties, which was published in 1949 [4]. He considered atoms with $Z < 40$ and photon energies above 2.5 MeV, since in this region the IPC is dominant with respect to the IC. His goal was to provide a method to determine the multipolarity of a transition using IPC measurements. The focus of the study is on multipolarities, here indicated with l, greater than 0. He used the Born approximation, a first order perturbation in scattering theory that consists in the use of the incident field instead of the total field, and is valid at low Z and small scattered field. He obtained an analytic expression of the distribution of the opening angle of the pair produced at fixed electron and positron energies:

$$\begin{aligned}\gamma_l(\Theta) &= (2\alpha/\pi(l+1))(p_+p_-/q)\frac{(q/k)^{2l-1}}{(k^2-q^2)^2} \\ &\times \{(2l+1)(W_+W_- + 1 - \frac{1}{3}p_+p_-\cos\Theta) \\ &+ l[(q^2/k^2)-2](W_+W_- - 1 + p_+p_-\cos\Theta) \\ &+ \frac{1}{3}(l-1)p_+p_-[(3/q^2)(p_- + p_+\cos\Theta) \\ &\times (p_+ + p_-\cos\Theta) - \cos\Theta]\} \qquad \text{for electric multipoles}\end{aligned} \tag{1.1}$$

$$\begin{aligned}\gamma_l(\Theta) &= (2\alpha/\pi)(p_+p_-/q)\frac{(q/k)^{2l+1}}{(k^2-q^2)^2}\{1 + W_+W_- \\ &- \frac{p_+p_-}{q^2}(p_- + p_+\cos\Theta)(p_+ + p_-\cos\Theta)\} \qquad \text{for magnetic multipoles}\end{aligned} \tag{1.2}$$

Here l is the multipolarity of the transition, p_+, p_-, W_+ and W_- the positron and electron momentum and energy, Θ is the pair separation angle and k is the photon energy in units of m_e. He also calculated the positron energy distribution, by integrating equations 1.1 and 1.2 for electric and magnetic multipoles respectively:

$$\begin{aligned}\Gamma_l(W_+) &= (\alpha/\pi(l+1)k^3)\{(l/2)k^2 J_{l+1} \\ &+ [2lW_+W_- - 1/4(7l+1)k^2]J_l \\ &+ [l(W_+^2 + W_-^2 + 1) + 1 - W_+W_-]J_{l-1} \\ &- 1/4(l-1)(W_+ - W_-)^2 J_{l-2}\} \qquad \text{for electric multipoles}\end{aligned} \tag{1.3}$$

$$\begin{aligned}\Gamma_l(W_+) &= \alpha/\pi k^3\{(1 + W_+W_-)J_l \\ &- (k^2/4)(J_{l+1} - x_1x_2J_{l-1}) \qquad \text{for magnetic multipoles}\end{aligned} \tag{1.4}$$

Here $x_1 = (p_+ - p_-)^2/k^2$, $x_2 = (p_+ + p_-)^2/k^2$, $J_l = \int_{x_1}^{x_2} x^l(1-x)^{-2}dx$. The angular distribution is peaked at small angles, and rapidly decreases at increasing Θ. The pair formation coefficient, which is the number of pairs per photon produced in the nuclear transition, can be obtained by integrating 1.3 and 1.4 in dW_+ for electric and magnetic multipoles respectively.

Figure 1.6 shows the pair formation coefficient as a function of k for $l = 1, ..., 5$. The sensitivity of pair formation coefficient is crucial to distinguish between different multipolarities. The plots show that the separation is good for large k, but gets worse when approaching low k values.

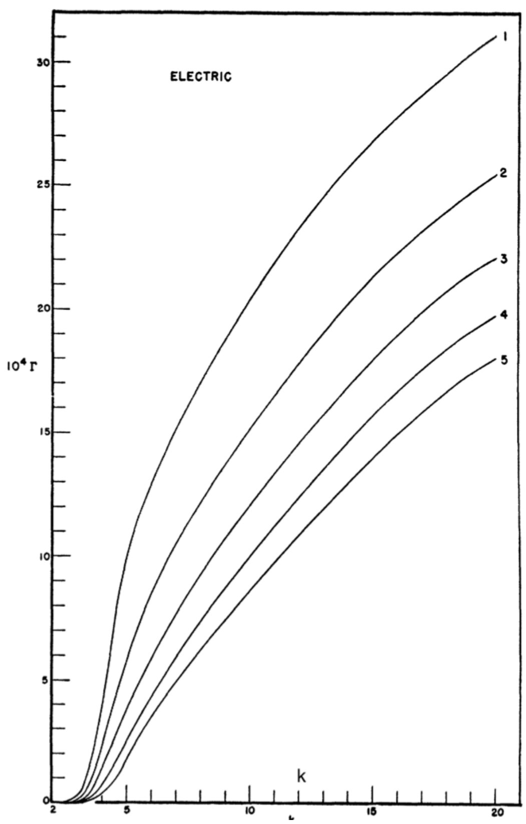

(a)

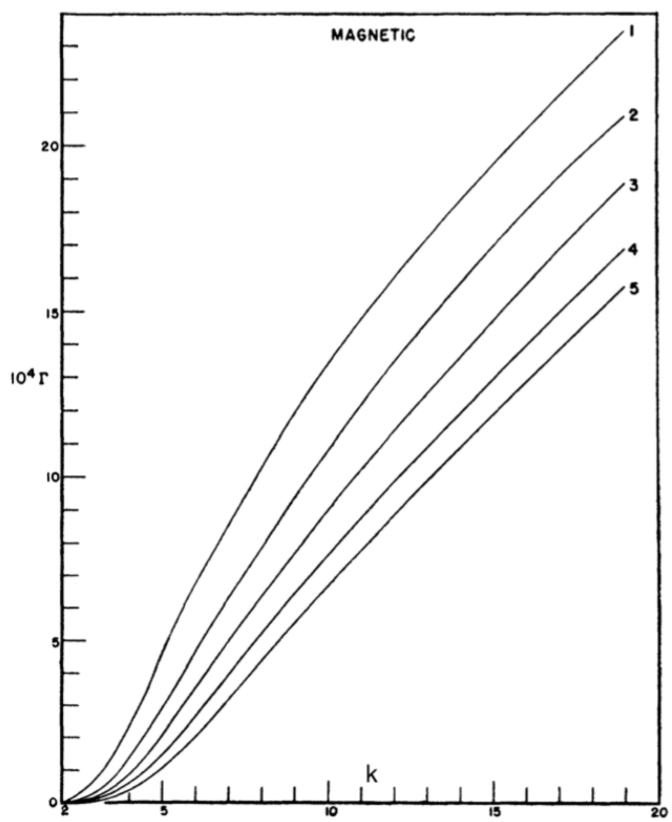

(b)

Figure 1.6: Total number of e^+e^- pairs as a function of the photon energy for several electric (a) and magnetic (b) multipoles. The order of the multipole is indicated beside the curves. Figures from [4].

The error induced by the use of the Born approximation has been estimated by comparing the results from Jäger and Hulme for $Z = 84$ [6]. For example for $k = 6$ the pair formation coefficient is 20% larger for $l = 2$ and 15% for $l = 1$, but since the region of interest is at smaller Z and larger k the prediction should be more accurate. Anyway, the approximation is good only for integral quantities such as this coefficient, since there is the effect of the Coulomb field, that suppresses slow positrons and increases fast ones. These effects cancel out only upon integration over the energy spectrum.

IPC model improvements

The Rose model is not sufficient to thoroughly explain the $^7\mathrm{Li}(p,e^+e^-)^8\mathrm{Be}$ reaction. There are two non negligible effects that have not been addressed: the anisotropy in the photon emission and the interference between the different components of the transition. Such interference can arise between M1 component, dominant in the resonance, and E1 component, dominant off resonance [7]. There can be also a contribution of higher order transitions (E2, M2, etc.), but they are usually negligible.

Goldring improved Rose's study in 1953 by taking into account these effects [8]. He calculated the probability of a pair being emitted per photon, which is, using the notation by Rose:

$$F_l(\Theta,\delta,\theta,\phi)d\Omega_+d\Omega_-dW_+ = \sum_m a_m f_l^m(\Theta,\delta,\theta,\phi)d\Omega_+d\Omega_-dW_+ \tag{1.5}$$

where $a_m = \sum_{m'} \alpha_{m'} b_{jm',j'm'-m}$, m' are the eigenvalues of J_z, $\alpha_{m'}$ fractional population of m' initial substate, $b_{jm',j'm'-m}$ relative strength of the transition and f_l^m the probability of the transition. In the isotropic case $a_0 = a_{\pm1} = ... = 1/(2l+1)$, hence $F_l(\Theta) = \sum_m a_m f_l^m(\Theta,\delta,\theta,\phi) = 1/(8\pi^2)\gamma_l(\Theta)$, where δ, θ, ϕ are the spatial orientation angles and $\gamma_l(\Theta)$ are the integrated correlations (equations 1.1 and 1.2). This result agrees with Rose's calculations. Goldring provides a table with the asymptotic values of the integrals over energy of the anisotropic terms, $\epsilon_l(\Theta)_\infty$ and $\eta_l(\Theta)_\infty$, where:

$$\epsilon_l(\Theta) = \frac{2\alpha}{\pi k^3}\int_1^{k-1} \frac{p_+p_-}{(k^2-q^2)^2}\left(\frac{q}{k}\right)^{2l-2}(\vec{p_+}\times\vec{p_-})^2 dW_+ \tag{1.6}$$

$$\eta_l(\Theta) = \frac{2\alpha}{\pi k^3}\int_1^{k-1} \frac{p_+p_-}{k^2-q^2}\left(\frac{q}{k}\right)^{2l-2}\frac{1}{2}k^2 dW_+ \tag{1.7}$$

He also provides an expression for the M{l} and E{$l+1$} interference term:

$$f^m_{l,l+1} = \frac{\alpha k}{32\pi^2} p_+ p_- \{v^m_{l+1}(W_- - W_+) + (\vec{p_-} - \vec{p_+}, \vec{a^m_{l+1E}})\}(\vec{p_+} \times \vec{p_-}, \vec{a^{m*}_{lM}}) \tag{1.8}$$

Notice that the integral of this quantity over δ and θ vanishes, meaning that the isotropic case has no interference. Thus, the best way to minimize the effects of the anisotropy and interference in a measurement is to place the pair detectors in the plane perpendicular to the particle beam. The experiment at Atomki that observed the ^{8}Be anomaly made this approximation, placing their detector perpendicular to the proton beam and neglecting anisotropy and interference.

New studies showed how these effects are not completely negligible, and can contribute to the observed peak. In fact, since the observation of the anomaly captured the interest of many scientists, the old calculations by Rose and Goldring have been recently improved by several nuclear physicists. The new models developed may partially explain the unexpected experimental results, but they need experimental confirmation. I will address this topic in more detail later in section 1.3.1.

1.2 Experiments at Atomki

Many physicists tested the IPC theoretical predictions with experiments, and some of them observed anomalies in the creation of 18.15 MeV MIS and 17.6 MeV MIV M1 transitions in ^{8}Be [9–14]. An experiment carried out in the Atomki laboratory in 2016 further investigated this phenomenon [15, 16], obtaining a quite significative deviation from the theory developed up to that moment. The separation angle of the pair produced in the ^{7}Li$(p, e^+e^-)^8$Be reaction showed in fact an enhancement around 140°, in contrast with the simulation showed in figure 1.7. Such simulation is based on the Rose theory at $E_\gamma = 17$ MeV, and does not account for anisotropy effect. Anyway, this effect is minimized by the design of the experimental apparatus, as will be explained in section 1.2.1.

In the following years the same collaboration published several papers with improved measurements and new results with a different nuclear reaction [17–19]. The anomaly was there every time, and no nuclear physics model could explain its presence. This led to fascinating particle physics beyond Standard Model (BSM) explanation, such as the creation of a light boson that decays in the observed e^+e^- pair, which is now referred to as X(17), because of its 17 MeV/c^2 measured mass.

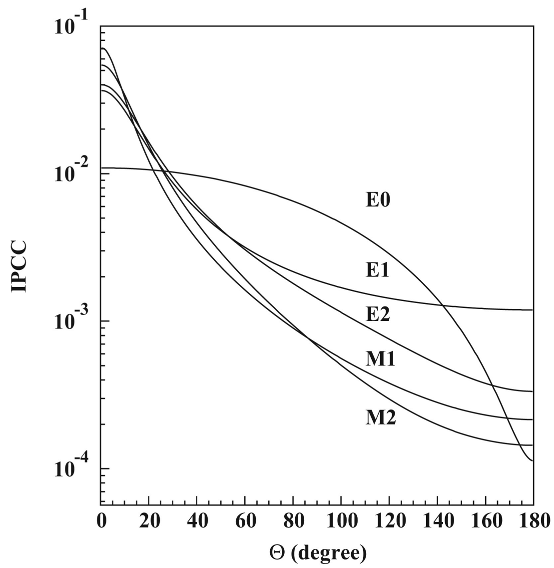

Figure 1.7: Angular correlations of e^+e^- pairs from IPC for different multipolarities calculated by the collaboration at Atomki in [15].

1.2.1 Experimental apparatus

In the first experiment [16] the $^7\text{Li}(p, e^+e^-)^8\text{Be}$ reaction was obtained from a 1 μA proton beam impinging on 15 $\mu\text{g/cm}^2$ thick LiF_2 and 700 $\mu\text{g/cm}^2$ Li_2O targets. The proton beam energy was adjustable, so that it was possible to populate both the 18.15 MeV and 17.6 MeV excited states. Such beam came from the 2MV Tandetron accelerator in Debrecen. The detector was built using the information from Stiebing and co workers in [20], who performed similar experiments with several target materials. The target was placed on a 10 μm thick Al strip foil, which is spanned between 3 mm thick perspex rods. The rods were used to minimize the scattering and external pair creation in the vicinity of the interaction point. The target was continuously monitored by measuring the photon spectrum, and it had to be changed every few hours with a new one because of its deterioration. Five plastic scintillators $\Delta E - E$ detector telescopes were used to detect e^-e^+ pairs, and five multi-wire proportional counters (MWPC) were placed in front of the scintillators to measure the position of the hits. The telescopes were placed in the plane perpendicular to the beam to minimise the impact of anisotropy and interference effects. The target was placed perpendicular to the beam and inserted in a 1 mm thick carbon fiber vacuum chamber, around which the telescopes were placed. A HPGe detector was used 25 cm from the target to detect the 17.6 MeV and 18.15 MeV γ-rays produced in the $^7\text{Li}(p, \gamma)^8\text{Be}$ reaction. A more detailed description of the detectors can be found in [15].

The collaboration repeated the experiment several time in the last years, with some modifications to the experimental setup. The second measurement [17] used the same setup except for a new more stable accelerator and for the hit position detector: five double sided silicon strip detectors (DSSSD) composed of 3 mm thick strips replaced the MWPC. Figure 1.8 shows a CAD drawing of the apparatus used in this measurement.

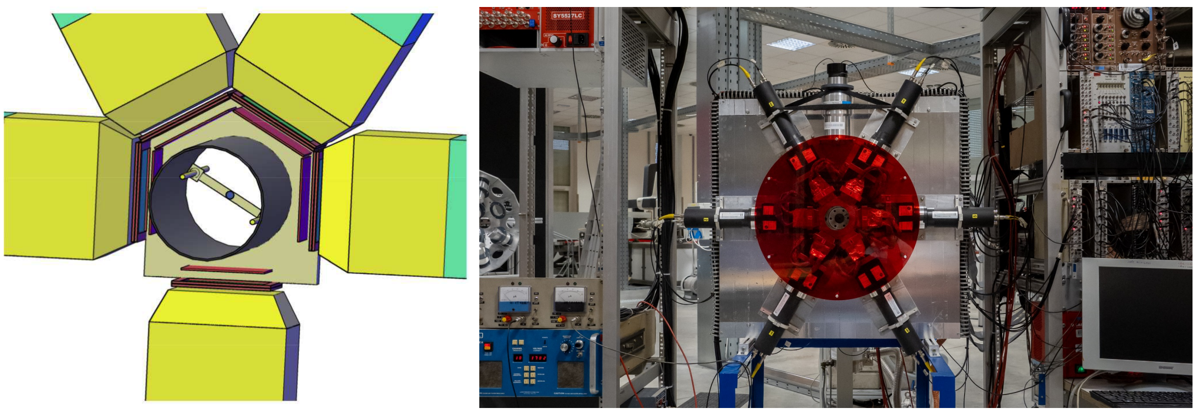

(a) (b)

Figure 1.8: (a) Layout of the experimental apparatus used in the second measurement at Atomki. The 5 telescopes are placed perpendicular to the proton beam and at relative angles of 0°, 60°, 120°, 180°, 270°. Figure from [17].
(b) Picture of the experimental apparatus used in the third measurement at Atomki. The number of telescopes is increased to 6, placed at relative angles of 0°, 60°, 120°, 180°, 240°, 300°.

The third measurement with ^{8}Be improved the results obtained previously [18]. This was achieved by increasing the number of scintillators and DSSSD from 5 to 6, placed perpendicularly to the beam direction at azimuthal angles of 0°, 60°, 120°, 180°, 240°, 300°. Figure 1.8 shows a picture of this version of the experimental apparatus. Moreover, the collaboration used a new backing for the target: a 20 μg/cm^2 thick carbon foil replaced the Al one, reducing the global thickness traversed by the protons that don't interact with the target. These modifications resulted in a different electron detection efficiency as a function of the separation angle.

The most recent measurement at the Atomki laboratory focused on the nuclear reaction ^{3}H$(p,\gamma)^{4}$He to investigate the He excited states instead of the Be ones [19]. The target for this measurement was a ^{3}H target absorbed in a 3 mg/cm^2 thick Ti layer evaporated onto a 0.4 mm thick Mo disk. The ^{3}H atoms density was 2.66×10^{20} atoms/cm^2, and the disk was cooled down using liquid N$_2$. The apparatus for e^+e^- pair detection was the same of the previous measurement.

1.2.2 First experiment

The first striking result on ^{8}Be IPC angular correlation obtained at Atomki was published in 2016 [16] by Krasznahorkay and coworkers. They studied the ^{7}Li$(p, e^+e^-)^8$Be reaction at $E_p = 0.441$ MeV and $E_p = 1.03$ MeV resonances to populate respectively the 17.6 MeV MIV and 18.15 MeV MIS 1^+ excited ^{8}Be states. They measured the angular correlation of the pairs originated in the decay of the two resonances and observed a deviation from the simulations based on Rose's IPC model only in the 18.15 MeV resonance.

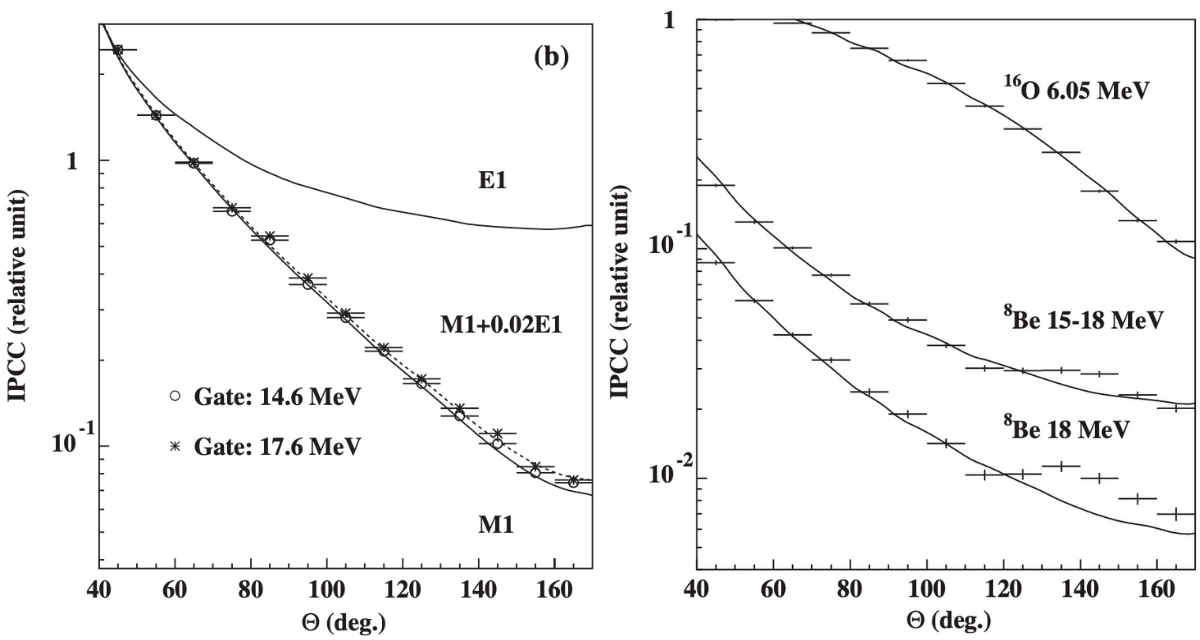

(a) (b)

Figure 1.9: (a) Measured angular correlation of the pairs created in 17.6 MeV $1^+ \to 0^+$ and 14.6 MeV $1^+ \to 2^+$ transitions. These values are compared to a simulation that assumes M1 (full line) and M1+E1 (dashed line) mixed transitions.
(b) Measured angular correlation of the pairs created in the 15-18 MeV region and 18 MeV transition. These values are compared to a simulation that assumes M1+E1 mixed transitions. The ^{16}O curve was used for a sanity check and compared to a simulation that assumes E0 transitions. Figures from [16].

Figure 1.9 shows the results of the measurement for both resonances. These plots show a slight deviation from the simulated M1 only curve in the case of 17.6 MeV transition around $\Theta = 110°$, but without any evident structure. This deviation can be explained by adding to the simulation a small amount of E1 transitions due to direct proton capture, which is dominated by transitions of that multipolarity [7]. Being the 18.15 MeV resonance larger than the 17.6 MeV one, the amount of E1 component expected is larger. In the simulations it was assumed to be 23% of the M1 component, but the data show a deviation from such simulations. The figure shows also a sanity check performed with the 6.05 MeV E0 transition in ^{16}O, which is due to the ^{19}F$(p,\alpha)^{16}$O reaction in the target contamination. In this case the angular correlation is in good agreement with the simulations.

Figure 1.10 shows the results of the same measurement performed at different proton beam energies. It is clear that the deviation happens only at proton energies near the resonance, and progressively disappear as this energy gets lower or higher. Notice that the deviation is bigger at $E_p = 1.1$ MeV because of the 70 keV proton energy loss in the target, meaning that the reaction happens at $E_p = 1.03$ MeV, i.e. the center of the resonance.

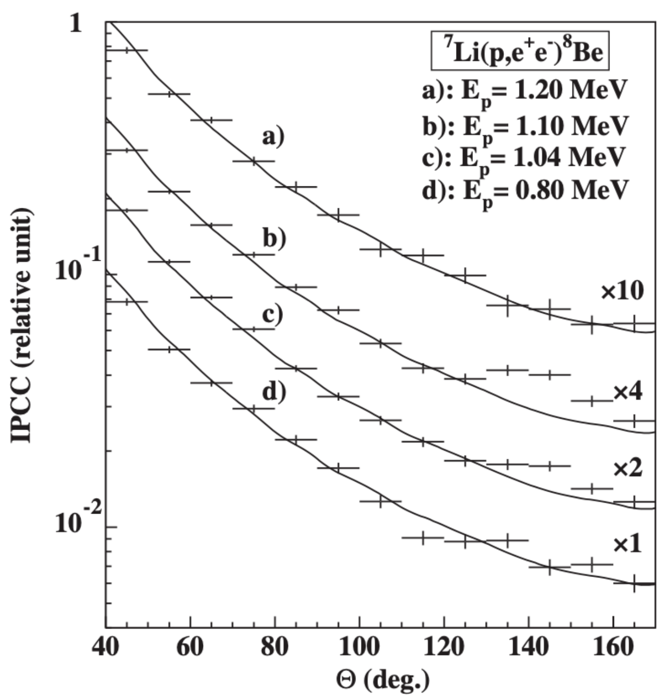

Figure 1.10: Measured angular correlation of the pairs created in the ^{7}Li$(p, e^+e^-)^8$Be reaction at different proton beam energies. The full curves represent the simulated IPC assuming M1+23%E1 mixed transitions. Curves are multiplied by a scale factor for better visualization. Figure from [16].

The peak measured at $E_p = 1.1$ MeV has a significance of 6.8 standard deviations. This deviation from the theory may be explained with the creation and subsequent decay of a light boson, called today X(17). Taking into account an IPC coefficient of 3.9×10^{-3} the Branching Ratio (BR) and mass of such particle were calculated to be 5.8×10^{-6} and 16.70 MeV/c^2 respectively. The collaboration calculated the significance of this excess with a χ^2 analysis, that was extended to study the mass of the hypothetical boson. They simulated masses in the range 15 MeV/c^2<m_X<17.5 MeV/c^2, and the mass that better fits the experimental data was 16.70 ± 0.35 MeV/c^2 with a $\chi^2/dof = 1.07$. The error quoted is statistical, and the uncertainty on the positioning of the detector, which is estimated to be $\Delta\Theta = 6°$, gives and additional 0.5 MeV/c^2 contribution. Figure 1.11 shows the angular correlation for different boson masses and the invariant mass distribution assuming a 16.6 MeV/c^2 boson mass. In both plots the data are in good agreement with the simulations that includes the IPC and the X(17) decay pairs.

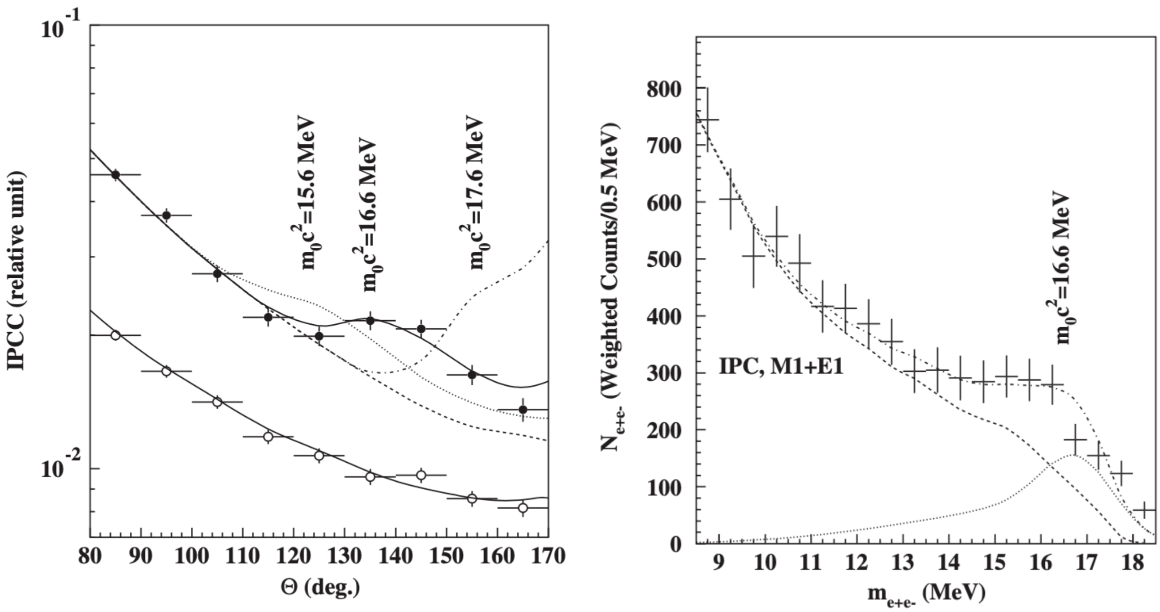

(a) (b)

Figure 1.11: (a) Experimental angular pair correlation at $E_p = 1.1$ MeV with $-0.5 \leq y \leq 0.5$ (closed circles) and $|y| \geq 0.5$ (open circles), where $y = (E_+ - E_-)/(E_+ + E_-)$ is the energy asymmetry, expected to be around 0 at an opening angle of 140°. The simulations includes IPC and X(17) decay pairs for different boson masses.
(b) Invariant mass distribution for 18.15 MeV transitions. The simulation includes IPC and X(17) decay pairs assuming a 16.6 MeV/c^2 boson mass. Figures from [16].

1.2.3 Latest results with ^{8}Be

The collaboration reinvestigated the anomaly in the same nuclear reaction in 2017 [17]. They used a new and more stable accelerator, and replaced the MWPC with DSSSD detectors. They used the HPGe photon detector to measure the photon spectrum at the two inspected proton beam energies, 441 keV and 1.1 MeV, both reported in figure 1.12. The broad peaks around 15 MeV are due to the transition to the first 2^+ excited state.

This transition is favored with respect to the one to the ground state when $E_p = 1.1$ MeV, with a BR of $\sim 70\%$. The situation is the opposite when $E_p = 441$ keV, where the BR of the transition to the 2^+ state is $\sim 30\%$.

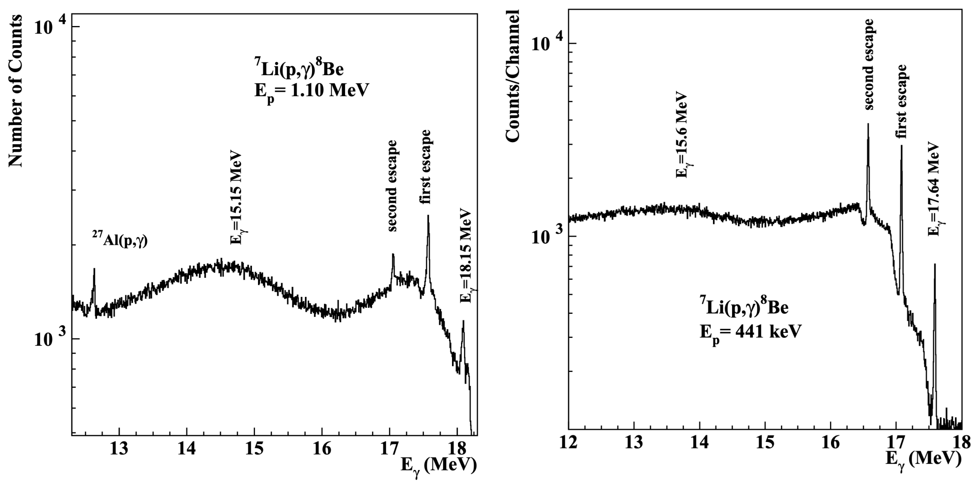

(a) (b)

Figure 1.12: Photon spectra measured at $E_p = 441$ keV (a) and $E_p = 1.1$ MeV (b). The peaks arise from the reaction of the proton in the Al substrate, the wide resonances at 15.15/15.6 MeV and the resonances at 17.6/18.15 MeV. The peaks due to first and second escape are also clearly visible. Such phenomena reduces the energy of 511 and 1022 keV respectively. Figures from [17].

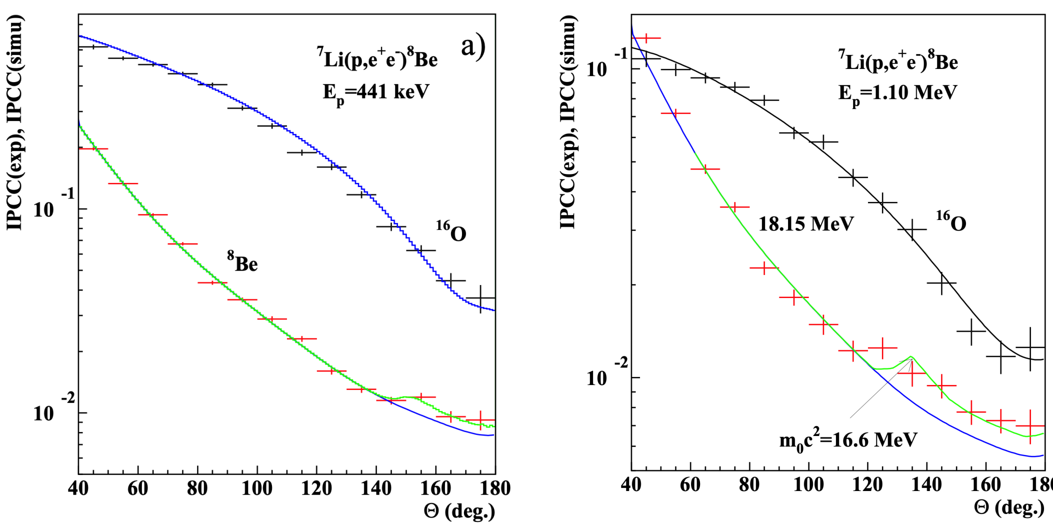

(a) (b)

Figure 1.13: Measured and simulated angular correlation of the e^+e^- pairs at $E_p = 441$ keV (a) and $E_p = 1.10$ MeV (b). Figures from [17].

The collaboration measured the pair angular correlation in the $^7\text{Li}(p, e^+e^-)^8\text{Be}$ reaction at both $E_p = 441$ keV and $E_p = 1.1$ MeV proton energies, and reported the results in figure 1.13. In this case the deviation from the simulated IPC, mixture of M1 and a small percentage of E1 transitions, is visible also in the MIV resonance, at a separation angle of $\sim 150°$, in contrast with the previous observation. This may be due to the improvement to the experimental apparatus. The peak is still visible in the MIS resonance.

The distribution of the angular correlation is well described by an exponentially falling distribution, extrapolated from the IPC simulation and the signal simulation of a boson decaying to e^+e^- pairs. The fit of such distribution is performed using the following probability density function (PDF):

$$PDF(e^+e^-) = N_{bkg} * PDF(IPC) + N_{sig} * PDF(signal) \tag{1.9}$$

where N_{sig} and N_{bkg} are the fitted number of background and signal events respectively. The 2D signal PDF is a function of the pair opening angle and the boson mass. The mass dependence is obtained from a linear interpolation of the pair opening angle distributions simulated for discrete particle masses. The background PDF was determined experimentally in the background region.

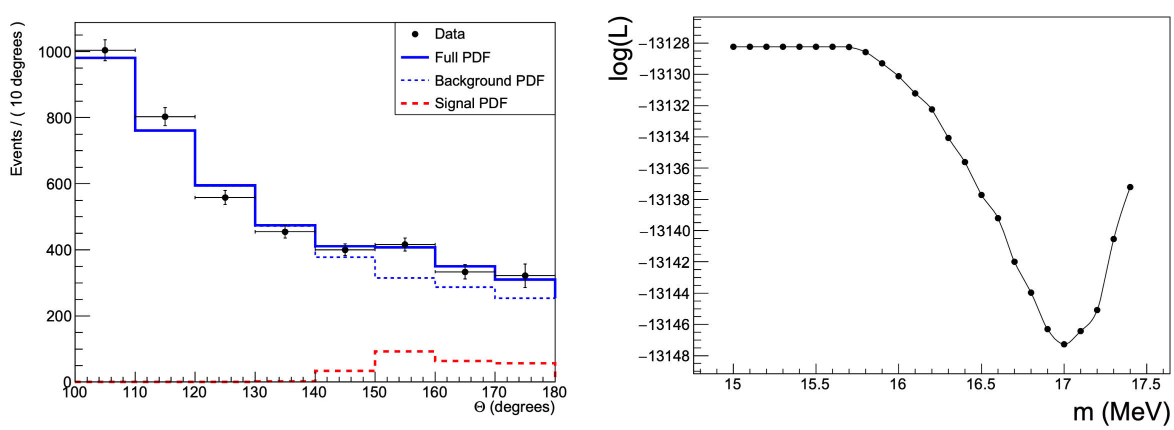

(a) (b)

Figure 1.14: (a) Fit of the pair correlation angle. The parameters to be tuned for the optimization are m, N_{sig}, N_{bkg}.
(b) Likelihood fit to the mass of the hypothetical X(17) boson. Figures from [17].

Figure 1.14 shows the results of the fit, from which the mass of the hypothetical X(17) boson is extrapolated. Such mass is $m_X = 17.0 \pm 0.2$ MeV$/c^2$. The BR of the boson decay in the 17.6 MeV state for the best fit is calculated to be 4.0×10^{-6}, in agreement with the result obtained for the 18.15 MeV state, which is 6.8×10^{-6}. These results are in good agreement with the prediction made by Feng and coworkers in [21]. More details about this topic in section 1.3.2.

Summary of ^{8}Be experiments

In 2018 the experimentalists at Atomki repeated the measurement at 18.15 MeV once more [18]. They improved the experimental apparatus by adding one more telescope and changing the backing of the Li target, as previously explained in section 1.2.1. They also developed a method to subtract the background from cosmic rays. They took background data for two weeks before and after the experiment, and subtracted them from the actual data. Moreover, they installed an active shield for cosmic rays suppression made by 12 pieces of $1.0 \times 4.5 \times 100$ cm^3 plastic scintillators placed above the spectrometer.

The experimental results were fit using the PDF in equation 1.9. They fitted also the data from the previous experiment with the same method, and reported the result of the two independent sets of measurement in table 1.1. Here the entry "previous results" refers to the old dataset with the old χ^2 analysis, "Exp1" refers to the same dataset but with the new likelihood analysis and "Exp2" refers to the new dataset with the new analysis. The best fit values for the particle mass in Exp1 and Exp2 are slightly different: this could be a result of the unstable beam position in Exp1.

	Previous result [16]	**Exp1 [16] [18]**	**Exp2 [18]**	**Average**
$\mathbf{m_X}$ **(MeV/c^2)**	16.7(51)	16.86(6)	17.17(7)	17.01(16)
$\mathbf{BR_X \times 10^6}$	5.8	6.8(10)	4.7(21)	6(1)
Significance (σ)	6.8	7.37	4.90	

Table 1.1: Summary of the Atomki experiments results. Exp1 refers to the old data set with the new fit. Data from [18]

Figure 1.15 shows the experimental results for both the old and the new dataset. The data are in good agreement, meaning that the result is reproducible. This is a further step in the direction of the existence of the hypothetical X(17) particle, which will be corroborated by another striking result obtained in the same laboratory but with another nuclear reaction, topic of section 1.2.4.

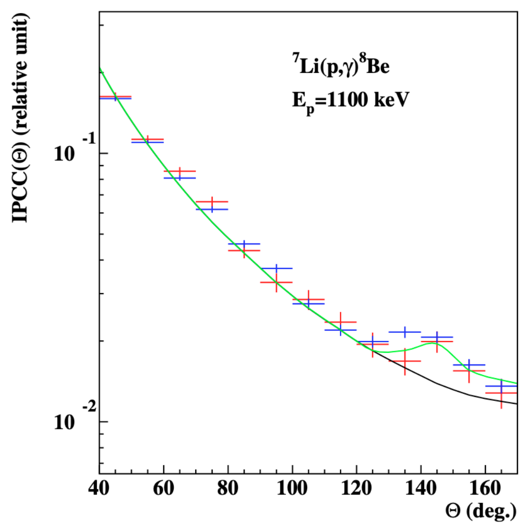

Figure 1.15: Measured angular correlation for old (blue) and new (red) data for the 18.15 MeV state transitions measured at Atomki. The black line represents the simulated background, and the green line the signal+background. Figure from [18].

1.2.4 Search for X(17) with ^{4}He

In 2019 the collaboration that observed the ^{8}Be anomaly conducted a search for the creation and decay of the hypothetical X(17) boson in the 21.01 MeV $0^- \to 0^+$ transition of ^{4}He [19, 22]. The experimental apparatus did not change from the previous ^{8}Be measurement except for the ^{3}H target. Also the cosmic rays background shielding and subtraction was the same.

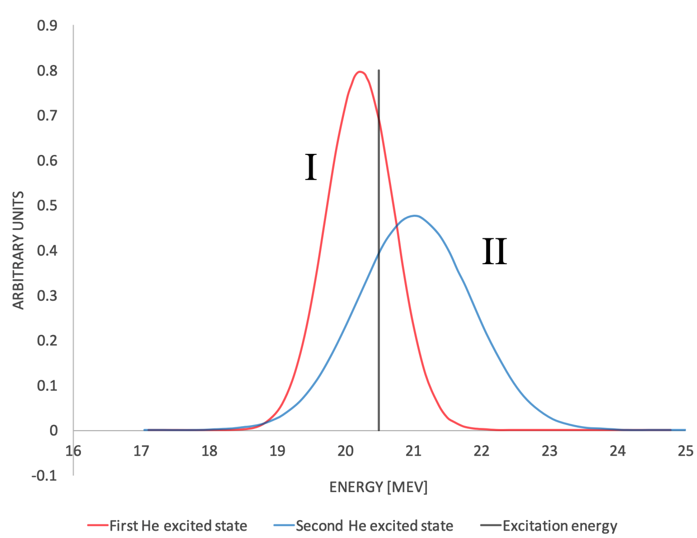

Figure 1.16: Normalized energy spectra of first (red) and second (blue) ^{4}He excited states. The black line highlights the 20.49 MeV excitation energy reached with a proton energy $E_p = 900$ keV.

They used the $^3H(p,\gamma)^4He$ reaction at $E_p = 900$ keV to populate the $\Gamma = 0.84$ MeV wide 0^- second excited state of ^{4}He, at $E = 21.01$ MeV. Actually the proton energy was below the threshold of the (p,n) reaction $E_{th} = 1.018$ MeV, thus the excitation energy was $E = 20.49$ MeV, slightly below the center of the resonance. Moreover, the investigated state overlaps with the first ^{4}He excited state $J^P = 0^+$ at $E = 20.21$ MeV, that has a width of $\Gamma = 0.50$ MeV. This means that also this state was partially populated, but its contribution gave a manageable background source to the e^+e^- spectrum. Figure 1.16 shows the two normalized ^{4}He excited states energy spectra and the excitation energy used in the experiment.

Figure 1.17 shows the results obtained from this measurement. Here the background is considered as the sum of the IPC and the conversion of photons on the target backing and experimental apparatus, the External Pair Creation (EPC). The IPC happens in the expected $0^+ \to 0^+$ E0 transition from the excited state to the ground state, and has been measured outside the signal region and extrapolated from a 4-th order exponential polynomial fit.

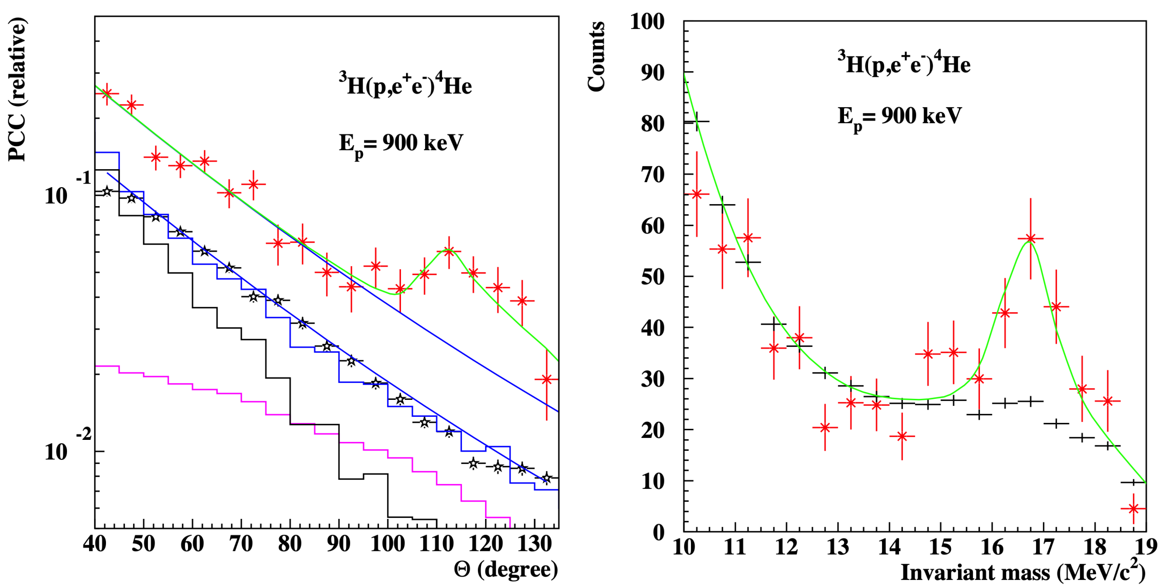

(a) (b)

Figure 1.17: Angular correlation (a) and invariant mass distribution (b) of the e^+e^- pairs generated by the decay of the 20.49 MeV state of ^{4}He, produced in the $^3H(p,\gamma)^4He$ reaction at $E_p = 900$ keV. The background is due to EPC (black histogram on the left plot) and IPC in E0 transition (magenta histogram). The measured background (black dots) is fitted by a 4-th order exponential polynomial (blue full curve). Figures from [22].

Also in this measurement there is an evident peak around $\Theta = 115°$, not included in the IPC background simulations and measurements. Such peak is evident also in the invariant mass distribution around 17 MeV/c^2, with a significance of 7.1 σ. The data have been fitted with the same method as for the ^{8}Be fit. The mass of the particle calculated from the invariant mass fit is $m_X = 17.00 \pm 0.13$ MeV/c^2, in agreement with previous results with ^{8}Be and with the result of the fit of the angular correlation, $m_X = 16.84 \pm 0.16$ MeV/c^2. The partial width of the X(17) decay is estimated to be $\Gamma_X = 3.9 \times 10^{-5}$ eV.

1.3 Theoretical interpretation of the Atomki result

At the time of the first experiment on ^{8}Be at Atomki there was no nuclear physics explanation for the observed excess. Since then many theoretical physicists around the world tried to explain this phenomenon, both in the nuclear and particle physics field. On one hand all the following Atomki measurements on ^{8}Be confirmed the first observation, and the peak observed in the ^{4}He measurement is in agreement with the hypothesis of the production of an intermediate particle. On the other hand, though, the nuclear physics model for the ^{8}Be has been improved, and it seems that a small peak-like structure in the angular correlation origins from higher order corrections to Rose's equation [1,23], in combination with the non optimal angular acceptance of the Atomki detectors.

Even though the nuclear physics theory improved, it still does not fully explain the data collected at Atomki. For this reason many new physics explanation have been proposed for this observation, mostly in the particle physics field. Among the most promising theories there is the hypothesis of the production of the X(17) boson mediator of a fifth fundamental force, proposed by Feng and coworkers in [2,21,24]. The existence of a new light vector boson is heavily challenged by numerous experimental constraints, summarized by Delle Rose and coworkers in [25], and to date none of the proposed explanations have been confirmed. More measurements to explore other nuclear reactions and other excitation energies are on the way to shed light on this mystery.

Table 1.2 reports a summary of the theories that will be presented in this section. I divided the discussion into particle and nuclear physics models, starting from the latter. The hypotheses are listed in order of plausibility given the Atomki observation.

Model	Process	Result
Higher order nuclear physics		
EFT [1]	$^7\mathrm{Li}(p, e^+e^-)^8\mathrm{Be}$	Significance of the anomaly reduced
NLO QED + 4π acceptance [23]	$^7\mathrm{Li}(p, e^+e^-)^8\mathrm{Be}$	Bump compatible with the anomaly
Single process [26]	$^7\mathrm{Li}(p, e^+e^-)^8\mathrm{Be}$ $^3\mathrm{H}(p, e^+e^-)^4\mathrm{He}$	Expected excess at angles compatible with the anomaly
Hard $\gamma\gamma$ process [27]	$^7\mathrm{Li}(p, e^+e^-)^8\mathrm{Be}$	In contrast with Atomki observation. Can be tested by a direct measurement of the $\gamma\gamma$ final state
Particle physics BSM		
New vector particle [21]	$^7\mathrm{Li}(p, e^+e^-)^8\mathrm{Be}$	Possible if gauge coupling with fermions is $g' \sim 10^{-3}$. Complies with experimental constraints, i.e. NA48/2 [28] (protophobic hypothesis, in contrast with [29])
	$^3\mathrm{H}(p, e^+e^-)^4\mathrm{He}$	Consistent with decay width measured at Atomki
	$^{11}\mathrm{B}(p, e^+e^-)^{12}\mathrm{C}$	Can be tested with a measurement of the width
New axial vector particle [30]	$^7\mathrm{Li}(p, e^+e^-)^8\mathrm{Be}$	Possible if gauge coupling with fermions is $g' \sim 10^{-4}$
	$^3\mathrm{H}(p, e^+e^-)^4\mathrm{He}$	Almost consistent with decay width measured at Atomki
	$^{11}\mathrm{B}(p, e^+e^-)^{12}\mathrm{C}$	Can be tested with a measurement of the width
New pseudoscalar particle [31]	$^7\mathrm{Li}(p, e^+e^-)^8\mathrm{Be}$	Possible if coupling with leptons and Higgs are similar. Can be tested with a He$\rightarrow \gamma\gamma$ measurement
	$^3\mathrm{H}(p, e^+e^-)^4\mathrm{He}$	Inconsistent with decay width measured at Atomki
New scalar particle	$^7\mathrm{Li}(p, e^+e^-)^8\mathrm{Be}$	Violates parity conservation

Table 1.2: Summary of the theoretical models presented in this chapter.

1.3.1 Improvement of ^{8}Be nuclear physics model

IPC cross section in ^{8}Be from EFT

After the publication of the first Atomki measurement, Zhang and Miller published a study in which they improve the $^7\mathrm{Li}(p, e^+e^-)^8\mathrm{Be}$ reaction model [1]. They added the photon emission anisotropy and the interference between different multipole transitions terms to the model used for the Atomki data. Moreover, they estimated the contribution of both E1 and E2 multipolarity to the cross section of the reaction, which turns out to be $\sim 50\%$ and $\sim 1\%$ respectively, in contrast with the 23% E1 contribution to the MIS transition estimated in the Atomki paper.

The model developed by Zhang and Miller is inspired by the Halo Effective Field Theory (EFT) [32] and calibrated on photon production data from the 90s published in [33–35] to predict the pair production cross section. Figure 1.18 shows the kinematics for the photon and pair production. The relevant degrees of freedom are θ for the photon and $\theta_\pm$, ϕ and E_+ for the e^+e^- pair.

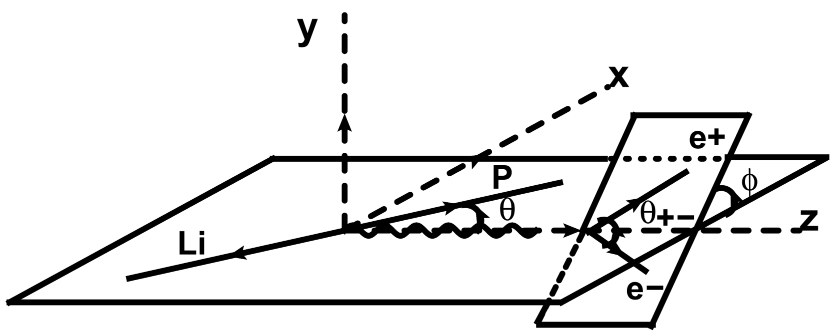

Figure 1.18: $^7\mathrm{Li}(p, e^+e^-)^8\mathrm{Be}$ reaction kinematics. Figure from [1].

They obtained the following analytical expression for the photon production cross section:

$$S = e^{2\pi\eta} E \times \frac{\mathrm{d}\sigma_\gamma}{\mathrm{d}\cos\theta}, \qquad \frac{\mathrm{d}\sigma_\gamma}{\mathrm{d}\cos\theta} = \frac{M}{4\pi}\frac{\omega}{p}\frac{1}{8}\sum_{a,\sigma,\lambda} |\mathcal{M}_\gamma|^2 \tag{1.10}$$

$$\sum_{a,\sigma,\lambda} |\mathcal{M}_\gamma|^2 = T_0 + T_1 P_1(\cos\theta) + T_2 P_2(\cos\theta) \tag{1.11}$$

Here ω is the photon energy, $M = M_n M_c/(M_n + M_c)$, M_n and M_c are the proton and Li masses, $k_c = Z_{\mathrm{Li}} Z_p \alpha_{em} M$ and $\eta = k_c/p$, p and E are the proton energy and momentum.

The indices are the particle spin projections (a for $J = 3/2$, σ for $J = 1/2$) and λ is the photon polarization. $P_n(\cos\theta)$ is the n-th Legendre polynomial and T_n are the coefficients that are combinations of the different multipolarities contributions (here M1, E1 and E2). Their interference give rise to the $\cos\theta$ modulation.

Figure 1.19 shows the photon production differential cross section versus the proton kinetic energy in the lab frame E_{lab}. Equation 1.10 contains the model parameters, that are fitted against the data from [33–35]. The other plots in the figure show also the coefficients $a_1 = T_1/T_0$, $a_2 = T_2/T_0$ and I(0°)/I(150°), that is the ratio between the cross section calculated at $\theta = 0°$ and $\theta = 150°$. The fit of the model, both with and without taking E2 transitions into consideration, agrees with the data except for the a_2 coefficient at high energy. Improved measurements are necessary to refine the model and determine a_2 more precisely.

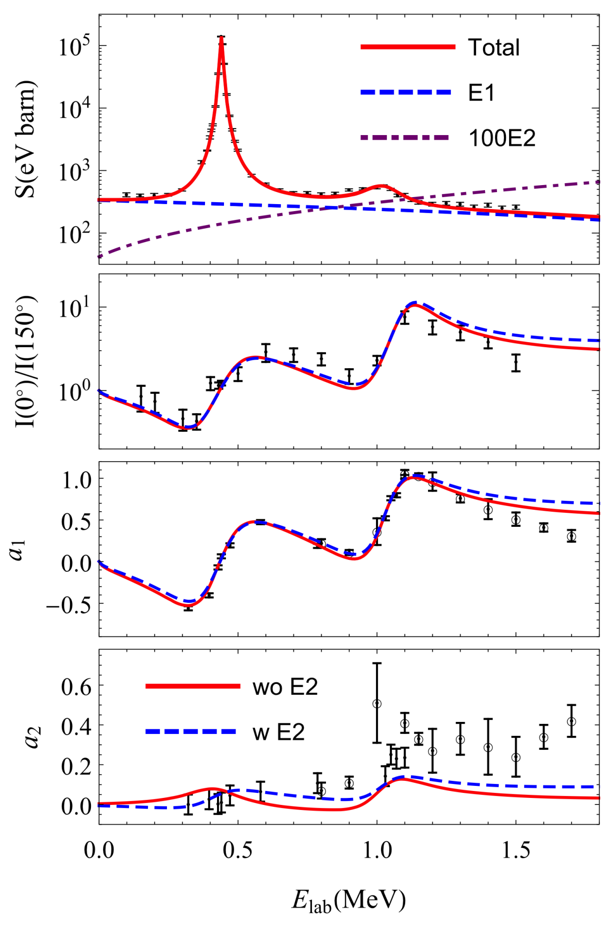

Figure 1.19: Photon production cross section and emission anisotropy vs proton kinetic energy in the lab frame. The model parameters are fitted against the data (black circles). Figure from [1].

By coupling the leptonic electromagnetic (EM) current with the nuclear EM current it is possible to obtain the expression for the pair production cross section (here $M_{\pm}$ is the pair invariant mass):

$$\begin{aligned} M_{\pm}^4 \sum |\mathcal{M}_{e^+e^-}|^2/2 = T_{0,0} + T_{0,2}\cos 2\phi + T_{1,0}P_1 + T_{2,0}P_2 + T_{2,2}P_2\cos 2\phi \\ + T_{3,1}\sin\theta\cos\phi + T_{4,1}\sin 2\phi\cos\phi \end{aligned} \tag{1.12}$$

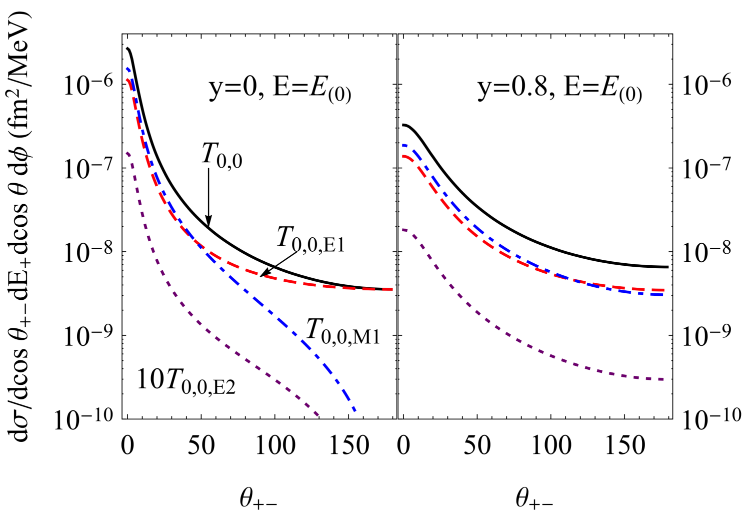

Figure 1.20: Different multipolarities contributions to the $T_{0,0}$ term in the pair production cross section vs separation angle at two different positron energies. Figure from [1].

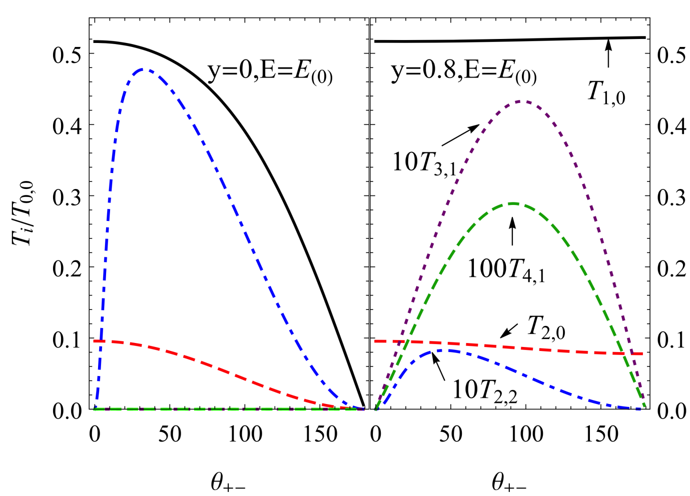

Figure 1.21: Ratios between $T_{i,j}$ coefficients and $T_{0,0}$ term in the pair production cross section vs separation angle at two different positron energies. Figure from [1].

Figure 1.20 and figure 1.21 report the plots of the coefficients in equation 1.12, showing the relative contributions of the different multipolarities. From this plot it is evident that the E1 contribution is as important as the M1 contribution (it is true for $y = \frac{E_+ - E_-}{E_+ + E_-} = 0.8$, but also in the integrated cross section), and is not limited to 23% as assumed in the measurement at Atomki. The estimate of the E2 contribution is $\sim$1% of the total.

Introducing a Form Factor (FF) to the resonance's EM coupling vertex may explain the anomaly observed in ^{8}Be transition. Zhang and Miller used a polynomial FF:

$$f(M_{\pm}^2) = 1 + f_1 r + f_2 r^2 + f_3 r^3 \tag{1.13}$$

where $r = M_{\pm}^2/\Lambda^2$ and $\Lambda = 20$ MeV$/c^2$. Figure 1.22 shows the differential cross sections for invariant mass and separation angle fitted on the data collected at Atomki. The anomaly is explained by the introduction of a FF, but the value obtained for such FF is in contrast with all the previous observations in nuclear physics. In conclusion, the anomaly could not be explained by any nuclear effect known at the time of this study, even with the introduction of a form factor for the M1 transition. Anyway, the improvements of the existing model for the inspected reaction helped to reduce the significance of the observed excess, and can be useful for future measurements.

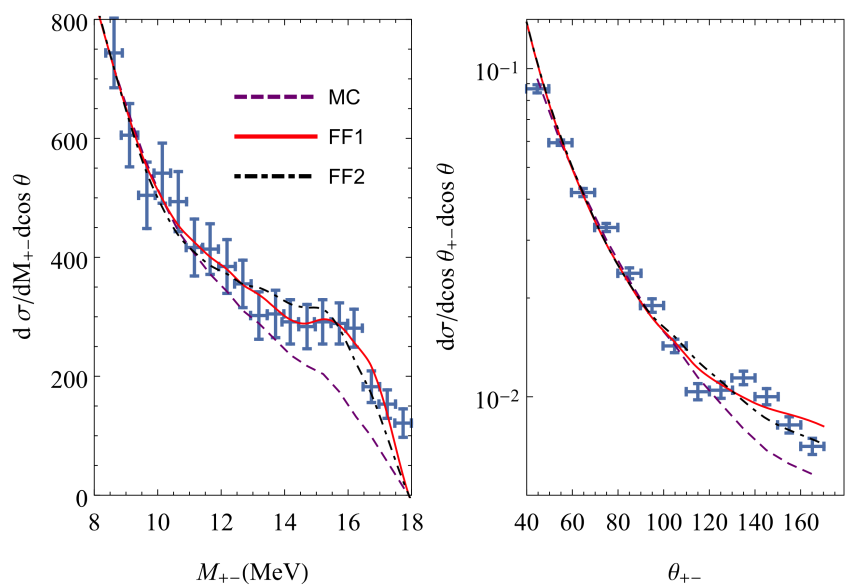

Figure 1.22: Pair production cross section with the introduction of a form factor. Figure from [1].

Higher order calculations in ^{8}Be IPC

The result obtained by Zhang and Miller was a starting point for other studies in the nuclear physics community, since it goes in the direction of a non BSM explanation of the measurements at Atomki. Aleksejevs and coworkers studied in 2021 the interference terms and the second order corrections to the Born approximation used by the collaboration at Atomki [23]. The Next-to-the-Leading-Order (NLO) quantum electrodynamics (QED) model of the ^{8}Be* decay gives a contribution to the doubly differential decay rate:

$$\frac{\mathrm{d}^2\Gamma}{\mathrm{d}\theta_+\mathrm{d}\theta_-} = \left(|M_{LO}|^2 + 2\Re[M_{LO}M^+_{NLO}]\right)\Phi \tag{1.14}$$

where $M_{(N)LO}$ are the matrix elements and Φ is the phase space element, that can be written as follows:

$$\Phi = \frac{1}{(2\pi)^3}\frac{J}{8m_{\mathrm{Be}^*}}\frac{E_-^2}{E_{\mathrm{Be}}}\frac{\sin\theta_-}{\sin\theta_+}, \tag{1.15}$$

$$J = \frac{\sin^2(\theta_+ + \theta_-)}{2R\sin^2\theta_-}\left[\frac{m_{\mathrm{Be}^*}}{(\cos(\theta_+ + \theta_-) - 1)}\left(\frac{m_{\mathrm{Be}^*}\sin(\theta_+ + \theta_-)}{\tan\theta_-} - R\right) - m_{\mathrm{Be}}^2\right] \tag{1.16}$$

$$R = \left\{m_{\mathrm{Be}}^2 + \frac{\sin\theta_+}{\sin\theta_-}\left(2m_{\mathrm{Be}^*} + m_{\mathrm{Be}}^2\frac{\sin\theta_+}{\sin\theta_-}\right) + (m_{\mathrm{Be}^*}^2 - m_{\mathrm{Be}}^2)\frac{\sin(2\theta_+ + \theta_-)}{\sin\theta_-}\right\}^{1/2} \tag{1.17}$$

They also implemented a MC simulation of the Atomki detector based on the information published in [15]. They fitted the simulated distributions of the opening angle with two variable parameters: the normalization of the Born contribution and the coefficient of the interference term.

Figure 1.23 shows the results of this simulation, along with the result of the predicted invariant mass distribution. This distribution is smeared with a resolution function that scales with the boson mass, and is extrapolated from the detector mass resolution at $\bar{m} = 16.7$ MeV$/c^2$ known from [16]. The smearing function is as follows:

$$g_{m_0}(m) = \mathrm{f}\left(\frac{m - m_0}{m_0}\bar{m} + \bar{m}\right) \tag{1.18}$$

where m_0 is the true e^+e^- mass and m is the measured mass. The plots in figure report also the original data collected at Atomki and the LO and NLO contributions to the simulation.

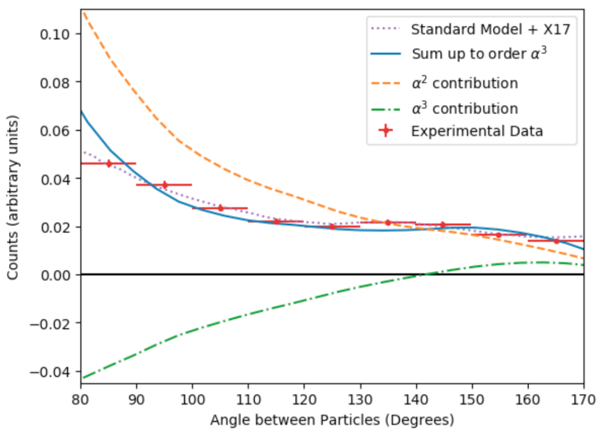

(a)

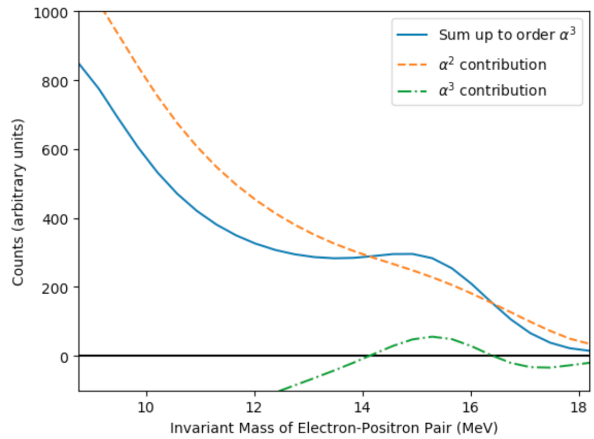

(b)

Figure 1.23: (a) Angular distribution from MC simulation result after applying detector acceptance and disparity limiting cuts. The data collected at Atomki are also reported on the same plot (red cross), as well as the their fit assuming the X(17) existence (purple dots).
(b) Invariant mass distribution from theoretical predictions. The plots report the contributions from both LO (orange dotted line) and NLO (green dotted line), as well as their sum. Figures from [23].

There is an evident bump in the predicted invariant mass distribution. This appears without requiring the presence of a new particle, and shows how non-resonant mixed SM processes can produce an excess in the measurement of the $^7\mathrm{Li}(p, e^+e^-)^8\mathrm{Be}$ reaction. Much of this effect is connected to the non uniformity in the angular acceptance of the detector. It is in fact highly suppressed when the simulation is run with a 4π acceptance. Thus, an independent measurement of the ^{8}Be nuclear reaction with a different angular acceptance can discriminate between a resonant and a non-resonant contribution to the IPC angular distribution.

Single process model for $^7\mathbf{Li}(p, e^+e^-)^8\mathbf{Be}$ reaction

In 2020 Kálmán and Keszthelyi inspected the possibility that the anomaly is generated by higher order nuclear physics processes [26]. The examined process is supposed to happen in two consecutive steps: first the creation of the excited state, and then the pair creation, which is a second order electromagnetic scattering process. The energy of the resonantly excited transition is $\Delta = E_+ + E_-$, sum of electron and positron energies.

Higher order reactions happen in one single process, in which the creation of the new nucleus and the pair are governed by strong and electromagnetic interactions. They have local maxima around a definite and sometimes large opening angle, and may be partly responsible for the observed enhancement in the IPC spectrum. The usual IPC is described by the interaction U^2_{EM}, whose matrix element $U^2_{EM,\nu\mu}$ contains the Green function. The transition wavenumber in this function is $K_{\alpha\beta} = |\Delta E_{\alpha\beta}|/(\hbar c)$, where $\Delta E_{\alpha\beta}$ is the energy change in the $\alpha\beta$ transition. By using plane waves and expanding the Green function in spherical harmonics the authors of this study obtained an expression for the matrix element:

$$U^2_{EM,\nu\mu} \sim \frac{1}{K_{\alpha\beta}\left(K_{\alpha\beta^2} - q^2\right)}\left(\frac{q}{K_{\alpha\beta}}\right)^L \tag{1.19}$$

where $q = k_+ + k_- + 2k_+k_- \cos\Theta$, Θ is the e^+e^- opening angle and k_- and k_+ are the particles momenta. In higher order processes $|\Delta E_{\alpha\beta}| \to 0$ so the term $K_{\alpha\beta^2} - q^2 \to -q^2$ decreases with increasing Θ, and the matrix element increases, contrary to what happens in usual IPC. There is also the possibility that $|\Delta E_{\alpha\beta}| < \Delta$, so that the condition $K^2_{\alpha\beta} - q^2 = 0$ determines the angles at which singularities appear:

$$\Theta = \arccos\left[\frac{K^2_{\alpha\beta} - (k^2_- + k^2_+)}{2k_-k_+}\right] \tag{1.20}$$

The minimum angle Θ_m of a possible singularity is at $k_- = k_+$.

The singularities are moderated into peaks that appear with a transition probability per unit time:

$$W_{fi} = \frac{2\pi}{\hbar}\sum_f \int\int |T_{fi}|^2 \delta(E) \frac{V^2}{(2\pi)^6} \mathrm{d}\mathbf{k}_+ \mathrm{d}\mathbf{k}_- \tag{1.21}$$

where $\delta(E) = \delta(E_- + E_+ + E_f - \Delta)$, V is the volume of normalization and E_f is the final states energy. T_{fi} may have many relevant terms $T^{(n)}_{fi}$, where n is the order. The first term inspected is the third order one. Here the $K_{\alpha\beta} \to 0$ approximation is valid. This term increases with increasing Θ.

The strong interaction leads to an excited state $|n\rangle$ of width Γ_n and energy $E_{n\nu}$. In the case of ^{8}Be there are two interesting resonant excitation with $l = 1, 2$. The expression for the matrix element in this case, considering $n = r_l$, is the following:

$$T_{fi}^{(3,r_l)} = U_{EM,fr_l}^{(2)} V_{st,r_l i} \frac{\Gamma_{r_l} - i d_l}{(d_l^2 + \Gamma_{r_l}^2)} \tag{1.22}$$

where d_l is the detuning, that depends on the proton energy loss in the target, and $V_{st,r_l i}$ is the matrix element of the strong interaction. This term decreases with increasing Θ. In the off resonance case it is written as follows:

$$T_{fi}^{(3,n)} = U_{EM,fn}^{(2)} \frac{V_{st,ni}}{i(\varepsilon_{n0} - \Delta_0 - \epsilon_{0l})} \tag{1.23}$$

where ϵ and ε indicates the center of the energy distribution of the proton and the state respectively, while Δ is the difference between initial and final state energy. This off resonance matrix element can have a peaked Θ dependence.

The same can also happen in the case of 4th order transitions between $|n\rangle$ and $|j\rangle$ nuclear states. The matrix element is as follows:

$$T_{fi}^{(4,jn)} = V_{st,fj} \frac{U_{EM,jn}^{(2)}}{i\varepsilon_{j0}} \frac{V_{st,ni}}{i(\varepsilon_{n0} - \Delta_0 - \epsilon_{0l})} \tag{1.24}$$

By using the approximations $|V_{st,r_l i}(\Gamma_{r_l} - i d_l)| \gg |V_{st,ni}/(\varepsilon_{n0} - \Delta_0 - \epsilon_{0l})|$ and $r_{r_l} \gg r_{jn}$ is it possible to write the following relation:

$$\left| T_{fi}^{(3,r_l)} + \sum_{j,n} T_{fi}^{(4,jn)} \right| = r_{r_l}^2 + \sum_{j,n} 2 r_{jn} r_{r_l} \cos\left(\varphi r_l - \varphi_{jn}\right) \tag{1.25}$$

where $\varphi_{r_l} = \varphi_{r_l 0} - \arctan(d_l/\Gamma_{r_l})$.

In the case of ^{4}He the 4th order process happens through the emission of a soft E2 photon. The corresponding matrix element is the following:

$$T_{fi}^{(4,jn)} = V_{\gamma,fj} \frac{U_{EM,j1}^{(2)}}{i\varepsilon_{j0}} \frac{V_{st,li}}{\Gamma_1} \tag{1.26}$$

where $V_{\gamma,fj}$ is the matrix element of E2 photon coupling. In ^{8}Be transitions the dominant term in the $T_{fi}^{(3)}$ matrix is $T_{fi}^{(3,r_l)}$, while the dominant terms in $T_{fi}^{(4,jn)}$ are the ones related to states 2 and 3. If $k_+ = k_-$ the respective minimum angles are $\Theta_{2,m} = 146.2°$ and $\Theta_{3,m} = 144.2°$, compatible with the data collected at Atomki. The transitions involved in ^{4}He are the ones related to states 2, 3 and 4, and the corresponding angles are respectively $\Theta_{2,m} = 138.7°$, $\Theta_{3,m} = 131.2°$, $\Theta_{4,m} = 123.5°$, to be compared to $\Theta = 115°$ observed at

Atomki. The uncertainty on these predictions is 12° in every case except for $\Theta_{4,m}$, for which it is 32°.

In conclusion there is the possibility to describe the anomaly in the usual IPC decay with a single process higher order reaction. The possible peaks in ^{8}Be transitions have been calculated to be at $\Theta_{2,m} = 146.2°$ and $\Theta_{3,m} = 144.2°$, similar to the angle at which Atomki observed the anomaly. The same explanation can be used to quantitatively explain the anomaly observed in ^{4}He too.

Modified Bethe-Heitler approach in a hard $\gamma\gamma$ process

Koch published a paper in 2021 in which he explores the possibility that the anomaly is due to a nuclear decay chain, and a subsequent conversion of the two resulting high energy γ in a e^+e^- pair [27]. The interaction between two electromagnetic waves is forbidden by classical physics, but in QED the production of an e^+e^- pair from a two photons interaction is possible. This has been confirmed over the years by successful experimental tests (see references in [27]). The IPC reaction is similar to the Bethe-Heitler (BH) process, the only difference being the initial state. Koch investigated an alternative explanation of the X(17) puzzle, adding an intermediate nuclear state in the decay chain of ^{8}Be*. He did this by studying a modified Bethe-Heitler (MBH) process, sketched in figure 1.24.

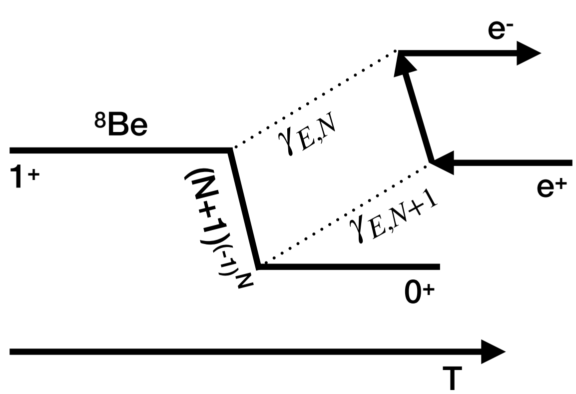

Figure 1.24: Feynman diagram of the Modified Bethe-Heitler process.

The goal of this study is to show whether the MBH process can give experimental signatures similar to the Atomki anomaly. It is based on three ingredients: a broad intermediate state, the orientation of the nuclear multipole coefficients due to a photon emission, the energy and momentum conservation. The process is explored in an on shell approximation. The intermediate state has to be broad because the two photons must be emitted almost simultaneously, i.e. with a short time delay $\Delta t \sim \frac{1}{\Gamma}$. There are three known intermediate states between the excited and the ground states: $\Delta M_{23} = 3.03$ MeV, $\Delta M_{23} = 16.63$ MeV, $\Delta M_{23} = 11.35$ MeV above the ground state. The best candidate is the broadest one, $M_{23} = 11.35$ MeV, whose width is $\Gamma_{4+} = 3.5$ MeV. The transitions studied in this paper are the following:

$$1^+ \to 4^+ \qquad \begin{aligned} &\Delta M_{12} = 6.8 \text{ MeV} \\ &\Delta N = 3 \\ &\Delta T = 0 \end{aligned} \qquad 4^+ \to 0^+ \qquad \begin{aligned} &\Delta M_{23} = 11.35 \text{ MeV} \\ &\Delta N = 4 \\ &\Delta T = 0 \end{aligned} \tag{1.27}$$

$$1^+ \to 4^+ \qquad \begin{aligned} &\Delta M_{12} = 6.3 \text{ MeV} \\ &\Delta N = 3 \\ &\Delta T = 1 \end{aligned} \qquad 4^+ \to 0^+ \qquad \begin{aligned} &\Delta M_{23} = 11.35 \text{ MeV} \\ &\Delta N = 4 \\ &\Delta T = 0 \end{aligned} \tag{1.28}$$

where transition 1.27 and transition 1.28 respectively conserve and violate isospin.

Koch showed that the two photons are emitted at a preferred relative angle θ_{rel}. The calculated angular distribution of a single radiation is the following:

$$\frac{\mathrm{d}P_{l0}}{\mathrm{d}\theta} \sim \sin(\theta)|a_{l0}|^2|\vec{X}_{l0}(\theta)|^2 \tag{1.29}$$

where $\vec{X}_{l0}(\theta)$ is proportional to the angular momentum operator acting on a spherical harmonic function Y_{l0} and $a_{l0} \neq 0$ is a multipole coefficient. From equation 1.29 it turns out that the most likely large relative angles with $\theta > 90°$ are the following:

$$\theta_{rel} \pm \delta\theta_{rel} = \begin{cases} (144 \pm 14)^\circ & \text{for} \quad N = 3, \\ (152 \pm 11)^\circ & \text{for} \quad N = 4, \\ \quad ... \end{cases} \tag{1.30}$$

The kinematics of the process is described by the following momenta: p_1 (^{8}Be initial state), p_2 (intermediate state), p_3 (final state), k_1 (first photon), k_2 (second photon), q_1 (outgoing positron), q_2 (intermediate lepton), q_3 (outgoing electron). The following approximations are allowed:

$$p_i^2 \gg (p_i - p_j)|_{i \neq j}^2 \gg m^2 \tag{1.31}$$

where m is the electron mass and all the particles are on shell. The invariant mass of the e^+e^- pair, under the aforementioned approximations, is then:

$$m_X^2 = (q_1 + q_3)^2 = 4(\Delta M_{12})(E_{13} - \Delta M_{12}) \sin^2\left(\frac{\theta}{2}\right) \tag{1.32}$$

where $\Delta M_{12} = \sqrt{p_1^2} - \sqrt{p_2^2}$ and $E_{13} - \Delta M_{12} = \Delta M_{23} = \sqrt{p_2^2} - \sqrt{p_3^2}$. Figure 1.25 shows the plot of the invariant mass m_X as a function of the pair separation angle θ_{rel}. The curves that represent the processes 1.27 and 1.28 are both in agreement with the experimental results within the error, also reported in the plot.

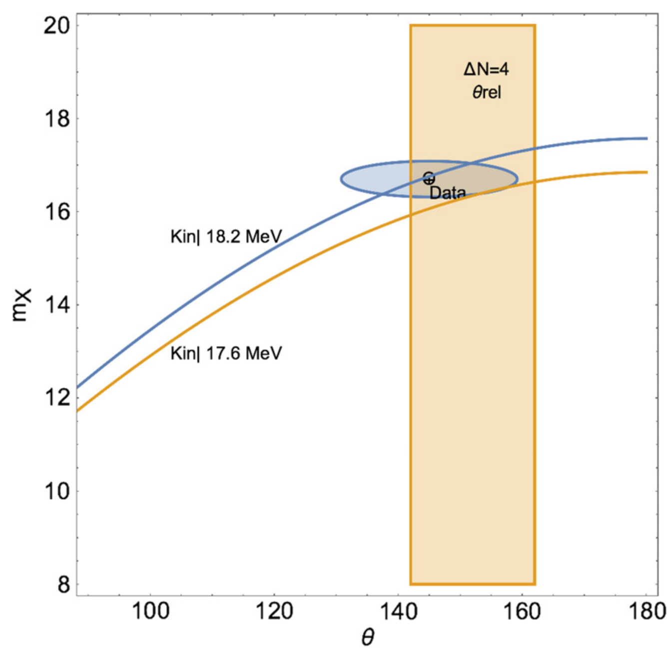

Figure 1.25: Invariant mass m_X as a function of the relative angle θ_{rel}. The curves represent the isospin conserving transition 1.27 (blue curve) and the isospin violating transition 1.28 (orange curve). The elliptic contour shows experimental results with errors, and the vertical orange region is compatible with the $\Delta N = 4$ transitions. Figure from [27].

Koch evaluated also the conversion probability of the hard $\gamma + \gamma \to e^+ + e^-$ process. The calculated total cross section is $\sigma = 3.5 \cdot 10^{-6}$ MeV^{-2}, and the conversion probability can be estimated as follows:

$$p_{\gamma+\gamma\to e^{+}+e^{-}} \approx \frac{\sigma}{A_t} \cdot F \tag{1.33}$$

where $A_t \approx \pi r_N^2$ is the collision transversal area and F is a suppression factor due to non simultaneous emission of both γ. This probability turns out to be $7 \cdot 10^{-4}$, below the IPC probability, which he estimates as $25 \cdot 10^{-4}$. However, the examined process is more concentrated in the signal region, while the IPC has a strong peak at low relative angles.

The X(17) excess was observed in an isospin conserving transition (18.15 MeV initial state) but was less significative in the isospin violating one (17.64 MeV initial state). However, this characteristic does not emerge from this study, and this is a strong argument against a solution of the X(17) puzzle with a simple MBH process, even though the kinematic agreement is good. Anyway, a simple direct test of this hypothesis made by measuring the angular distribution in the two γ final state of the ^{8}Be transitions can give a definitive answer.

1.3.2 Possible particle physics interpretations

The anomaly in ^{8}Be and ^{4}He transitions raised the interest not only of the nuclear physics community. Many particle physicists around the world, in fact, tried to explain the results obtained at Atomki through the creation of a new BSM light boson.

Nature of the hypothetical boson and constraints on its couplings

Delle Rose and coworkers in 2019 published a study in which they inspect the nature of the hypothetical X(17) boson in BSM frameworks [25]. The candidates for the X(17) boson are four, depending on its spin-parity: scalar or pseudoscalar particle if the spin is 0, vector or axial vector if the spin is 1. In the scalar case $J^P = 0^+$, which implies that the emitted boson has angular momentum $L = 1$ since the ^{8}Be*$\to$^{8}Be transition is $J^P(1^+ \to 0^+)$. From parity conservation, it should have $P = (-1)^L = -1$, in contrast with the assumptions of it being a 0^+ scalar so, in a situation in which the parity is conserved, the particle cannot be a scalar. In the pseudoscalar case $J^P = 0^-$, and the angular momentum should be $L = 1$. Ellwanger and Moretti showed in [31] that this is possible if the Yukawa couplings with the SM fermions are of the same order of the ones with the SM Higgs. A lot of studies focused on the vector case [2, 21, 36–43], and it was shown that it can be valid if its coupling is $g' \sim 10^{-3}$. The pure axial vector case is also possible if its coupling is $g' \sim 10^{-4}$, as showed in [30, 44].

The experimental constraints on the pseudoscalar hypothesis concern the reduced couplings ξ_q and ξ_l of a pseudoscalar to quarks and leptons respectively, and are the following:

$$\xi_u + \xi_d \sim 0.6, \qquad \xi_e > 4 \tag{1.34}$$

The experimentalists at Atomki can confirm or disprove the pseudoscalar hypothesis with their already foreseen measurement of the ^{4}He$\rightarrow \gamma\gamma$ decay. The decay of a vector boson in 2 photons is forbidden by the Landau-Yang theorem, but it is allowed for a pseudoscalar particle. If this will be the case, the 2 photons angular correlation will peak at $\cos\theta = 1 - M_A^2/(2E_\gamma E_{\gamma'})$.

In the vector hypothesis, where Z' is the new vector boson, the experimental constraints can be summarised as follows:

$$|2C_{u,V} + C_{d,V}| \lesssim \frac{3.6 \times 10^{-4}}{\sqrt{BR(Z' \to e^+e^-)}} \tag{1.35}$$

$$\frac{C_{e,V}^2 + C_{e,A}^2}{BR(Z' \to e^+e^-)} \gtrsim 1.6 \times 10^{-8} \qquad \left(C_{e,V}^2 + C_{e,A}^2\right) BR(Z' \to e^+e^-) \lesssim 3.7 \times 10^{-7} \tag{1.36}$$

for quarks and leptons couplings respectively. Here the subscripts V and A refer to vector and axial component of the boson respectively. The coupling with quarks is constrained by the $\pi^0 \to Z' + \gamma$ searches at the NA48/2 experiment [28, 45]. The lower limit on the coupling to the leptons comes from the non observation of the bump in the NA64 electron beam dump experiment in [46]. The upper limit is set from the KLOE experiment [47] from processes like $e^+e^- \to \gamma, Z, Z' \to e^+e^-$ at electron-positron collider, that would be sensitive to a new spin 1 gauge boson.

Another constraint for lepton coupling of the hypothetical boson can be set from the $(g-2)$ anomaly in muons and electrons. The muon anomalous magnetic dipole moment is a long standing anomaly in particle physics: there is a discrepancy between the SM prediction and experimental measurements. Such discrepancy was measured at the Brookhaven National Laboratory to a precision of 0.54 ppm, and the average of the experimental results published in [48–50] was different from the SM prediction by $\sim 3.6\sigma$.

A recent measurement of the magnetic dipole moment of the muon at Fermilab by the Muon $(g-2)$ collaboration was published in 2021 [51]. It increased the tension between experiment and theory up to 4.2σ. The combination with previous measurements with both μ^+ and μ^- gave the following result:

$$a_\mu = (g_\mu - 2)/2 = 116592061(41) \times 10^{-11} \tag{1.37}$$

The contribution of a Z' to the magnetic moment δa_l is constrained, for $M_{Z'} \simeq 17$ MeV$/c^2$, by the following relations:

$$\delta a_e = 7.6 \times 10^{-6} C_{e,V}^2 - 3.8 \times 10^{-5} C_{e,A}^2 \simeq -10.5(8.1) \times 10^{-13} \tag{1.38}$$

$$\delta a_\mu = 0.009 C_{\mu,V}^2 - C_{\mu,A}^2 \leq 2.9(90) \times 10^{-9} \tag{1.39}$$

Several BSM scenarios have been investigated for the vector hypothesis. The first one is a generic extension to the SM with a new Abelian U(1)' group with a light and weakly interacting boson. There are three different situations at this point: the first one is that the SM scalar sector is unchanged (the mass of the Z' is entirely generated in the dark sector); the second one is that the SM scalar sector is extended with an additional Higgs doublet and standard Yukawa interactions (Z' mass from both dark and electroweak sector); the third one is that the SM scalar sector has a single Higgs doublet but more complicated Yukawa structures. The simplest case is the second one, for which an acceptable range of couplings is provided by Feng and coworkers in [2, 21]:

$$|C_{p,V}| \lesssim 1.2 \times 10^{-3} e \tag{1.40}$$

$$|C_{n,V}| = (2 - 10) \times 10^{-3} e \tag{1.41}$$

$$|C_{e,V}| = (0.2 - 1.4) \times 10^{-3} e \tag{1.42}$$

$$\sqrt{|C_{\nu,V} C_{e,V}|} \lesssim 3 \times 10^{-4} e \tag{1.43}$$

Here it is assumed $BR(Z' \to e^+e^-) = 1$. In this scenario the vector boson is dubbed protophobic, since its coupling with protons is almost null. These conditions assures that the Atomki anomaly is well reproduced and avoid the strong constraint from the NA48/2 data on the $\pi^0 \to Z'\gamma$ decay.

The list of possible theoretical interpretations of the anomaly observed at Atomki that the authors provided is extensive and covers several scenarios. All of them are proven to be feasible within the constraints set up by previous experiments, but none of them can be proved with the actual experimental data. For this reason new measurements are welcome, since they can help to improve the set of constraints on the coupling of the hypothetical boson, and possibly exclude or confirm some of the theoretical models.

Search for a dynamical evidence of the X(17) existence

Feng and coworkers proposed in [2, 21] an explanation for both the ^{4}He and ^{8}Be anomalies that is based on the existence of a fifth fundamental force mediated by the X(17) vector protophobic boson. I already discussed the constraints on the couplings for such boson in the previous paragraph. They also published a study in 2020 [24] in which they examine if the available results can give a dynamical evidence for the existence of the new particle. The consistence between the results obtained for the two different nuclear transitions provides a kinematical evidence for the existence of a boson with 17 MeV/c^2 mass, so it is reasonable to look also for a dynamical evidence. The goal of the study is to predict the decay rates of several nuclear reactions assuming different particle characteristics so that, by performing new experiments, it is possible to exclude or confirm the different scenarios.

The authors inspected ^{4}He, ^{8}Be and ^{12}C excited nuclei, and different J^P for the hypothetical boson, considering the possibility of the particle to be a scalar, pseudoscalar, vector or axial vector. Assuming parity conservation the scalar case is forbidden and the pseudoscalar case is disfavored. The vector gauge boson hypothesis that they proposed to explain the ^{8}Be anomaly works also for the ^{4}He anomaly. It is not possible to know from which of the two ^{4}He excited states the anomaly rises, since the measurement was performed at an energy between the 0^+ and 0^- resonances. Because of this there is no possibility to safely exclude one of the hypotheses. If the X(17) is produced both in ^{4}He 0^- state and in ^{8}Be states it can be a pseudoscalar or axial vector, while if it is produced both in ^{4}He 0^+ state and in ^{8}Be states it can only be a vector.

In the X(17) pseudoscalar hypothesis, the ratio of the decay rates for ^{4}He and ^{8}Be would be:

$$\frac{\Gamma_P^{^8\mathrm{Be}}}{\Gamma_P^{^4\mathrm{He}}} \approx 10^{-6} \tag{1.44}$$

which is inconsistent with the experimental result $\Gamma_P^{^8\mathrm{Be}} \sim \Gamma_P^{^4\mathrm{He}}$. All the predicted decay widths depend on the X(17) mass, which has been assumed to be 17 MeV/c^2 for these estimates. In the axial vector hypothesis the ratios are:

$$\frac{\Gamma_A^{^8\mathrm{Be}}}{\Gamma_A^{^{12}\mathrm{C}}} \approx 10^3, \qquad \frac{\Gamma_A^{^8\mathrm{Be}}}{\Gamma_A^{^4\mathrm{He}}} \approx 10^{-2} \tag{1.45}$$

which is possible within the uncertainties of the measurements of ^{4}He and ^{8}Be, and could be confirmed or disproved by a measurement of ^{12}C transitions. In the vector hypothesis the decay widths are bounded by the nucleon couplings constraints from other experiments, as previously reported. Most noticeably is the proton coupling constraint from a NA48/2 result published in [28] on $\pi \to X\gamma$, that makes the X(17) vector boson protophobic. An additional constraint is given by the experimental ^{8}Be measurement at Atomki, that requires $\varepsilon_n \approx 10^{-2}$. For a vector X(17) boson that can explain the measured ^{8}Be anomaly, the predicted decay widths for ^{4}He and ^{12}C are:

$$\Gamma(^4\mathrm{He}(20.21) \to ^4\mathrm{He}X) = (0.3 - 3.6) \times 10^{-5} \quad \mathrm{eV}, \tag{1.46}$$

$$\Gamma(^{12}\mathrm{C}(17.23) \to ^{12}\mathrm{C}X) = (0.4 - 2.2) \times 10^{-3} \quad \mathrm{eV} \tag{1.47}$$

The calculation for He are in agreement with the experimental results, so the observation of C decays with this predicted width could be a strong evidence for the existence of a protophobic vector boson that already simultaneously explains He and Be experiments.

X(17) links with QCD

Veselsky and coworkers presented in 2020 an alternative hypothesis, published in [52]. Such hypothesis states that the anomaly observed at Atomki can be related to the cluster structure of the decaying state. They suggest that the hypothetical boson produced in ^{8}Be and ^{4}He transitions can mediate the nucleon-nucleon interaction in low-energy quantum chromodynamics (QCD), in the weakly bound cluster states $p+^7$Li and $p+^3$H.

The ^{8}Be nucleus is practically unstable, and it is stabilized only by the Coulomb barrier. It can be considered as consisting of two α particles, because its ground state is just above $2m_\alpha$. For energies up to 17 MeV the basic decay channel is in two α particles, while for greater energies this channel is suppressed, favouring the emission of a proton. This is unexpected, since the energy of such states is larger than the Coulomb barrier, which is 1.5 MeV for $l = 0$, thus the α decay should be feasible. The reason for this may be tied to the proton separation energy, which is 17.25 MeV, and to the excited states at 17.6 MeV and 18.15 MeV that can be cluster configurations. Thus the states with energy greater than 17 MeV can be molecular states, stabilized mainly by the Coulomb barrier.

The ^{3}H or ^{7}Li interaction with protons may be the source of the X(17) boson anomaly. In this hypothesis the observed signal can be an evidence for an exchange boson mediating strong nucleon-nucleon interaction at the low-energy regime of QCD. The authors provide a set of equations to describe this possibility using quantum hydrodynamics (QHD-I) and instanton liquid model. This model is based on the existence of instantons as gluonic solutions to QCD equations, where the vacuum is described by a granular configuration of these gluonic fields where quarks can be hopping between them. More details on the instanton model can be found in [53]. The values obtained by Veselsky and coworkers for incompressibility and coupling constants are not unlikely.

Another possible link between the X(17) and the QCD is the interpretation of the anomaly as a proof of the existence of the QCD axion, investigated by Alves in [54,55]. This particle is a light pseudoscalar predicted to solve the strong CP problem: this symmetry is violated in the weak sector, but as of today there is no evidence of this violation in the strong sector. If the QCD axion exists it should be ultralight and cosmologically long-lived, thus a good candidate for dark matter. The viable QCD variants in the X(17) mass range are experimentally constrained to be piophobic, electrophilic and $2^{\text{nd}} - 3^{\text{rd}}$ generation-phobic, i.e. muonphobic, charmphobic, bottomphobic etc. The study shows how the QCD axion existence is compatible with ^{8}Be and ^{4}He anomalies, and naturally explains its suppression in MIV transitions. Moreover it predicts other dark photons signals that can be searched in rare meson decays at meson factories, for example the $\eta^{(\prime)} \to \pi\pi e^+e^-$ decay at future η, η' factories, thus acting as a probe for this theory.

Arguments against the protophobic vector boson

Zhang and Miller, after having excluded the possibility of a nuclear physics explanation for the anomaly as discussed in section 1.3.1, reported in [29] their study on the hypothesis of the existence of the X(17) as a protophobic vector boson. They derived an isospin relation between photon and X(17) couplings to nucleons, to compare the boson production cross section to the photon production one, already studied in [1]. The diagram of the X(17) production is the same of the one showed in figure 1.5, the only exception being a change between the photon and the boson line.

The expressions they provide for E1 and M1 transitions operators $\mathcal{O}_{E1}$ and $\mathcal{O}_{M1}$ implies that those transitions are isovector in nature. They are in fact corrected by two-body meson exchange current, mainly transverse and isovector. The analytical expressions of the operators are the following:

$$\mathcal{O}^{\gamma}_{E1} = e_{EM}\sqrt{\frac{3}{4\pi}}\sum_{i=1}^{A}\mathbf{r}_{(i)}\frac{\tau_{(i),3}}{2} \tag{1.48}$$

$$\mathcal{O}^{\gamma}_{M1} \approx \sqrt{\frac{3}{4\pi}}\frac{e_{EM}}{2M_N}\sum_{i}\left[\left(\lambda^{(1)}+\frac{1}{4}\right)\sigma_{(i)}+\frac{1}{2}\mathbf{J}_{(i)}\right]\tau_{(i),3} \tag{1.49}$$

where $N=(p,n)^T$, $\lambda^{(1)}=1.85$, τ_3 is an isospin component, $\mathbf{J}$ is the matrix element of the total angular momentum and σ is the proton spin projection. Being ε_s and ε_v the ratios between the X and γ coupling constants in the isoscalar and isovector components, the resulting operators for the X(17) production are the following:

$$\mathcal{O}^{X}_{E1} = -\varepsilon_v\mathcal{O}^{\gamma}_{E1} \qquad\qquad \mathcal{O}^{X}_{M1} \approx -\varepsilon_v\mathcal{O}^{\gamma}_{M1} \tag{1.50}$$

Notice that a protophobic X(17) boson would imply $\varepsilon_s \approx \varepsilon_v$. The approximation in equation 1.50 would fail only in this case:

$$\left|\frac{\varepsilon_s}{\varepsilon_v}\right| \gtrsim \left|\frac{\lambda^{(1)}+\frac{1}{2}}{\lambda^{(0)}+\frac{1}{4}}\right| \approx 12 \tag{1.51}$$

i.e. the isoscalar piece in $\mathcal{O}^{X}_{M1}$ is not much smaller than the isovector piece.

The authors, after defining the operators, calculated the expression for the X(17) production cross section. The total squared transition amplitudes for the X(17) production and the differential cross section are described as follows:

$$\sum_{a,\sigma,\bar{\lambda}}|\mathcal{M}_{\gamma,X}|^2 = T_0^{\gamma,X} + T_1^{\gamma,X}P_1(\cos\theta) + T_2^{\gamma,X}P_2(\cos\theta) \tag{1.52}$$

$$\frac{\mathrm{d}\sigma_{\gamma,X}}{\mathrm{d}\cos\theta} = \frac{M}{4\pi}\frac{q}{p}\frac{1}{8}\sum_{a,\sigma,\lambda}|\mathcal{M}_{\gamma,X}|^2 \tag{1.53}$$

Figure 1.26 reports this cross section for different M_X values, along with the photon production cross section, which is in agreement with the result published in [1].

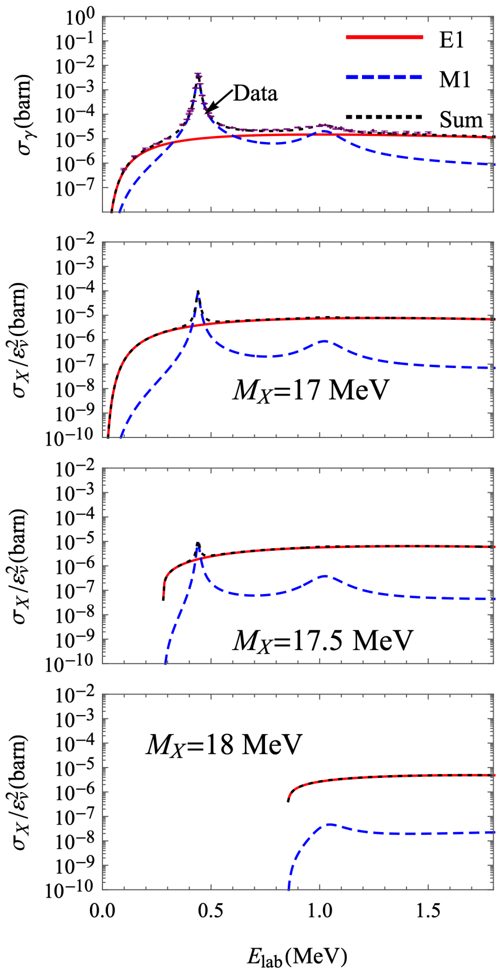

Figure 1.26: The top panel shows the photon production cross section vs the proton energy in the lab frame. The three bottom panels shows the X(17) boson production cross section scaled by ε_v^2 for different M_X values. Figure from [29]

From these plots emerges that the X(17) boson can be produced via the dominant E_1^X component (where the ^{X} indicates that the transition is the one responsible for the X(17) production) for almost any energy above the kinematic threshold. This is in conflict with the experimental observation of the anomaly, which is located almost exclusively in the higher energy 1^+ state, and is associated only to an M1^X transition. The E_1^X dominance at the MIS resonance is explained by the following calculations:

$$\frac{\sigma_{X,E1}(E)}{\sigma_{X,M1}(E)} = \frac{\sigma_{\gamma,E1}(E)}{\sigma_{\gamma,M1}(E)} \frac{3\omega^2 - q^2}{2q^2} \tag{1.54}$$

$$\left.\frac{\sigma_{X,E1}(E)}{\sigma_{X,M1}(E)}\right|_{MIS} = \frac{2\omega^2 + M_X^2}{2(\omega^2 - M_X^2)} \left.\frac{\sigma_{\gamma,E1}(E)}{\sigma_{\gamma,M1}(E)}\right|_{MIS} \overset{M_X=17}{\approx} 8.6 \tag{1.55}$$

This value is true if the approximation in equation 1.50 is valid so, to evade this conflicted conclusion, $|\varepsilon_s/\varepsilon_v|$ must be around 12 or even higher, forcing the X(17) boson to be protophilic instead of protophobic. Thus, the conclusion of the authors is that the protophobic vector boson explanation for the anomaly cannot be correct, in contrast with the hypothesis proposed by Feng and coworkers in [21].

Need for future measurements

The common thread between all the studies that I reported in this section is the need for more experimental data to understand the nature of the anomaly observed at Atomki. Many theories have been proposed: some of them were disproved, while others represented a step forward in the understanding of this phenomenon. But, in order to be confident in claiming the existence (or the non existence) of a new particle not foreseen by the SM, it is necessary to search for the anomaly in other decays. The collaboration working at Atomki already started to take some data with ^{12}C transitions, populating the excited states of the atom with the $^{11}\text{B}(p, e^+e^-)^{12}\text{C}$ reaction at $E_p = 2.25$ MeV. Another fundamental test is to repeat the Atomki measurement with an independent experiment, to confirm that the peak in the ^{8}Be and ^{4}He angular distribution is not an effect of the experimental setup chosen for this measurement. The goal of my thesis is to prove that it is possible to repeat the ^{8}Be measurement in a different experiment, built with another purpose. The detailed description of such experiment, which is MEG II, is the main focus of chapter 3.

Chapter 2

Searches for X(17) around the world

The existence of a new light boson involved in the interaction of the dark matter sector would be a huge step towards new physics beyond the SM. This is the reason why many experiments all over the world looked for such particle in different channels, or plan to do so. Many of these experiments already managed to set constraints on the coupling of this hypothetical particle with ordinary matter, while other are still in the R&D phase, but they will soon contribute to the general knowledge of the phenomenon.

An important aspect in this search is the repeatability of the Atomki measurement. While it was shown that the same detector gives the same result, it still has to be proven that the anomaly is not an artifact of the detector geometry, as stated in [23]. Also measuring the peak with a better precision can add information. For example, if the width of the peak remains unchanged even though the resolution gets better, this would rule out the existence of the hypothetical boson, that has a much narrower predicted width (order of 10^{-5} eV) than the experimental resolution.

This is where my thesis work comes into play: repeating the measurement with a different setup can give an answer to these questions. I will show that it is possible to perform this measurement with a better invariant mass resolution and angular acceptance with the MEG II experiment. This can be achieved by using a Cockcroft-Walton accelerator (CW) to produce 1.1 MeV protons and a high resolution tracker for e^+e^- pairs detection.

In this chapter I will briefly report the X(17) searches in different channels that are ongoing around the world. I will also introduce some experiments that are planning to further study the IPC in several nuclear reactions. Table 2.1 reports a list of the experiments that I will discuss in this chapter alongside their results, obtained and/or expected. I divided the experiments in two sections: the IPC experiments and all the other

X(17) production channels, starting from the latter. Here I started from the experiments that already achieved a result, and then I continued with the experiments that are already existing and are planning to measure the coupling of this particle in the future. I concluded with the experiments that are not yet in operation but are in the construction or upgrade phase.

Experiment	Process	Present Result	Future Result
NA64	$e^- Z \to e^- Z X$	$\epsilon_e \lesssim 6.8\text{E}{-4}$ excluded	Search $\epsilon_e \lesssim 1.4\text{E}{-3}$
N48/2	$\pi^0 \to \gamma X$	$\epsilon^2 \sim 2\text{E}{-7}$	/
BESIII	$J/\Psi \to \eta_c X$	$\lvert\varepsilon_c\rvert \gtrsim 5\text{E}{-3}$	$\lvert\varepsilon_c\rvert \gtrsim 3\text{E}{-3}$
BelleII	$J/\Psi(\eta_c + X) + l\bar{l}$ $J/\Psi + X$	/ /	$\lvert\varepsilon_c\rvert \gtrsim 1.8\text{E}{-2}$ $2.0\text{E}{-4} \leq \lvert\varepsilon_e\rvert \leq 8.0\text{E}{-4}$
PADME	Resonant production	/	$\epsilon^2 \sim 1\text{E}{-6}$
DarkLight	$e + p \to e + e + e^+e^-$	/	Search m_X=10-100 MeV/c^2
Mu3e	$\mu^+ \to e^+ \nu_e \bar{\nu}_\mu A'$	/	Search m_X=10-80 MeV/c^2
LHCb	$D^*(2007)^0 \to D^0 A'$	/	Search m_X<100 MeV/c^2
VEPP-3	$e^+e^- \to \gamma A'$	/	$\epsilon^2 = 5\text{E}{-8}$
MESA	$e-$target	/	Search m_X=10-40 MeV/c^2
HPS	$e-$target	$\epsilon^2 < 6\text{E}{-6}$	$\epsilon^2 < 1\text{E}{-6}$
JLab	e^- Bremsstrahlung	/	$7.2\text{E}{-8} < \epsilon^2 < 5.9\text{E}{-9}$
COPE	IPC	/	e^+e^- angular correlation invariant mass distribution
LNL	IPC in ^{8}Be and ^{12}C	/	e^+e^- angular correlation invariant mass distribution
nToF	IPC in ^{4}He	/	e^+e^- angular correlation invariant mass distribution
LUNA	IPC in ^{4}He	/	e^+e^- angular correlation invariant mass distribution
CCPAC	IPC in ^{8}Be and ^{10}B	/	e^+e^- angular correlation invariant mass distribution

Table 2.1: Summary of the measurements introduced in this section.

2.1 Experiments involved in the X(17) search

2.1.1 Direct search with electron beam at NA64

If the X(17) exists, it can be produced in the $e^- Z \to e^- Z X$ Bremsstrahlung reaction. This reaction can be obtained from a high energy electron beam that impinges on an active target. The NA64 experiment at CERN was able to perform this measurement in 2017-2018 [46, 56–58], collecting an accumulated statistics of 8.4×10^{10} electrons. It used the Super Proton Synchrotron (SPS) accelerator to obtain a 150 GeV electron beam and produce the Bremsstrahlung reaction in which the boson can be generated. This measurement improved the previously existing limits on the coupling with electrons ϵ_e, i.e. $2 \times 10^{-4} \lesssim \epsilon_e \lesssim 1.4 \times 10^{-3}$.

Figure 2.1 shows the experimental setup used in the search for $X \to e^+e^-$ decays from Bremsstrahlung X produced in $e^-Z \to e^-ZX$. Notice that this is the setup used in the 2018 run, which is optimized for the region of parameter space with a large coupling with electrons. This improved the sensitivity of the setup used previously in 2017.

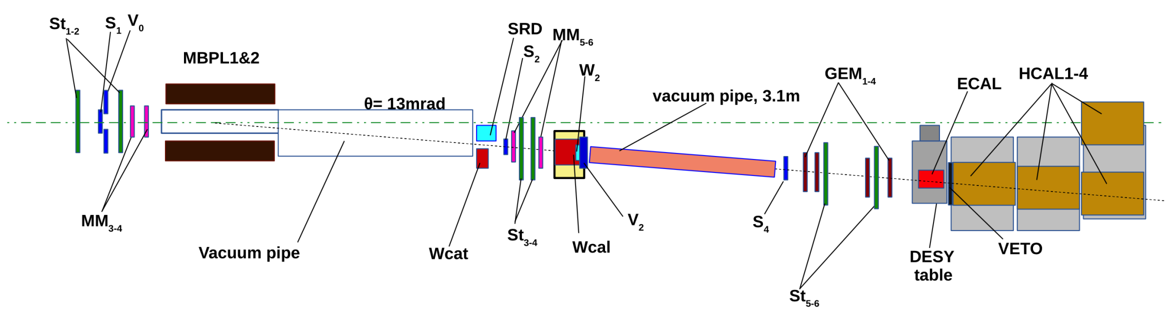

Figure 2.1: Experimental layout of the NA64 detectors for the $X \to e + e^-$ search. Figure from [57].

The two electromagnetic calorimeters are the crucial detectors in the experiment. The first one is a compact target-tungsten-calorimeter (WCAL), a tungsten and plastic scintillators assembly with a wavelength shifter readout. The second one is an Electromagnetic CALorimeter (ECAL) built as a matrix of 6×6 shashlik-type lead-plastic scintillator modules. The hypothetical X(17) is produced via high energy electrons scattering off the WCAL nuclei, and then decays in flight producing the e^+e^- pair. The WCAL is used also to absorb the electromagnetic showers from secondary particles emitted by primary electrons and the one from the recoil electron of the reaction, while the ECAL measures the energy of the primary electron downstream. The boson production and subsequent decay would appear as an excess over the background of two electromagnetic showers in the detectors, one in the WCAL and the other in the ECAL, with a total energy compatible with the beam energy.

The NA64 collaboration did not find any evidence of the existence of the X(17) particle, but managed to set constraints to its coupling with electrons. The ranges excluded by the experiment for such coupling in the vector [57] and pseudoscalar [59] hypotheses are respectively:

$$1.2 \times 10^{-4} \lesssim \epsilon_e \lesssim 6.8 \times 10^{-4}, \qquad 2.1 \times 10^{-4} \lesssim \epsilon_e \lesssim 3.2 \times 10^{-4} \tag{2.1}$$

They are planning to upgrade the experimental setup, e.g. optimizing the X(17) production target, increasing the nominal beam energy and decreasing the dump length. Moreover, they developed a new efficient and accurate reconstruction of two close decay tracks, already validated by its application to old data. More details on the upgrade can be found in [60]. These improvements will help to further probe a portion of the allowed parameter space, exploring the region up to the present upper limit $\epsilon_e \lesssim 1.4 \times 10^{-3}$.

2.1.2 Search at NA48/2

The NA48/2 experiment at CERN SPS collected in 2003-2004 a sample of π^0 from $\sim 2\times10^{11}$ charged kaon decays in flight [61]. The decay of π^0 mesons produced in the $K^\pm \to \pi^\pm\pi^0$ and $K^\pm \to \pi^0\mu^\pm\nu$ decays is a good tool to search for a hypothetical dark boson, expected to be produced in $\pi^0 \to \gamma X$, $X \to e^+e^-$. Figure 2.2 shows a drawing of the experimental setup. The principal subdetectors are a magnetic spectrometer, composed of four drift chambers, a scintillator hodoscope and a liquid Krypton calorimeter.

The BR of the $\pi^0 \to \gamma X$ decay is the following:

$$\mathrm{BR}(\pi^0 \to \gamma X) = 2\epsilon^2 \left(1 - \frac{m_X^2}{m_{\pi^0}^2}\right) \mathrm{BR}(\pi^0 \to \gamma\gamma) \tag{2.2}$$

It depends on two free parameters: the boson mass m_X and the mixing parameter ϵ^2, and is sensitive to the mass range $m_X < m_{\pi^0}$. In the X(17) mass range the NA48/2 experiment obtained an upper limit of order $\epsilon^2 \sim 2 \times 10^{-7}$, improving existing limits from other experiments as reported in figure 2.3. The collaboration explored also the $K^\pm \to \pi^\pm X$ channel, but it resulted to be not competitive for a dark boson search. The experiment upgrade NA62, which is currently running, will achieve a larger statistics with an improved e^+e^- invariant mass resolution and a better background rejection [62]. This will result in an improvement of the existing result on this search.

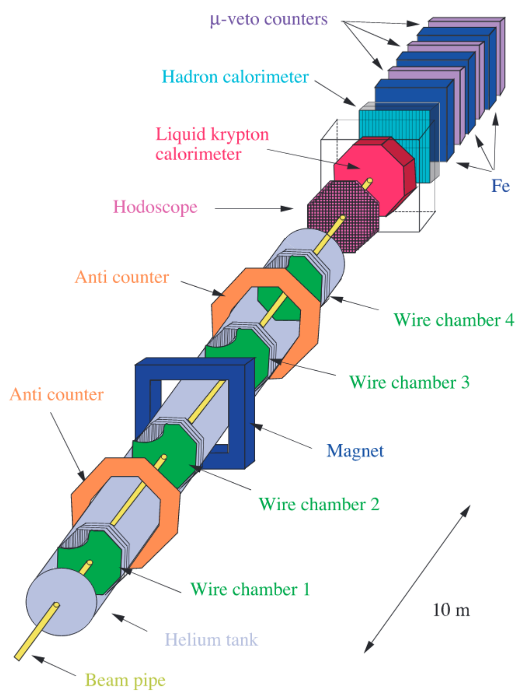

Figure 2.2: Drawing of the NA48/2 experiment. Figure from [61].

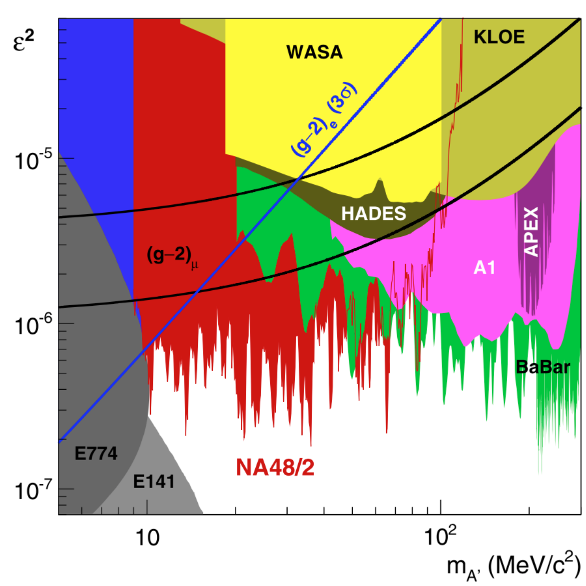

Figure 2.3: Existing constraints on the existence of a dark boson (A' in this plot) in the $m_{A'}\varepsilon^2$ parameters space. Figure from [28].

2.1.3 Search in heavy mesons decays

Castro and Quintero proposed to investigate the possibility of the production of a light vector boson weakly coupled to the SM, such as the X(17), in $H^* \to He^+e^-$ decays, where H is a heavy $Q\bar{q}$ meson [63]. Such decays are free from nuclear isospin mixing theoretical uncertainties. Moreover, the mass splitting in heavy mesons is large enough to produce the boson on shell, and the strong decays of H^* are suppressed by the kinematics in favor of the EM ones. They found out that the D^{*+} and D_s^* mesons BR are the most sensitive ones to the presence of the X(17), as reported in table 2.2. Therefore studying these decay channels can improve the constraints on the existence of this particle, or even confirm it.

Transition	Photon	X(17)	Total
$D^{*+} \to D^+e^+e^-$	$(6.7 \pm 0.3) \times 10^{-3}$	$(1.1 \pm 0.1) \times 10^{-3}$	$(7.7 \pm 0.3) \times 10^{-3}$
$D^{*0} \to D^0e^+e^-$	$(6.7 \pm 0.3) \times 10^{-3}$	$(3.0 \pm 0.1) \times 10^{-5}$	$(6.7 \pm 0.3) \times 10^{-3}$
$D_s^{*+} \to D_s^+e^+e^-$	$(6.8 \pm 0.6) \times 10^{-3}$	$(1.0 \pm 0.1) \times 10^{-3}$	$(7.8 \pm 0.6) \times 10^{-3}$
$B^{*+} \to B^+e^+e^-$	$(4.9 \pm 0.3) \times 10^{-3}$	$(1.9 \pm 0.1) \times 10^{-5}$	$(4.9 \pm 0.3) \times 10^{-3}$
$B^{*0} \to B^0e^+e^-$	$(4.9 \pm 0.2) \times 10^{-3}$	$(4.0 \pm 0.2) \times 10^{-4}$	$(5.3 \pm 0.2) \times 10^{-3}$
$B_s^{*0} \to B_s^0e^+e^-$	$(5.0 \pm 0.3) \times 10^{-3}$	$(4.1 \pm 0.2) \times 10^{-4}$	$(5.4 \pm 0.3) \times 10^{-3}$

Table 2.2: Photon and X(17) contributions to BR($H^* \to He^+e^-$) normalized to $H^* \to H\gamma$ radiative decay width to cancel out model dependent terms. Data from [63].

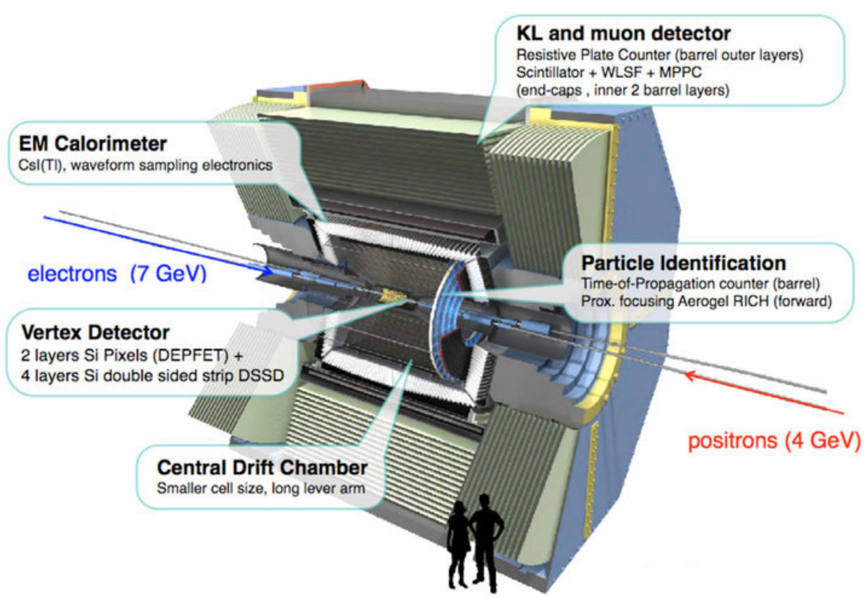

Figure 2.4: Layout of the BelleII experiment at the SuperKEKB accelerator. Figure from [64].

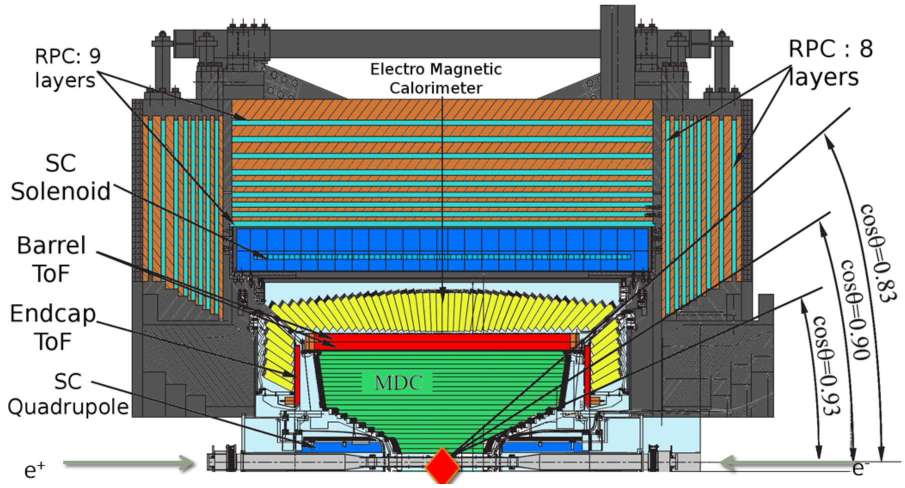

Figure 2.5: Layout of the BESIII experiment at the BEPCII accelerator. Figure from [65].

The authors point out that there is a large amount of data produced at heavy meson factories that can be used to test the proposed channel. For example, they propose to study this kind of decays in the clean environment provided by the transition that are studied in Belle II at SuperKEKB and BEijing Spectrometer (BESIII) at BEPCII, whose detector layouts are reported in figure 2.4 and 2.5.

J/Ψ decays at BESIII and Belle II

In a similar fashion, Ban and coworkers investigated the possibility of a vector boson search at BESIII and Belle II [66]. They focused on three channels: $J/\Psi \to \eta_c X$ with the 10^{10} J/Ψ collected at BESIII; $J/\Psi(\eta_c + X) + l\bar{l}$ production at Belle II; $J/\Psi + X$ with a displaced $X \to e^+e^-$ vertex at Belle II. This last channel is almost free of background if the vertex is required to be within the beam pipe. Here it is possible to probe the vector coupling with electrons in the range $10^{-4} \leq |\varepsilon_e| \leq 10^{-3}$. The mass range is 9 MeV/$c^2 \leq m_x \leq$ 100 MeV/c^2, so this includes also the X(17) observed at Atomki. From this study emerges that the BESIII channel can be used to constrain the coupling with the charm quark, excluding the following region:

$$|\varepsilon_c| \gtrsim 5 \times 10^{-3} \tag{2.3}$$

This result can improve to $|\varepsilon_c| \gtrsim 3 \times 10^{-3}$ when the number of J/Ψ produced will reach 10^{11}. The MC study on the Belle II $J/\Psi \to \eta_c X \to \eta_c e^+e^-$ channel resulted in this achievable sensitivity on the charm quark coupling:

$$|\varepsilon_c| \gtrsim 1.8 \times 10^{-2} \tag{2.4}$$

The other inspected channel at Belle II, $e^+e^- \to J/\Psi X \to e^+e^-l^+l^-$, directly constrain the boson coupling with electrons. In this case it is possible to reach this sensitivity:

$$2.0 \times 10^{-4} \leq |\varepsilon_e| \leq 8.0 \times 10^{-4} \tag{2.5}$$

The results for the coupling constants depend on the mass of the hypothetical boson, which is here assumed to be $m_x = 17$ MeV$/c^2$.

X(17) measurement at BESIII

The BESIII experiment has the opportunity to search for a new light vector gauge boson. Jiang and coworkers showed that it is possible to make a new measurement of the X(17) by looking at $e^+e^- \to X\gamma$ and $J/\Psi \to X\gamma$ events, followed by the boson decay in a pair [67,68]. In this study the authors adopted the vector/axial-vector interpretation of the new particle and analyzed decay length, production rate, e^+e^- invariant mass spectrum and signal to noise ratio. They estimated the X(17) production to be ~ 6000 measurable events per year in e^+e^- collisions and only 52 in J/Ψ decay, but the latter with a better signal to noise ratio. These calculations assume a coupling strength of the boson to the vector/axial-vector currents of $g_f^{v/a} \sim 10^{-3}$.

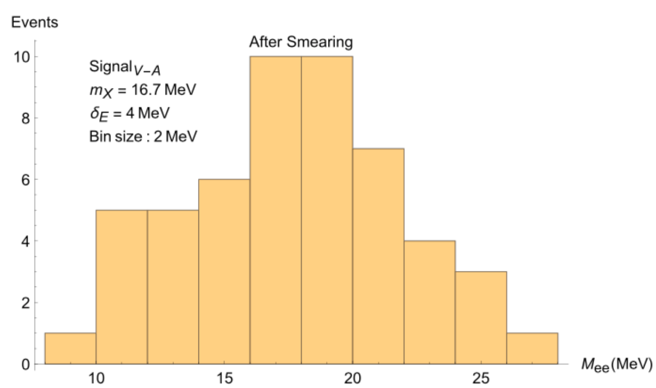

Figure 2.6: Invariant mass distribution of 52 simulated X(17) signal events in J/Ψ decays. Figure from [67].

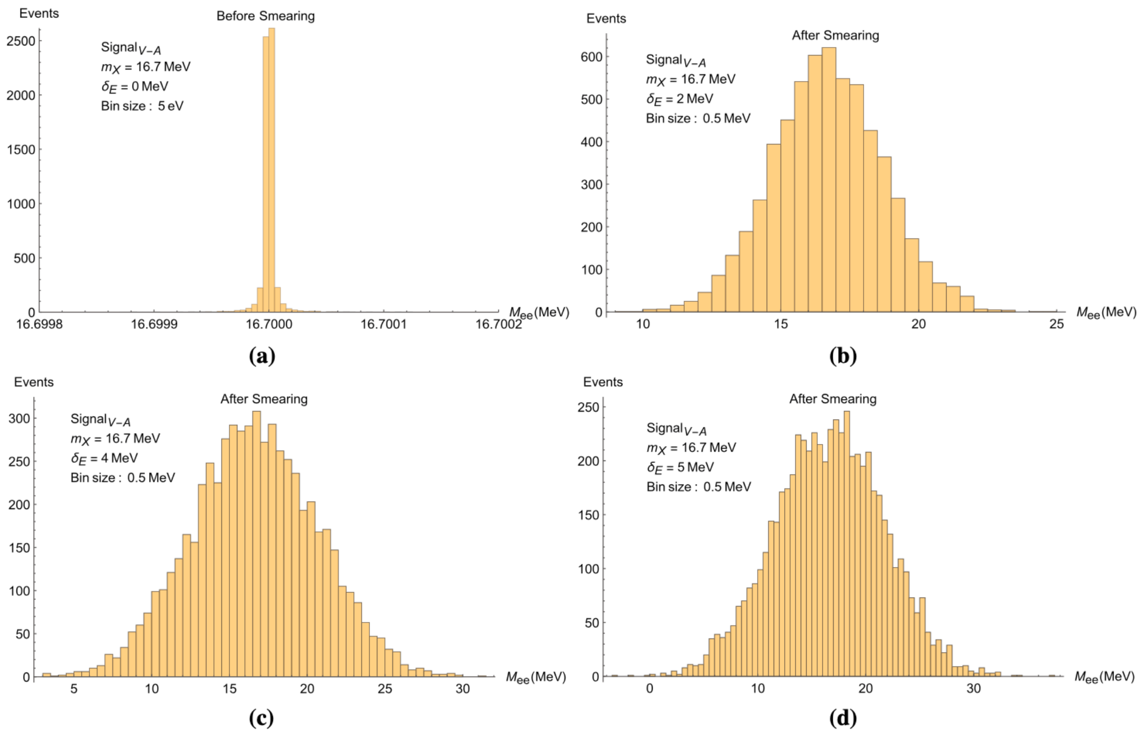

Figure 2.7: Invariant mass distribution of 6000 X(17) simulated signal events in e^+e^- collisions. The 4 plots a) to d) have respectively $\delta_E = 0,\ 2,\ 4,\ 5$ MeV energy resolution. Figure from [67].

Figure 2.6 and figure 2.7 show the simulated invariant mass distributions for the hypothetical boson production events in J/Ψ decays and e^+e^- collisions at $\sqrt{s} = 3.7$ GeV respectively. The result for the X(17) decay length is 0.27 mm$< L <$27 mm in e^+e^- collisions. Here the expected events per year are $60 \sim 6000$ and the signal to noise ratio decreases after the smearing of the distribution with the detector energy resolution. The authors also found that in this type of events the contributions of vector and axial currents are comparable, while in J/Ψ decays the axial-vector current is predominant.

2.1.4 Future searches for a dark photon

The dark photon A' is an hypothetical force carrier connected to the dark sector. The simplest scenario that involves this particle introduces a new abelian U(1) gauge symmetry with a corresponding spin 1 gauge boson A'. It can couple weakly with charged particles through kinetic mixing with the SM photon. The existence of such particle is one of the proposed explanation for the ^{8}Be anomaly, but is in contrast with the protophobic vector boson hypothesis as stated in [21] due to incompatible coupling constants. Many experiments around the world are going to investigate the existence of such particle, and discovering its characteristics can confirm (or disprove) its role in the Atomki anomaly.

FASER

The ForwArd Search ExpeRiment (FASER) is going to look for new light and weakly interacting particles at CERN [69]. These particles can be produced at the Large Hadron Collider (LHC), and may travel long distances without interacting. The FASER detector, placed 480 m downstream the ATLAS interaction point in the collider, is built to look for the decay products of such particles. Figure 2.8 shows a layout of the detector: it is composed of scintillators, dipole magnets, tracking stations, and a calorimeter. The focus of the experiment is the search for light particle with a mass in the MeV/c^2-GeV/c^2 range and weakly coupled to the SM that can resolve the tension between low energy experiments and theoretical predictions (such as the Atomki excess and the $(g-2)_\mu$ anomaly), and the X(17) perfectly fits this description.

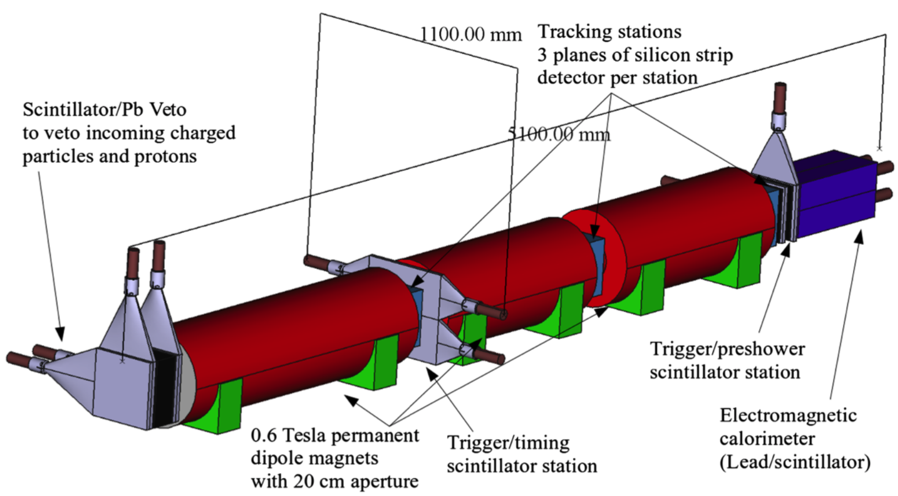

Figure 2.8: Layout of the FASER detector. Figure from [69].

PADME

The Positron Annihilation into Dark Matter Experiment (PADME) at Laboratori Nazionali di Frascati (LNF), shown in figure 2.9, will search for resonant production of dark photons in positron beam dump experiments [70–72]. It is composed of an active diamond target, scintillating strips for charged particles veto, a dipole magnet to sweep out the fraction of the beam that survives the dump, a beam monitor and a calorimetric system composed by 616 BGO crystals and the central Small Angle Calorimeter (SAC) made of PbF_2. This experiment can look for resonant production of new particles from the annihilation of positrons from the beam with the atomic electrons of the target. In this kind of experiment the dark photon A' production is of first order in the electromagnetic coupling α, unlike the reaction $e^+e^- \to \gamma A'$ which is $O(\alpha^2)$, and A' Bremsstrahlung in e^--nucleon reaction which is $O(\alpha^3)$. The accelerator used in this experiment can produce a positron beam with energy in the range 250-550 MeV, which is sufficient to explore the X(17) mass range. PADME is expected to set new bounds in the region of large and small values of the boson mixing parameter ϵ, which are $\sim 10^{-3}$ and $\sim 10^{-4}$ respectively, achievable by varying the thickness of the target. The collaboration already took some test data, as reported in [73–75]. They collected data from $\sim 5 \times 10^{12}$ positron interactions on the target, and the analysis is ongoing. Even though the detectors are not optimized for the X(17) decay products measurement because they are not able to fully reconstruct the particles track and momentum, the expected sensitivity on this measurement with the available data is $\epsilon^2 \sim 10^{-6}$.

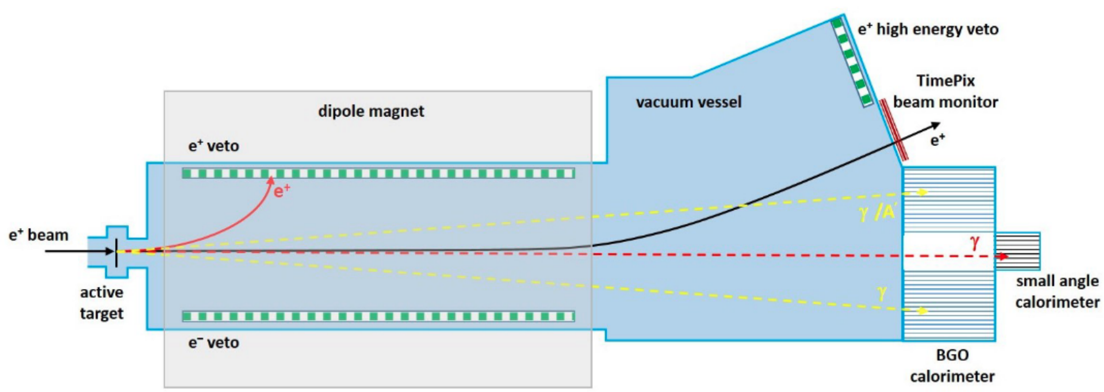

Figure 2.9: Layout of the PADME experiment. Figure from [72].

DarkLight

The DarkLight experiment at JLab proposes to look for BSM physics [76, 77]. The experiment is built to look for dark photons decays in e^+e^- pairs in a mass region between 10 MeV/c^2 and 100 MeV/c^2. Figure 2.10 shows a drawing of the proposed second phase of the detector. The JLab 100 MeV electron beam passes through a H gaseous target, and the final state of the produced reaction is measured with a cylindrical 60 cm long gaseous H chamber acting as a proton and lepton detector. In the gaseous target an hypothetical dark photon A' can be produced, and the recoil proton can be measured by a detector outside the gas chamber. The measured final state is the one from the reaction $e + p \rightarrow e + e + e^+e^-$, in which the pair can possibly be produced by A'.

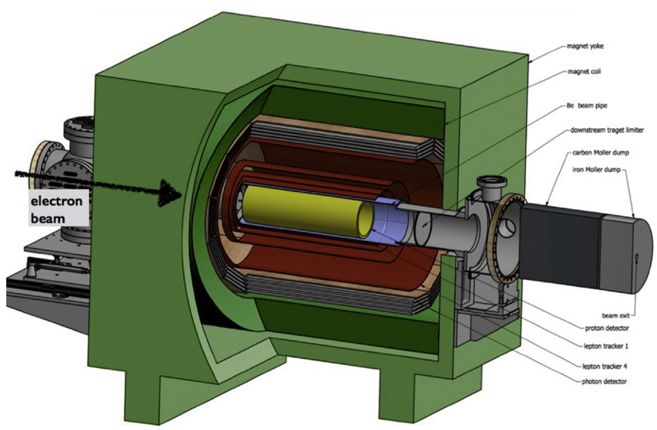

Figure 2.10: Drawing of the proposed DarkLight Phase 2 detector. Figure from [77].

Mu3e

A search for the dark photon A' is foreseen also at the Mu3e experiment at Paul Scherrer Institut (PSI) [78]. The experiment is built to look for charged Lepton Flavor violation (cLFV) in the $\mu \rightarrow eee$ channel, but can also be used to search for dark photons in the mass range 10-80 MeV/c^2 in the decay $\mu^+ \rightarrow e^+\nu_e\bar{\nu}_\mu A', \quad A' \rightarrow e^+e^-$. It can explore the kinetic-mixing parameter region up to $\epsilon^2 \sim 10^{-8}$. To make this measurement there is no need to modify the experimental setup, which is shown in figure 2.11. Its tracking detectors, made of silicon pixels, are used to measure the electron-positron tracks, while the timing is measured by two detectors: a fiber hodoscope placed around the target and a scintillating tile detector. The experiment is expected to take $\sim 10^{15}$ μ decays in its first phase, and the dataset collected for the cLFV search can be used also to look for the dark photon in case the $A' \rightarrow e^+e^-$ vertex is near the μ decay vertex. Otherwise, for displaced vertex, changes in DAQ and reconstruction are needed.

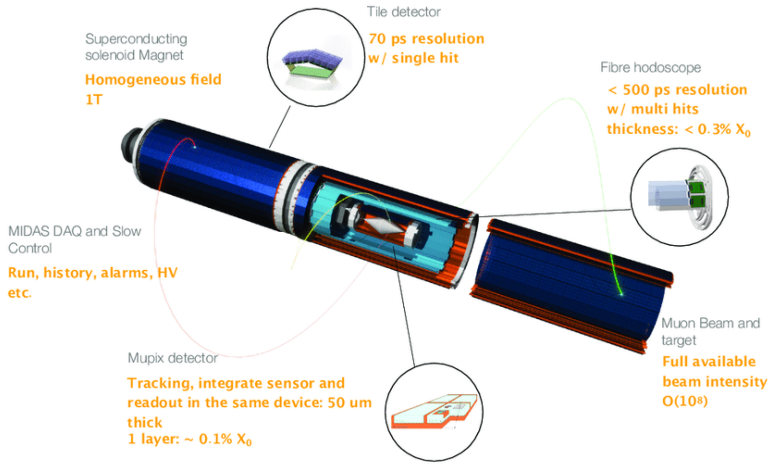

Figure 2.11: Layout of the Mu3e experiment. Figure from [79].

LHCb

Also LHCb at CERN proposed a search for the dark photon A' in the mass region below 100 MeV/c^2 [80] in Run3, after having explored higher mass regions in previous Runs. The goal of the collaboration is to explore this low mass region by investigating the charm meson decay $D^*(2007)^0 \to D^0 A'$.

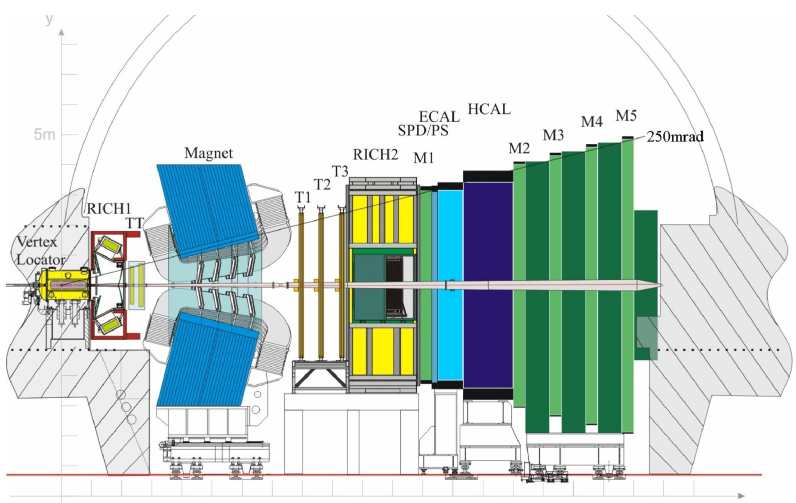

Figure 2.12: Drawing of the LHCb experiment. Figure from [81].

Figure 2.12 shows a drawing of the detector, sensitive to dark photons that decay into electron-positron pairs. They proposed two strategies to look for this particle: the displaced strategy and the resonant strategy. The first one exploits the Lorentz boost of the boson: when the A' decay vertex is far from the primary vertex the search is almost background free. The second strategy exploits the large event rate and good invariant mass resolution of the detector. In the target mass region the experiment can explore a significant fraction of the parameter space.

VEPP-3

An experimental collaboration at the VEPP-3 facility at Novosibirsk proposed a new experiment to search for a new gauge boson A' [82]. Figure 2.13 shows the layout of the experiment. Its goal is to measure the missing mass spectrum in the reaction $e^+e^- \to \gamma A'$, positron annihilation on a gaseous H target internal to the VEPP-3 storage ring. The collaboration aims to an upper limit on the coupling constant $\epsilon^2 = 3 \times 10^{-8}$, with a signal to noise ratio of 2/1 in the investigated A' mass range 5-20 MeV/c^2. The result of the first simulations on the expected sensitivity on the coupling gives the following result:

$$\epsilon^2 = 5 \times 10^{-8} \text{ for } m_{A'} = 15 \text{ MeV/c}^2 \text{ @95\% CL} \tag{2.6}$$

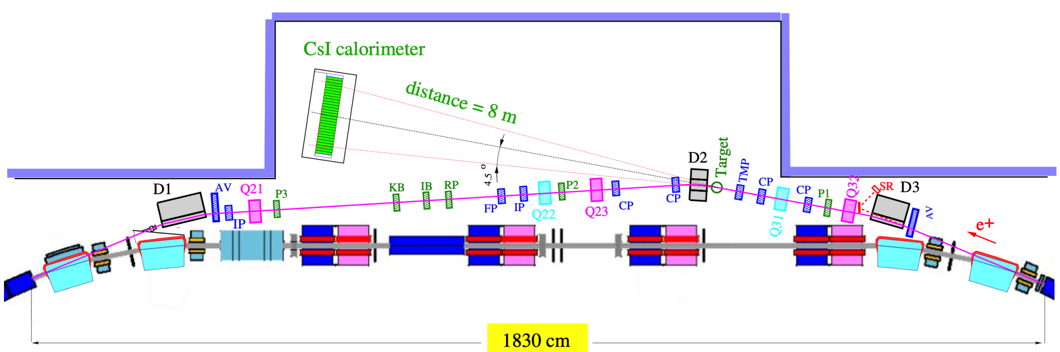

Figure 2.13: Sketch of the proposed experiment at VEPP-3. Figure from [82].

MESA

The experiments at the Mainz Energy-Recovery Superconducting Accelerator (MESA) plan to search for the dark photon in the 10-40 MeV/c^2 mass range [83]. Figure 2.14 shows the MESA accelerator complex with its three foreseen experiment: MAGIX, darkMESA and P2, the first two being focused on the A' search. They exploit a high luminosity electron beam impinging on a gaseous target. MAGIX will be able to search for visible and invisible decays of the boson, and the electron beam dump experiment darkMESA will investigate the production, decay and interaction of the dark photon.

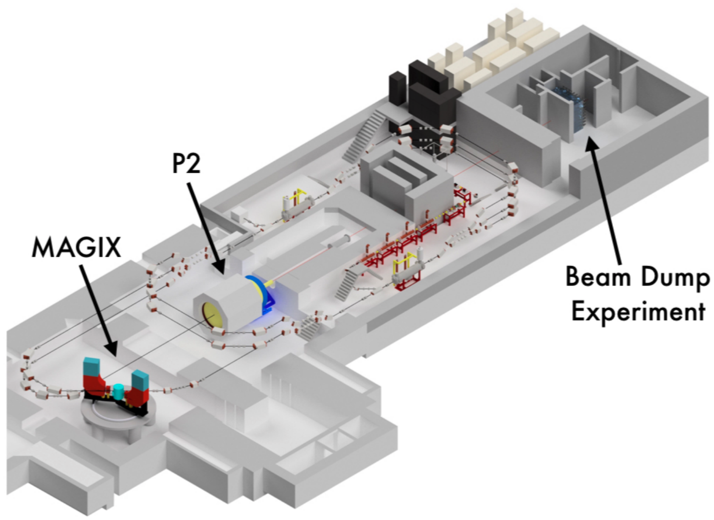

Figure 2.14: Layout of the MESA accelerator complex. The three foreseen experiments are MAGIX, P2 and darkMESA (beam dump experiment). Figure from [83].

HPS

The Heavy Photon Search (HPS) experiment at JLab took data in 2015, exploring the A' mass range 19-81 MeV/c^2 [84–86]. The detector, shown in figure 2.15, is built to look for a resonance in the e^+e^- invariant mass distribution. The boson is produced in the reaction of an electron beam impinging on a tungsten target. The beam is a 1.056 GeV, 50 nA electron beam provided by CEBAF at the Thomas Jefferson National Accelerator Facility. In 1.7 days of DAQ the experiment collected 1170 nb^{-1} of data, and found no excess in the invariant mass distribution. This allowed to set an upper limit on the dark photon coupling to the SM:

$$\epsilon^2 < 6 \times 10^{-6} \tag{2.7}$$

This confirms the results obtained from earlier searches, but future upgrades of the detector will allow to explore a wider range of the coupling constant. The final goal is to achieve a coverage for ϵ^2 below the level of 10^{-6}.

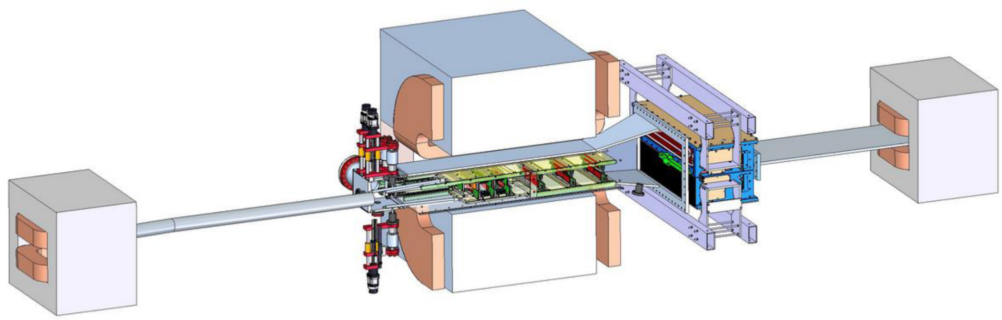

Figure 2.15: Layout of the HPS experiment. Figure from [85].

Direct search at JLab

A collaboration at JLab proposed a new experiment for a direct search of a dark photon that can also explore the X(17) anomaly [87]. Figure 2.16 shows a schematics of the proposed experiment. The two main detectors are a $PbWO_4$ calorimeter for photon measurement and two Gas Electron Multipliers (GEM) placed in front of it that provide a limited tracking. The calorimeter is the inner part of an already existing detector, the HyCal, and is a 34×34 crystals matrix that covers a 68×68 cm^2 area, the same area covered by the two planes of GEM.

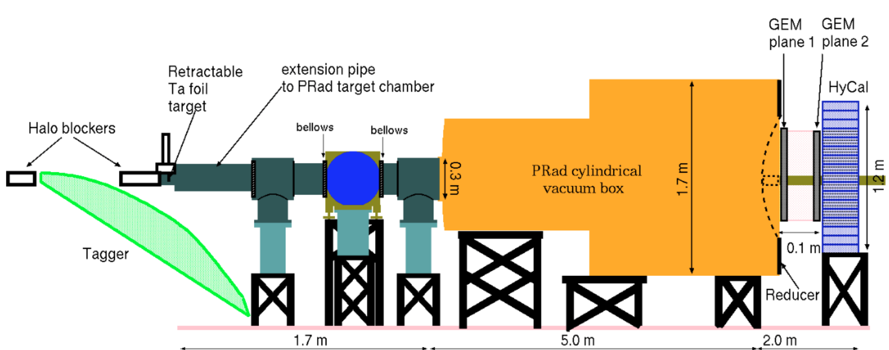

Figure 2.16: Schematics of the new experiment proposed at JLab. Figure from [87].

The dark photon is produced in the Bremsstrahlung reaction of a 2.2 GeV or 3.3 GeV CW electron beam incident on a thin target of 1 μm Tantalum. The experiment will detect the scattered electron and the products of the decay of the dark boson, allowing for a full reconstruction of the event. Moreover, it is equally sensitive to the neutral decay channel $A' \to \gamma\gamma$. The mass range explored by this experiment is 3-60 MeV/c^2, with a design sensitivity on ϵ^2 in the range $7.2 \times 10^{-8} - 5.9 \times 10^{-9}$, which is competitive with the currently expected experiments involved in this search.

Summary

The X(17) may be identified with the dark photon A', that is a candidate to explain the ^{8}Be anomaly. Figure 2.17 shows a projection of the A' mass and electron coupling ranges that will be inspected by future experiments. In this plot the focus is on the mass scale in which the anomaly appeared.

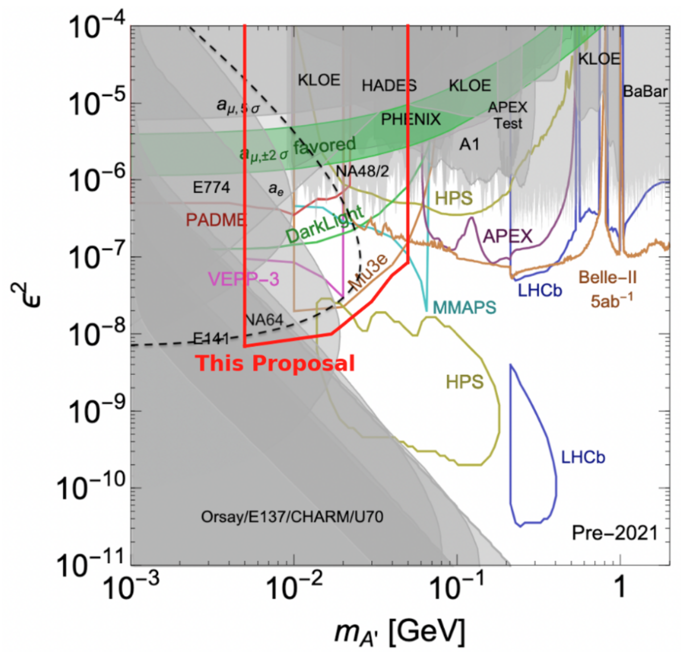

Figure 2.17: Projection of the hypothetical boson mass and electron coupling ranges that will be inspected by future experiments. The red contour refers to the expected sensitivity at the new experiment proposed at JLab. Figure from [87].

2.2 X(17) searches in other IPC experiments

Besides the studies on the dark photon ongoing at accelerator facilities, there are numerous experiments that wants to look for the hypothetical X(17) in IPC from nuclear transitions, as the experiment at Atomki did. The parallel measurement planned at the MEG II experiment falls in this category, but I will dedicate a separate chapter to it. Therefore here I will briefly describe the other planned IPC measurements around the world.

IPC measurement with COPE detector at CTU

The Institute of Experimental and Applied Physics (IEAP) at Czech Technical University (CTU) in Prague is designing a new experiment to measure IPC in different nuclear reactions. The experimental apparatus is based on the Timepix3 (TPX3) detector, which is a pixel silicon detector composed of a matrix of 256×256 55 μm$\times$55 μm pixels for $e^{\pm}$ measurement. They can be used for X-rays imaging, track reconstruction and also as readout for gas and semiconductor based detectors. In 2018 the IEAP started the X(17) search using a set of three TPX3 placed around a CeF_3 target, as shown in figure 2.18. The setup was installed at the CTU Van de Graaff accelerator, which provides a proton beam with an energy $E_p = 0.2 - 2.2$ MeV and a current $I = 0.5 - 10$ μA. They were able to measure the tracks of the e^+e^- pairs with a good spatial resolution, but no energy measurement was possible.

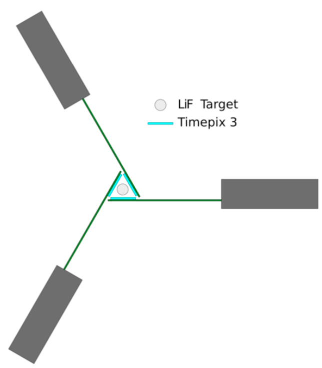

(a)

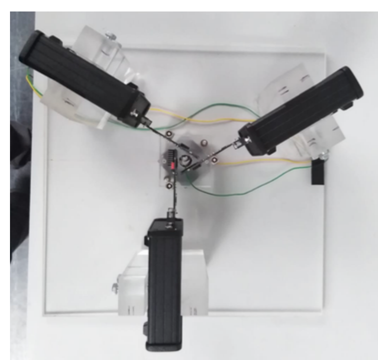

(b)

Figure 2.18: Drawing (a) and picture (b) of the experimental setup used at IEAP for the first test in the X(17) search.

The IEAP proposed the COmpact Positron Electron spectrometer (COPE) to have a full measurement of the X(17) decay products. Figure 2.19 shows the design of the experimental setup. An hexagonal array of 6 TPX3 is placed around the target, and everything is installed inside a vacuum tube. In front of the TPX3 but outside the tube there is a MWPC that provides a second point on the particle track far from the interaction point. Finally, a Time Projection Chamber (TPC) is installed behind the MWPC to complete the e^+e^- measurement. The whole detector is placed inside a magnetic field that allows to distinguish a positron from an electron. This detector will allow to measure with high precision the pairs from IPC in different nuclear reactions and to contribute to the global search for an explanation of the X(17) anomaly.

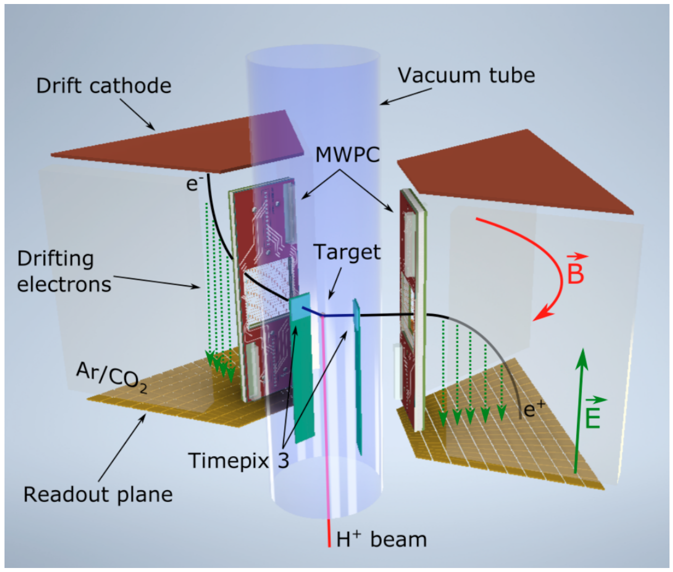

Figure 2.19: Drawing of the COPE detector proposed for the X(17) measurement at CTU.

IPC experiment at Legnaro Laboratory

The Laboratori Nazionali di Legnaro (LNL) are equipped with a 2 MV Van de Graaff accelerator that can reach a proton beam current of 1 μA. The protons from this accelerator can be used to excite the nuclear states from which an X(17) can be emitted, so a $e^{\pm}$ modular detector have been proposed to perform a measurement similar to the Atomki one [88].

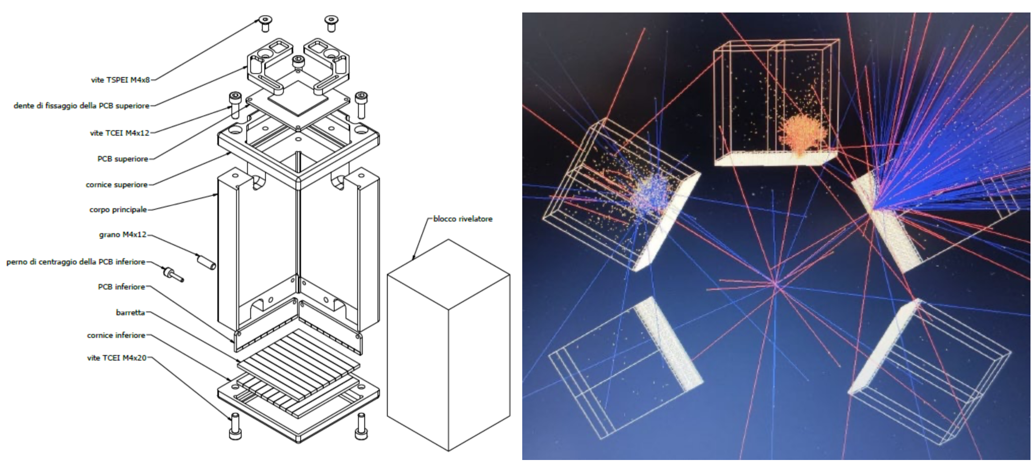

(a) (b)

Figure 2.20: (a) Schematics of a single detector module for $e^{\pm}$ measurement. (b) Drawing of a possible configuration of the modules for the experiment.

Figure 2.20 shows the design of a single module of such detector and a possible configuration for the experiment. The goal is to measure the X(17) decay products in the ^{8}Be and ^{12}C de-excitation with a good angular resolution thanks to the low material budget and a good angular coverage thanks to the possibility to measure out of plane correlations. The first test already started: a prototype of a module has been built and tested with a ^{60}Co source.

IPC measurement at nToF

The anomaly in the ^{4}He de-excitation can be studied at the nToF facility at CERN, shown in figure 2.21. The nToF provides a pulsed neutron beam with an energy up to $E_n = 100$ MeV, and can be used to produce the $^{3}\mathrm{He}(n, X)^{4}\mathrm{He}$ reaction, which was not explored at Atomki.

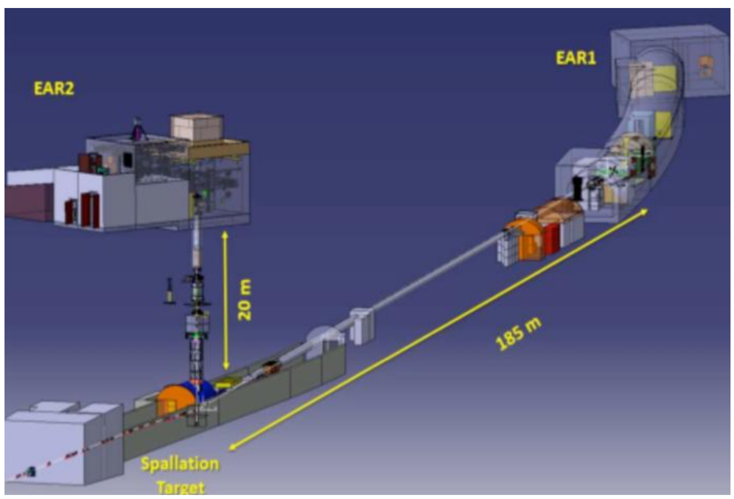

Figure 2.21: Drawing of the nToF facility at CERN.

Figure 2.22 shows a conceptual design of the detector to be used for the X(17) measurement at nToF. A high intensity neutron beam with energy $0 < E_n < 3$ MeV impinges on a high density ^{3}He target, and the resulting e^+e^- pair is detected by a combination of a tracker and an EM calorimeter. The tracker should be composed of two Ring Imaging CHerenkov detectors (RICH), one above and one below the target, but another option is to use a TPC with a Micro Pattern Gas Detector (MPGD) readout. A prototype of the latter detector is already being tested. The same goes for the calorimeter: two options are being tested, one with Ej-200 segmented scintillator and one with LYSO crystals.

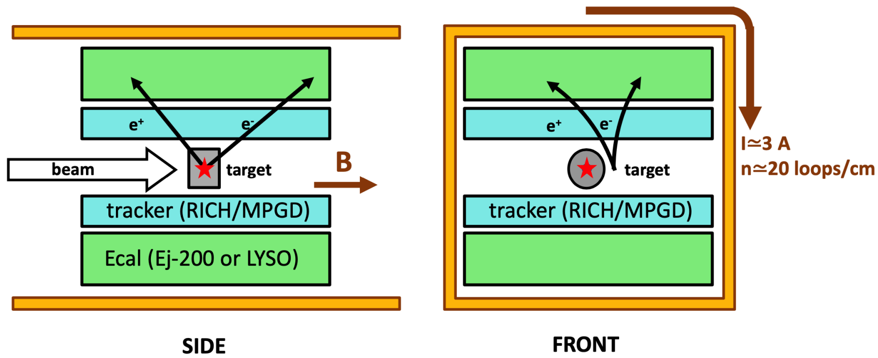

Figure 2.22: Conceptual design of the detector for the X(17) measurement at nToF.

IPC measurement at LUNA

The ^{4}He de-excitation can also be explored at the LUNA-MV facility at Laboratori Nazionali del Gran Sasso (LNGS), shown in figure 2.23. LUNA-MV is a high intensity proton beam accelerator that can provide a proton beam with a maximum current of 100 μA, thus being able to produce the ^{3}H$(p, X)^4$He reaction. More theoretical details about this reaction and the one explored at nToF can be found in [89].

Figure 2.23: Picture of the LUNA-MV facility at LNGS.

X(17) measurement at Montreal

The UdeM 6 MV Tandem Van de Graaff Facility at CCPAC in Montreal is able to produce a ^{3}He beam, and has a beamline dedicated to the X(17) measurement. Its goal is to measure IPC in ^{8}Be and ^{10}B nuclear reactions with a 95% angular acceptance to remove the possible bias introduced by the experimental apparatus. The detector is based on a part of the DAPHNE tracking chamber, a MWPC with an angular resolution of $\sim 2°$. The $e^{\pm}$ timing is measured by a set of 16 scintillators installed at both ends of the MWPC. Figure 2.24 shows a drawing of the detector. A first test of the tracker was performed, and the 16 scintillators have been already brought to Montreal.

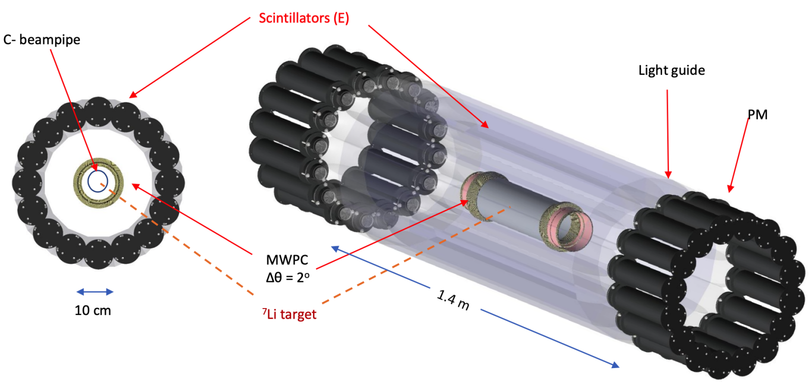

Figure 2.24: Drawing of the detector for the X(17) measurement at Montreal.

MEG II

The MEG II experiment at the Paul Scherrer Institut in Switzerland is planning to repeat the ^{8}Be measurement in which the anomaly has been observed. It will employ a proton beam from a Cockcroft-Walton accelerator impinging on a Li_2O target. A more detailed description of the experiment can be found in chapter 3.

Chapter 3

MEG II experiment

The MEG II experiment is built to search for charged Lepton Flavor Violation (cLFV) in the $\mu^+ \to e^+\gamma$ decay. The first phase of MEG [90–93] with the full dataset achieved a upper limit at 90% Confidence Level (CL) on the branching ratio of:

$$\mathrm{BR}(\mu^+ \to e^+\gamma) < 4.2 \times 10^{-13} \tag{3.1}$$

MEG II wants to improve this result of a factor 10, reaching a sensitivity of $\sim 6 \times 10^{-14}$ [94, 95]. It was also able to set a limit on the branching ratio of the $\mu \to eX,\ X \to \gamma\gamma$ decay [96], where X is not the X(17) particle but a generic new particle with $m_X < m_\mu$.

In this chapter I will focus on the MEG II experimental setup. I will show its detectors and CW accelerator in detail, and then I will report some specifics about the X(17) measurement.

3.1 Overview of the MEG II experiment

The main detectors of the experiment, shown in figure 3.1, are a Liquid Xenon photon detector (LXe), a magnetic spectrometer for the positron detection and a Radiative Decay Counter (RDC) as a Radiative Muon Decay (RMD, $\mu^+ \to e^+\gamma\nu_e\bar{\nu_\mu}$) background tagging detector. The magnetic spectrometer is composed of a pixelated Timing Counter (pTC) for time measurement and a Cylindrical Drift CHamber (CDCH) for energy measurement and tracking. These detectors are placed inside a COnstant Bending RAdius (COBRA) magnet that generates an axially graded magnetic field with an intensity ranging from 0.49 T to 1.27 T.

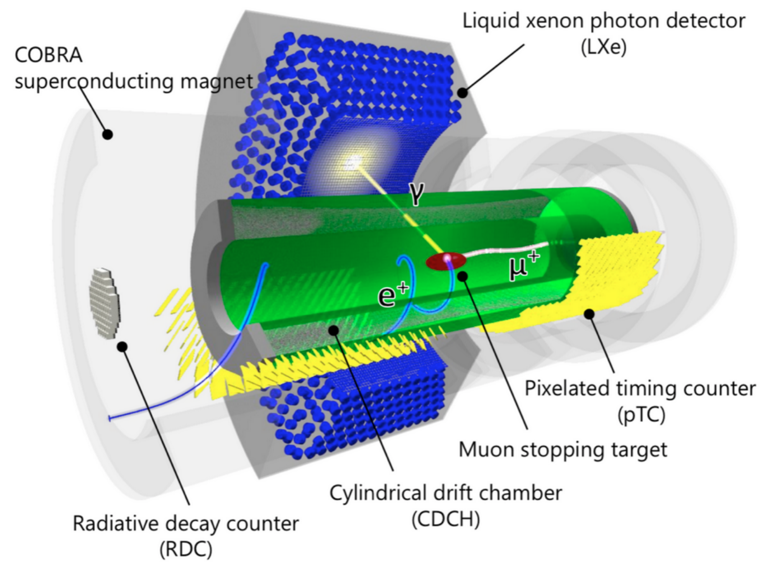

Figure 3.1: Layout of the MEG II experiment. Figure from [95].

The goal of the upgrade is to improve the sensitivity, which is achieved by building new detectors, or improve old ones, to make them compatible with an higher μ^+ beam rate and to have better resolution and efficiency to improve background rejection. With this in mind, the old target was replaced by a thinner one, the old modules of drift chamber were replaced by a new single volume wire DCH and the old timing counter scintillating bars were replaced by fast scintillating tiles. Moreover, the inner face of the LXe, that hosted Photo Multiplier Tubes (PMT) in the first phase of MEG, is now covered by Multi-Pixel Photon Counters (MPPC). These improvements increased the granularity of the detector readout, requiring a new Trigger and Data Acquisition (TDAQ) integrated system. Also the RDC detector is a new addition in the MEG II experiment. More details about it can be found in [97, 98].

There are several calibration procedures for the main detectors. For example the LXe is calibrated with photons produced by a dedicated Cockcroft-Walton (CW) accelerator. The CDCH is calibrated using cosmic rays triggered by a set of Cosmic Ray Counters (CRC) built using the old TC scintillating bars. Another CDCH calibration uses e^+e^- pairs produced by the interaction of the CW proton beam with a Lithium Tetraborate ($Li_2B_4O_7$) target. They are mostly produced by External Pair Creation (EPC) of the photon produced in the ^{7}Li$(p, \gamma)^8$Be reaction that interacts with the material of the detectors. Thanks to the small CW accelerator it is possible to repeat the Atomki ^{8}Be measurement with some modifications to the MEG II original apparatus. In the next paragraphs I will focus on the detectors that are essential for such measurement, giving some details on their performances.

3.2 Cockcroft-Walton accelerator

The CW accelerator is used for the frequent MEG II calibrations needed to maintain good detector resolutions [99]. The proton beam can reach an energy up to $E_p = 1.1$ MeV and a current up to 100 μA, and is brought to the center of the experiment by a special bellows insertion system. The accelerator is placed in the DownStream (DS) side of the apparatus, thus the proton beam travels in an opposite direction with respect to the μ beam used for the $\mu^+ \to e^+\gamma$ measurement. The target used for LXe calibrations is made of $Li_2B_4O_7$, so that the impinging protons can produce two reaction: ^{7}Li$(p,\gamma)^8$Be or ^{11}B$(p,\gamma\gamma)^{12}$C*. The first reaction is used to produce one 17.6 MeV photon at $E_p = 441$ keV, needed for energy calibration, and the second reaction is used to produce two coincident 11.67 MeV and 4.4 MeV photons for energy and time calibration.

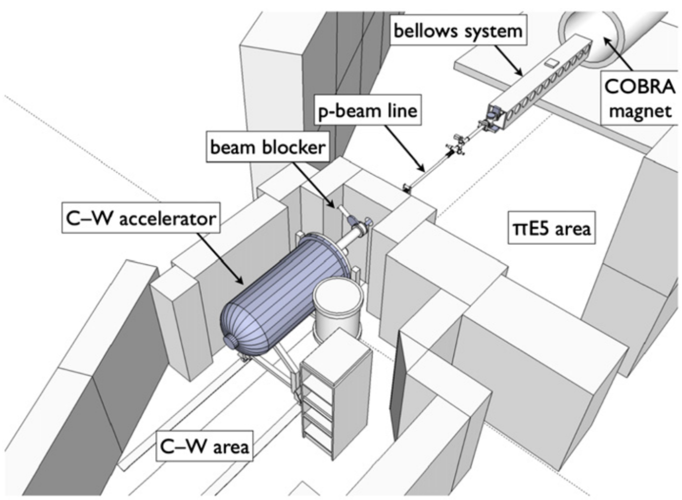

Figure 3.2: Layout of the CW accelerator and insertion system. Figure from [99].

Figure 3.2, 3.3 and 3.4 show respectively the drawing of the CW accelerator and beamline, the schematics of the bellows insertion system and a picture of both. The accelerator is hosted in a separate radiation-safety monitored area, and the proton beam is transported to the πE5 area of the PSI experimental hall in which MEG II is hosted using a beam transport system. It is composed of vacuum pipes and horizontal and vertical steering magnets. A controlled beam pipe insertion system is used to insert the target used to produce the calibration reactions. The system is automated, and brings the target at the center of the magnetic spectrometer inside COBRA.

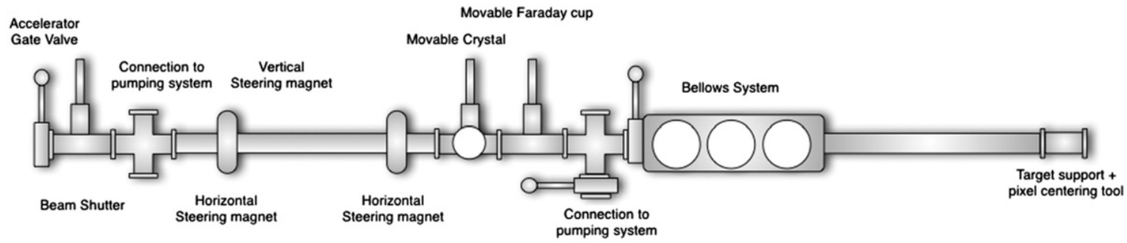

Figure 3.3: Schematics of the beam optics and the bellows insertion system. Figure from [99].

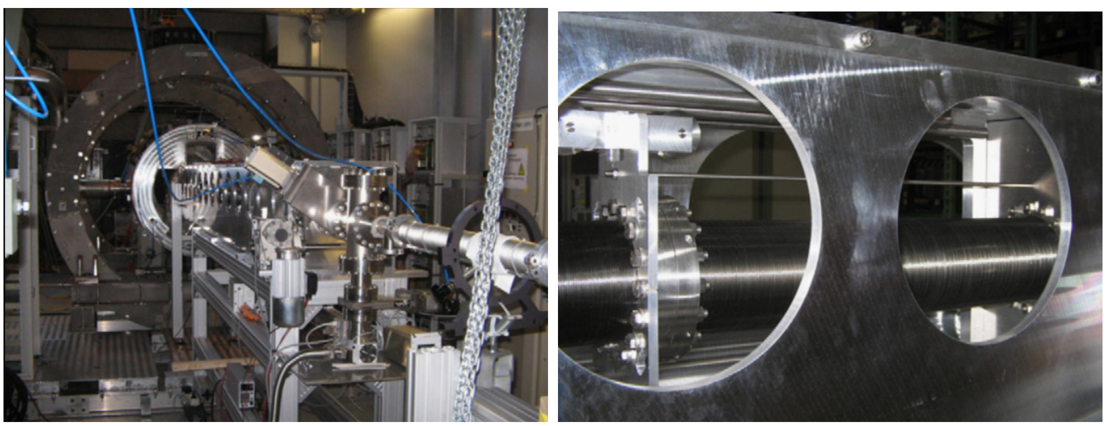

(a) (b)

Figure 3.4: Pictures of the CW beamline (a) and bellows insertion system (b). Figure from [99].

An additional rubber bellows insertion system with a larger diameter is needed to allow the insertion of the beam pipe with the target. It is connected to the DS endcap of the apparatus and is coupled to the CW bellows system so that they can be simultaneously moved inside the CDCH volume. During the calibration both bellows are fully extended inside the detector, and they are retracted during MEG II muon beam data taking. The outermost bellows, though retracted, remains inside the detector, while the beam pipe goes completely outside the endcap. The Al beam pipe is 223 cm long, and can be moved by 221 cm in total. The bellows system has a total length of 360 cm.

Table 3.1 reports the characteristics of the CW accelerator reported in [99]. Albeit it is reported to reach 1 MeV proton energy, it has been successfully tested with 1.1 MeV energy. It is also possible to reach higher currents: it was successfully tested to run at 50 μA at E_p = 1.1 MeV and 100 μA at E_p = 1.05 MeV. These specifications fulfill the requirements for the X(17) measurement, most importantly the proton energy, that allows to populate the 18.15 MeV ^{8}Be excited state.

Energy (keV)	300-1000
Energy spread (FWHM) (keV)	<0.5
Angular divergence (FWHM) (mrad×mrad)	<3×3
Spot size at 3 meter (FWHM) (cm×cm)	<3×3
Energy setting reproducibility (%)	0.1
Energy stability (FWHM) (%)	0.1
Range of the average current (μA)	1-10
Current stability (%)	3
Current reproducibility (%)	10
Duty cycle (%)	100

Table 3.1: Characteristics of the CW accelerator. Data from [99].

3.3 Magnetic spectrometer

The measurement of the positron in $\mu^+ \to e^+\gamma$ is entrusted to a magnetic spectrometer. This is the detector that was most subject to changes with respect to the first phase of MEG. In fact, both the timing detector and the tracker were completely changed to ensure a finer granularity and a lower material budget, thus improving the overall performance. Conversely the COBRA magnet is the same one used for MEG. The resolution of the detector allows for a competitive measurement of the ^{8}Be anomaly: the CDCH can reach a better invariant mass resolution with respect to the experiment at Atomki, as I will quantitatively show in section 5.1.4. Moreover the pTC can be used as a trigger, reducing the efficiency but increasing the cosmic rays background rejection. To maximize the quality of the measurement it is necessary to optimize the COBRA magnetic field, since the e^+e^- pairs from X(17) decay have energies lower than the usual 52.8 MeV MEG II positrons.

3.3.1 COBRA magnet

The magnetic field necessary to bend the positron track is generated by the COBRA superconducting magnet [100]. Figure 3.5 and 3.6 show respectively the schematics of the magnet and a picture of it, taken before its integration in the experimental apparatus. It has a total length of 2.8 m along the beam axis, and its radius at the center is about 30 cm. The field is graded by five coils with three different radii: one central coil, two end coils and two gradient coils. The wall of COBRA must be as thin as possible in order to reduce the photons absorption: for such reason a high strength Al stabilized conductor was developed. The total COBRA thickness in the central part is 0.197 X_0.

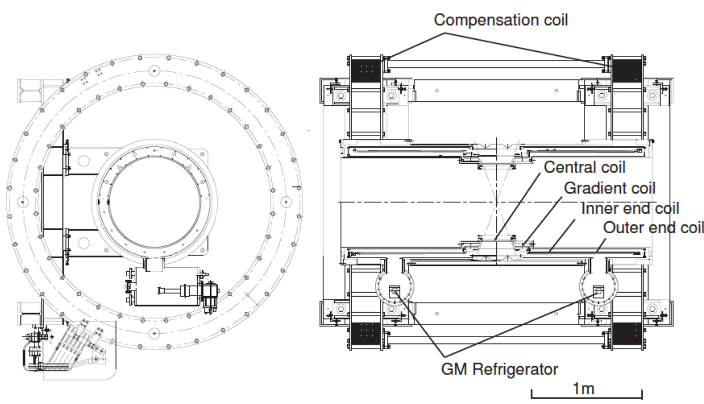

Figure 3.5: Schematic view of the COBRA magnet. Figure from [100].

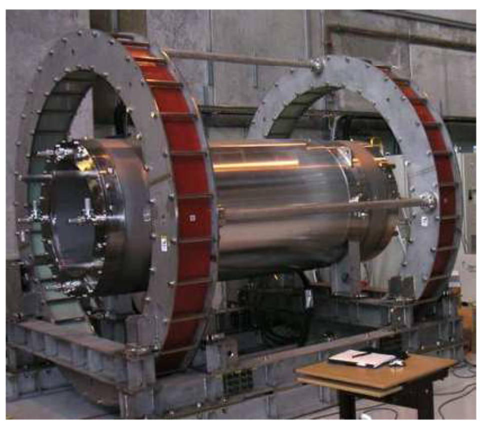

Figure 3.6: Photograph of the COBRA magnet in the PSI experimental hall.

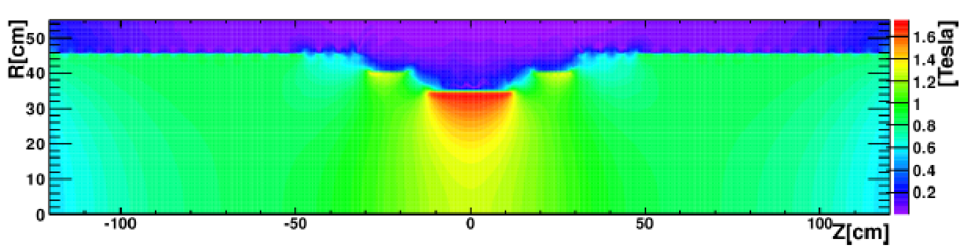

Figure 3.7: Contour plot of the COBRA magnetic field in the (z, r) plane. Figure from [90].

The magnetic field is measured with a three-axis Hall probe, and it ranges from 1.27 T at the center to 0.49 T at both ends. Figure 3.7 shows the map in the (z, r) plane. The non-homogeneity of the magnetic field prevents the positrons emitted almost perpendicular to the beam axis to repeatedly cross the CDCH sensitive volume. Figure 3.8 shows how this happens by keeping constant the bending radius of the positron, regardless of its emission angle. This allows the positron tracker to be confined at large radius, so to avoid large pileup from low energy positrons from the Michel decay ($\mu^+ \rightarrow e^+\nu_e\bar{\nu_\mu}$).

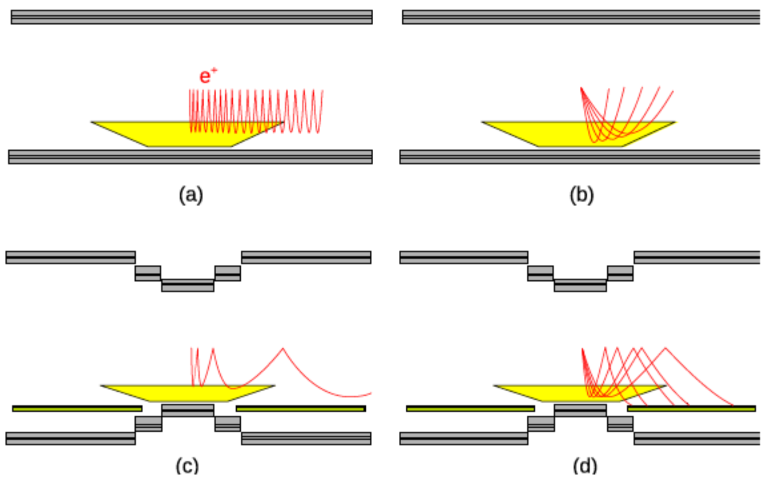

Figure 3.8: Concept of the COBRA gradient magnetic field compared to a uniform field. In (a) and (b) the behavior of two positrons with different emission angle are shown in the uniform field case, in (c) and (d) the same events are shown in the COBRA field case.

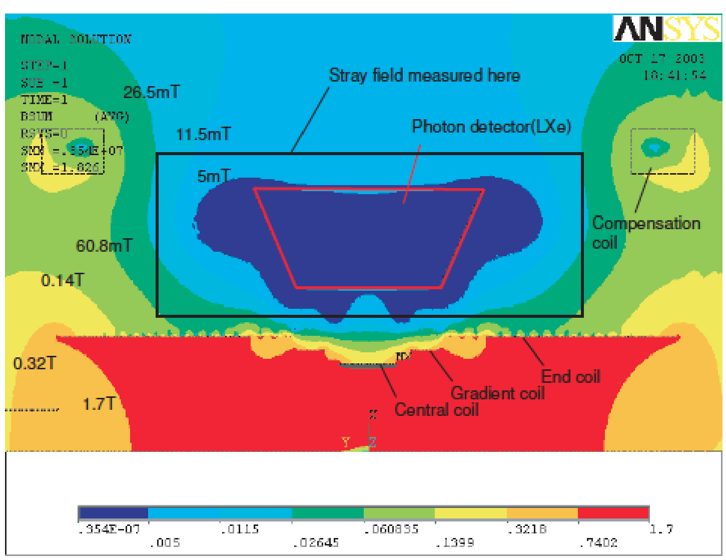

Figure 3.9: Distribution of the magnetic field around the LXe detector. The red box is where the PMTs are placed and the magnetic field is suppressed by the compensation coils. Figure from [90].

A pair of compensation coils was installed to keep the field in the area surrounding the LXe detector below 5×10^{-3} T. This prevents the efficiency loss of its PMTs, as shown in figure 3.9. The compensation coils, in fact, cancel the magnetic field from the main magnet because the shape of the flux lines they produce is very similar to that produced in the LXe region by the main magnet.

3.3.2 Pixelated Timing Counter

The detector used to measure the positron timing is a pixelated timing counter [101, 102]. Since the CDCH cannot provide a fast signal due to the latency introduced by the drift time, the trigger signal for the positron has to be issued by a fast detector that can provide prompt time and direction information. Such detector needs to have an excellent time resolution and to be fast.

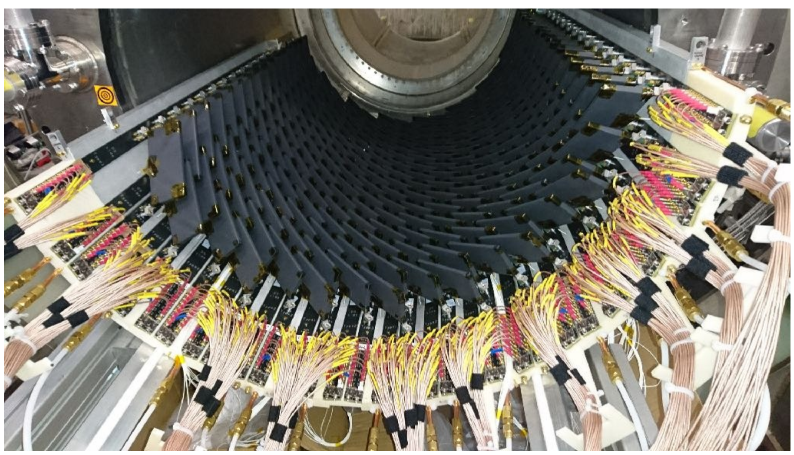

Figure 3.10: Picture of a single pTC module installed inside the COBRA volume. At the time of the picture the CDCH was not installed yet.

To comply with the requirements the pTC is designed as follows: it is composed of two identical modules, one placed DS and another placed UpStream (US) the target, each one containing 256 scintillating tiles read out by Silicon PhotoMultipliers (SiPM). This high granularity guarantees a good number of hits, resulting in a time resolution improvement. Figure 3.10 and figure 3.11 show respectively a picture and a drawing of a single module of the detector. The pTC calibration is possible thanks to a laser system that simultaneously irradiates every tile through several optical components, so that the time offset of each tile can be measured [103]. The detector is also equipped with a cooling system, needed to limit the dark count rate in the SiPMs [104].

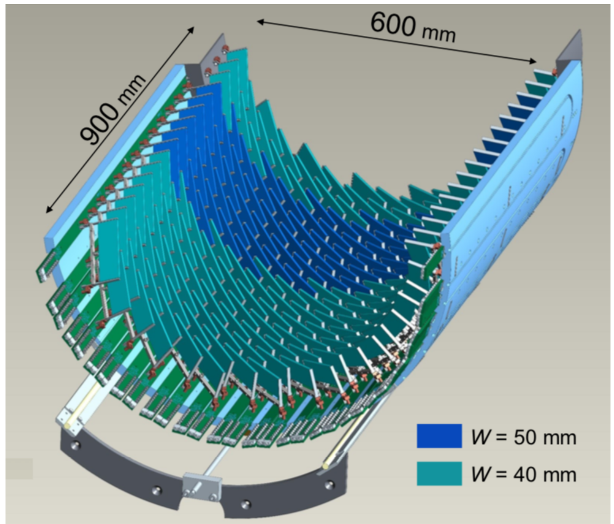

Figure 3.11: Drawing of a single pTC module. Figure from [95].

A single tile is composed of a fast plastic scintillator plate coupled to six SiPMs in series at each end. The scintillator is a BC-422 from Saint Gobain [105] with two different dimensions depending on the tile location: $120 \times 40 \times 5$ mm^3 and $120 \times 50 \times 5$ mm^3. Figure 3.12 shows both types of tiles. A measurement with a ^{90}Sr source proved that all tiles have a resolution below 100 ps. Moreover, the average resolution of a single tile is 72 ps and 81 ps for $W = 40$ mm and $W = 50$ mm scintillators respectively.

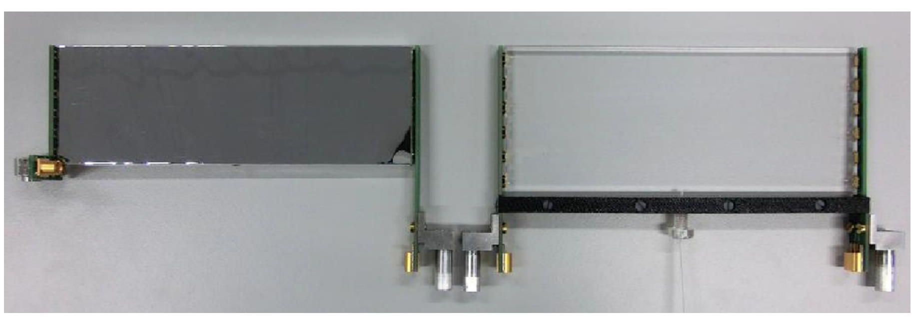

Figure 3.12: Picture of both types of pTC tiles. The left one is a $W = 40$ mm tile wrapped in the reflector, the right one is a $W = 50$ mm tile without reflector but connected to the laser optical fiber. Figure from [106].

The pTC commissioning ended in the 2017 MEG II pre-engineering run [106]. Using the PSI μ^+ beam at 7×10^7 μ/s intensity the detector hit rate, radiation damage and resolution have been studied. Since the CDCH was not yet installed in the experiment, the pTC-alone tracking was used to evaluate the time resolution. The positron timing was reconstructed by combining hit times after known Time of Flight (ToF) subtraction, and the overall resolution was estimated to be 35 ps, slightly worse than the one estimated from ^{90}Sr tests due to the worse noise condition. This value is expected to deteriorate up to 41 ps at the end of the MEG II physics run due to radiation damage, but it still complies with the requirements.

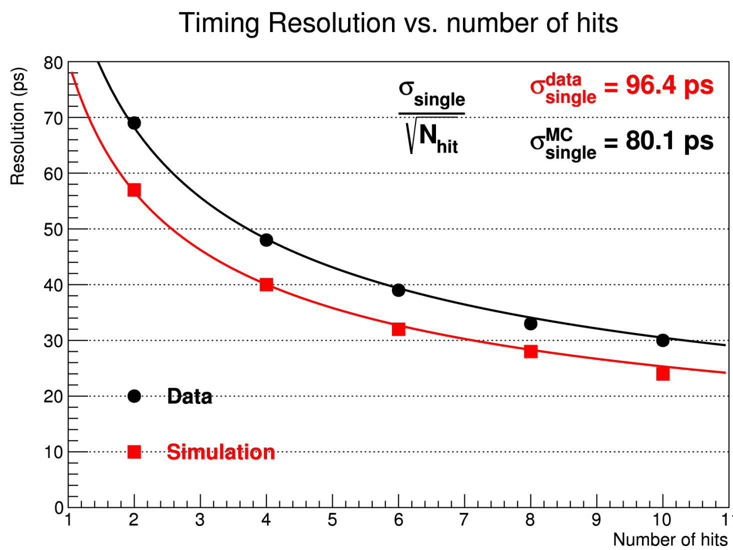

Figure 3.13: pTC time resolution as a function of the number of the hits on all tiles. MC expectation is also reported. The small discrepancy can be explained by the difficulty of simulating off target decays. Figure from [106].

Figure 3.13 shows the measured and simulated time resolution as a function of the number of hits in all the tiles. The detector is designed to have 9 hits per track on average to keep a good resolution, since $\sigma(t_{e^+}) = \frac{\sigma_{\text{single}}}{\sqrt{N_{\text{hit}}}}$. For this reason the overall resolution is calculated as the resolution at 9 hits. Table 3.2 summarizes the detector performance. The pTC e^+ time resolution, combined with the LXe γ time resolution that I will address later, allows for a relative time resolution of 70 ps.

	$\sigma(\mathbf{t_{e^+}})$	$\sigma(\mathbf{t_{e^+\gamma}})$
TC	35 ps	70 ps

Table 3.2: Summary of the MEG II pTC performance.

3.3.3 Cylindrical Drift Chamber

The MEG II tracker is a single volume cylindrical drift chamber, shown in figure 3.14 during its construction [107]. It is used to measure the momentum and track of the positron and its resolutions are very sensitive to the multiple scattering, so all the detector parts have to be as light as possible. It has 1728 20 μm thick golden tungsten sense wires arranged in 9 planes and 40/50 μm thick silver plated Al cathode wires, with a ratio 5:1. The 50 μm cathodes are the ones between the anodes on the same plane, the 40 μm cathodes are the ones between the planes. Two guard layers of 50 μm thick silver plated Al cathodes, the innermost and the outermost one, are used for gain equalization. The total radiation length crossed in a single positron turn is 1.58×10^{-3} X_0. The wires are placed with a stereo geometry in order to measure the z coordinate, along the beam axis. The CDCH is filled with a light gas mixture of 90:10 He:iC_4H_{10} and two additives that guarantee the detector stability: isopropyl alcohol and oxygen in small concentrations, 1% and 0.5% respectively.

Figure 3.14: CDCH before closing it with the Carbon Fiber (CF) cover. Figure from [107].

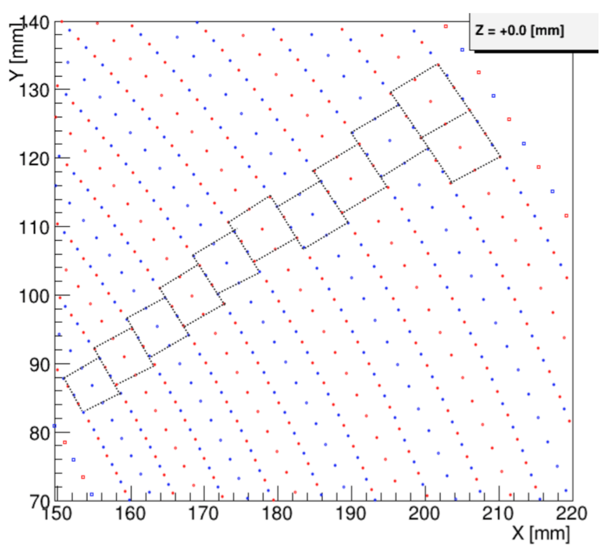

Figure 3.15: CDCH drift cells schematics at the center of the detector. The anode wires are in blue and the cathode wires are in red. Figure from [95].

The CDCH is placed co-axial to the MEG II muon beam. It is 1.91 m long and the inner and outer radius are 17 cm and 29 cm respectively. The wires are arranged in 9 concentric layers, each divided in 12 sectors. Each sector contains 16 drift cells with a sense wire surrounded by the cathode wires. Figure 3.15 shows an example of the drift cells at the center of the detector. The single drift cell is, to a good approximation, a square with a side that ranges from 6.6 mm to 9.0 mm, smaller in the innermost layer and bigger in the outermost ones because of the stereo geometry.

The stereo geometry of the wires is obtained by mounting each layer with alternating stereo angles, ranging from 6° to 8.5°. This is clarified in figure 3.16, that shows a drawing of the spectrometer using different colours for the criss-crossing layers.

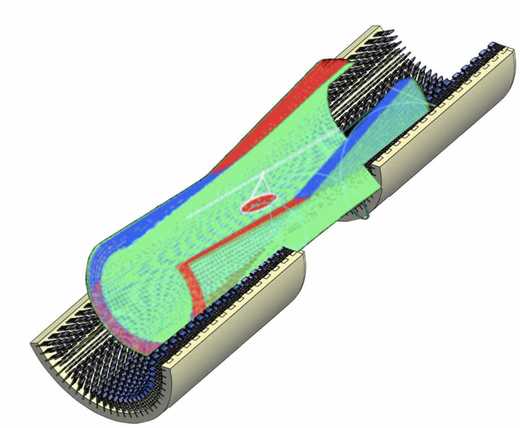

Figure 3.16: Drawing of the CDCH and pTC detectors. The red and blue color scheme highlights the stereo geometry of the wires. The figure represents a portion of the CDCH, which is actually a full cylinder. Figure from [94].

This peculiar geometry allows for a precise reconstruction of the z coordinate, supported also by a double readout structure that makes charge division and time difference measurements possible. The expected performance of the CDCH is summarized in table 3.3. I will provide more detailed information on the CDCH construction and commissioning in chapter 4.

	$\sigma(\mathbf{E_{e^+}})$	$\sigma(\vartheta_{\mathbf{e^+}})$	$\sigma(\varphi_{\mathbf{e^+}})$	$\sigma(\mathbf{z_{e^+}}/\mathbf{y_{e^+}})$	$\varepsilon(\mathbf{e^+})$
CDCH	100 keV	6.7 mrad	3.7 mrad	1.6/0.7 mm	65%

Table 3.3: Summary of the MEG II CDCH performance.

3.4 Photon detector

The MEG II photon detector is a large 900 L tank filled with liquid xenon [108]. It measures the energy, time and conversion point of the incoming photon with high precision, using the liquid xenon, which emits scintillation light in the UV, as active material.

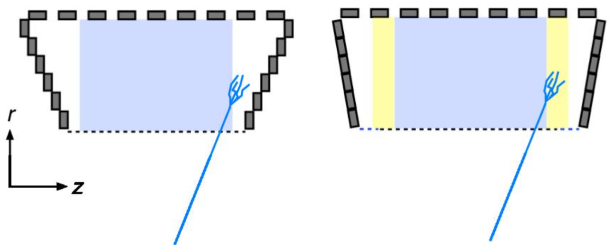

Figure 3.17: Section of the LXe photon detector in MEG (a) and MEG II (b). In yellow the increased acceptance after the new lateral PMTs arrangement for MEG II. Figures from [95].

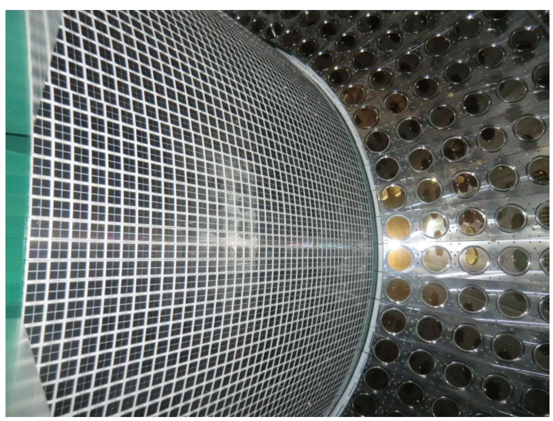

Figure 3.18: Picture of the LXe inner faces. Figure from [95].

In the first phase of MEG the signal was collected by 846 2 inches PMTs sensitive to Vacuum UltraViolet (VUV) light at T=165 K. Since the coverage of the detector was not uniform, it was upgraded for MEG II: the 216 PMTs at the entrance face have been replaced by 4092 VUV-sensitive 12×12 mm^2 MPPCs. They are insensitive to the COBRA magnetic field and increase the granularity, spatial resolution and efficiency of the detector, because of the less material crossed by the photon. Moreover, the active volume has been increased so that the photons shower leakage near lateral faces is better contained, as shown in figure 3.17. Figure 3.18 shows a picture of the inner side of the new LXe detector with MPPCs and PMTs installed.

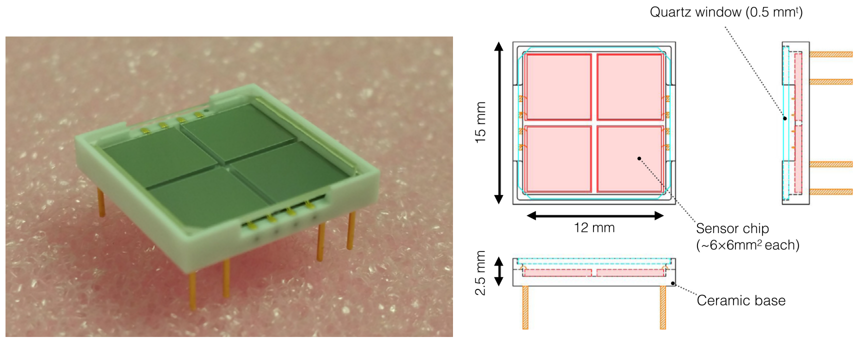

(a) (b)

Figure 3.19: Picture (a) and schematics (b) of the four chips connected to form an MPPC. Figures from [109].

The MPPC was developed by the MEG II collaboration together with Hamamatsu Photonics [109]. It has a photon detection efficiency (PDE) $>$ 10% for LXe scintillation light and a decay time of $\sim$ 50 ns. Figure 3.19 shows a picture and a schematics of an MPPC: it consists of four independent 6×6 mm^2 sensor chips connected on a PCB in series to reduce the capacitance. Thus the signal can be read out by one channel per MPPC. The installation of these detectors improved the imaging of the LXe, increasing the separation power of two pileup photons.

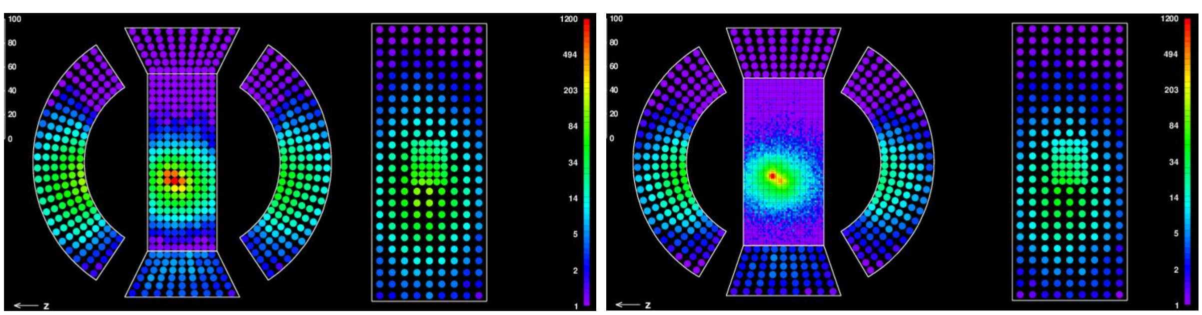

(a) (b)

Figure 3.20: Event display of MEG (a) and MEG II (b) LXe. The scintillating light from two pile up photons is indistinguishable in MEG, but the finer granularity of the MPPC in MEG II allows for a better separation. Figures from [95].

Figure 3.20 shows an example of event display for MEG and MEG II, highlighting this improvement. Here the same two photons event appears as a single cluster in the MEG configuration, while in the MEG II configuration two separate clusters are clearly visible.

The performance of the detector is monitored with several calibration procedures that span the full energy range of the detector. The low energy region is monitored with 4.4 MeV γ from an AmBe source, from 5.5 MeV α from ^{241}Am sources deposited on thin wires inside the detector and from 9.0 MeV γ from neutron capture by ^{58}Ni, produced by a neutron generator. The intermediate region is monitored with the nuclear reactions from the CW generator: γ from $^7\mathrm{Li}(p,\gamma)^8\mathrm{Be}$ and $^{11}\mathrm{B}(p,\gamma\gamma)^{12}\mathrm{C}$ have energies of 17.6 MeV, 4.4 MeV and 11.6 MeV respectively. The first reaction is the one that will be investigated for the X(17) search, albeit at a different proton beam energy; the second reaction is used also for the time calibration. The high energy range is monitored using photons from π^0 decays produced in the Charge EXchange (CEX) reaction obtained from a dedicated pion beam impinging on a liquid hydrogen target: $p(\pi^-,\pi^0)n$.

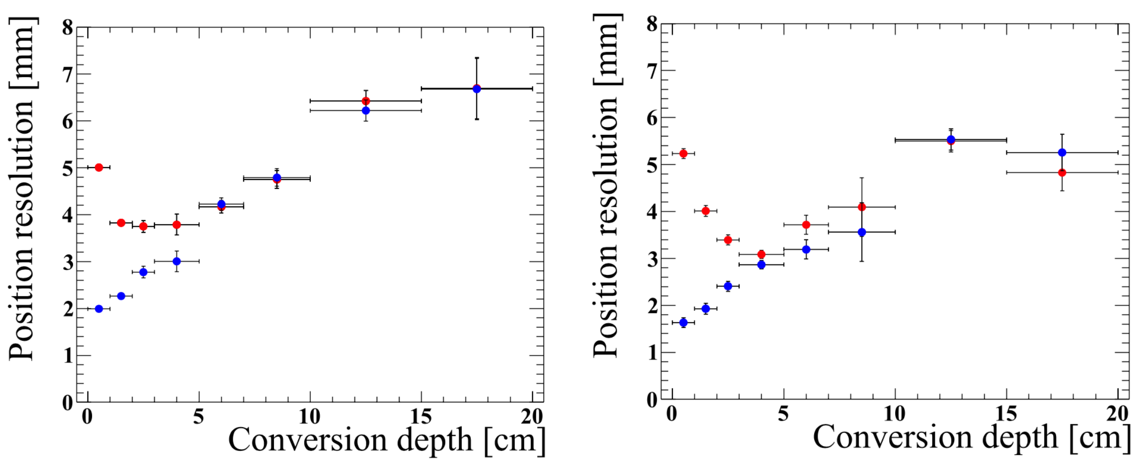

(a) (b)

Figure 3.21: Spatial resolution as a function of the conversion depth w for horizontal (a) and vertical (b) directions. MEG resolutions are reported in red, while MEG II resolutions are reported in blue. Figures from [95].

Figure 3.21 shows the spatial resolution as a function of the conversion depth w for 52.8 MeV signal photons. The improvement from MEG is evident in the shallow region of the detector because of the smaller size of the MPPC with respect to the PMT. Figure 3.22 shows the fit to the measured background photon spectrum obtained from muon decays. The energy resolution is estimated by the best fit of the MC spectrum convoluted with several energy resolution assumptions: the result is $\sigma(E_\gamma)/E_\gamma = 1.7\%$, valid for the signal region. Table 3.4 summarizes the performance of the LXe detector.

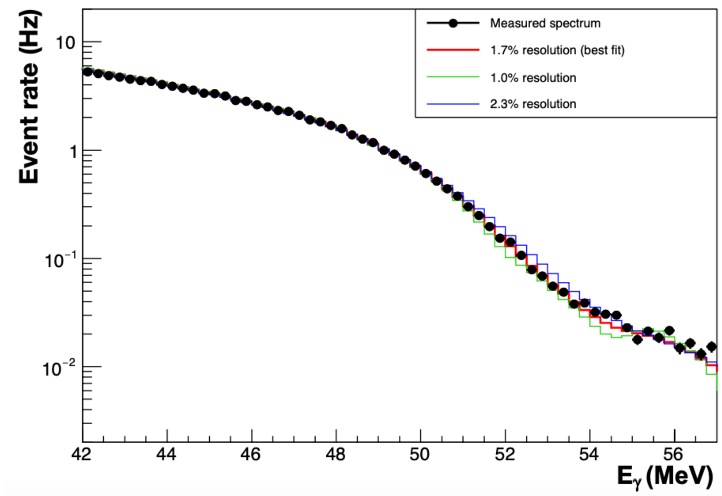

Figure 3.22: Measured and simulated background photon spectrum. The different colors represent the convolution of the spectrum with different energy resolution assumptions. The best fit is the red histogram, corresponding to 1.7% resolution. Figure from [110].

	$\sigma(\mathbf{x}_\gamma)$	$\sigma(\mathbf{E}_\gamma)/\mathbf{E}_\gamma$	$\sigma(\mathbf{t}_\gamma)$	$\sigma(\mathbf{t}_{\mathbf{e}^+\gamma})$
LXe	2.5 mm	1.7%	39 ps	70 ps

Table 3.4: Summary of the MEG II LXe performance.

3.5 Trigger and data acquisition

The upgrade of the detectors caused a huge increase in the number of readout channels. For such reason MEG II needed a new TDAQ system able to fit all the electronics in the same physical space used in the first phase of MEG. This system combines the previous DAQ, trigger and HV systems into a single one, and is called WaveDAQ [111–113]. It is composed by three different types of board hosted in a custom crate with an integrated power supply (24 V/360 W). The backplane of the crate is also custom and is equipped with Gigabit serial links. The three boards are the WaveDREAM (DRS4 based REAdout Module) Board (WDB), the Trigger Concentrator Board (TCB) and the Data Concentrator Board (DCB).

The WDB is a digitizer that can reach a sampling frequency of 5 GSPS. It is based on the Domino Ring Sampler (DRS) [114], a fast digitizer developed at PSI. Figure 3.23 shows its simplified schematics: the write switches are controlled by an inverter domino chain, hence the name of the chip, and the variable resistors and capacitance between the inverters allows to modulate the sampling speed. The latest version of this digitizer is the DRS4, that has eight data readout channels. A WDB contains two DRS4 chips, so it is possible to connect 16 readout channels to a single board. It also has a Field Programmable Gate Array (FPGA) and a 80 MHz Analog to Digital Converter (ADC) used for preliminary trigger operations, such as the discrimination of the sum of input channels with a set threshold. The design of the WDB allows also to supply bias voltage to the pTC SiPMs and the LXe MPPCs, thus saving the physical space needed for an additional HV system. Figure 3.24 shows the schematics of a WDB.

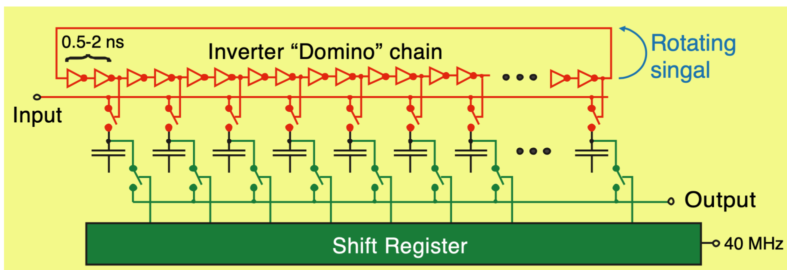

Figure 3.23: Simplified schematics of a DRS chip. Figure from [114].

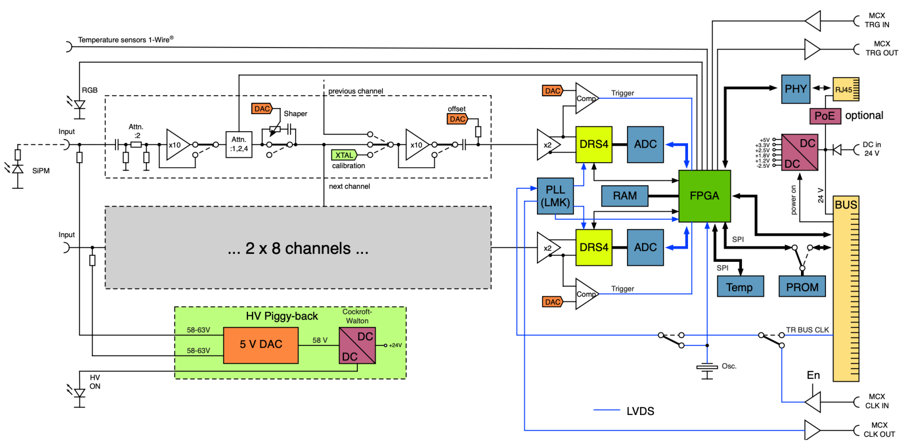

Figure 3.24: Schematics of a WDB. Figure from [95].

The trigger information provided by the WDB are collected by the TCB. Each crate hosts one of these boards, used to send the information to a dedicated trigger crate that merges everything and makes the final decision. The TCB are custom made boards based on FPGA and can perform complex trigger algorithms simultaneously. A single crate hosts, in addition to 16 WDB and a TCB, also a DCB. This board manages the readout of the WDBs with a standard Gigabit Ethernet link and communicates with them, distributing the clock, the trigger and the synchronization signal. The DCB transmits the data to the main DAQ computer where, after event building, they can be handled by the Maximum Integration Data Acquisition System (MIDAS), a framework developed at PSI and TRIUMF [115]. This system uses a web interface from which it is possible to control the DAQ, to record data in special formatted files and to manage the slow control of the detectors and the alarm system.

Figure 3.25 shows a picture of the three main boards out of the crate, while the complete TDAQ system with all the boards installed is shown in figure 3.26.

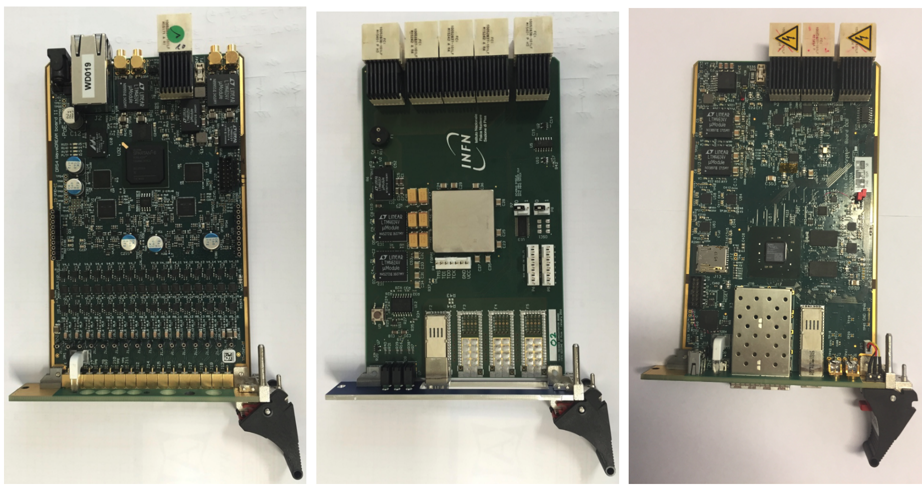

(a) (b) (c)

Figure 3.25: Picture of a WDB (a), a TCB (b) and a DCB (c). Figures from [112].

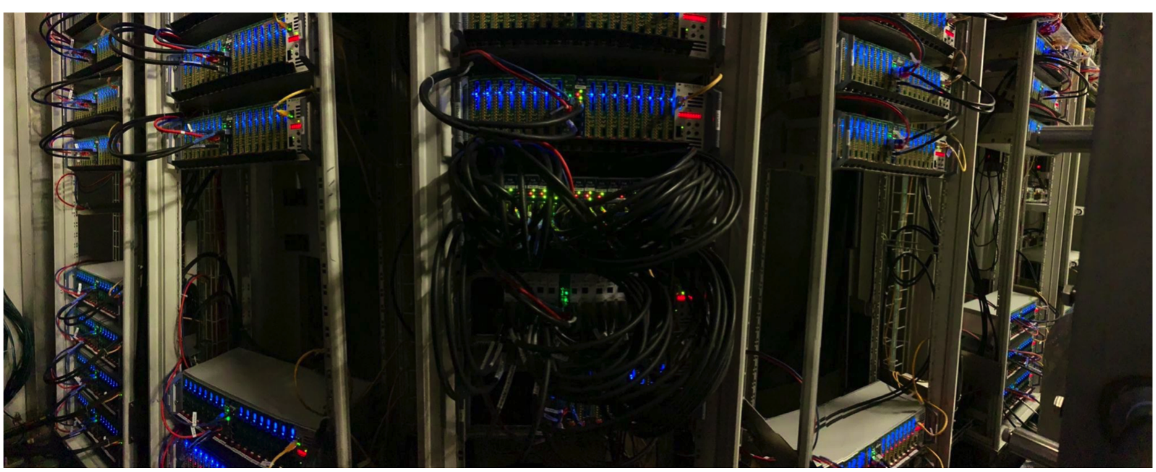

Figure 3.26: Picture of the complete TDAQ system installed in the MEG II experimental area.

3.6 Preface to the X(17) search at MEG II

The characteristics of the MEG II experiment allows for a precise measurement of the hypothetical X(17) boson. In fact, the CW accelerator used to produce LXe calibration photons can generate a proton beam of sufficient energy to inspect both the 17.6 MeV and the 18.15 MeV ^{8}Be excited states. The pTC can be used to produce the trigger, the LXe or another auxiliary LaBr(Ce) calorimeter foreseen for the CEX calibration can be used to continuously monitor the photon spectrum and the CDCH can be used for the e^+e^- pair tracking and momentum measurement.

The original experimental apparatus can be used without major modifications, the only exception being the target, its support structure and the area surrounding the interaction vertex. A redesign of this region is necessary because the actual target for the LXe calibration is too thick, and there is too much material in the surroundings, reducing the tracking capabilities because of the multiple scattering and the e^+e^- energy loss. I will extensively address this topic in section 5.1, while in this section I will concentrate on the kinematics of the reaction and how it will affect the measurement at MEG II in terms of production rate, multiple scattering and magnetic field tuning. This will give a quantitative idea of the numbers to deal with in this measurement and provides a starting point for the simulations that I will show in chapter 5.

3.6.1 Premise

The preliminary calculations on the X(17) measurement at MEG II are based on the following assumptions:

- the proton kinetic energy is $K_i = 1.1$ MeV;
- the reaction $p+^7\text{Li}\rightarrow^8\text{Be}^*\rightarrow^8\text{Be X}$ is produced on a Lithium Oxide (LI_2O) thin target;
- the target thickness is between 5 and 10 μm
- the proton current can range from 1 to 100 μA;
- the mass of the X(17) is 17.01 MeV/c^2 and the BR relative to the production of a photon is 6×10^{-6}, as reported in [22];
- the examined ^{8}Be excited state is the one at 18.15 MeV.

The target thickness and the proton current are free parameters because they have to be optimized with simulations. I will show the results of such simulations in section 5.1.4. Using the above assumptions it is possible to study the kinematics and the production rate of the X(17), the multiple scattering contribution in the target and the magnetic field necessary to keep the electron and the positron within the tracker acceptance. A summary of the relevant quantities follows, refer to appendix A for complete calculations.

3.6.2 Kinematics

In the laboratory frame, the maximum (minimum) $e^{\pm}$ energy corresponds to the particle emitted in the same (opposite) direction of the X(17), and hence:

$$E_e^{min} = 5.9 \text{ MeV}, \qquad E_e^{max} = 12.2 \text{ MeV} \tag{3.2}$$

Since $\beta_e^* \sim 1 > \beta_X = 0.35$ (where the superscript $*$ indicates the X(17) rest frame), the maximum angle between the electron and the positron in the laboratory rest frame is 180°. The minimum angle is obtained when $\theta^* = \pm 90°$. This corresponds, in the laboratory frame, to an angle of:

$$\theta = \pm 70° \rightarrow \theta_{e^+e^-} = 140° \tag{3.3}$$

Production rate

Considering a non-relativistic Breit-Wigner distribution for the cross section of the resonant production of ^{8}Be*→^{8}Beγ and using the proton flux integrated over the whole beam profile area and the numerical density of the target nuclei, it is possible to derive the production rate in a slice of target of thickness dx. By integrating this over the target thickness, assumed to be 10 μm for this calculation, and knowing the energy loss rate in the target, assumed constant for simplicity, it is possible to obtain the following rate at proton current of 1 μA:

$$R_\gamma = 1849\,\text{s}^{-1} \tag{3.4}$$

The X(17) production rate, that scales with the proton current, is then:

$$R_X = R_\gamma \times \frac{BR(^8\text{Be}^* \rightarrow ^8 \text{Be}X)}{BR(^8\text{Be}^* \rightarrow ^8 \text{Be}\gamma)} = 1.11 \times 10^{-2}\,\text{s}^{-1} \tag{3.5}$$

In order to obtain a more precise result that does not rely on the assumption of a constant energy loss, I estimated these rates with GEANT4 [116] simulations for several target thicknesses and assuming a variable energy loss. I will report the results in section 6.2, where I show the background estimate for the X(17) measurement.

Multiple scattering contribution

If a target of thickness t_0 is slanted by an angle α, the thickness seen by the proton is $t_p = t_0/\sin\alpha$, and the thickness seen by the $e^{\pm}$ is $t_e = t_p/2\tan\alpha$. A slant angle of 45° gives t_p=14 μm and t_e=7 μm for $t_0 = 10$ μm. The corresponding Coulomb scattering contribution is:

$$\langle\theta_{MS}\rangle \in [9.5, 19.6] \text{ mrad} \rightarrow 20.5 \text{ mrad} < \sigma_{\theta,MS} < 21.8 \text{ mrad} \tag{3.6}$$

Considering the average values $\sigma_{\theta,MS} = 21.15$ mrad and $E_{e^+} = E_{e^-} = 9.1$ MeV, this translates into a contribution to the invariant mass resolution of:

$$\sigma_{M,MS} \sim 102 \text{ keV} \tag{3.7}$$

3.6.3 Magnetic field optimization

In a cylindrical tracker with 15 cm inner radius a particle enters the acceptance volume if $2R > 15$ cm, where R is the radius of curvature. Requiring a e^+e^- pair from a X(17) decay to enter the tracker implies, considering that $p_{\min} = 5.9$ MeV/c and $p_{\max} = 12.2$ MeV/c:

$$\begin{aligned} \frac{p_{\min}[\text{GeV/c}]}{0.3B[\text{T}]} &> 0.075 \text{ m} \\ B[\text{T}] &< \frac{p_{\min}[\text{GeV/c}]}{0.3 \cdot 0.075 \text{ m}} = 0.26 \text{ T} \end{aligned} \tag{3.8}$$

The most energetic and the average 9 MeV particles will have a radius of curvature of:

$$R_{\max}[m] = \frac{p_{\max}[\text{GeV/c}]}{0.3B[\text{T}]} > 15.5 \text{ cm} \tag{3.9}$$

$$R_{\text{ave}}[m] = \frac{p_{\text{ave}}[\text{GeV/c}]}{0.3B[\text{T}]} > 11.5 \text{ cm} \tag{3.10}$$

Requiring both particles to recurl within the the tracker would require an outer radius of at least 35 cm.

These numbers can be applied to the specific case of the MEG II spectrometer and compared to the values obtained from the simulations. Since the magnetic field is optimized for the 52.8 MeV positrons of the $\mu^+ \to e^+\gamma$ reaction, a reduction factor for the magnetic field is needed. This factor is optimized by taking into account signal efficiency, invariant mass resolution and background yield. The results of the simulation are reported in figure 3.27: here a Figure of Merit (FoM) is calculated for several reduction factors. The FoM is $\varepsilon_{\mathrm{S}}/\sqrt{\varepsilon_{\mathrm{B}}}$, with the efficiency calculated in the early simulation model that I will describe in section 5.1.1. The FoM turns out to be maximum at a 0.174 reduction factor, which means that the optimal COBRA reduced magnetic field ranges from 0.085 T to 0.22 T, not far from $\mathrm{B}_{\mathrm{max}} = 0.26$ T calculated in 3.8.

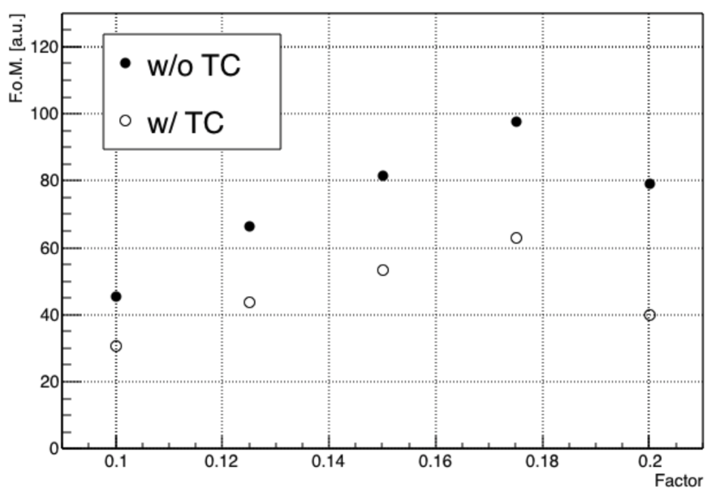

Figure 3.27: Magnetic field reduction factor optimization. The Figure of Merit used is $\varepsilon_{\mathrm{S}}/\sqrt{\varepsilon_{\mathrm{B}}}$, with B evaluated in a range of $\pm 2\sigma_M$ around the X(17) mass. The FoM has a maximum because with a low reduction factor the magnetic field would be too strong and the radius of curvature would be shorter than the inner radius of the CDCH sensitive volume for most of the tracks, reducing the signal efficiency; the same would happen with a high reduction factor, for which the magnetic field would be too weak, causing the radius of curvature to be higher than the external radius of the CDCH sensitive volume.

3.6.4 Summary and expected results

The performance of the MEG II detectors allows to repeat the ^{8}Be measurement performed at Atomki with an improved geometrical acceptance and invariant mass resolution. The

CDCH, in fact, is capable of e^+e^- precise tracking and momentum measurement, and can be supported by the pTC for an efficient trigger and by the LXe for photon spectrum measurement. Moreover, the CW accelerator can provide a proton beam with which it is possible to populate both the interesting ^{8}Be excited states at 17.6 MeV and 18.15 MeV. With a fine tuning of the usual MEG II magnetic field and a redesign of the CW target region reduce multiple scattering, it is possible to observe the anomalous peak in the e^+e^- invariant mass distribution with a resolution approximately a factor 2 better than Atomki, and give an independent confirmation of this anomaly. I will quantify this with simulations in chapter 5, but before moving to that I will report in chapter 4 the details on the CDCH construction and commissioning carried on during the last three years.

Chapter 4

MEG II drift chamber

Before proceeding with the details on the X(17) measurement at MEG II I will focus on the CDCH that will be used for the e^+e^- pair measurement. This detector is crucial, since it is the main difference with respect to the Atomki detector. Its excellent tracking resolution allows to better resolve the peak in the invariant mass distribution, and the higher angular acceptance is important to investigate the hypothesis that the anomaly can be the result of a bias introduced by the limited acceptance.

The detector was built and assembled in Italy and shipped to PSI in 2018 to be installed in the experiment. Its commissioning started in the MEG II pre-engineering run at the end of 2018 and continued in the following runs until 2021. Since the CDCH uses a combination of materials and techniques never used before, several problems arose during the construction and commissioning phase. These problems have been understood and solved, but the process took several years.

Despite the fact that the CDCH is now stable and ready for the MEG II physics run and the X(17) measurement, the past instabilities and the subsequent ageing of the detector led to the decision of building a backup drift chamber, the CDCH2. The design of this new detector is the same of the CDCH, the only difference being the choice of the wires, that will be slightly thicker and will undergo a different production process. The construction of the CDCH2 started in 2021, in parallel with the MEG II engineering run.

In this chapter I will describe the design of the detector, providing some details on the construction and wiring phase. After that I will focus on the problems that affected the detectors and on its commissioning, describing the activities and the data taken in the last years.

My contribution in the work presented in this chapter consists in the active participation in the activities in which the CDCH was involved. I participated in the 2018-2021 data taking campaigns and in the repair works between them. I also contributed to the data analysis with the wire-by-wire time calibration from 2018 data and the gain estimate from 2021 data.

4.1 Detector design and prototypes

The design of the new CDCH for MEG II is tailored on the stringent requirements of the $\mu^+ \to e^+\gamma$ measurement, most notably the low overall radiation length of the detector and the excellent tracking performance. The active volume has a cylindrical symmetry along the z axis, parallel to the beam. It covers the whole azimuthal angle ϕ and is divided into 12 identical 30° sectors. In the radial direction it is divided into 9 layers, each containing 192 drift cells. The inner and outer radii ranges from $r_{in} = 174.500$ mm-$r_{out} = 234.260$ mm at $z = 0$ to $r_{in} = 201.490$ mm-$r_{out} = 270.500$ mm at both UpStream (US) and DownStream (DS) endplates at $z = \pm 956$ mm, and the total length is 1912 mm.

The different dimensions are due to the stereo geometry of the wires, that gives an hyperbolic shape to the active volume. Wires that are in a given sector S in the US endplate ends up in the sector $S \pm 2$ in the DS endplate, the sign being positive or negative for even/odd layers, defining two projective views, U and V. Figure 4.1 shows a schematics of this geometry. The wire is not parallel to the beam axis, but has a stereo angle ε_k that ranges from 6° to 8.5° in the innermost and outermost layers respectively. The hyperbolic shape is due to the sagitta δ, defined as the difference between the wire radius at the endplate R_k and the wire radius at $z = 0$, $R_{k0} = R_k \cos(\alpha_k/2)$, where $\alpha_k = \pm 60°$ is the azimuthal shift.

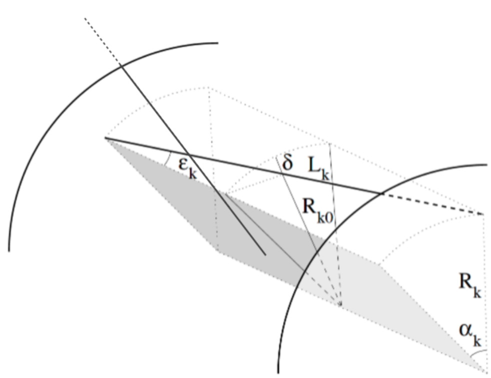

Figure 4.1: Schematics of the stereo geometry of the CDCH.

4.1.1 Single-hit resolution measurements with prototypes

The geometry of the CDCH provides a good spatial resolution thanks to the high granularity and the stereo configuration of the wires, that allows a precise measurement of the z coordinate. Moreover the choice of a light gas and thin wires minimized the mass of the detector, reducing the multiple scattering contribution and improving the overall performance. The single-hit resolution was measured using three different prototypes operated with a He:iC_4H_{10} gas mixture similar to the one used in experiment. The measurements were performed with cosmic rays, electron beams and radioactive sources [117].

Figure 4.2 shows a drawing of the experimental setup of the measurement with the first prototype. It is a three tubes system composed of parallel Cu drift tubes of 8 mm internal diameter, 30 cm length and 500 μm wall thickness, with the middle tube staggered by $\Delta = 500$ μm with respect to the others. The anodes are 20 μm Au-plated tungsten wires and are operated at a bias voltage of 1500 V. The cosmic rays trigger for this system is made of three plastic scintillators, two placed just above and below the tubes and one under a 3.5 cm thick iron slab. The coincidence of the three selects only vertical tracks, ensuring the presence of a hit in each tube.

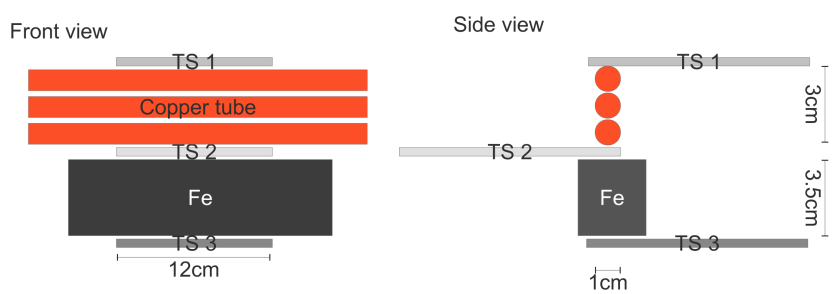

Figure 4.2: Schematic view of the three-tubes prototype. Figure from [117].

The second prototype is a three-cells system, as showed in figure 4.3 together with the experimental setup of the measurement. The three adjacent cells have a 7 mm square geometry with a wire pattern that simulates the one in the CDCH. Also in this case the anodes are 20 μm Au-plated tungsten wires and the central one is staggered by 500 μm. The cathodes and guards are 80 μm Ag-plated Al wires, same material as the CDCH ones but twice as thicker. The overall length of the prototype is 20 cm. It is enclosed in a Plexiglas box with two windows, which is gas-tight and internally covered by a thin Al foil. The anodes and guards are operated respectively at 1700 V and 375 V. The time to distance relations and spatial resolution measurements are performed with a ^{106}Ru source placed above the prototype, with a plastic scintillator below it that acts as a trigger device. A 500 μm thick Cu foil is placed on the scintillator to select only the high energy component of the ^{106}Ru spectrum.

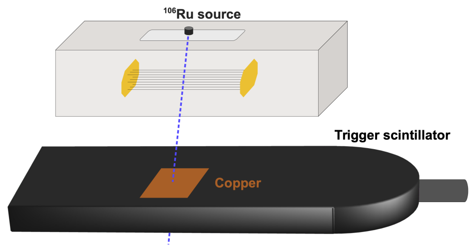

Figure 4.3: Schematic view of the three-cells prototype. Figure from [117].

Figure 4.4 shows the setup of the measurement that involves the third prototype. It is a multi-cells prototype enclosed in a $200 \times 200 \times 500$ mm^3 Al structure closed by two Al faces and two golden endplates. It has an 8×8 array of 7 mm square cells with 25 μm Au-plated tungsten sense wires and 80 μm Au-plated tungsten cathode wires. The sense wires are operated at 1620 V. While for the other two prototypes the gas mixture was 85:15 He:iC_4H_{10}, for this one it was 89:11. This difference has been taken into account during the resolution estimate. The measurement was performed at the Beam Test Facility (BTF) in the INFN LNF in Frascati, using the 447 MeV electron beam monitored by a pixelated detector upstream and a calorimeter downstream.

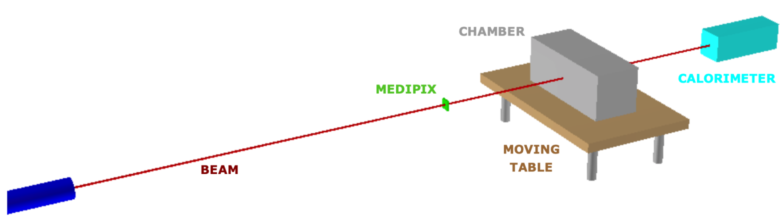

Figure 4.4: Schematic view of the three-tubes prototype. Figure from [117].

The resolutions of the three prototypes have been measured both directly and indirectly. The indirect measurements with cosmic rays for the three-tubes prototype and with the ^{106}Ru source for the three-cells prototype resulted in a spatial resolution of 93 ± 5 μm and 106 ± 4 μm respectively. The difference is due to the larger impact parameter range in which the resolution is averaged in the three-tubes measurement, that reduces the impact of the high resolution in the low impact parameter range. The three-tubes prototype was used to measure also the resolutions with different gas mixtures, and the expected value for the 89:11 mixture used in the multi-cells prototype was estimated to be around 100 μm. The result of the indirect measurement with this prototype at BTF, extrapolated from the hit-to-track residuals distribution in figure 4.5, is in agreement with the expectations: the core resolution from the data, in fact, is around 120 μm, but from a comparison with MC simulations it is overestimated by 25%, meaning that the final result is $\sim$ 100 μm, as expected from the measurements with other prototypes.

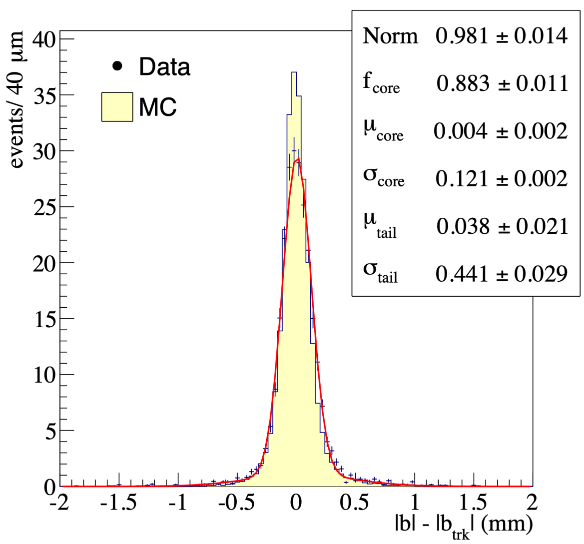

Figure 4.5: Spatial resolution of multi-cells prototype obtained from electron beam measurement. The data are represented by the black markers, fitted by a red line double Gaussian, while the yellow histogram is from a MC simulation. Figure from [117].

The direct measurement required an additional tracking device that measures independently the impact parameter in the cell with a resolution better than the tested prototype. Such tracker is a four planes double-sided silicon strip detector that was used as a spare detector in the BaBar experiment [118]. The direct measurement resulted in a resolution $\sigma \approx 110$ μm, in agreement with the indirect measurements in which the single-hit resolution is underestimated by $\sim$ 10%.

4.1.2 Construction and mechanics

The CDCH is the first cylindrical drift chamber built in a modular way [107,119,120]. The high wire density, 12 wires/cm^2, makes the use of the feed-through technique impossible.

This led to the design of a multi-layer geometry with wires soldered at both ends to PCBs that are then mounted on the detector endplates, as showed in figure 4.6. Each layer of PCB is separated from the adjacent ones with PEEK spacers that ensure the proper cell dimension and fill the gaps between the spokes of the golden wheel-shaped endplate. The assembly of the PCBs is entrusted to a DEA Ghibli coordinate measuring machine that puts the boards in place with a position accuracy of 20 μm and 40 μm on the horizontal and vertical axes respectively. This way it is possible to keep the boards as parallel as possible, reducing the stress on the wires soldering points.

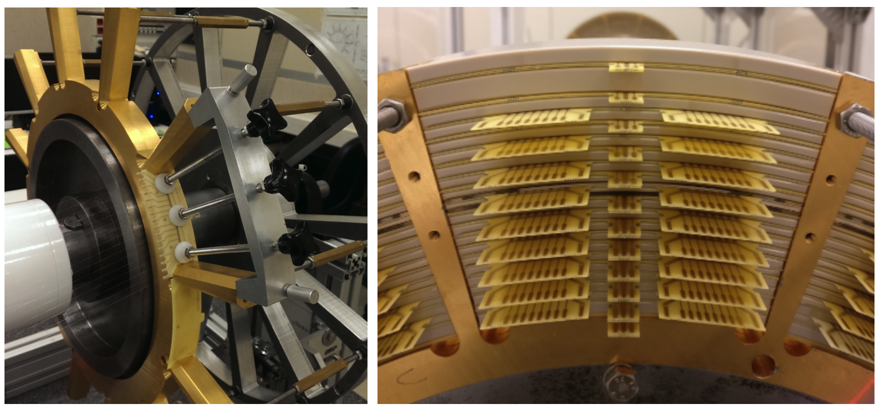

(a) (b)

Figure 4.6: Pictures of the PCBs during mounting (a) and of a complete sector mounted (b).

The CDCH gas volume is delimited by a thin 20 μm Mylar foil at the innermost radius and a Carbon Fiber (CF) support structure at the outermost radius. The Mylar foil separates the active volume from the target volume, called COBRA volume, which is filled with He: the choice of the light gas in this volume and of the light separation foil minimizes the material crossed by the decay products. The CF is instead used as a support structure that bears the longitudinal wire tension. During the PCBs installation this task is charged to a structural iron shaft screwed to both endplates, visible in figure 4.6(a), but inside the experiment this is not possible, so there is the need of a light structure that can keep the endplates in position. It is composed of two half cylinders with a 50 μm thick Al foil glued in the inner face to electrically protect the wires, same as the Mylar foil does at the inner radius. Since it has to keep the mechanical stability, the CF is carefully screwed to the endplates with 12 couples of radial screws per end. This operation is performed with a torque screwdriver to have a uniform grip in each point. Figure 4.7 shows a picture of both the inner Mylar foil and the outer CF structure. The gaps between the CF structure and the endplates are sealed with ThreeBond 1530 glue [121] to prevent gas leaks in the active volume, and the PCB stack is sealed with Stycast 2850 resin [122].

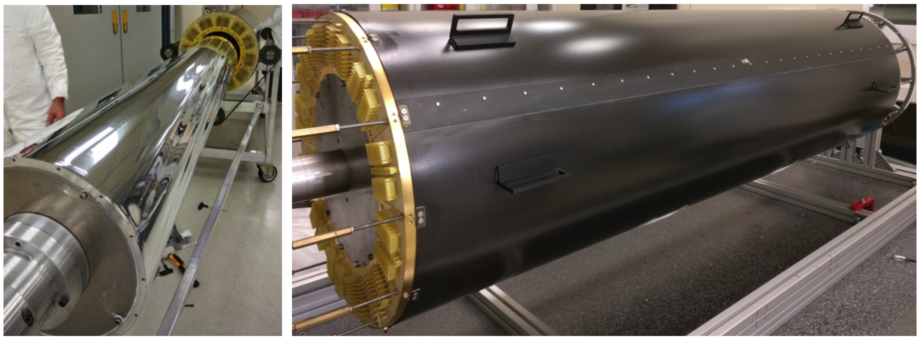

(a) (b)

Figure 4.7: Pictures of the CDCH internal Mylar foil (a) and external CF structure (b).

The Front End (FE) electronic boards that are connected to the wire PCBs must be firmly kept in position because of their high density in the endplate. This is possible thanks to two set of 12 Al card holders specially prepared for this task, with 9 grooves per side at the same radius of the CDCH layers. Figure 4.8 shows a picture of the card holders for a single endplate before and after the installation on the detector. The holders are connected to each other by the Cu pipes of the cooling system and the plastic pipes of the dry air system.

(a) (b)

Figure 4.8: Pictures of the 12 FE card holders for one endplate before (a) and after (b) the installation on the detector.

The cooling system is needed to keep the temperature of the FE cards under the operating threshold of their components. This is possible thanks to a chiller and a hydraulic circuit that lets cold pure water flow inside the Cu pipes that are in thermal contact with the card holders, keeping them at low temperature. The dry air system is used to minimize the humidity on the FE cards, thus preventing unwanted discharges on their surface.

The connection of the CDCH to the beamline of the experiment is possible thanks to two Al inner extension, one for each end of the detector. They are screwed to the endplates and sealed with ThreeBond 1530 to prevent He leaks from the COBRA volume. These Al structures are connected via support rings and Al pillars to two CF cylinders, one per each end of the detector. These cylinders are the outer extension of the CDCH, and are the ones that ensures the mechanical connection of the detector with the COBRA magnet. Figure 4.9 shows pictures of the inner and outer extensions.

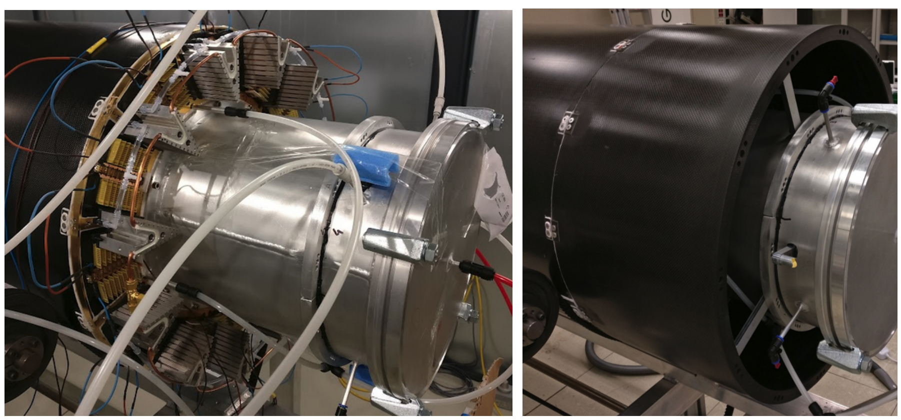

(a) (b)

Figure 4.9: Pictures of the inner (a) and outer (b) extensions of the CDCH.

Since knowing the exact position of the wires is important in the data analysis, the mechanical stability of the detector is monitored by a periodical geometrical survey. This operation is performed at PSI with a laser tracker, both before and after the installation of the detector in the experiment. This allow to measure the distance of the two endplates, i.e. the wires elongation, their planarity and parallelism with a precision of some μm.

4.1.3 Wiring

The choice of the wires is the result of a detailed R&D phase in which several candidates have been taken into account. Transparency is the essential feature of the CDCH, so the wires radiation length must be as small as possible. Moreover, the material has to be adapt for the soldering on the PCB. The main candidates for cathodes and guards were Al, Ti, CuBe and Stainless Steel. The final choice was the Al (5056) alloy from California Fine Wires (CFW) [123], with diameters of 40 μm and 50 μm. Such alloy is composed by 94.6% Al, 5.2% Mg, 0.1% Cr, 0.1% Mn, has a density $\rho \approx 2.7$ g/cm^3 and a resistivity of ~ 20 Ω/m. Furthermore, the wires are Ag plated, with a coating thick less than 1 μm: the overall density is then $\rho \approx 3$ g/cm^3. For the sense wires there were two main options: pure tungsten or tungsten with ~ 3 % Rhenium. The final choice was a 20 μm diameter pure W anode wire, because of its smaller resistivity with respect to W-Re. The density of such wires, considering also the applied Au coating, is $\rho \approx 19.25$ g/cm^3.

The wiring was realized with an automatic wiring robot that assembled the multi-wire layers [124–126]. The robot is composed of three systems:

- wiring system: a semiautomatic high precision machine that puts the wires in place with the correct mechanical tension;
- soldering system: a infrared laser soldering tool;
- extraction system: a machine that extract the multi-wire layers and stores them in a tray for the transport.

The layers, after the transport, are installed in the CDCH by stacking the PCBs on the endplates as shown previously in figure 4.6. Figure 4.10 shows a picture of the whole system and a zoom of a multi-wire layer.

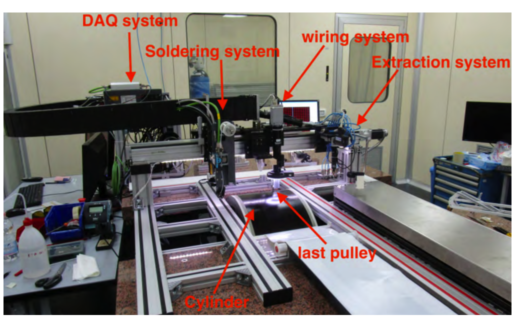

(a)

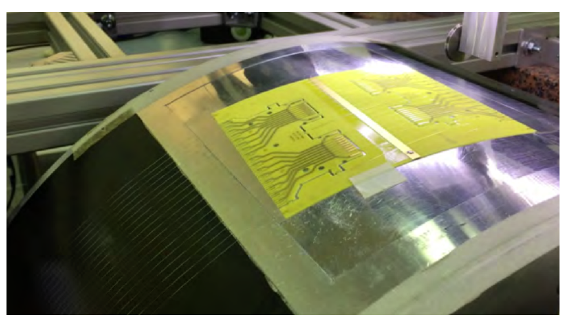

(b)

Figure 4.10: (a) Picture of the wiring robot. (b) Picture of a multi-wire layer. Figures from [126].

4.1.4 Front End electronics

The signal on the CDCH wires is collected by the FE electronics, that has the task to amplify and transport it to the DAQ system [127]. Moreover, the FE boards of the CDCH supply the HV to the wires. They are designed to meet the requirements of the cluster timing, which is an analysis technique used in the CDCH to reach the best resolution possible [128]. This technique requires the measurement of the time of arrival of all the ionization cluster, thus the FE electronics has to process high speed signal with low noise and wide bandwidth.

Figure 4.11 shows the schematics of a board. It is divided into 3 phases:

- input stage: decoupling and protection, matches the characteristic impedance of the drift cell, which is on average 354 Ω and varies less than 10% with the frequency;
- first gain stage: amplification with ADA4927 [129] wide bandwidth, low distortion, low noise, high speed differential amplifier with a current feedback;
- second gain stage: amplification with the fully differential operational amplifier THS4509 [130] and handling of the output of the board.

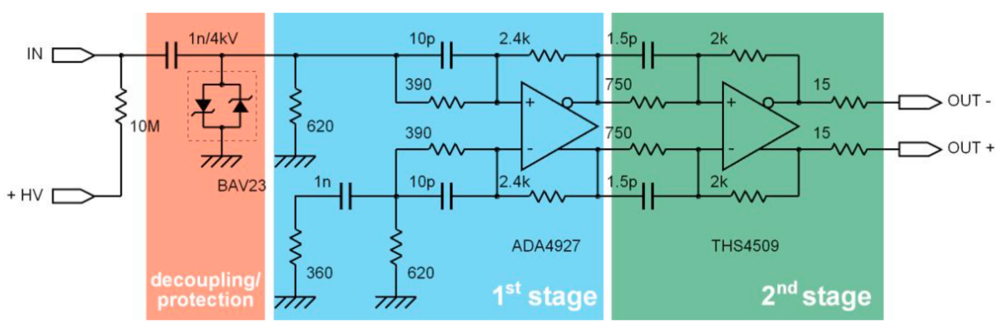

Figure 4.11: Schematics of a FE board. Figure from [127].

Figure 4.12 shows a picture of the top and bottom faces of a single board. Each board has 8 channels, meaning that to power and read out a single sector 18 boards are needed, two for each layer. Because of the high density of the channels the boards are designed in three different variants to fit in the small space: type L, type C and type H, the only difference being the position of the output/Low Voltage (LV) connector position. The total number of FE boards needed to readout and power all CDCH wires both US and DS is 432.

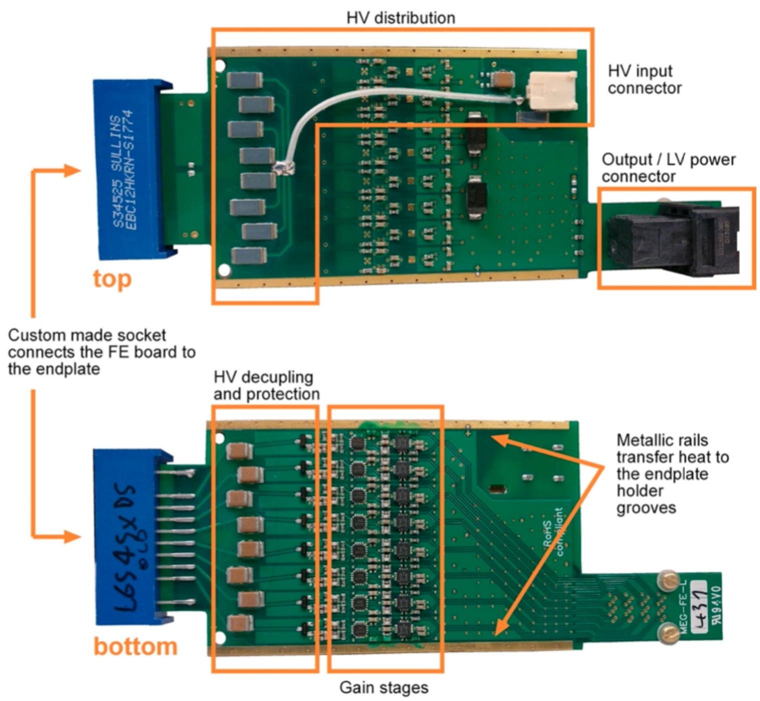

Figure 4.12: Top and bottom view of a FE board. Figure from [127].

4.1.5 High Voltage system

The 1728 drift cells of the CDCH are powered in group of 8, with each HV channel powering 1 FE board on one side, which is the US side for almost all the boards. The 216 channels needed are supplied by 9 modules installed in a crate. The modules are 16-channels ISEG EHS F430p [131] with SHV outputs. The SHV cables from the modules output are connected to 3 CAEN A648 SHV-to-Radiall adapters [132], and the 3 Radiall cables are connected to custom patch panels. The HV is supplied to the FE boards by the Draka coaxial cables [133] that are connected to the patch panels. Figure 4.13 shows a picture of the HV crate and of a patch panel.

The HV control software is integrated in the MIDAS DAQ system, thus the voltage supplied to the wires and the values of the current can be monitored and registered. This proved to be a crucial feature, since during the commissioning the CDCH experienced a problem of internal discharges, resulting in the wires drawing potentially dangerous high currents. Being able to study the history of the HV and the currents for each channel helped in finding a solution for this issue, as I will discuss in more details in section 4.2.

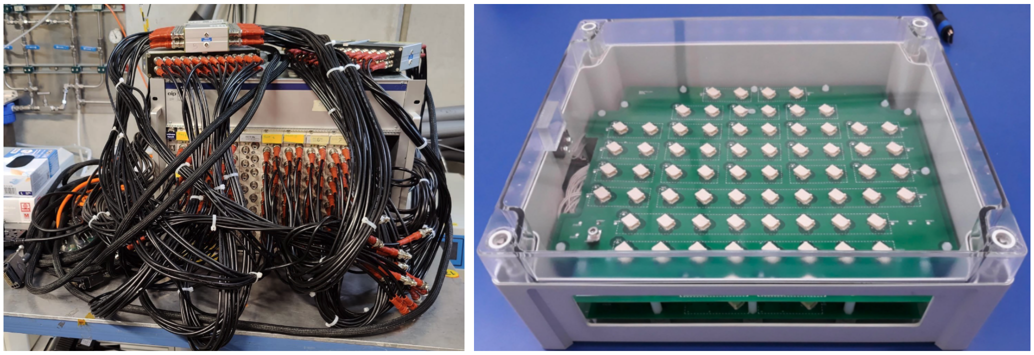

(a) (b)

Figure 4.13: (a) Picture of the CDCH HV crate with the 3 CAEN SHV-to-Radiall converters on top of it. (b) Picture of the custom patch panel with the Draka cables connectors.

4.1.6 Gas system

The CDCH gas system provides a stable, pure and light He:iC_4H_{10} gas mixture with the possibility to include additives when needed [134]. The quality of the mixture is crucial, since the detector performance strongly depends on the electron multiplication and drift properties. The He and iC_4H_{10} are continuously flowed with a purity of 99.9999% and 99.995% respectively, preventing an eventual contamination that would spoil the mixture and make the drift velocity unpredictable, impacting on the quality of the data analysis.

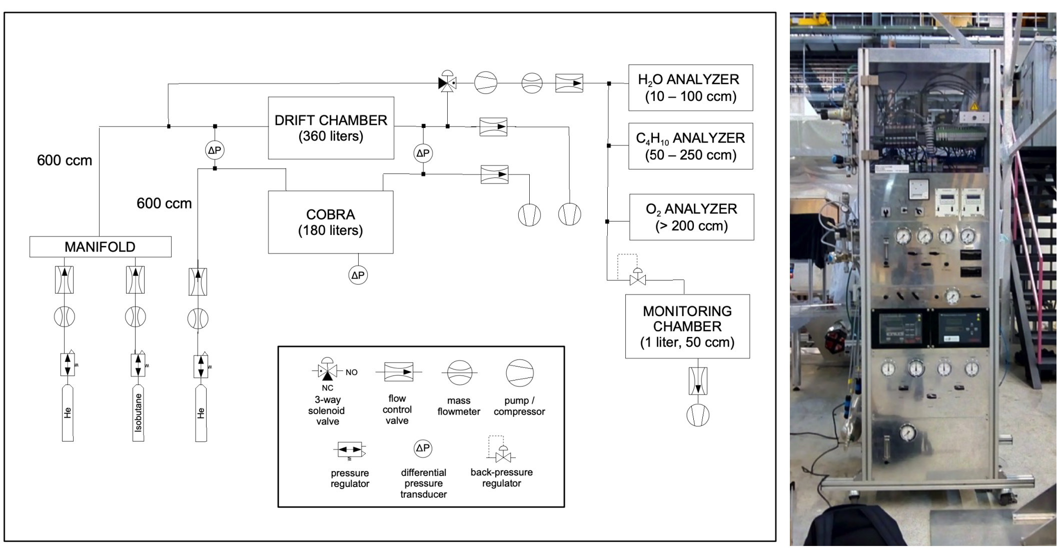

(a) (b)

Figure 4.14: Simplified drawing (a) and picture (b) of the CDCH gas system. Figure (a) from [134].

The gas system mixes the two gases with the desired percentage, with the possibility to add a third gas to modify the mixture properties. The final composition of the gas used in MEG II is 90:10 He:iC_4H_{10} with the addition of 0.5% O_2 and 1% isopropyl alcohol to suppress the discharges that were observed during the commissioning period. This last additive is preferred over H_2O to avoid wires corrosion, which is sensitive to humidity and was observed during the construction of the detector. The system flows 600 ccm in the CDCH active volume and 600 ccm in the COBRA volume, and since the two volumes are 360 and 180 liters respectively one volume exchange takes around 10 hours and 5 hours. The system allows also to keep the volumes at a pressure slightly over the atmospheric pressure to prevent air from entering the detector: the over-pressures are 10 Pa and 5 Pa in the COBRA and CDCH volumes respectively.

Figure 4.14 shows the schematics and a picture of the gas system. It is composed of four apparatuses, each with a different task:

- Gas Supply and Distribution System: it takes care of providing a constant and uniform gas flow thanks to a set of mass flow controllers. It has five gas lines: two of pure He (one for the chamber and one for the COBRA volume), one of iC_4H_{10}, one extra for additives (O_2 in the final mixture) and one high rate line connected to the COBRA volume which is used to compensate the pressure changes during the insertion/extraction of the CW beamline;

- Pressure Control System: it maintains the constant differential pressure between the two volumes and the atmosphere thanks to a set of manometers and driving proportioning valves;

- Control System: it manages the safety procedures and is interfaced to the slow control system of the experiment;

- Gas Monitoring System: it analyzes a sample of the CDCH flow to accurately measure the percentage of O_2, iC_4H_{10} and moisture in the mixture, along with the gas gain and drift velocity.

The contaminants and composition of the mixture are measured by three commercial gas analyzers, while a 16 drift tubes small drift chamber measures the gain and drift velocity. Figure 4.15 shows a picture of the open gas monitoring chamber with its 36 μm tubes, each containing a 20 μm golden tungsten sense wire. The detector performance have been studied with X-rays, cosmic rays and electron beam measurements. The whole monitoring system can detect variations in the drift velocity and gas gain within 1%, allowing to correct for them and avoid the deterioration of the detector performance from uncontrolled variations, estimated to be around 5%. More details about these measurements can be found in my master thesis [135].

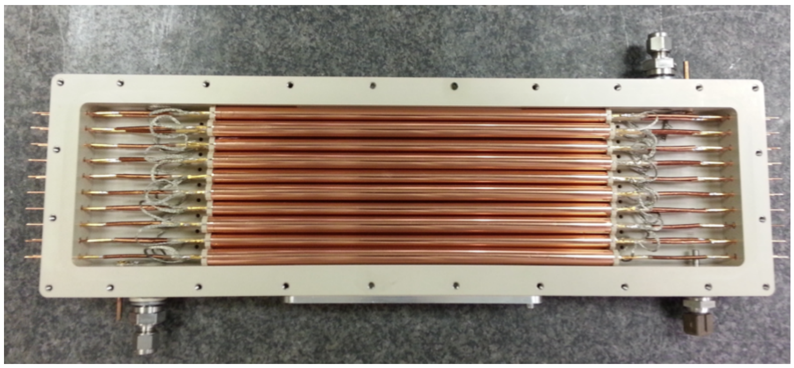

Figure 4.15: Picture of the gas monitoring drift chamber before closing.

4.2 Known problems

The CDCH faced several problems of different nature during its construction and commissioning. The first issue observed was the unexpected breaking of some wires during the construction. After an in-depth study the problem was traced back to the presence of humidity. Furthermore, during the first complete HV test with the whole detector powered on, before the start of 2018 pre-engineering run, the detector showed electrostatic instability. This was due to the mechanical tension of the wires being too low, since it was discovered that the more the wires were tensioned, the more the corrosion sped up and was likely to cause their breaking. The last problem faced by the CDCH is the presence of discharges inside the active volume, discovered at the end of the 2018 pre-engineering run. From an eye inspection the discharges were found to be correlated to the presence of white areas on the cathode wires. A solution was found for all these problems, thus the CDCH is currently able to take data for both the $\mu^+ \to e^+\gamma$ and X(17) measurements. Nevertheless, there is a chance that the life of the detector was shortened by these events, thus a backup CDCH2 is under construction, with the same conceptual design but slightly different cathode wires.

4.2.1 Wire breaks

The CDCH was the first drift chamber to observe a drastic effect of the humidity. The reason was identified in the cracks present on the wires surface, most likely generated in the last drawing phase of the wires, the ultra-finish. This conclusion comes from the observation of the wires at the microscope: the 40 μm wires, which underwent a more stressful ultra-finish procedure, showed more cracks. Such cracks allowed the water molecules to start a corrosion process that ended in the breaking of the wire. This phenomenon happens only in presence of a silver coating: the galvanic coupling between Ag and Al, in fact, makes the localized corrosion possible [136]. Figure 4.16 shows a picture of two wires taken with the Scanning Electron Microscope (SEM). The first picture highlights the presence of cracks on the surface of the wire, while the second is an image of the breaking point. An Energy-Dispersive X-ray Spectroscopy (EDS) analysis of this region showed the presence of several contaminants, mostly Al_2O_3, Cl and Na. Independent tests performed outside of the CDCH showed the same phenomenology when the wires where sprayed with water. Wires stored in a dry environment didn't show any sign of ageing, while wires exposed to a humid atmosphere quickly started to deteriorate. Moreover, it was observed that the deterioration is sped up by stretching the wires: this led to the decision of extra stretching the CDCH after the first run to let all the weak wires break. Removing the broken wires and returning back to the original wire tensioning prevents wire breaks due to corrosion during the CDCH operation.

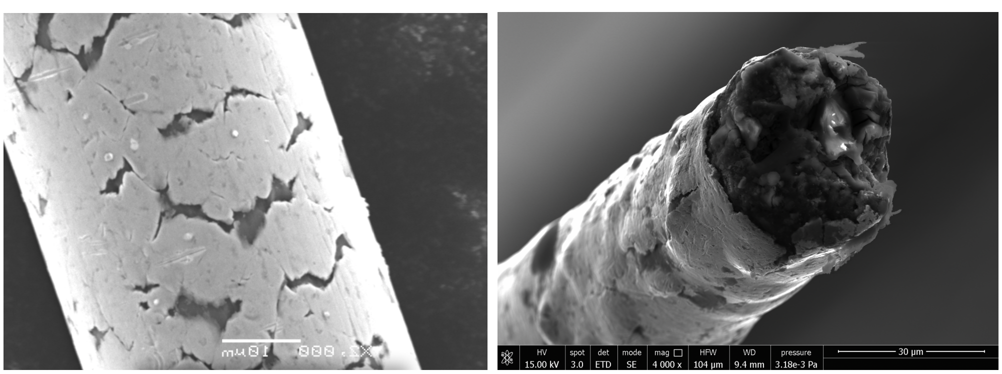

(a) (b)

Figure 4.16: Pictures of the wires taken with the SEM. (a) Cracks on the wire surface. (b) Wire breaking point.

The first broken wires were observed during the construction phase, in March 2016. It was realized that the cause was the humidity, so the wiring phase restarted from scratch with a more controlled environment equipped with safety systems. The successive breaks happened in October 2016, during a test phase: this led to the review of some wiring procedures. After that, 14 broken wires were found inside the CDCH in August 2017: these were removed with the help of a hook mounted on a commercial photography system for precise movements. Though risky, this operation was necessary because the presence of the wires segments kept a big portion of the detector to ground voltage. Before the shipping of the CDCH to PSI for its installation in the experiment it was decided to keep the detector at a smaller mechanical tension than planned, in order to not accelerate the corrosion of the wires. This decision led to an electrostatic instability, as it will be observed during the first run with the CDCH.

The removal procedure was needed again in 2019, since several wires broke inside the closed detector during the first pre-engineering run with the CDCH installed in the experiment in 2018. Thus, after the end of the run the CDCH had to be removed from the experimental area and moved to the PSI cleanroom. Figure 4.17 shows a picture of the setup used for wires removal. The CDCH had to be re-opened for this operation, thus it was placed on a table and coupled to the iron shaft used during the construction period. The SEM and EDS analysis confirmed the humidity-related nature of the problem.

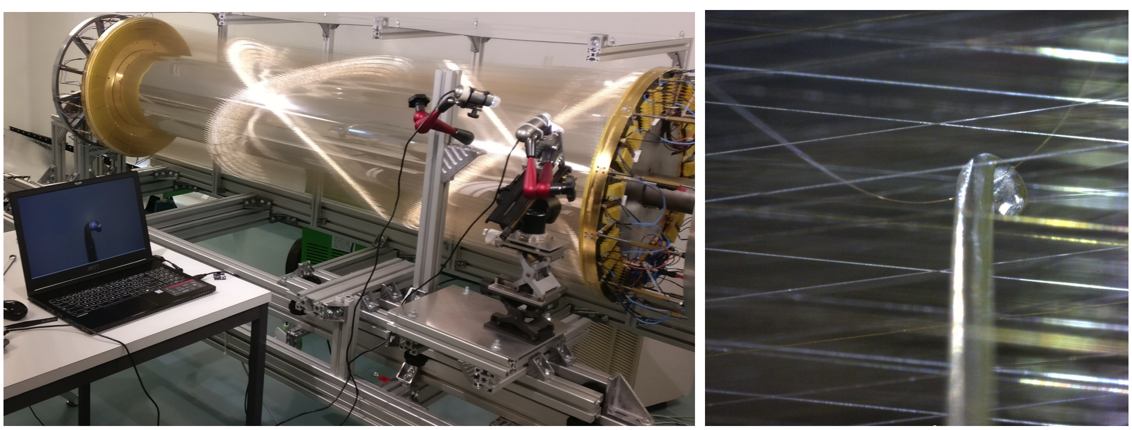

(a) (b)

Figure 4.17: (a) Picture of the setup for broken wires removal. (b) Picture of the hook during the removal of a wire.

After the wires removal the CDCH was extra-stretched to let the weak wires break, and then it was closed again with the CF shell, following the same procedure used during construction. Unfortunately the same procedure had to be repeated again in 2020, because during the 2019 run another wire broke. This time it was due to the contact with a small

~ 1 mm remnant of an anode wire that broke during the construction phase. This caused the second re-opening of the drift chamber during winter 2020, needed to remove the broken wire segments that kept many anode wires to ground voltage. After the 2020 pre-engineering run other broken wires were found in the drift chamber. This time the detector was extra stretched even more than the previous year, so to be sure to break all the weak wires to be able to operate the detector in the 2021 run. This, along with the extra care taken in keeping the CDCH in the most dry possible atmosphere, prevented more wire breaks due to corrosion. Table 4.1 reports a summary of the broken wires during the CDCH construction and commissioning period.

Year	**Broken wires**	**Cause**
Construction	14	Corrosion
2018	56	Corrosion + stretching
2019	8	Stretching + contact with broken anode
2020	29	Corrosion + stretching
2021	0	/
Total	107	

Table 4.1: Summary of the broken wires and the cause of the breaks during the CDCH construction and commissioning phase. In 2019 and 2020 there was only one wire break per year inside the chamber, the others were due to the following overstretching.

All the wires broken due to corrosion were 40/50 μm cathode/guard Al Ag plated wires. The stretching procedure caused tens of wires to break, so a performance evaluation without such wires was necessary. MC simulations showed that the drift cells surrounded by one missing cathode are completely operative, with only small distortions of the field. Moreover, the effects on the overall efficiency and resolution of the detector was estimated to be marginal. A phenomenological model was developed to predict the number of wires break by taking into consideration several factors. Knowing the humidity conditions and the wires characteristics and extrapolating the data obtained from the past breaks it was possible to estimate the rate of broken wires. This allowed to calculate a safe amount of exposure to humidity and extra stretching without the risk to break more wires. The prediction of such model was accurate for 2020 run, during which only one wire broke. For these reasons it is safe to assume that the wire breaking problem due to corrosion caused by humidity will not affect the CDCH operation and performance.

4.2.2 Electrostatic instability

Electrostatic instabilities showed up in the CDCH during the first HV test, before the installation in the experiment in the second half of 2018. Above a bias voltage of 1000 V, in fact, the wires in the inner layers started to show high fast oscillating currents up to 150 μA, much higher than expected. This is the effect of anodes and cathodes in a drift cell approaching and finally touching each other. The cause of this phenomenon is the insufficient mechanical tensioning of the wires, adopted after the wire breaks to slow down the corrosion process.

This was a threshold effect that disappeared by lowering the HV below a certain value, variable for each layer depending on the drift cell size. The inner cells, the smallest ones, were the most problematic, while the outer cells were brought to the expected HV working point without major issues. This working point was estimated to be 1400-1480 V from simulations, with the higher and lower values valid for the outermost and innermost layer respectively, reducing/increasing by 10 V for each subsequent layer.

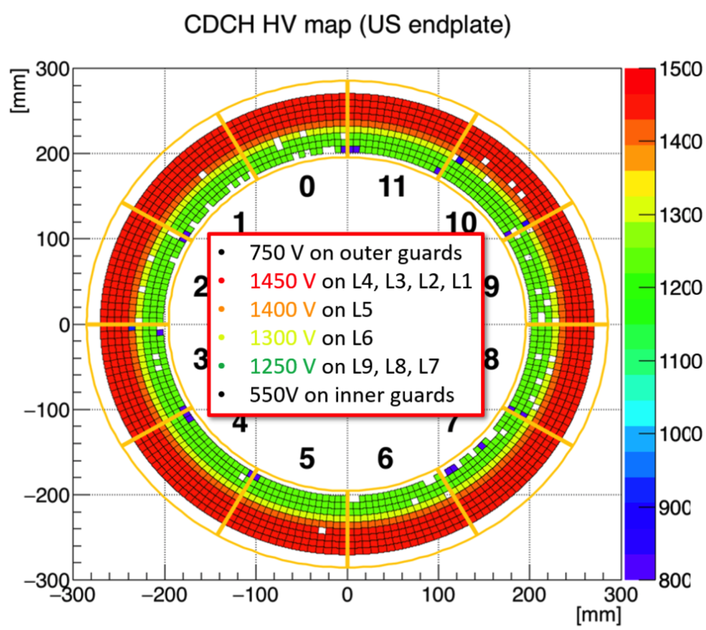

Figure 4.18: HV map before the starting of 2018 pre-engineering run. Each point in the plot corresponds to one drift cell.

Figure 4.18 shows the map of the HV applied to each drift cell during the run. With great difficulty it was possible to reach 1250 V at the innermost layer, a value lower than the working point but still useful to keep the electric field stable inside the detector. The inner guards were kept at 550 V instead of the 700 V used for outer guards for balance purpose. Sometimes the instabilities caused two wires to attach, creating a permanent short circuit, indicated by the white cells in figure 4.18.

To avoid the severe damages to the CDCH that can be caused by the shorts, a safety feedback in the HV system was implemented. This ramps down the HV of the whole detector when the current on a wire exceeds a threshold for a selected amount of time (order of 100 μA and 1 s). The permanent shorts found in the CDCH were isolated on the corresponding FE board. The issues related to the electrical instability have been solved by increasing the operating mechanical tension of the wires, operation performed during the re-opening of the detector happened after the pre-engineering runs to remove the broken wires. The over-stretching of the CDCH allowed also to remove most of the permanent shorts, making the wires detach from each other.

4.2.3 Discharges in the active volume

The CDCH suffered a problem of discharges on the sense wires when exposed to the full intensity muon beam. It was observed for the first time at the end of the 2018 pre-engineering run: the discharges appeared when the beam was on, and didn't disappeared by blocking the beam, but only when the HV was lowered enough to stop the amplification of the internal avalanches started by the electrons, at values around 800 V. The HV threshold at which the currents appeared/disappeared varied in time and were also different for different sectors of the CDCH, with the most problematic one being sector 3. The effect of these discharges was a large current readout on the sense wires: it reached values up to ~ 350 μA on some wires, but the effect was not uniform, since there were areas completely unaffected. Figure 4.19 shows a layer 2 current readout from the ISEG HV system connected to MIDAS. Here the currents affected many sectors and reached values up to 350 μA, very high with respect to the expectations of $\sim 20 - 30\mu$A and possibly dangerous for the detector.

The problem persisted also in 2019 pre-engineering run, making difficult to take muon beam data. At that time, in fact, the high currents showed up erratically even without the exposure to the muon beam. After some hypotheses it was found that the cause of the currents was the presence of discharges in some specific areas of the CDCH. It was possible to observe this because after the opening of the detector in 2020 to remove the wires broken in 2019, instead of the usual CF shell it was decided to temporarily install a

Plexiglas shell to see what was going on inside the active volume. Figure 4.20 shows a picture of the CDCH with the Plexiglas shell inside the PSI cleanroom.

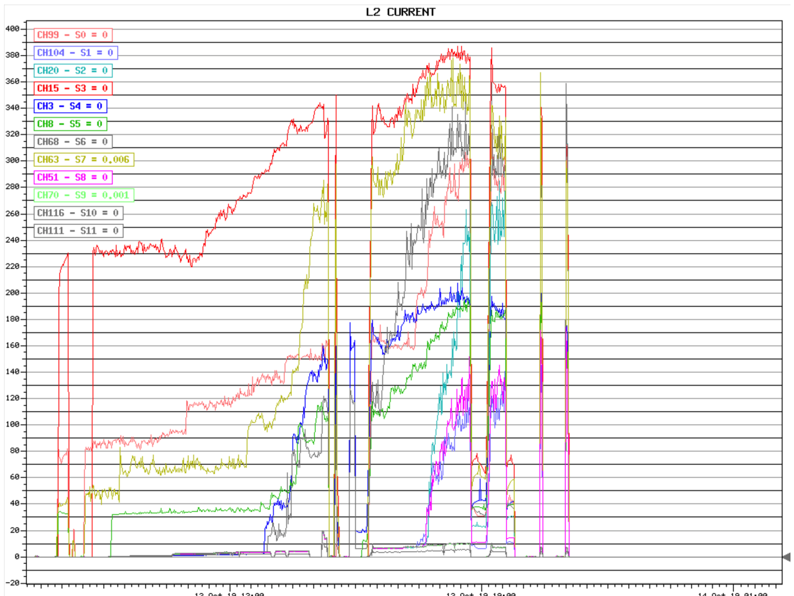

Figure 4.19: MIDAS history plot of the CDCH current on layer 2 during 2019 run. The vertical axis is the current in μA, the horizontal axis is the time.

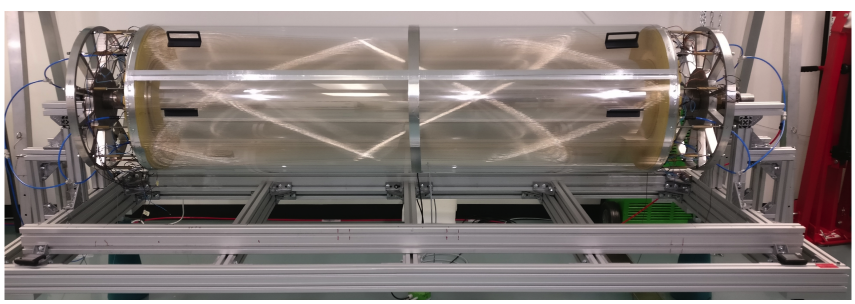

Figure 4.20: CDCH after Plexiglas shell installation replacing CF in 2020 commissioning.

When powered on the CDCH started to show corona discharges, visible by eye in several spots thanks to the Plexiglas' transparency. Upon closer inspection it was discovered that the discharges showed up in white areas, where the cathode wires presented this different color instead of the usual one. These areas are ~ 10 in number and are distributed almost flatly along the longitudinal z and azimuthal ϕ coordinate.

Figure 4.21 shows a picture of one of such areas, along with an example of the signals that generates the high currents, present on both endplates readout and higher and larger than the signals expected from positrons. This strange phenomenology can indicate that some areas of the detector may have suffered from ageing more than it was expected for the time, maybe due to the other issues that affected the CDCH during the years.

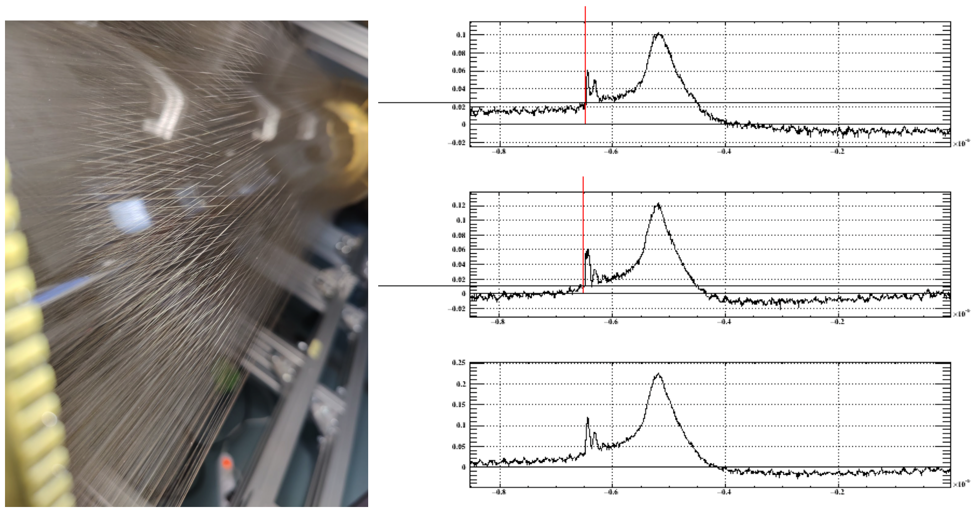

(a) (b)

Figure 4.21: (a) White region where the discharges have been observed by eye. (b) CDCH signal corresponding to the discharges. The first two waveforms are readout respectively US and DS, while the third is the sum of the two. The vertical scale is the amplitude in [V], the horizontal scale is the time in [s].

The solution to this problem was to modify the gas composition by adding some quencher to suppress the discharges. The tested additives were CO_2, O_2, H_2O and isopropyl alcohol. The final choice for the gas mixture was to add 0.5% of O_2 and 1% of isopropyl alcohol. The CO_2 was discarded because even though it was possible to mitigate the discharges with its addition, it suppressed the gas gain with a severe impact on the signal to noise ratio (S/N) and thus on the detector performance. This is true also for high concentration of O_2, but the addition of a small percentage of H_2O helped to reach a O_2 concentration of 0.5%, which has negligible impact on the analysis (refer to section 4.3 for more details). Later on also H_2O was discarded because of the previous problems with wire corrosion due to humidity: isopropyl alcohol was chosen to replace it, and after several tests it was found that the optimal fraction to suppress the discharges was 1% of the total mixture. The last week of the 2020 pre-engineering run the CDCH operated with the final gas mixture without major issues under the muon beam at full intensity, i.e. 7×10^7 μ/s, and after a commissioning period it was possible to operate the detector without discharges throughout the whole 2021 engineering run.

4.2.4 CDCH2

Despite all the problems that affected the CDCH during the years it was possible to find a suitable working configuration to operate it without worsening its expected performance. Nonetheless, because of the fragile nature of this detector, the construction of a backup CDCH2 started in the second half of 2021. It will have the same design of its predecessor, since its performance complies with the experiment requirements and it is already compatible with the rest of the apparatus. Moreover it was shown that its mechanical structure is highly stable: it was opened and closed three times after its first installation, a procedure not expected and not standard for such kind of detectors, and there were almost no displacement of the structure overall.

The only thing that will change in the CDCH2 is the material of the cathode and guard wires. This is because of the discovery of the present wires weakness to humidity, caused by the cracks in the Ag coating from which a corrosion process may start. To avoid this problem several kind of wires have been considered, with both 40 and 50 μm diameters: pure Al (50 μm), Al/Ag ($40-50$ μm), Ti (50 μm), Al/Au ($40-50$ μm), Ti/Au(50 μm) and Cu (50 μm).

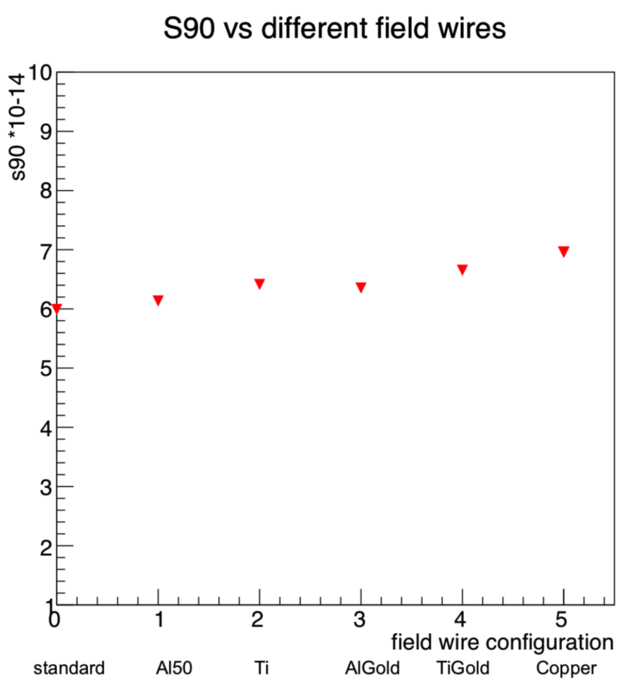

Figure 4.22: Sensitivity of the MEG II experiment as a function of the different cathode wires explored for CDCH2.

The standard MEG II wire is the Al/Ag (40 μm), which is the best one in terms of resolution but is the one that presents humidity issues. The Al/Au wires should be similar to Al/Ag, while the pure Al (50 μm) wires were discarded after many tests because even though they are insensitive to humidity and their impact on the resolution is minimal, there is no possibility to reliably solder them to the wire PCB. Same goes for pure Ti wires, while for Ti/Au wires there is no producer. Finally the Cu wires were discarded because of their impact on the CDCH performance and consequently on the whole experiment, as shown in figure 4.22. Here the sensitivity of the experiment have been simulated for each kind of wire examined: the use of Cu wires would imply a 20% worsening of the MEG II final result.

The final choice for the CDCH2 cathode wires was Al/Ag (50 μm) from CFW without the ultra-finish phase. Several test performed by submerging wires inside pure water showed that the ones that did not receive the last stage of drawing, called ultra-finish, were less sensitive to humidity. This was also confirmed by looking at those wires with a microscope: the number of cracks in the coating is heavily reduced, thus it is less likely for them to start the corrosion. Moreover it was observed with the present CDCH that the 50 μm wires are less likely to break, hence the choice of this diameter. The phenomenological model, developed for wire breaks from the past experience with the CDCH taking into account the material, diameter and expected exposure to humidity, gives an upper estimate of 2.5 broken wires during the CDCH2 construction. These wires can be removed before the installation, avoiding breaks during the operation phase. This estimates assumes that the exposure to humid atmosphere (60% of relative humidity) will last 30 days: this means that extra care has to be taken during the expected 9 months of wiring phase, in which the detector has to be kept in dry atmosphere whenever is possible.

4.3 Commissioning

After its installation in the PSI experimental area in 2018, the CDCH was able to take data during four pre-engineering and engineering runs [137]. The PSI muon beamline was in fact available for MEG II during the last 2-4 months of the years 2018-2021. During these years the CDCH operation was thoroughly tested, and several problems have been found and solved, as extensively described in section 4.2. Moreover, the final detector performance have been preliminarly estimated, at first with limited readout channels, and in the end with the complete readout configuration. The status of the CDCH and the whole experiment at the beginning of the engineering run of 2021 is summarized in [110, 138], where the most recent estimate of the sensitivity on the $\mu^+ \to e^+\gamma$ search, 6×10^{-14}, is reported.

4.3.1 Pre-engineering run 2018

The pre-engineering run of 2018 was the first one with the CDCH installed in the experiment. Due to the electrostatic instability it was not possible to reach the estimated HV working point in the inner layers, and since the readout electronics was not completely available yet it was only possible to readout a small portion of the detector. The HV maps reported in figure 4.23 shows the HV values reached in operation: the three outer layers L1, L2 and L3 could reach up to 1540 V, while L4 is kept to 1000 V to balance the electric field, acting as the inner guard layer. In the same figure there is also the map of a second configuration tried at the end of the run to see if it was possible to take some data also with inner layers. In this configuration the HV is much lower since the inner layers couldn't reach their working point, which is 1430 V, 1420 V and 1410 V for L6, L7 and L8 respectively.

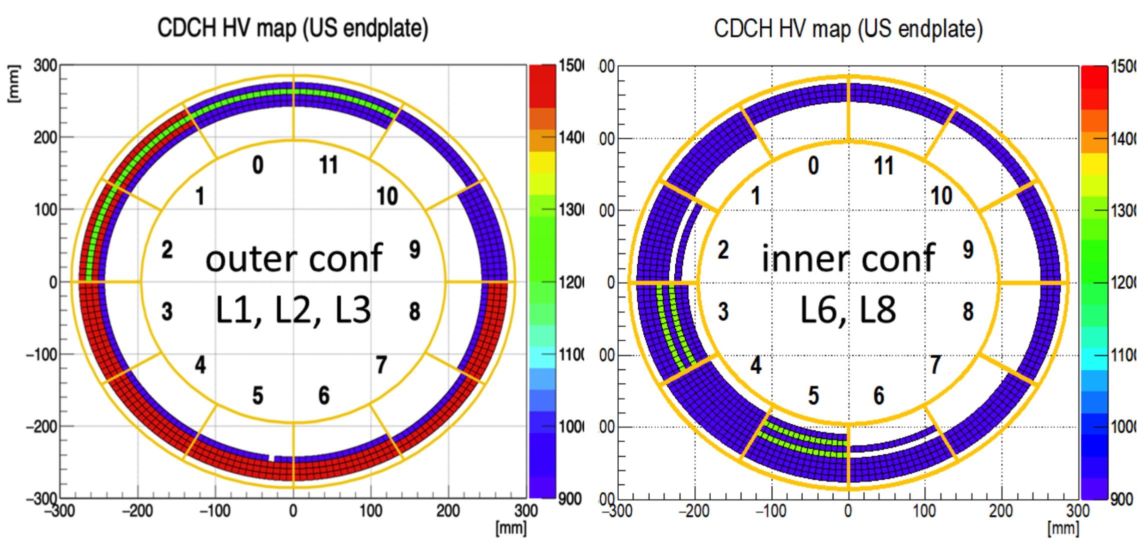

Figure 4.23: CDCH HV map for 2018 pre-engineering run, for both outer and inner configurations. The view is from the US side, where most of the HV channels are connected.

Since only the outer layers could reach the HV working point and since there were only 12 WDB available for the CDCH readout, 6 US and 6 DS, the readout scheme was chosen to be two sectors for three layers. Figure 4.24 shows the position of the readout area which is, in the notation used in software, sectors S1 and S2 for layers L1, L2 and L3.

The choice of the area is also affected by the position of the Cosmic Ray Counters (CRC) used as a trigger to take cosmic rays data, also shown in the figure. They are composed of 8 bars of the old TC used in MEG, 4 placed above the drift chamber and 4 placed below, installed at z=0. This readout scheme is also optimized to combine information with the pTC, since the tracks that crosses those sectors are the ones that have the highest occupancy in the timing counter.

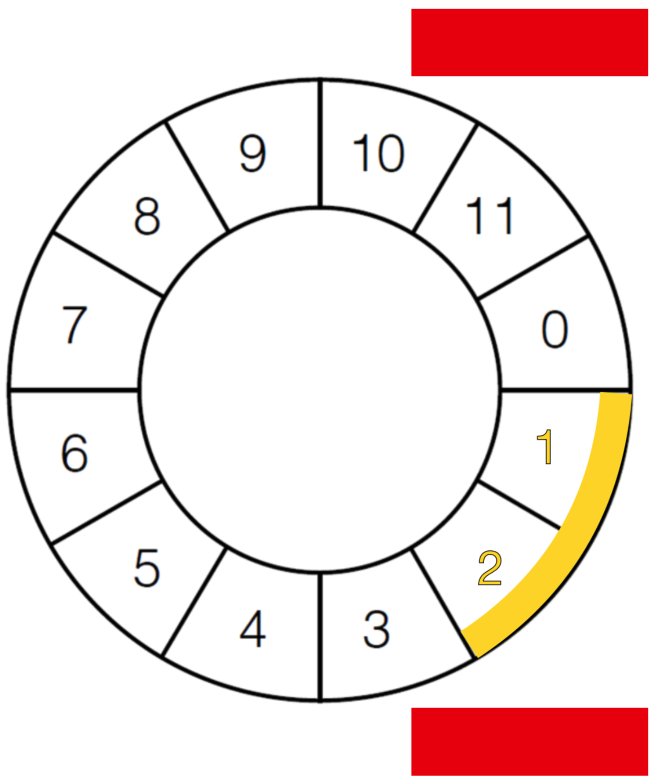

Figure 4.24: Drawing of the readout area, in yellow, during pre-engineering run 2018. The red bars are the CRC, placed at z=0. Notice that the numbering of the sectors is slightly different from the one used in the hardware notation (figure 4.23), where sector 0 is considered to be at 0°.

The goal of this run was to test the possibility to operate the CDCH inside the experiment and to take the first data both with cosmic rays and muon beam. It was possible to estimate the working point both for HV and gas mixture, and to test the stability of the detector under the muon beam. Moreover, with the data collected, it was possible to give a preliminary estimate of the gain and to test the wire-by-wire time calibration procedure.

An HV scan with CRC trigger and without muon beam was performed from 1450 V to 1540 V, both with a 90:10 and 93:7 He:iC_4H_{10} mixture. Figure 4.25(a) shows an example of signal from a cosmic ray event. Here an important low frequency noise is evident: after some investigation it was correlated to the presence of the differential to single-ended conversion boards that were used at the time to convert the CDCH differential signal to a single-ended signal readable by the WDB. This problem was solved in the following years with the introduction of a new type of WDB with a differential input, built explicitly for the drift chamber. The data collected with the old WDB were analyzed with the use of a baseline subtraction technique, as visible in the figure, and a high-pass filter, mostly used for muon events where the baseline subtraction wasn't possible due to the pileup. Figure 4.25(b) shows the result of the HV scan with a 90:10 gas mixture extrapolated from CR data: here the actual gain is not quoted because of the large uncertainty on the electronics gain, nonetheless it was interesting to see the behavior of the mean amplitude of the signal as a function of the HV. From these data and a confrontation with MC simulation it was decided to use as a working point the 90:10 mixture and the HV from 1480 V to 1400 V from L1 to L9, decreasing 10 V each layer to compensate the smaller dimension of the drift cells.

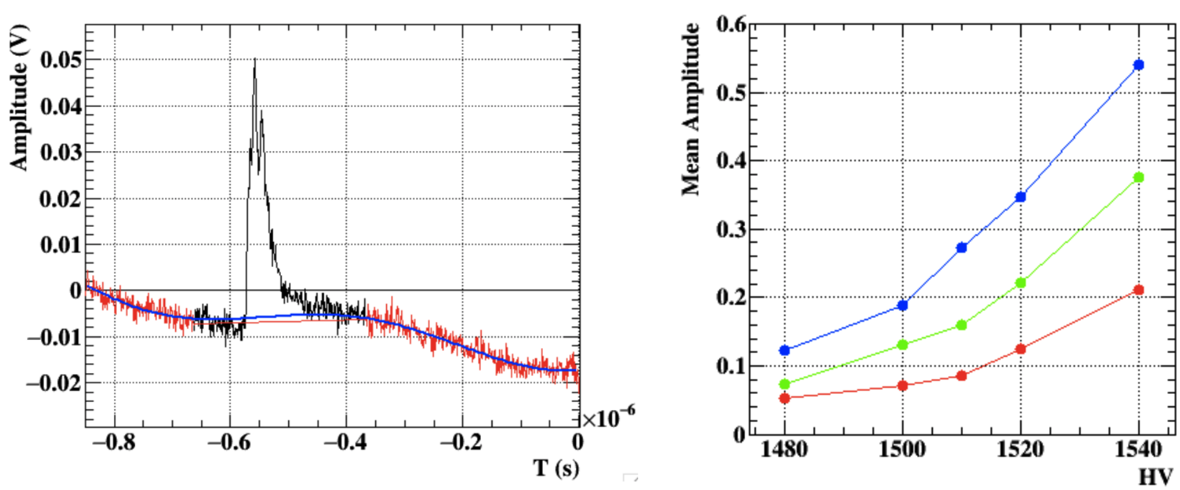

(a) (b)

Figure 4.25: (a) Example of a CR signal in the CDCH. The red part of the waveform is where the baseline is calculated, and the blue line is the fit of the baseline that is subtracted from the waveform in the baseline subtraction procedure. (b) Mean amplitude as a function of the HV for L1 (red), L2 (green) and L3 (blue).

The behavior of the detector under muon beam was also studied during this run. The positrons that produced the signal in the detector were originated in the Michel decay of the muon. The Michel events were triggered by a hit on a tile of the pTC. Three different muon beam intensity were tested: low intensity 6×10^6, MEG intensity 3×10^7 and MEG II intensity 7×10^7. Figure 4.26 shows an example of a signal from a Michel positron. Here an high pass filter was applied to the waveform: the baseline subtraction algorithm was in fact impossible to apply due to the pileup, which is visible in this event and is due to the high intensity of the beam. It was also possible to take some Michel data using the inner configuration with L6 at 1300 V and L8 at 1280 V: some signal showed up but the gain was too low, thus the amplitude were not enough to make them analyzable.

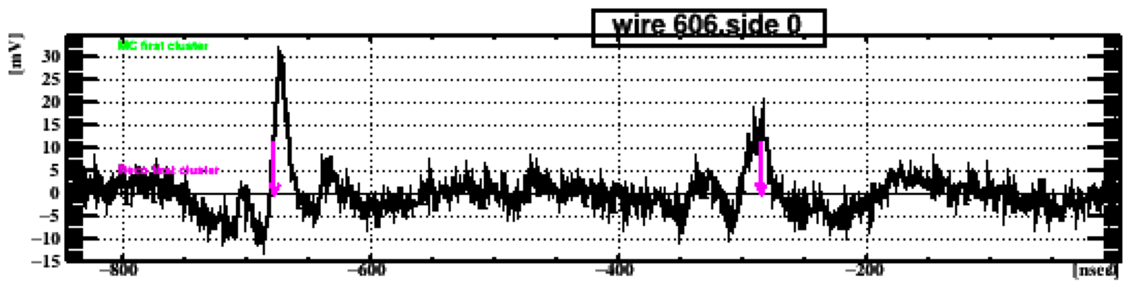

Figure 4.26: Signal from a Michel positron with a pileup event. The arrows indicate the different signals.

Despite the already described electrostatic instability, wire breaks inside the chamber and the discharges under muon beam, during this run it was possible to take the first data ever with the CDCH in the experiment and set a starting point for the next years' run, with an estimate of the working points of the HV and gas mixture and the knowledge of the critical issues in the detector operation.

4.3.2 Pre-engineering run 2019

After the removal of the broken wires and the extra stretching of the chamber during the first half of 2019, the CDCH was installed again in the experimental area for another pre-engineering run. This run was divided into two phases: the first one with the old 12 WDB and the second one with 12 additional WDB with a differential input, the WD2A-diff. The instability issues were solved, as can be seen in figure 4.27 that shows the 2019 HV map: here the HV working point was reached on all the layers, with the exception of only few drift cells. For such reason it was possible to look at signals both in the inner and outer part of the CDCH. Despite this the discharges issue was even worse than previous year, so it was impossible to take Michel data good for the analysis. Nonetheless a good set of CR data was taken to be analyzed and confronted to the past year's one.

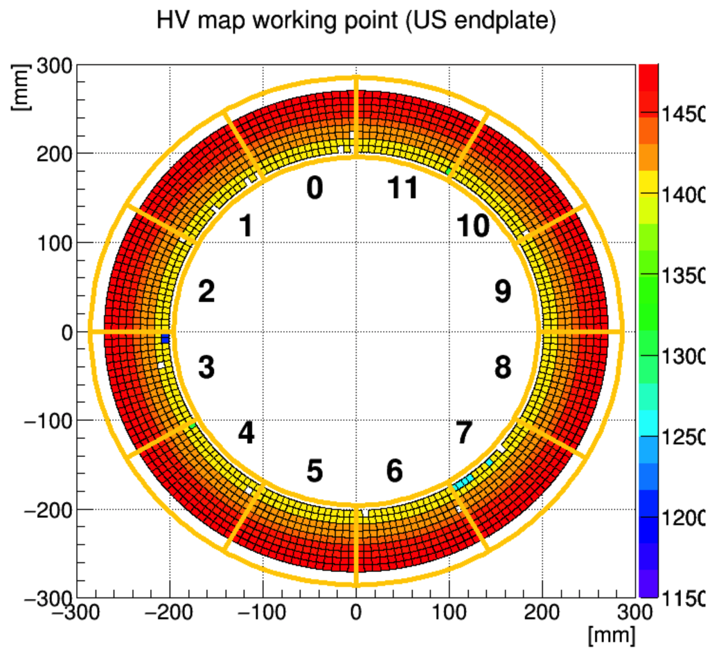

Figure 4.27: CDCH HV map during 2019 pre-engineering run.

During the first phase two different readout schemes have been implemented, while during the second phase only one was needed to readout all the layers, since the number of readout channels doubled.

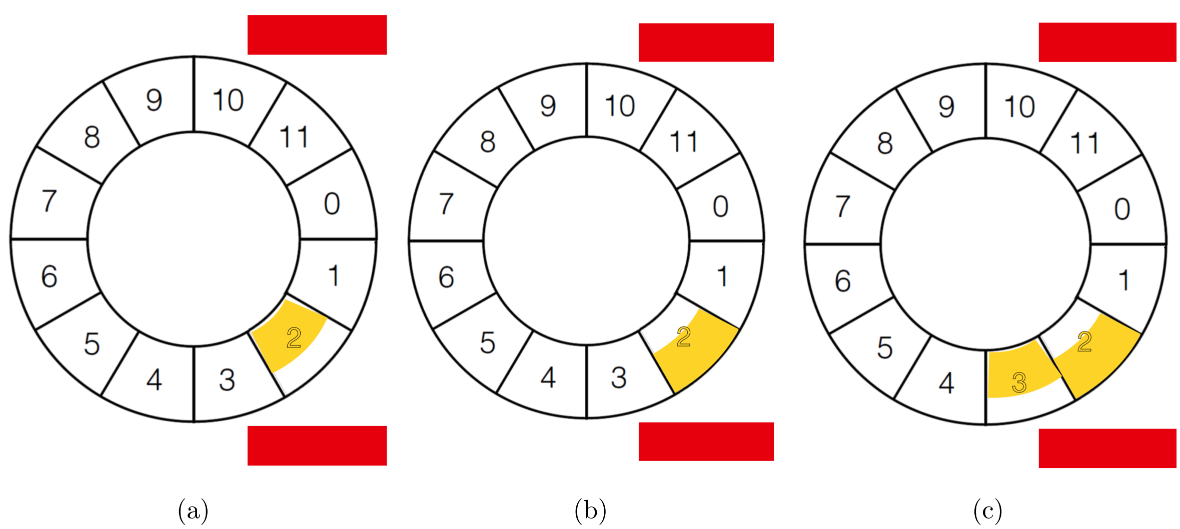

Figure 4.28: CDCH readout configurations during pre-engineering run 2019. (a) Inner configuration during first phase. (b) Outer configuration during first phase. (c) Configuration during second phase with doubled readout channels.

The first two readout schemes were necessary to look at all the 9 layers for the first time, since in 2018 only the first 3 layers were read out. Each configuration has only S2 connected on 6 layers, L1-L6 in the outer one and L4-L9 in the outer one. The readout during the second phase was a combination of the two of the first phase: S2 on L1-L6 and S3 on L4-L9 at the same time, with the new 12 WD2A-diff boards connected to S3. Figure 4.28 shows a scheme of the three readout configurations.

The introduction of the new WDB was crucial for the data analysis due to the noise reduction. In fact the low frequency noise disappeared after removing the differential to single-ended conversion boards needed with the old WDB, as can be seen in figure 4.29. The figure shows a CR signal read out by a WD2A-diff without any kind of software noise reduction algorithm applied. The intrinsic noise level of these boards is as good as the old ones', ~ 0.7 mV, and the same goes for the noise with a FE card connected to the WDB, which is ~ 2.3 mV, as shown in figure 4.30.

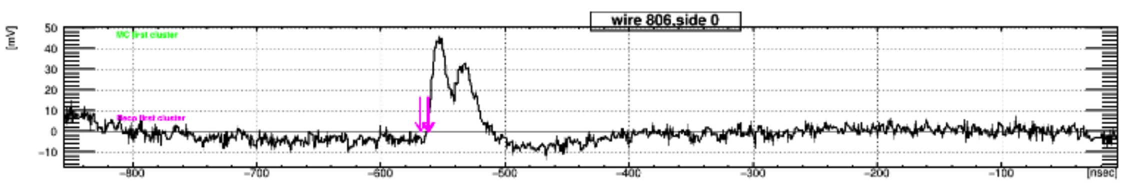

Figure 4.29: Example of a CR signal with a WD2A-diff without software noise reduction.

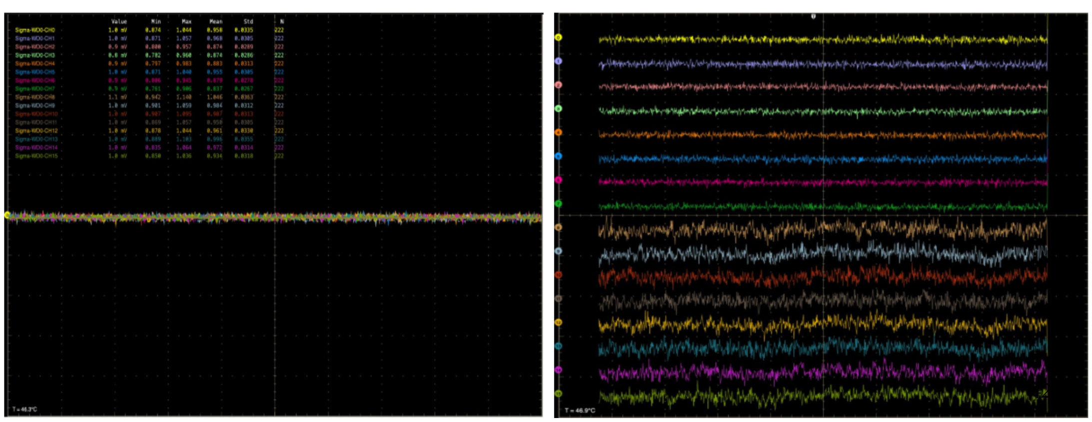

Figure 4.30: Intrinsic noise of the WD2A-diff for all 16 channels. On the right picture the last 8 channels are connected to a FE card, while the first 8 channels are not.

Unfortunately it wasn't possible to collect Michel data due to the discharges issue, but the CR data collected were used to better understand the CDCH behavior. They were used to improve the MC simulations by including a new template for the noise, so to allow a comparison with data. Moreover it was possible to compare this year's data with last year's, at least for L1, L2 and L3 at 1480 V, showing the impact of the electric field unbalance of 2018. In fact, the mean amplitude showed in figure 4.31 is slightly different from the one calculated the previous year, mostly for L3. The expectations from the MC simulations and the results obtained from actual data were in disagreement, indicating that the electronics gain estimate still had to be improved. For such reason the overall gain of the detector has not been estimated until 2020 run.

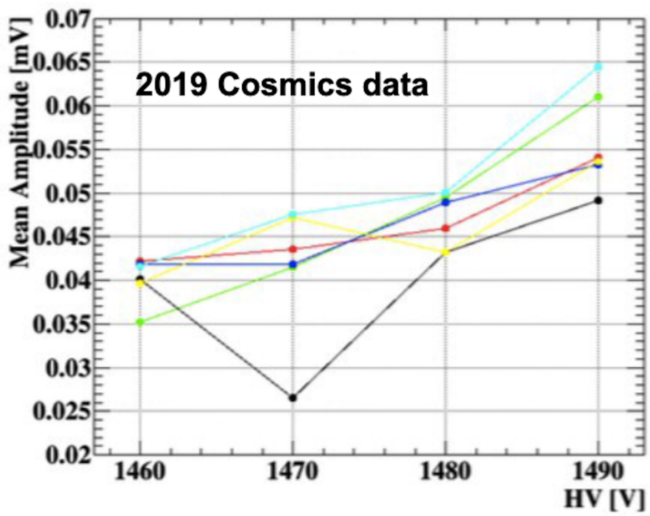

Figure 4.31: Mean amplitude as a function of HV from 2019 CR data. Each curve represents a layer: L1 (red), L2 (green), L3 (blue), L4 (black), L5 (yellow), L6 (cyan).

4.3.3 Pre-engineering run 2020

During 2020 the CDCH has been opened again to remove the residual broken wires and to install the Plexiglas shell for the discharges investigation. After having reinstalled the CF shell and localized the discharges, the detector has been installed in the experiment for the third time. The goal of this run was to improve the stability of the detector under the muon beam using additives to the gas mixture. Moreover, since the performance of the detector are affected by the amplitude of the signal, new FE boards with increased gain were tested. This is in fact the only way to increase the overall gain without increasing the gas gain, which would speed up the ageing of the drift chamber. Finally, the MC simulation was improved with realistic noise and electronics gain, allowing for a good comparison with data and thus a reliable estimate of the CDCH gain. The reconstruction algorithms were also optimized and tested with success, even though with a limited amount of readout channels.

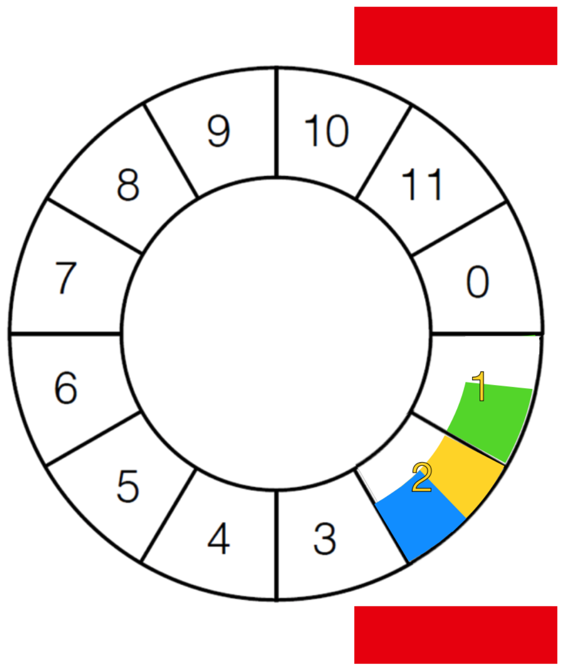

Figure 4.32: Schematic view of the CDCH readout configuration used during 2020 pre-engineering run. The three colors represent the different FE board gain: standard gain (green), x2 gain (yellow) and x4 gain (blue).

The HV map for the 2020 pre-engineering run is the same of 2019, except for some removed drift cell due to the wire breaks. Since the inner layers have been tested the previous year, the choice of the readout was limited to the first 6 layers in 1.5 sectors, all read out with WD2A-diff, whose number increased to 16. Figure 4.32 shows a schematic of the readout, optimized to reconstruct some positron track. The three different colors used in the image are for the three different FE boards used: one with the standard gain as was in 2018 and 2019, one with x2 gain and one with x4 gain.

The noise reduction was improved thanks to the implementation of several software filters. Figure 4.33 shows the effect of three of these algorithms: the Median Filter, which is a low-pass filter; the Moving Average, which is a high-pass filter; the Burst noise suppression, that mitigates the effect of the burst noise observed in some events. The figure shows the original waveform with the filtered one superimposed. It also shows the result of the application of the filters to the time distribution obtained from a dataset of CR collected with air and water as additives for the gas. It is clear from this distribution that the filters remove the noise hits, leaving only real hits with good hit times. From the same dataset it was also possible to calculate the time offset wire-by-wire, which has been calculated to be of the order of 1 ns for every channel.

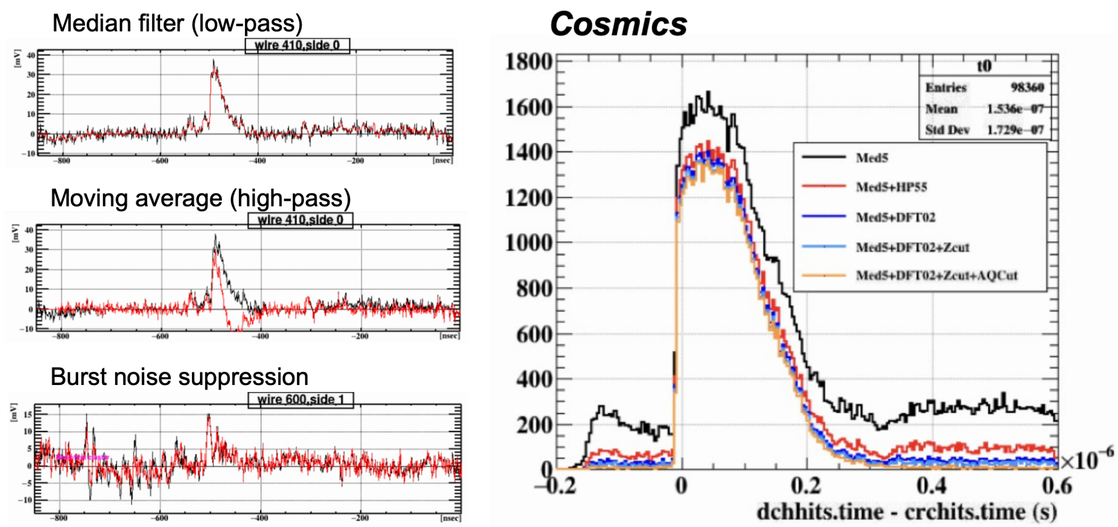

(a) (b)

Figure 4.33: (a) Example of filtered waveforms. The original waveform is in black, while the filtered one is in red. (b) Time distribution from a CR dataset. The different colors represent a different combination of the filters applied to the waveforms. Even the application of the high-pass filter alone (in red) drastically improves the shape of the distribution.

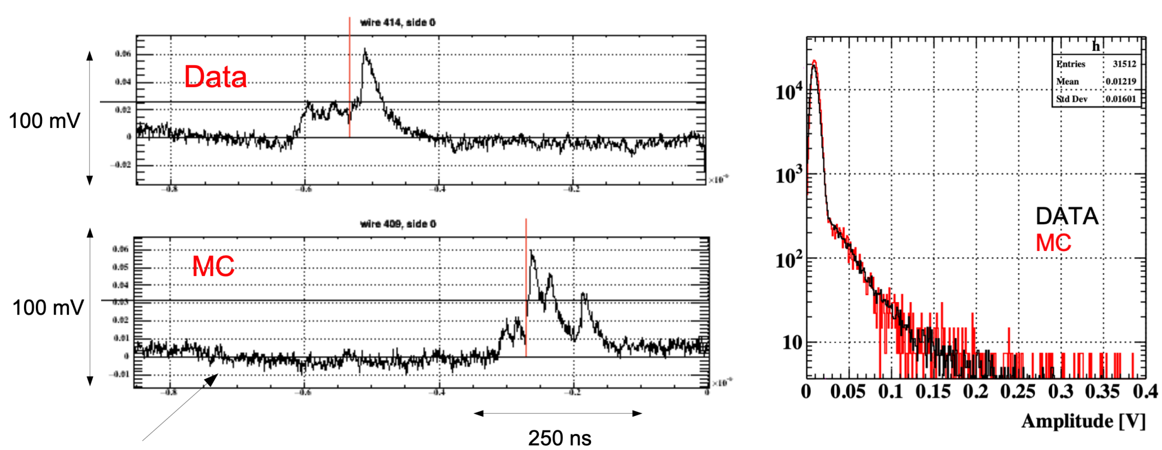

(a) (b)

Figure 4.34: (a) Comparison between a waveform from data and a waveform from MC. The time offset can be adjusted in the simulation and will be aligned to the data. (b) Comparison between the amplitude distribution of a dataset with the corresponding MC simulation.

The MC simulation was also improved: a proper simulation of the electronics chain was implemented, allowing to estimate the overall gain, which is the product of the gas gain and the FE gain. Figure 4.34 shows an example of waveform from simulations and data, together with a distribution of the maximum amplitude for a CR dataset took with the 90:10 gas mixture with the addition of water. Here the amplitude is measured on L3 in a sector with standard FE gain and no noise reduction filters are applied. The figure shows how the improved MC simulation are now in good agreement with the data.

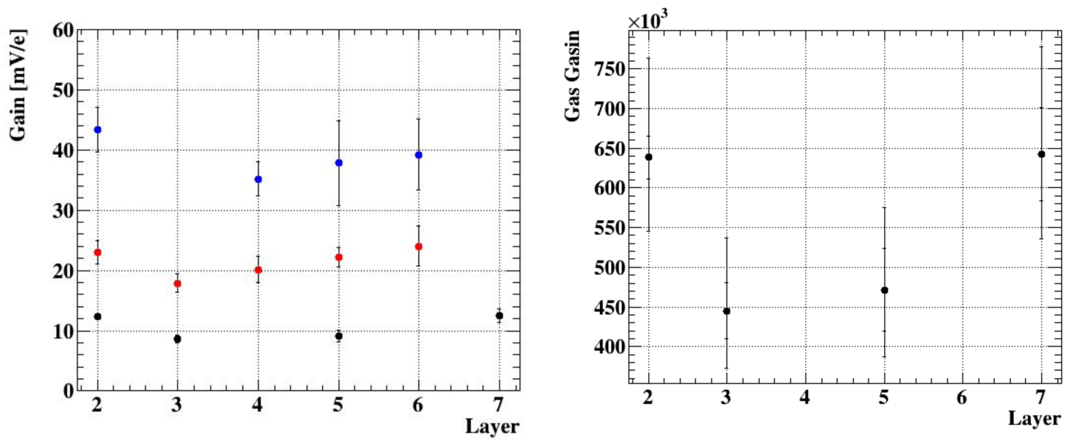

(a) (b)

Figure 4.35: Gain vs layer. (a) Gain per electron for standard (black), x2 (red) and x4 (blue) FE gain. (b) Overall gain of the CDCH in the standard gain configuration.

The result of the gain calculation is reported in figure 4.35 layer by layer. The gain per single electron is compared for the three different FE gain configurations. Here the trend is the same for the three gains, but the S/R calculation favors the FE gain x4, which is then the one chosen for the future CDCH operations. The overall gain is then estimated in the standard FE gain configuration, and ranges from 4 to 7×10^5, in good agreement with the design value of 5×10^5.

The main goal of this run was to reach a stable working condition of the CDCH. The electrostatic instability and wires corrosion problems were solved, but the discharges triggered by the presence of the muon beam were an issue, since they made impossible to take good Michel data in 2019. Different additives were tried in the gas mixture to mitigate the discharges: dry air, oxygen, water and isopropyl alcohol. The electron attachment that happens in the presence of the additives molecules prevents the creation of discharges that generates high current on the wires. The first tests were made with air instead of oxygen and water instead of isopropyl alcohol because of their availability: that is why the first studies on the software filters and gain were made with air and water additives. Upon their availability, O_2 and isopropyl alcohol were used: the first gas was flowed in the extra line of the gas system, while the alcohol was brought to the CDCH active volume by flowing a small percentage of the He flux inside a bubbler containing the liquid. The use of isopropyl alcohol instead of water has a small impact on the signals, almost negligible, but it is safer in terms of wires corrosion.

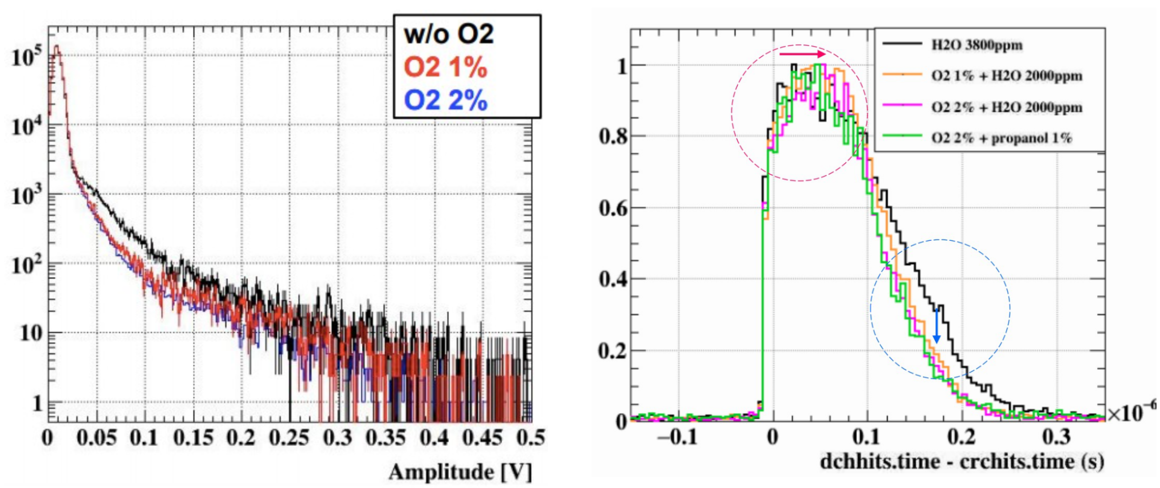

(a) (b)

Figure 4.36: Example of amplitude (a) and time (b) distributions from CR data with H_2O and different concentration of O_2.

A stable running condition was found with 0.5% of O_2 and 1% of isopropyl alcohol. With this mixture the CDCH could take data under the full intensity muon beam for a whole week without showing discharges. The impact of these two additives had to be studied to confirm that it is possible to run in this condition without worsening the performance. Figure 4.36 shows an example of amplitude and time distributions from a CR dataset. Here the gas mixture has water and a variable percentage of oxygen: the relative gain drop from the 0% case is evident, and ranges from 20% to 30% for 1% and 2% O_2 concentration respectively. Figure 4.37 shows the number of hits per track as a function of the drift distance in the same dataset. Here the impact is less evident: there is a 7%-9% relative drop in the number of hits on track when the O_2 concentration is 1%-2%. The results of this analysis is inconsistent with the predictions from MC simulations made with the GARFIELD software [139], and that may indicate that GARFIELD overestimates the attachment coefficient of the oxygen. The results from data are in fact in agreement with the simulation when the attachment coefficient is reduced by a factor 6. The final choice of the 0.5% concentration for O_2 is due to the fact that it is sufficient to suppress the discharges, albeit the 1% concentration is already enough to lose only a small amount of efficiency on positron reconstruction.

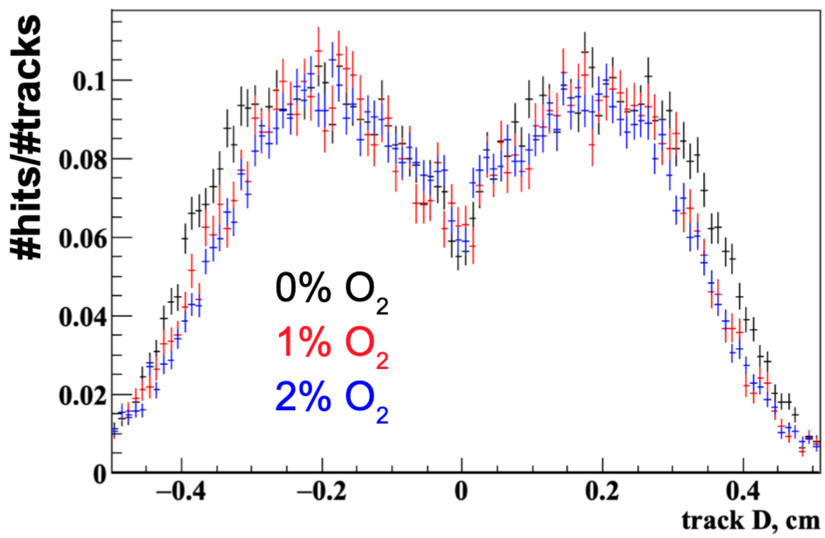

Figure 4.37: Number of hits per track vs drift distance calculated from CR data with H_2O and different concentration of O_2.

The good quality of data collected in 2020 allowed to better understand the detector capabilities. It was in fact possible for the first time to obtain good fitted tracks both in CR and Michel positron runs: figure 4.38 shows an example of a fitted positron track. Moreover it was possible to give a reliable estimate of the gain, both of the gas and the electronics, and to find the final working point of the FE gain. Finally, the optimal gas mixture found allowed to take data under full intensity muon beam without discharges for one week. The reconstruction tools were tested both with CR and Michel data sets collected during the run, and proved to be functioning. The tests were carried out on the small part of the CDCH that were connected to the readout electronics, thus more complete and reliable results had to wait for the installation of the complete set of WDB that happened in 2021, before the engineering run.

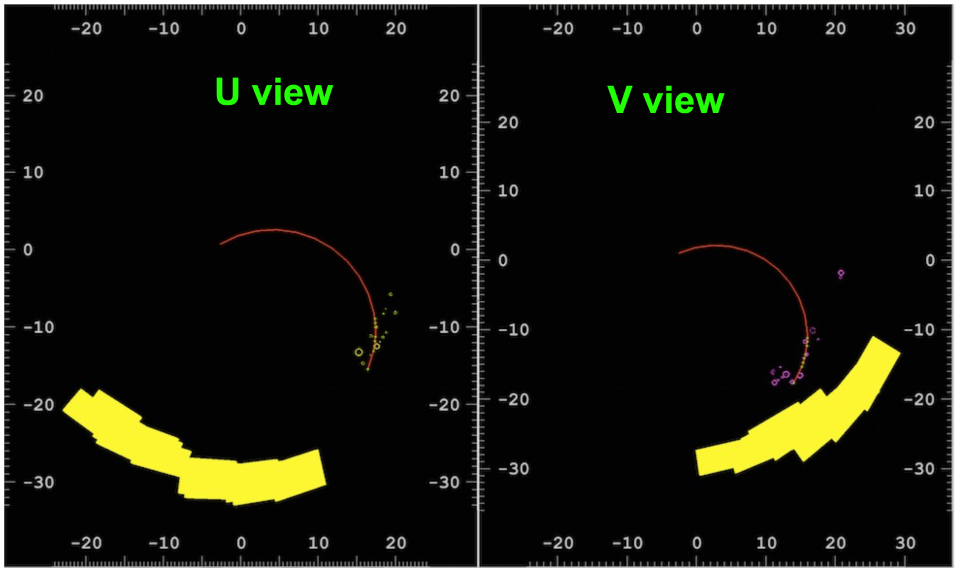

Figure 4.38: Example of a Michel positron fitted track in the two stereo projective views.

4.3.4 Engineering run 2021

After the last opening of the CDCH for the broken wire removal in 2021 the detector was installed again in the experiment. During this time the full TDAQ electronics was also installed, and for the first time it was possible to test all the detectors in the final configuration of the physics run. The beam time granted from the PSI to the MEG II experiment in 2021 can be divided into two phases: the engineering run, from August to October, and the physics run, started after the end of the development of the $\mu^+ \to e^+\gamma$ trigger in October and lasted until the end of the year.

The goal of the engineering run period was to extensively study the long term stability of the detector with the final 90:10 He:iC_4H_{10} + 0.5% O_2 + 1% isopropyl alcohol gas mixture. The CDCH was equipped with the new FE boards with modified gain, 4 times higher with respect to the old one, and read out with WD2A-diff on 8 sectors in every layer as designed. Figure 4.39 shows the readout scheme and the map of the short circuits at the beginning of the run. The CDCH can be rotated around its axis in step of 30°, which corresponds to one sector. It was then possible to minimize the number of short circuits in the readout area by finding the optimal rotation angle. Detailed MC simulations that included the absence of the short circuited wires showed that there is a 1% improvement on the positron detection efficiency when the detector is rotated by 8 sectors clockwise in the DS view. This rotation configuration where S2, S3, S4 and S5 in the HW notation (figure 4.39(b)) are not read out was chosen for the 2021 run. The SW notation is kept the same as usual, with S0 being the first sector in the readout area.

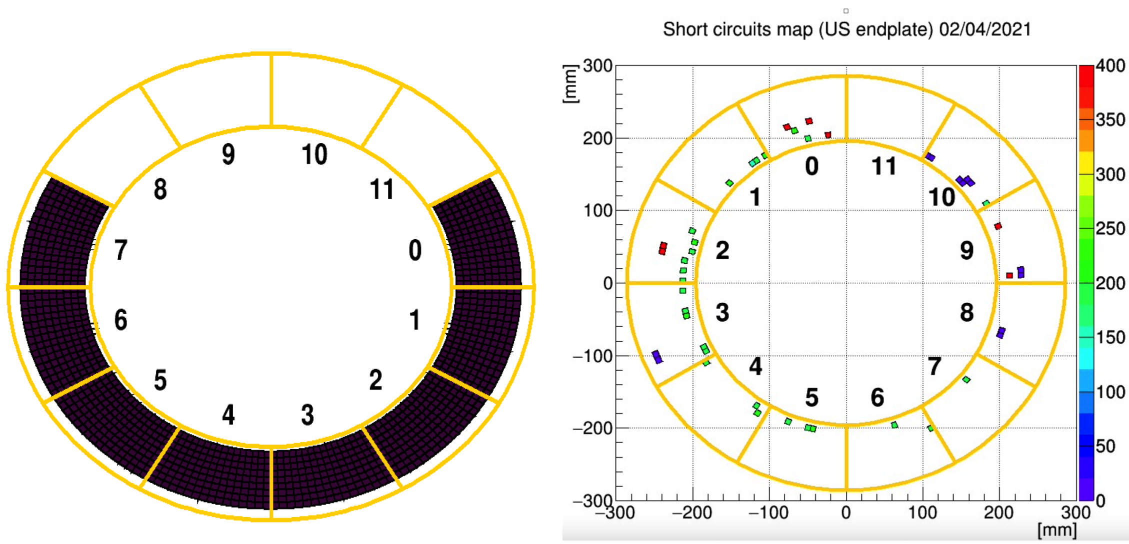

(a) (b)

Figure 4.39: (a) CDCH readout channels during 2021 run (SW notation from the DS view). (b) CDCH maps of the short circuits at the beginning of the 2021 run (HW notation from the US view).

The new mixture proved to be sufficient to suppress the discharges without affecting the detector performance. Nonetheless a small change in the isopropyl alcohol concentration can cause the reappearance of the discharges. Since this concentration depends on the capability of the He flow to capture alcohol molecules in the bubbler, and this depends on the temperature, a new thermostated bubbler was installed before the start of the physics run, so to keep the concentration in the mixture constant over time and independent on environmental changes.

Once a working condition was reached and the CDCH proved to be stable enough, the 2021 physics run started. In the engineering part of the run only Michel data with pTC trigger were collected, while in the physics run it was possible to collect physics data with all the detectors using the $\mu^+ \to e^+\gamma$ coincidence trigger. These data allowed to preliminarily estimate the resolution and efficiency of the detector.

Many software improvements were applied to the analysis code thanks to the data collected during the run. The results of the optical survey performed just after the installation of the CDCH in the experimental area were included for the first time in the code, so to improve the precision on the knowledge of the position of the wires, crucial in the evaluation of the tracking performance. The TXY tables were also computed from scratch to take into consideration the new gas mixture with the additives.

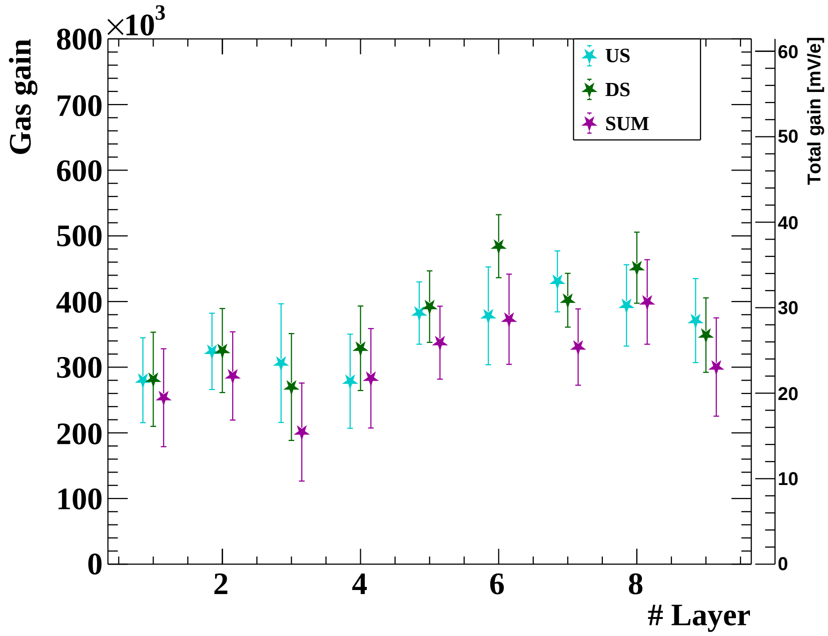

Figure 4.40: Estimated gas gain for each layer and each end. The total gain, that includes also the electronics gain, is reported as well.

The gain was estimated again in 2021, this time for all the layers. The estimate is based on MC simulations: a set of data was simulated with different gain values, and then a χ^2 test between the simulated gains and the cosmic rays data collected during the run was performed. The χ^2 trend with the gain was then fitted with a parabola, and the position of the minimum of the fit was identified as the best gain estimate. The procedure was repeated for each layer and for each wire end, including the sum of the two ends. Figure 4.40 shows the result of this study: the gain looks lower on average with respect to 2020, most likely due to the use of isopropyl alcohol instead of water.

Figure 4.41 shows a preliminary estimate of the drift distance resolution. It is obtained as the width of the distribution of the track residuals, and resulted to be 230 μm with the new TXY tables, with a core/tail ratio of 4.2 using a 2σ cutoff. The result is a factor 1.6 worse than the MC expectation, which is 145 μm: this is due to the non perfect software alignment, that needs further improvements. A first attempt in applying a software alignment based on the average of the residuals improves this estimate to 180 μm, only 25% worse than MC. A track based software alignment will further improve this result. Angle and vertex resolutions were also estimated to be $\sim 25\%$ worst than MC expectation, partly due to the worst hit efficiency, which is itself due to the worse drift distance resolution.

Even though there is a discrepancy between MC and data in the performance estimate, the reason can be ascribed to the need for small software improvements. Thus, with future data and algorithm refinements the CDCH will be able to reach its target resolutions and efficiency. Moreover, the long term stability during the 2021 run proved that it can be used during the MEG II physics data taking in the upcoming years.

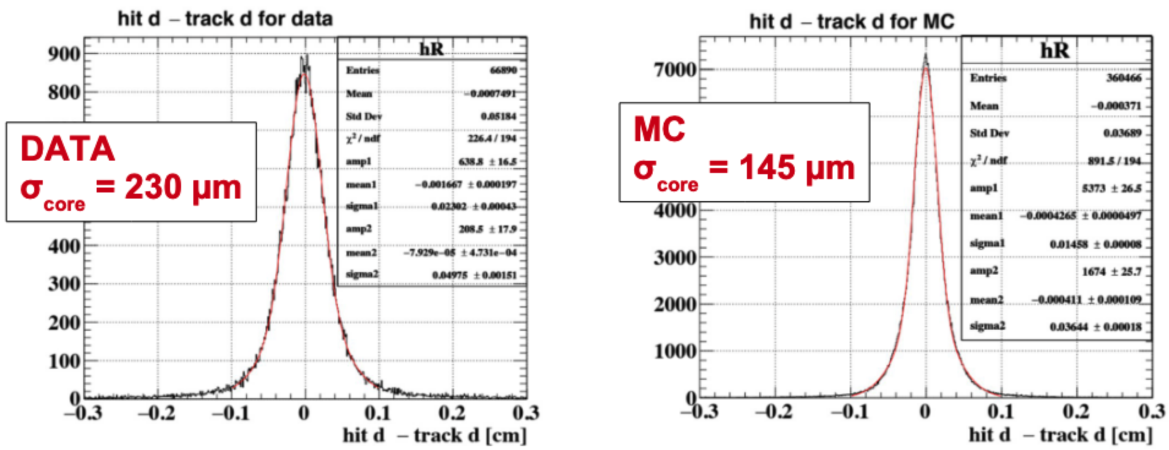

(a) (b)

Figure 4.41: Track residuals distribution from data (a) and MC (b).

Chapter 5

Experimental setup for X(17) measurement at MEG II

The X(17) measurement with the MEG II detectors can be an independent confirmation of the Atomki anomaly with improved invariant mass resolution and angular acceptance. The improvements in the invariant mass resolution require a redesign of the CW target region: the thick $Li_2B_4O_7$ target used for the LXe calibrations and the Al beam pipe increase the radiation length and have a sizable impact on the CDCH tracking performance. For this reason a redesign of the CW target region is needed to minimize the material and fully exploit the MEG II ability to make this measurement. Moreover, the larger angular acceptance of the CDCH allows to study the X(17) production not only in the plane perpendicular to the beam, as was done at Atomki. An angular analysis like this can provide information on the particle's quantum numbers, allowing to discriminate between the different scenarios proposed for the anomaly interpretation, as reported in section 1.3.

In this chapter I will report the results of the simulations made to optimize the redesign of the target. I will start with a description of the first design developed for the target and its support structure to be attached to the CW beamline, reporting the expected resolution and efficiency for different materials. The optimal material and thickness in terms of balance between heat dissipation capability and resolution has been chosen with this first target design. After that, another design has been tested to further optimize the apparatus: I will report the results of the simulations of heat dissipation, resolution and efficiency that have been refined and repeated for this final design. I will finally show the details of the IPC background model and its implementation that, together with the EPC model, completes the MEG II simulation software for the X(17) measurement.

My contribution in the work presented in this chapter consists in the implementation of the GEANT simulations to estimate the resolution and efficiency of the X(17) measurement at MEG II. I tested different target and support materials and dimensions, both for the first design and for the definitive one. I also implemented the background simulation from the Zhang and Miller theoretical model [1].

5.1 New target design

The design of the new target region underwent two main revisions. The first one was a swap between the last part of the Al pipe of the CW line with a vacuum Carbon Fiber (CF) chamber of the same size. Inside this chamber a metallic arm holds a substrate of the same material on which the Li_2O target is sputtered. This design does not interfere with the CW insertion system since it is just a replacement of the terminal part of the beam pipe. Nonetheless the presence of the internal bellows severely affects the tracking of the e^+e^- pair, thus a second design has been implemented. Here the support arm and target remains the same, but the small CF vacuum chamber is replaced by a larger one, with the largest possible diameter, slightly smaller than the internal radius of the CDCH. For its installation the internal bellows must be removed, thus the material crossed by the particles is drastically decreased. The drawback of this design is the incompatibility with the MEG II data taking, since the insertion system is required to perform the LXe calibration during the $\mu^+ \to e^+\gamma$ measurement.

The large CF chamber configuration is the one chosen for the final data taking since it is the most efficient one in terms of resolution. Nonetheless the first design with the small CF chamber was used to carry out the first studies and better understand the experiment capability in the X(17) measurement. Moreover it was also implemented and used to take some preliminary data during the 2021 engineering run, since the incompatibility of the final design with MEG II runs forced the measurement to be postponed to the beginning of 2022. These data were used to successfully test the target stability in terms of heating and detachment of the Li_2O from the substrate and to test the analysis algorithms.

5.1.1 First design with small CF chamber

The first design of the target has been developed accounting for the need to dissipate the heat that comes from the CW proton beam and, at the same time, limiting the amount of material to improve resolution and efficiency. A support structure holds a substrate on which the target is sputtered, as shown in the drawings in figure 5.1. The support includes a ring that has to be attached to the flange of the CW beam line and is connected to the target substrate using a bar. This object is placed inside a CF vacuum chamber with the same diameter of the ending part of the CW beam line used for LXe calibrations. The figure shows also the support structure placed inside the vacuum chamber. The volume between the CF and the bellows is in air, while the volume between the bellows and the inner Mylar foil of the CDCH is filled with He.

(a) (b)

Figure 5.1: Drawing of the first design of the target support (a) and of the small CF vacuum chamber (b).

The substrate and support material has to be carefully selected. The resolution, efficiency and heat dissipation have been simulated with GEANT4 [116] and ANSYS [140] for different configurations of the target substrate and support, varying thickness, material, target inclination, etc.

Table 5.1 sums up the results of the ANSYS simulations performed with this first design, reporting the assumed proton current, substrate thickness and material, support bar thickness, maximum temperature reached and temperature at the CW beam line flange. As a reference, the Cu and Al melting temperatures are 1085° and 660° respectively. Here no external cooling is assumed, and the heat is carried away from the target only via the support structure, which is in thermal contact with the CW beamline by means of an Al flange.

The maximum power that heats up the target is ~ 100 W, since the accelerator can reach currents up to 100 μA for 1 MeV protons. However, the temperature reached with this current is too high even using a thick Cu substrate, which is the configuration that dissipates the most among the ones tested, thus the operating current has to be set to a value lower than 10 μA. The Cu is a better choice in terms of heat dissipation, but since it has a larger X_0 with respect to Al its impact on the resolution has to be evaluated. Figure 5.2 shows the result of the simulation in one example configuration with a 10 μm Al substrate and 10 μA proton current. This thickness is not feasible since the heat does not dissipate through the support, as evident from the figure.

I_p [μA]	Sub mat	Sub thick [μm]	Supp thick [mm]	T Max [°C]	T Flange [°C]
1	Cu	100	6.0	35	30
1	Al	100	6.0	39	29
1	Al	50	4.5	51	31
5	Cu	50	4.5	135	60
5	Al	50	4.5	183	76
5	Al	50	6.0	109	70
10	Cu	100	4.5	231	91
10	Cu	10	4.5	383	102
10	Al	100	6.0	236	93
10	Al	100	4.5	317	120
10	Al	10	4.5	573	83
100	Cu	100	4.5	2111	718

Table 5.1: Maximum temperature reached for different target support thicknesses and materials.

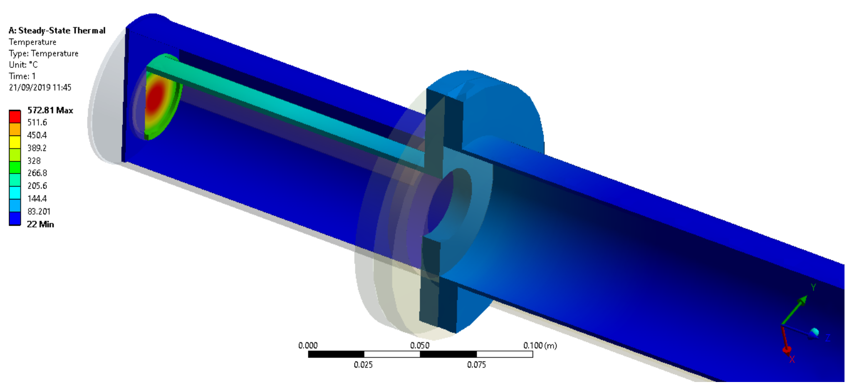

Figure 5.2: Example of a simulation of the heat dissipation in an Al target support with a 10 μm thick Al substrate. Here the assumed proton current is 10 μA.

These simulations showed that it is not possible to reach more than 5 μA and that the substrate thickness must be well above 10 μm, and a compromise between these requirements and the resolution requirements had to be found. For this reason the efficiency and invariant mass resolution have been studied for different configurations using GEANT4. Table 5.2 summarizes the results obtained for this first design. Here the resolution is reported as the σ of a Gaussian fit to the invariant mass distribution, and the efficiency includes also the requirement of one hit in the pTC.

The simulations have been repeated in many configurations to better understand the components that most affect the performance. The first step was to implement a simple geometry, called here "*test geometry*", which includes only the target and the CF tube. Then, adding a Cu support with a 100 μm Cu substrate and using a more precise description of the CF tube, the resolution and efficiency gets worse ("*new geometry*").

#	Description	ε (w/TC) [%]	σ_m (w/VtxConst) [keV]
100	Test geometry	19.9 (8.3)	345
001	New geometry	16.6 (5.9)	536
002	No substrate	18.4 (7.8)	422
003	No support	18.6 (8.3)	422
004	No tube (w/substrate)	14.8 (4.9)	705
005	100 μm Al sub	17.8 (7.6)	516
006	10 μm Al sub	18.5 (6.8)	416
007	1 μm Al sub	18.3 (7.3)	343
008	10 μm Cu sub	17.9 (7.4)	490
009	1 μm Cu sub	17.8 (7.1)	357
010	50 μm Cu sub	17.9 (6.5)	488
011	50 μm Al sub	18.4 (7.7)	437
012	011+thick Al sup	11.9 (3.4)	775
013	012+45° z tilt	13.4 (3.7)	613
014	012+bellows	5.6 (1.2)	794
015	013+bellows	8.3 (2.4)	734 (659)
016	015+Al tube	7.1 (2.3)	864

Table 5.2: Efficiency and resolution calculated from GEANT4 simulations in different configurations.

By removing the pieces of the geometry (substrate, support or tube) one by one it is clear that the object that most affects the resolution is the target substrate. Other configurations have then been tested, using different substrate thicknesses and materials, including the Atomki configuration in their first measurement, *"10 μm Al sub"*. From the configuration labeled as 011 the code has been improved, correcting the particles generation angle and considering a 1 cm σ wide beam instead of a point-like beam as it was before. These modifications worsened both efficiency and resolution, but provided more reliable results. The bellows, previously not included in the simulations, has been added in the last configurations as pointed out in their descriptions. This has a big impact on the performance, that can be partially recovered by rotating the target 45° around the x axis. This happens because the CDCH is readout only on the lower 2/3 of the sectors, thus most of the reconstructed tracks are the one emitted towards the bottom of the system, when they do not cross the target substrate. Another improvement is the addition of a vertex constraint, used in the configuration 015 (which is a promising compromise between heat dissipation and resolution): this constraint forces the tracks to cross the target in the same point. The last configuration shows the results obtained using the ending of the beam line in Al instead of CF: even if it would be useful for heat dissipation purpose, this configuration is not feasible due to the resolution worsening.

Figure 5.3 and figure 5.4 show respectively the results of the ANSYS and GEANT4 simulation for a promising configuration, which is a 50 μm thick Al substrate that guarantees a low enough temperature on the target at 5 μA proton current (109°C, well below the Al melting point) and a good resolution (659 keV, better than the $\sim$ 1 MeV reached at Atomki).

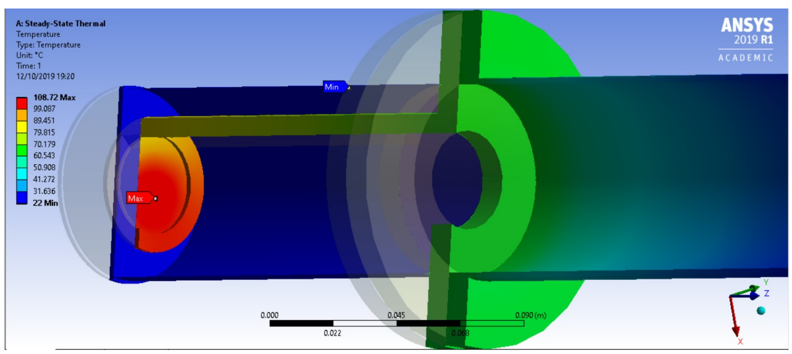

Figure 5.3: Simulation of the heat dissipation in the target support with 5 μA of proton current on a 50 μm thick Al substrate using a thicker bar in the support.

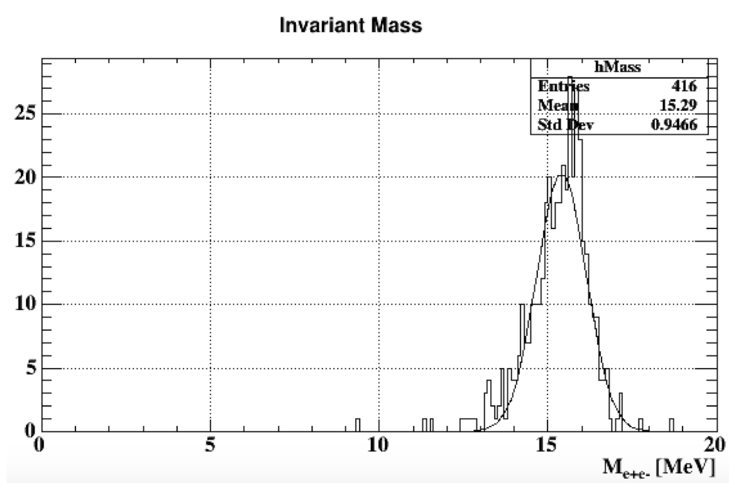

Figure 5.4: Invariant mass distribution from the simulation with a 50 μm Al target substrate.

This result may be overestimated, both in terms of heat dissipation and resolution. This version of the ANSYS simulation, in fact, does not take into account the possibility of the detachment of the target from the substrate: the improved version of the simulation includes also this circumstance, and will be applied to the final version of the target design (more details about this in section 5.1.3). Also the resolution estimate is optimistic: the bellows is schematised in the simulation with a 2.5 mm thick polyethylene cylinder, but it is actually a more complicated object. The fact that it has a noticeable impact on the resolution and it is difficult to be accurately implemented in the simulations is the reason why a new design of the system has been developed. This new design allows to insert a larger CF chamber and the target support as a replacement of the internal bellows.

5.1.2 Final target design

From the results of the simulations performed on the first target design emerges the necessity to further improve the resolution. Moreover, without an external cooling system, the heat dissipation is not efficient for a proton current greater than 5 μA. This led to a redesign of the target region: the first idea was to modify the internal bellows of the CW insertion system to make it thinner but still compatible with the LXe calibration. This solution proved to be technically too difficult, thus the final choice was to completely remove the bellows and use a large CF vacuum chamber as the ending of the CW beam line. This makes the experiment more performing on the X(17) measurement but makes it incompatible with the MEG II calibrations, forcing it to be performed during the PSI muon beam shutdown period at the beginning of each year, during which the experiment cannot take data for the $\mu^+ \to e^+\gamma$ measurement.

Modified bellows system

The first proposal was to modify the bellows system by adding a Mylar extension, so that the particles crosses a much thinner and lighter material. From figure 5.5(a), that shows the simulated electron and positron reconstructed tracks projected on the ZY plane, it emerges that the optimal length for this extension is around 20 cm along the z axis: most of the tracks, in fact, are within this length. Moreover, from figure 5.5(b) that shows the same plot but projected on the XY plane, it emerges that the lateral sides of the CF chamber are less crossed by the tracks. With this information it is possible to think of a modification to the CF chamber, adding two Al stripes on the sides in order to improve the heat dissipation and to affect the resolution as little as possible, since not many tracks will cross them. In this case the target support can be directly connected to the Al stripes with two Al pillars, instead of the CW flange with the support bar of the first design. Figure 5.6 shows a drawing of the bellows: the best place to put the Mylar extension would be the one in the red circle, but in order to do this the cap on the left must be removed.

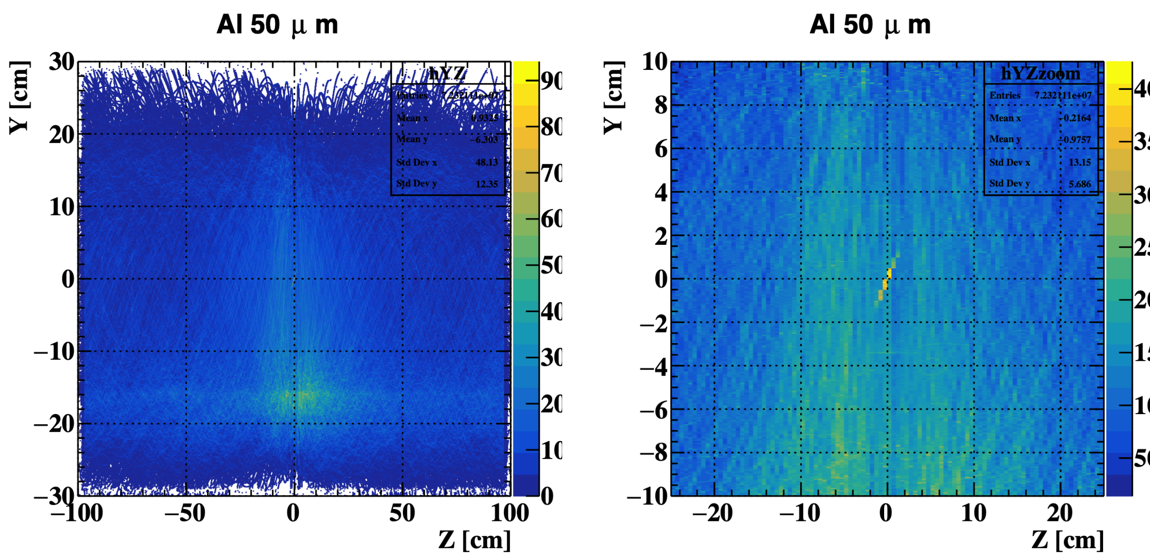

(a)

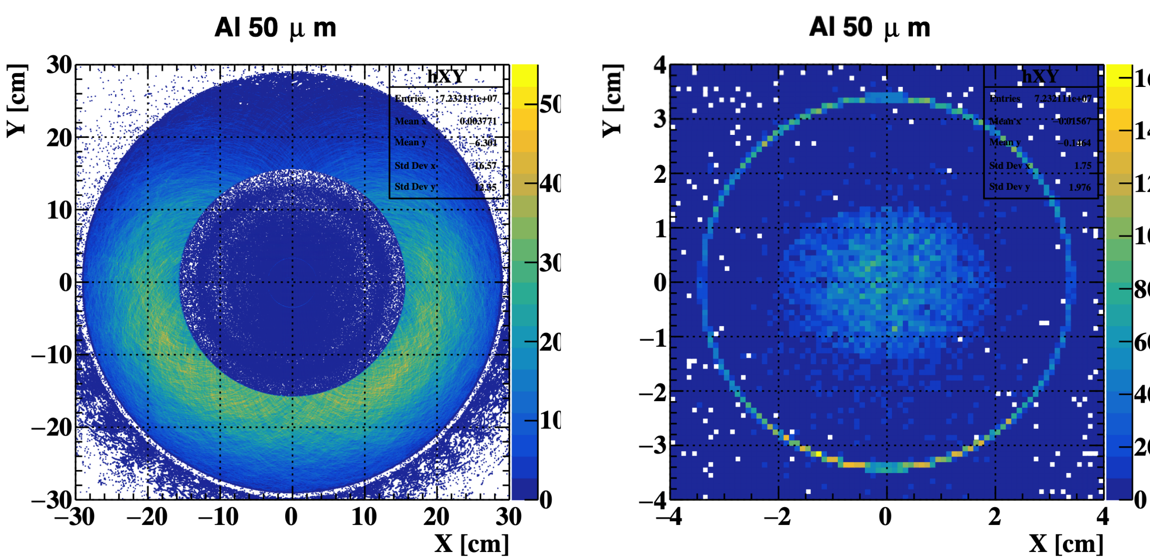

(b)

Figure 5.5: Projection on the ZY plane (a) and on the XY plane (b) of the simulated tracks that are reconstructed in the CDCH. The right plot is a zoom of the left plot.

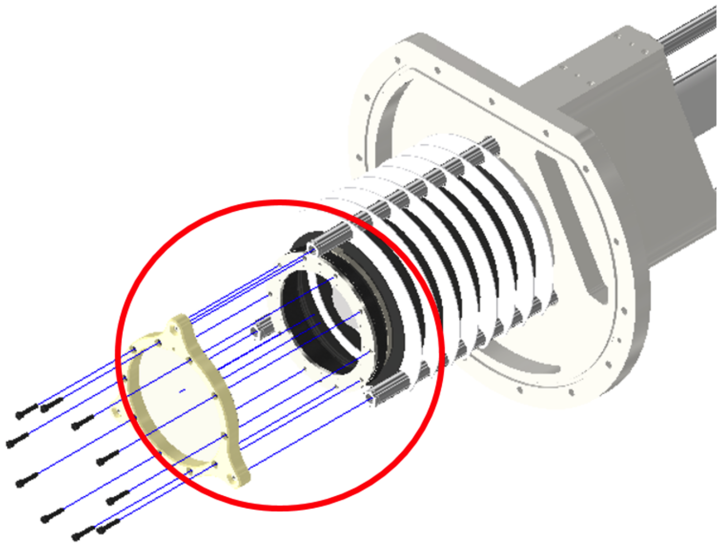

Figure 5.6: Drawing of the final part of the CW insertion system with the bellows. The extension can be placed in the region highlighted by the red circle by removing the cap on the left.

This configuration has been implemented in the simulation: figure 5.7 and figure 5.8 show a sketch of this design. The result of the simulation is reported in figure 5.9, where the invariant mass distribution is shown. The efficiency in this case is 11.1% (4.3% with the requirement of a hit on the TC) and the invariant mass resolution is 575 keV, that becomes 500 keV by applying the vertex constraint. This result is better than the first target design and it is also more reliable, since the bellows, on which there is not much control in the simulation, does not have a big impact on the measurement. However, this configuration has been finally discarded since removing the bellows cap is not trivial and can affect the MEG II calibration setup.

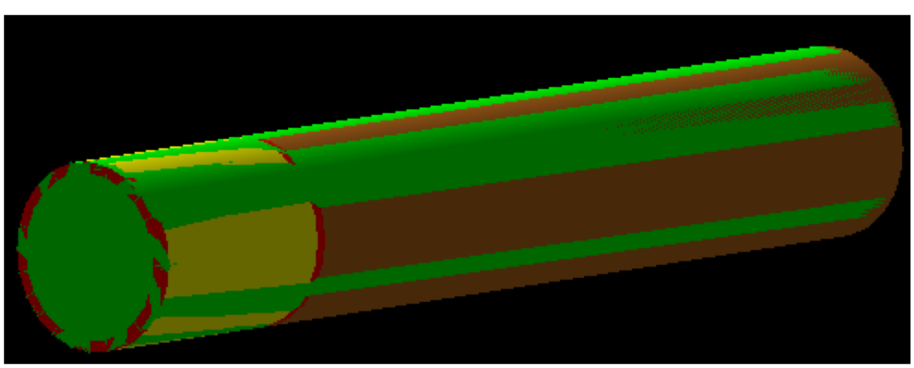

Figure 5.7: GEANT4 design for the system with the extension. The yellow part indicates the Mylar extension, the brown part indicates the bellows.

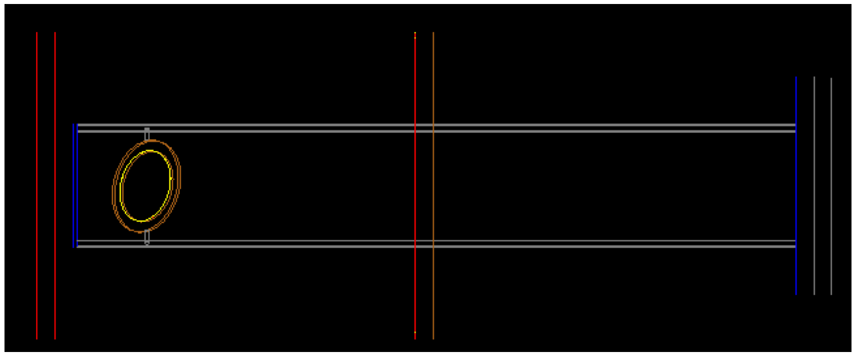

Figure 5.8: Wireframe design of the GEANT4 implementation of the Mylar extension viewed in the XZ plane. The gray part represents the Al stripes that runs along the CF tube.

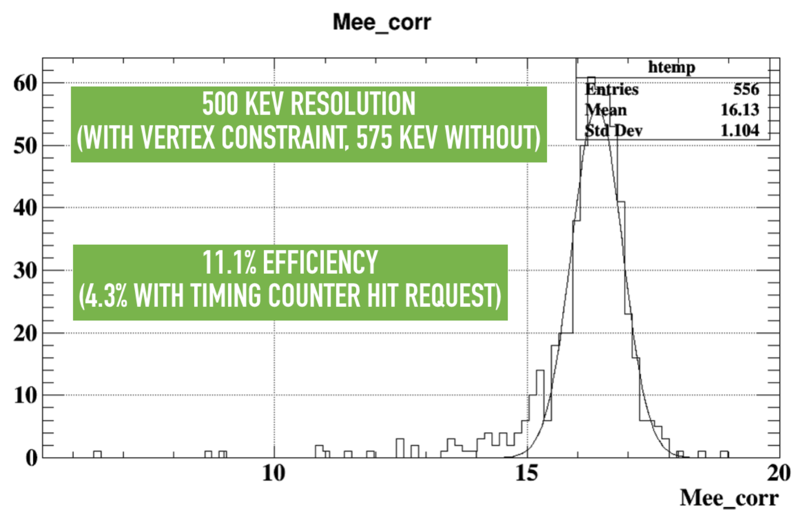

Figure 5.9: Invariant mass distribution from the simulation with the modified bellows configuration. The results obtained from this simulation are reported in the green boxes.

CF tube without bellows

An alternative design has been studied, in which the bellows is completely removed and the CF tube is larger, in order to keep the particles in vacuum as much as possible. In this case the X(17) data taking is incompatible with the MEG II data taking, because without the internal bellows the CW beam line cannot be moved in and out the COBRA volume when it is sealed during the muon beam data acquisition. Figure 5.10 shows the drawing of this new target region, which is the definitive one chosen for the X(17) measurement. The target, the substrate and the support structure with the metallic bar and the flange are the same as the first design, and the only thing that changed is the CF chamber. Its diameter is now 260 mm, with a minimal safety separation from the CDCH internal volume, and its length and thickness are 250 mm and 400 μm respectively. The simulations that I will describe in section 5.1.3 and section 5.1.4 led to the final choice of the material, slant angle of the target, thermal load, and cooling. The support and the substrate are made with Cu to improve the heat dissipation with a small impact on the resolution. Particular care has to be taken in the Li_2O/Cu interface, since there is the risk of detaching of the target. The optimal slant angle of the target to maximize the resolution is 45° around the x axis. The risk of detachment limits the thermal load well below 5 W, with a safe choice being 1 W (which means running with a 1 μA proton current), making the use of an eventual external cooling superfluous. However this is not a problem, since as I will show in section 6.4 the DAQ time needed to reach a good significance is of the order of few days and can largely fit in the available period.

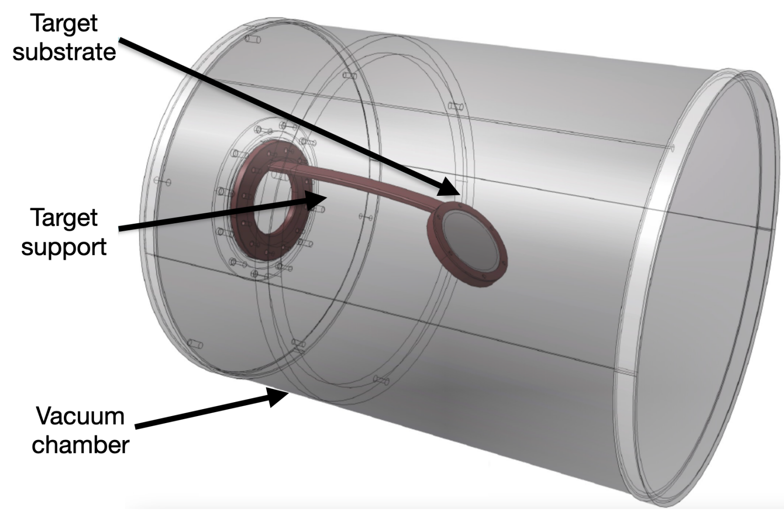

Figure 5.10: Drawing of the design with the large CF tube.

5.1.3 Heat dissipation

After the decision of the final design of the new target region the heat dissipation simulations have been repeated and improved. Figure 5.11 shows a simulation of the heat on the target with the new design. The substrate and support structure are made of Cu, since it is more efficient than Al in heat dissipation. This solution is viable since this design improves the overall resolution with respect to the previous design, and the worsening of this parameter coming from the use of Cu instead of Al is not crucial.

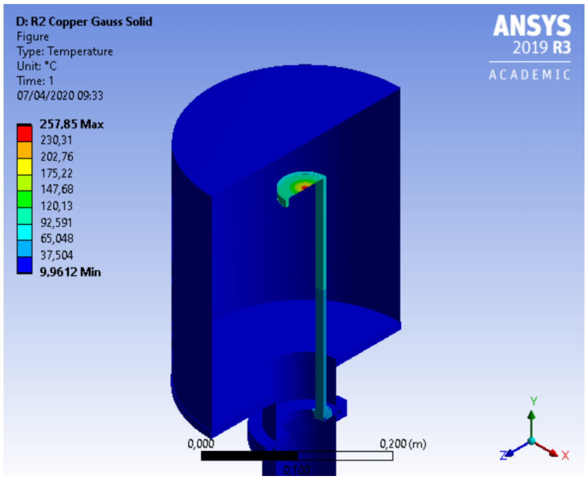

Figure 5.11: Simulation of the heat dissipation with the final design of the target region. Here no external cooling is assumed.

Finite element analysis

The final and more detailed study of the heat dissipation is based on Finite Element Analysis (FEA). The thermomechanical analyses have been performed considering the model reported in figure 5.12. The considered thermal load is 5 W distributed with a Gaussian on a 25 μm thick Cu substrate, which is optimal in terms of resolution. The 5 W thermal loads correspond to a 5 μA proton beam, assuming that the proton loses all its energy: this is a reasonable assumption since the energy loss for 1 MeV protons is $\sim$ 400 MeV/cm and $\sim$ 1000 MeV/cm in Li_2O (the 10 μm target) and Cu (the 25 μm substrate) respectively.

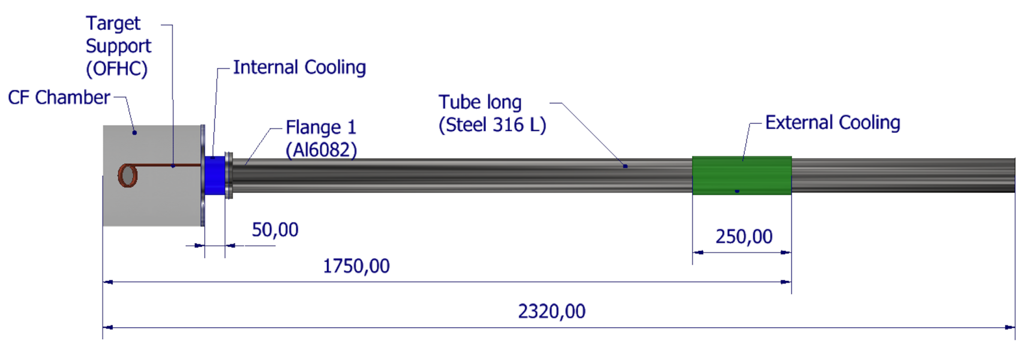

Figure 5.12: FEA model with the possible internal/external cooling in blue/green.

Since the target is tilted by 45° around the x axis, the Gaussian distribution of the load is characterized by $\sigma_x = 2.5\sqrt{2}$ mm and $\sigma_y = 2.5$ mm. The natural convection is applied on the CF chamber flange connected to the beam line ($H_c = 3.5$ W/m^2 °C), and the presence of an external cooling system is simulated with a low temperature fixed on a defined surface. Since the convection is dominant, the radiative cooling is not considered in the simulation. The structural part of the thermomechanical simulation is performed considering a fixed support in the position where the hypothetical external cooling is placed. Moreover, the effect of gravity and thermal stress are included.

Three different cooling configurations have been investigated:

- Case A: no cooling system;
- Case B: internal cooling (inside COBRA volume);
- Case C: external cooling (outside COBRA volume).

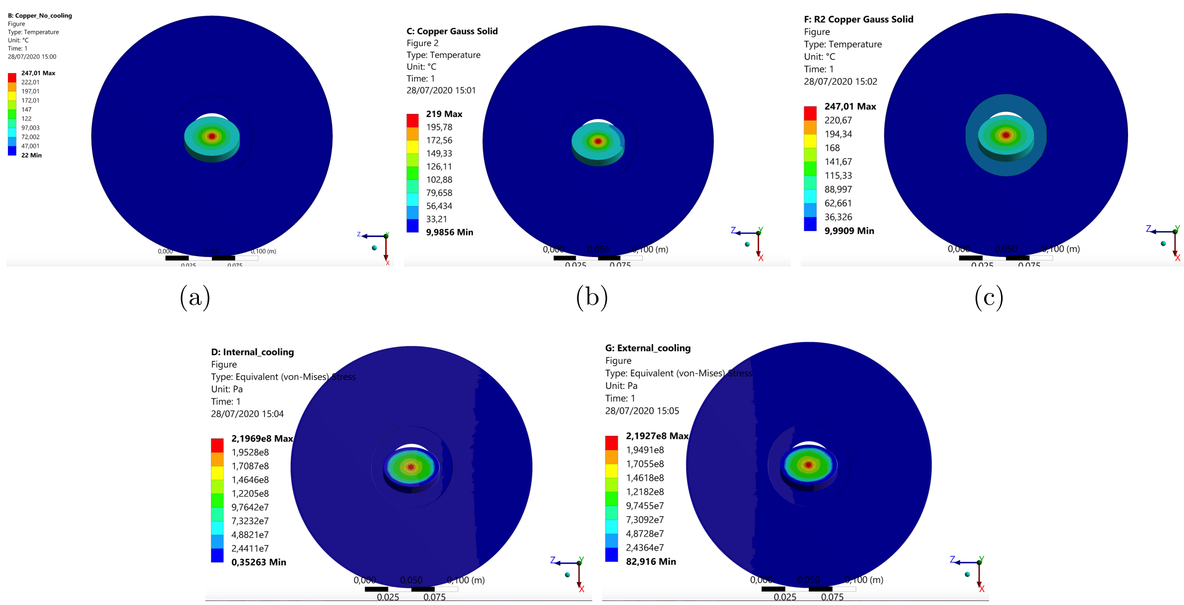

(a) (b) (c) (d) (e)

Figure 5.13: (a) Maximum temperature with no cooling. (b) Maximum temperature with internal cooling. (c) Maximum temperature with external cooling. (d) Maximum Von Mises Equivalent Stress with internal cooling. (e) Maximum Von Mises Equivalent Stress with external cooling.

The main results of the thermomechanical simulations are summarized in table 5.3. The table reports the maximum temperature reached, the equivalent stress on the target and its deformation. Here the maximum stress turns out to be higher when the maximum temperature is lower, because in that case the thermal gradient is concentrated in a smaller region and consequently there are greater differences between adjacent areas.

Moreover the external cooling (case C) results in the same peak temperature of the no cooling configuration (case A), thus the stress and deformation distributions are identical: therefore these values are reported only for case C. The results calculated with the ANSYS Mechanical module are reported in figure 5.13.

	T_{max} [°C]	Eq Stress [MPa]	Def [mm]
Case A	247.01		
Case B	219.00	219.69	0.92
Case C	247.01	219.27	0.86

Table 5.3: Maximum temperature, stress and deformation in the three different cooling scenarios.

All cases have been verified through dedicated reaction probes to check the heat dissipated in each condition. In the three cases analyzed the realization of the apparatus is feasible in terms of temperature and stress distribution.

Interface between target and substrate

The study of the thermomechanical behavior of the interface between the Cu substrate and the Li_2O is crucial to verify the possibility of the detachment of the target due to the stress. A detailed model was developed to simulate this possibility, as showed in figure 5.14. The 10 μm thick Li_2O target properties used in this model are reported in [141], and the yield stress ranges of considered materials are reported in table 5.4.

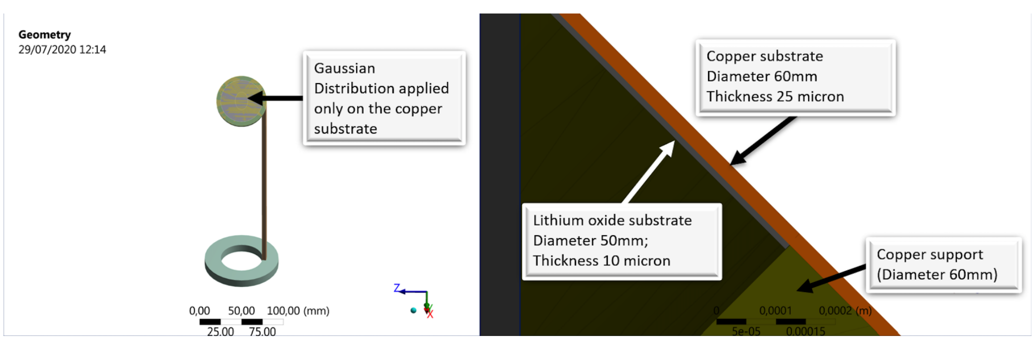

Figure 5.14: Detailed model used for the simulation of target detachment.

Copper (OFHC)	69 – 365 MPa
Li_2O	235,96 – 281.64 MPa

Table 5.4: Yield stress range for oxygen free copper and lithium oxide.

Figure 5.15 shows the stress distributions. From these numbers emerges that the stress, both the Von Mises equivalent (a quantity that predicts the yield of ductile materials under complex loading) for the Cu structure and the frictional stress on the interface, is higher than the safety values for tensile and compressive failure shown in figure 5.16.

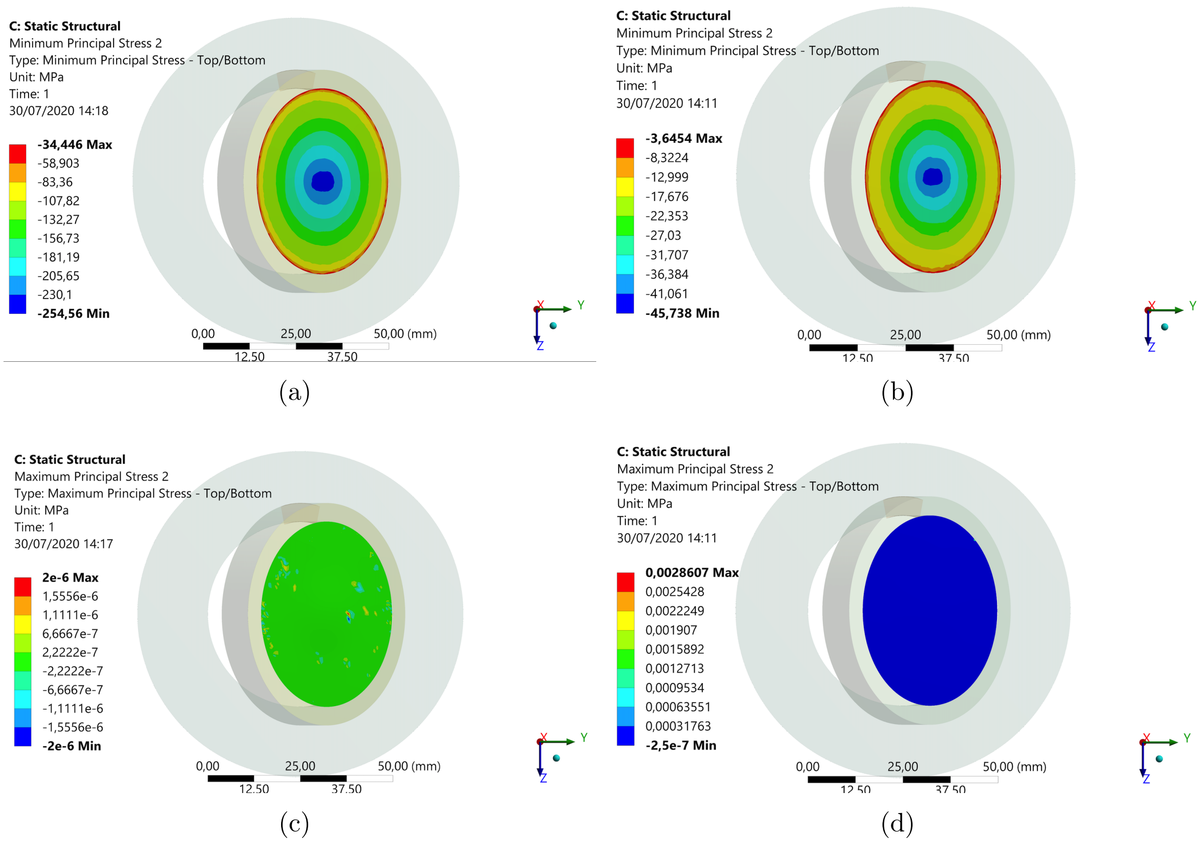

Figure 5.15: Minimum (a,b) and maximum (c,d) stress on Lithium Oxide for 5 W (a,c) and 1 W (b,d) thermal load.

Cu and Li_2O are respectively ductile and brittle materials. The plasticity of a ductile material prevents sudden breakage, while a brittle material breaks instantly when the elastic limit is exceeded. The yield stress value for Li_2O, unlike for Oxygen Free Cu (OFHC), is not available in literature: it has been deduced from experimental data available in [142] using the Hook's law. The stress calculated from this detailed model is higher with respect to the one calculated previously: this may be the consequence of using a reduced model as was done before. A reduced model is characterized by a reduced accuracy in the temperature distribution and thermal expansion evaluation, due to a not realistic heat dissipation and thermal inertia of the whole system.

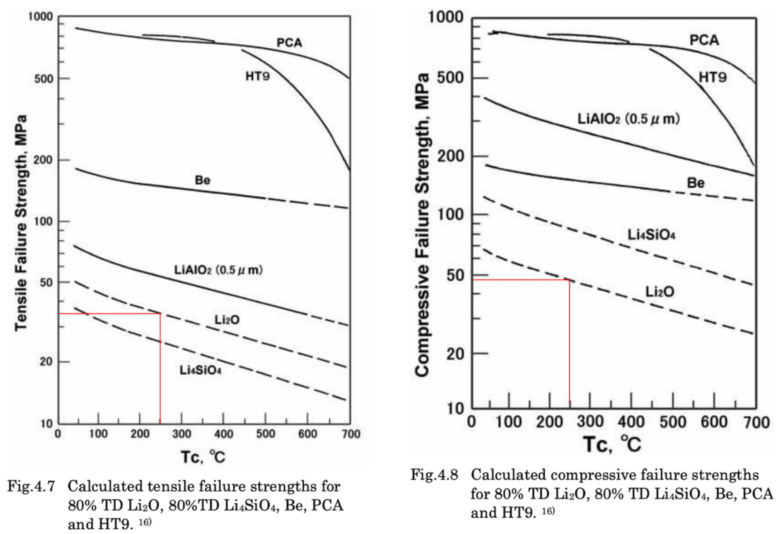

Figure 5.16: Yield stress values for Li_2O [143].

Figure 5.17 reports all the results for the simulations with the detailed model, showing the temperature distributions, total deformation, equivalent stress and frictional stress in the case of 5 W and 1 W thermal loads. All the numerical results are summarized in table 5.5. From the figures emerges that the stress distribution is concentrated in the target center, which may indicate that the resistance of the substrate is not sufficient. In fact, by removing Li_2O from the simulations, the stress on the Cu substantially decreases. In addition, using the properties reported in the literature for Li_2O with 80% theoretical density, the stress decreases also in the oxide itself.

P	T	Def	Eq Stress	Frc Stress	Min Stress	Max Stress
5 W	239.9 $°C$	0.524 mm	250 MPa	2.2 MPa	-254.6 MPa	2×10^{-6} MPa
1 W	55.92 $°C$	0.082 mm	71.21 MPa	0.288 MPa	-45.7 MPa	0.0028 MPa

Table 5.5: Results of the detailed simulation.

In the 5 W configuration the stress limit is exceeded both in Cu and Li_2O. Since the material nature is different, the Li_2O stress is expressed by the Coulomb-Mohr equivalent (a quantity that predicts the yield of brittle materials with a compressive strength higher than the tensile strength). Using the Coulomb-Mohr failure criteria in the 5 W configuration and assuming a Li_2O compressive strength of 48 MPa (value quoted in literature but not confirmed), it is possible to evaluate the safety factor SF to prevent damages:

$$\frac{1}{SF} = \frac{2 \times 10^{-6}}{35} + \frac{245.56}{48} = 5.11 \Rightarrow SF = \frac{1}{5.11} = 0.19 \ll 1. \tag{5.1}$$

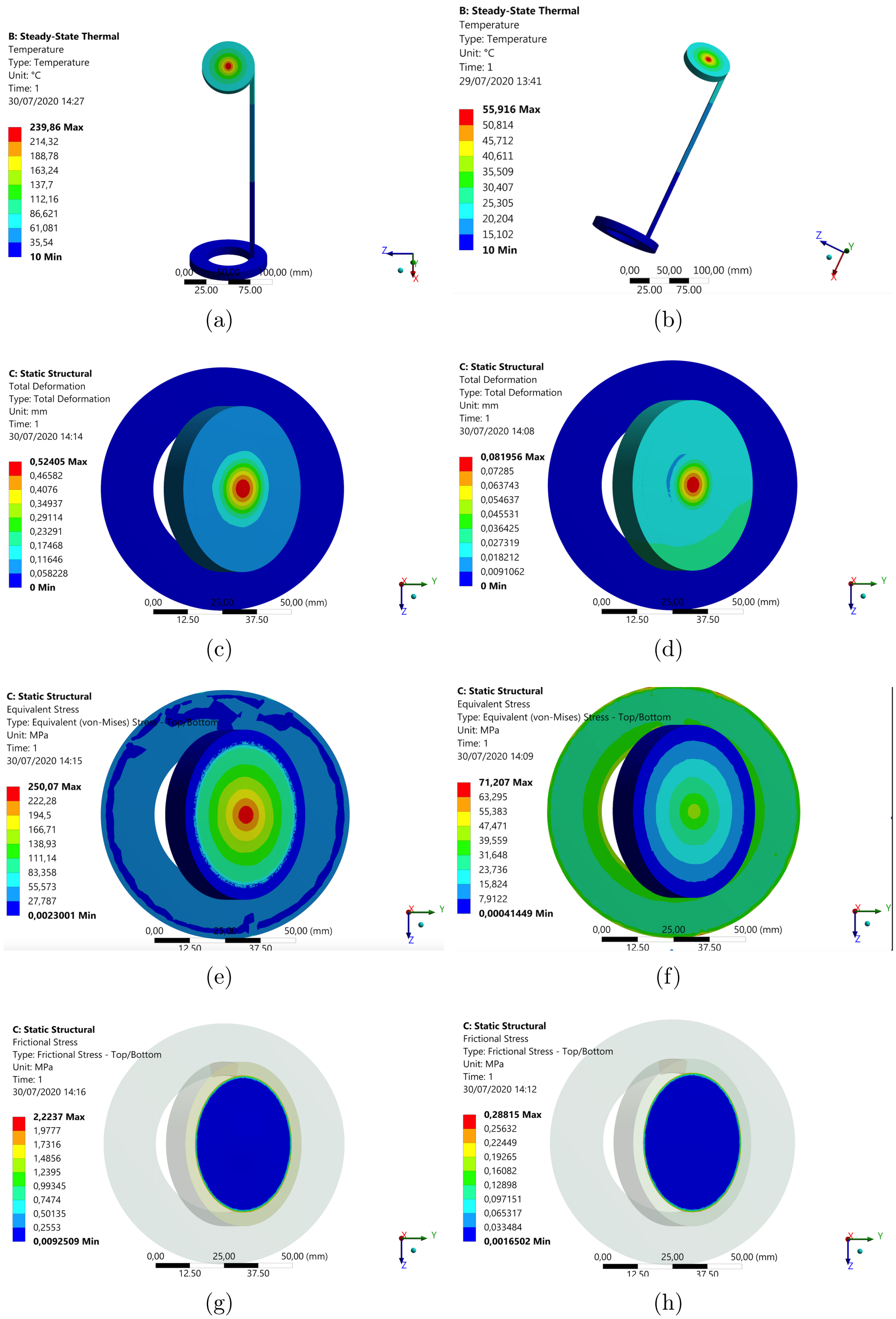

Figure 5.17: Temperature distribution (a,b), total deformation (c,d), equivalent stress (e,f) and frictional stress (g,h) from the simulations with the detailed model. The results are reported both for 5 W (a,c,e,g) and 1 W (b,d,f,h) thermal loads.

This means that, if the Li_2O properties quoted in literature are confirmed, the risk of failure in this configuration is high: the safety factor should be ≥ 1.25 for static application.

For a 1 W thermal load the previous calculation gives a result closer to the requirements:

$$\frac{1}{SF} = \frac{0.0028}{35} + \frac{46}{48} = 0.958 \Rightarrow SF = \frac{1}{0.958} = 1.04 > 1. \tag{5.2}$$

The result of this calculation is heavily affected by the Li_2O properties, on which the literature is not conclusive. Anyway, the 1 W thermal load looks almost safe even in the worst case scenario, meaning that the CW proton current has to be limited to 1 μA. Due to the uncertainties concerning the materials properties, an experimental test to validate the final geometry of the simulated target is needed.

5.1.4 Resolution and efficiency

The simulations of the $^7\mathrm{Li}(p, e^+e^-)^8\mathrm{Be}$ reaction have been performed also for the new target region design with the large CF chamber. Notice that these simulations use a e^+e^- pair tracking algorithm based on reconstructed hits, and not on MC hits as it was for the first target design. Moreover, an event selection is applied to the analysis to exclude events that are not related to the X(17) decay.

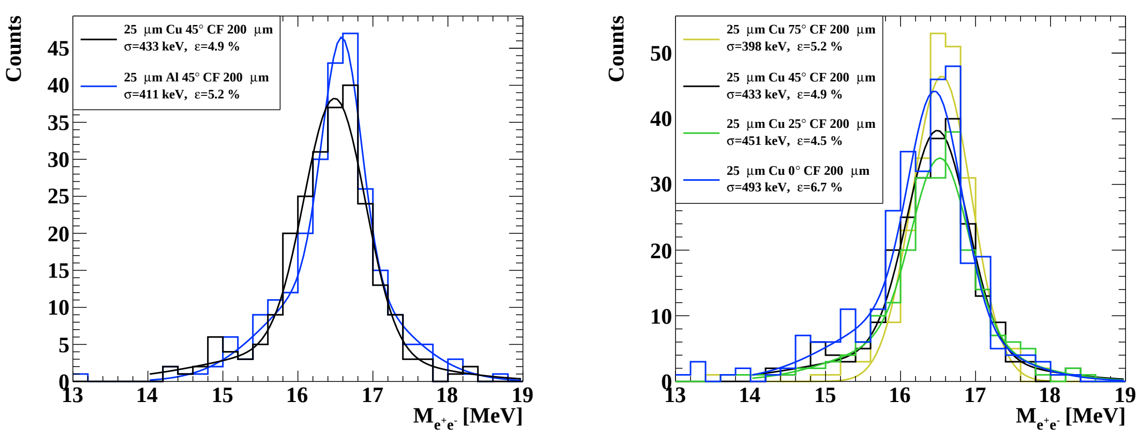

(a) (b)

Figure 5.18: Resolution with different target substrate materials (a) and rotation angles around the horizontal axis (b).

First of all, the accepted events have to include both a positron and an electron; then, a χ^2 cut is applied to the momentum and angle distributions, so that only the reconstructed particles with characteristics similar to the MC truth are considered; finally, the vertex constraint is applied, so that the two tracks are forced to cross the target plane in the same point. The combined application of these energy and vertex cuts reduces the tail of the invariant mass distribution, that can be well fitted by a double Gaussian. The resolution quoted here is the core width of the distribution, conversely to the width of the single Gaussian used in the first target design resolution estimate. Figure 5.18 summarizes the results obtained for different target rotation angles and substrate materials. It turns out that the best choice in terms of resolution is Al and the best target angle is 75° around the x axis. Since the difference between Al and Cu is not relevant, the latter was considered for the final configuration because of its better heat dissipation properties. Also the difference between 45° and 75° is not relevant, and a 45° rotation angle was selected in the final configuration for simplicity.

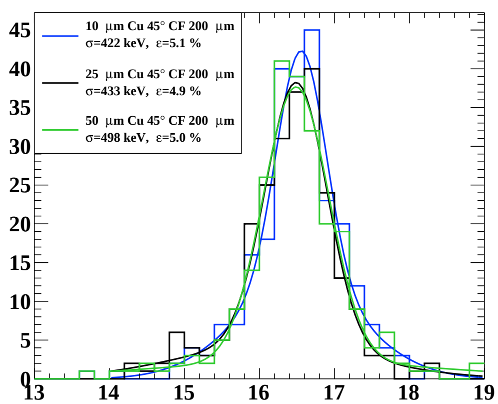

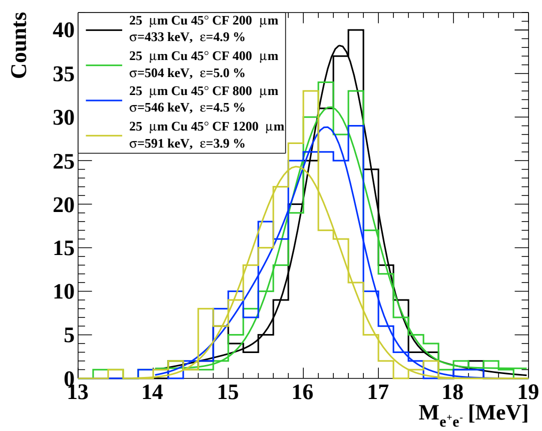

Figure 5.19: Resolution with different target substrate (a) and CF chamber (b) thicknesses.

Technical problems may arise in the construction of the pieces needed for the measurement. For example a 25 μm thick substrate may be not trivial to build, and a 200 μm thick CF chamber may be not sturdy enough to bear the vacuum needed. Therefore the simulations account also for different substrate and CF chamber thicknesses, as shown in figure 5.19. The 10 μm substrate and 200 μm CF chamber are not viable solution: the first one cannot efficiently dissipate the heat from the proton beam, the second one is not sufficiently stable from the mechanical point of view. The final choice was then 25 μm and 400 μm, with a resolution slightly worse but still acceptable. Moreover, the resolution worsening with the 50 μm substrate and the 800 μm CF chamber is not dramatic, thus it can be a viable choice in case the final configuration fails the mechanical test. The 1200 μm thick CF, instead, looks worse both from efficiency and resolution point of view, and the distribution is biased towards a lower invariant mass of the pair, indicating a possible energy loss of the particles in the chamber wall.

Figure 5.20 shows the result of the simulation performed with the final configuration: 45° target rotation around the x axis, 25 μm thick Cu substrate and 400 μm thick CF chamber. The resolution and efficiency are the following:

$$\sigma = 504\,\mathrm{keV}, \qquad \varepsilon = 5.0\%\,(2.0\%\ \text{with pTC}) \tag{5.3}$$

This configuration is satisfactory both from heat dissipation point of view, thanks to the use of Cu, and from resolution point of view, since it is a factor ~ 2 better with respect to the Atomki detector. Notice that the efficiency decrease with respect to the simulations in section 5.1.1 is due to the use of reconstructed hits instead of MC hits.

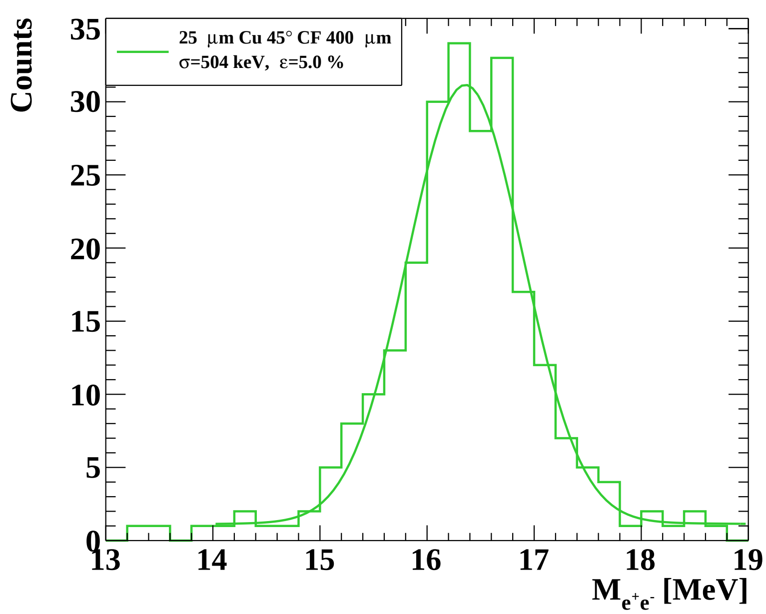

Figure 5.20: Results obtained from the simulation with the final design of the target support.

Impact of the trigger on the efficiency

The choice of the trigger for the X(17) events has consequences on the efficiency, which is considered as the ratio between the number of reconstructed events and the total number of simulated events. There are several possibilities to choose from:

- CDCH self trigger on a programmable number of hits US and/or DS;
- pTC trigger on 1 or more tiles;
- CDCH+pTC hit.

The CDCH self trigger is the one that guarantees the highest efficiency, but it does not provide the time reference for the tracking, which needs the pTC. Moreover, the cosmic rays rate is comparable to the IPC rate (both of order of $10^1 - 10^2$ Hz), and without an external trigger it is difficult to reject the cosmic rays background. Having a pTC only trigger with one or more tiles hit has the drawback of triggering on particles different than the IPC pairs, such as electrons from Compton scattering of the photons in the detector.

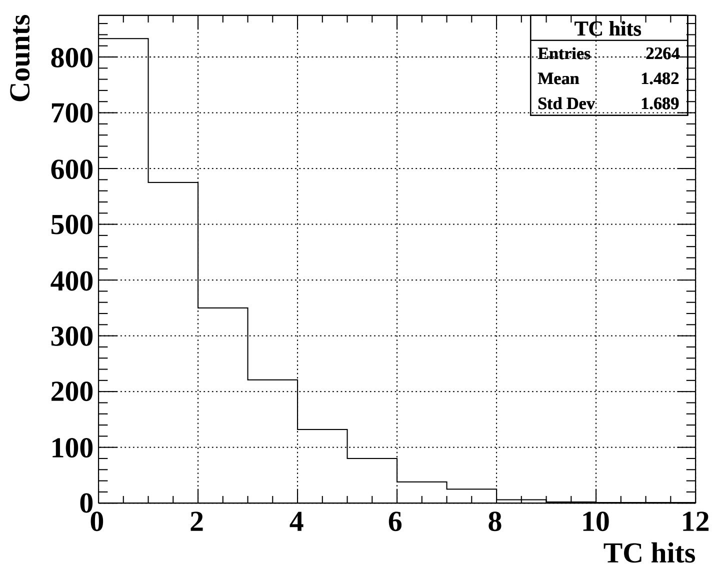

Figure 5.21: Distribution of the number of reconstructed hits on the TC in one event

The optimal choice would be having a CDCH multiplicity trigger in coincidence with 1 hit in the pTC. This way the cosmic rays background is reduced and the information on the timing is available. Moreover, using the pTC in the tracking can further improve the performance. By requiring 1 hit on the pTC the efficiency decreases by a factor ~ 2.5, which becomes a factor ~ 3.2 by requiring 2 hits. Figure 5.21 shows the distribution of the number of hits on the pTC in one event, that is 1.5 on average.

5.2 Background estimate

A deep understanding of all the background sources is crucial in this measurement. A comprehensive and reliable theoretical model, in fact, can validate the hypothesis that the anomaly is generated by a new physics signal and not by the combination of the background sources. The first step in the background implementation in the simulation code was to consider only the IPC background from M1 transitions in the 18.15 MeV resonance, which is the dominant one. The model used in this case is the Rose's one, described in section 1.1.2. This model is incomplete, thus for the final version of the simulation that included the definitive target design, it was replaced by the Zhang-Miller model described in section 1.3.1. Moreover, the background events from EPC were also included the simulation. The background from cosmic rays, instead, has been considered negligible since it can be suppressed by the use of the pTC as an external trigger.

5.2.1 Internal Pair Creation

Simulations with Atomki photon spectrum

The first step in the improvement of the IPC background simulation was to take into account not only the 18.15 MeV photons in the resonance but the whole photon spectrum produced in the apparatus. The target that will be used in MEG II will be thicker than the one used at Atomki, to let the proton scan all the resonance. The energy loss inside it can make the proton reach energies below 1 MeV, but even in this case the nuclear reactions in the atoms of the target, including possible contamination, take place in a region of the spectrum far from the region of interest of 18.15 MeV. For example, for $E_p = 1$ MeV, the lines in the photons spectrum are constrained by the kinematics to be below 12.5 MeV for ^{27}Al, 9.9 MeV for ^{65}Cu and 1.5 MeV for ^{16}O. For this reason the photon spectrum measured at Atomki, shown in figure 1.12, will be similar to the one expected in the MEG II apparatus, and thus it can be used to randomly generate the photon energy in the simulation.

A reproduction of this spectrum is reported in figure 5.22, together with the result of the random generation of the photon energy that was used to simulate the IPC background. The region of interest of this spectrum is defined as 5σ around the 18.15 MeV resonance, where σ is the resolution on $E_{e^+} + E_{e^-}$, which is ~ 250 keV (originally estimated using the configuration of the target labeled as 013 in table 5.2).

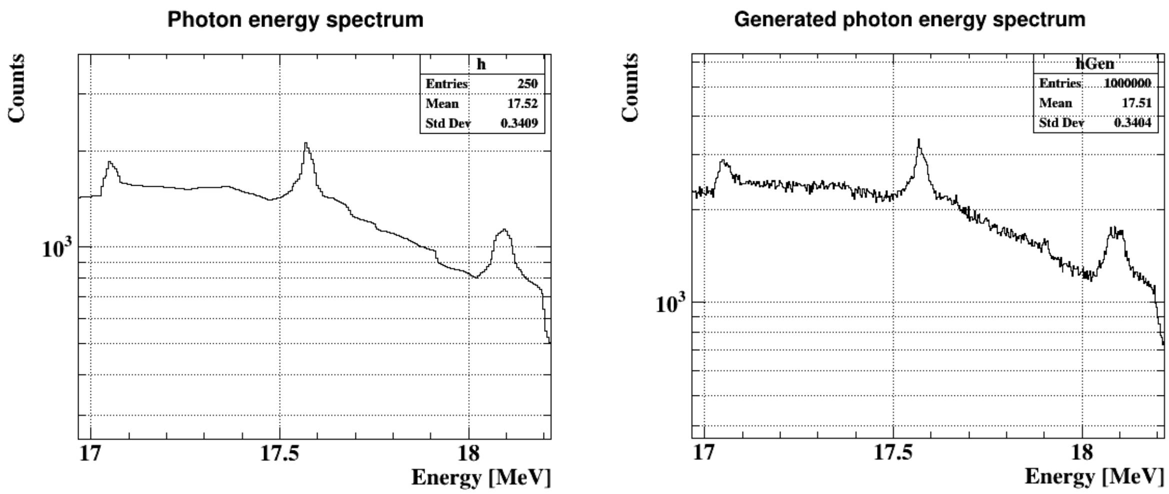

(a) (b)

Figure 5.22: Actual fraction of the spectra in figure 1.12 used for the generation, which is from $E_\gamma = 18.21 - 5\sigma$ to $E_\gamma = 18.21$, where σ is the estimated resolution on the sum of the positron and electron energy.

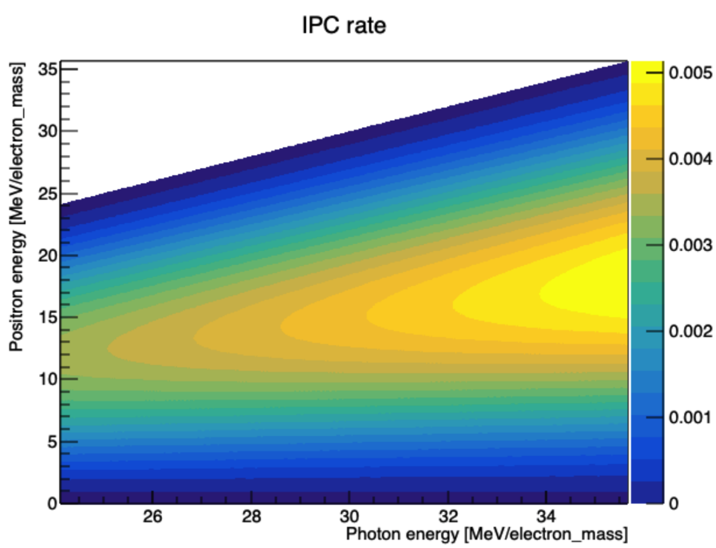

Figure 5.23: IPC rate from Rose's model $\Gamma(E^+, E_\gamma)$ for different values of positron energy E^+ and photon energy E_γ. The function is evaluated at $\cos\theta = 1$.

The IPC background is calculated generating photons in the target with an energy E_γ distributed following this spectrum. The positron energy is then randomly generated in the range 1 MeV$<E_{e^+}<E_\gamma - 2$ MeV. Using the generated (E_{e^+}, E_γ) couple it is possible to generate the e^+e^- pair using the hit or miss algorithm with a probability determined by the value of $\Gamma(E_{e^+}, E_\gamma)$ predicted by Rose in [4].
This probability is normalized to its maximum, which is for maximum E_γ, $E_{e^+} = E_\gamma/2$ (as showed in the plot in figure 5.23), and $\cos\theta = 1$ (as showed in the angular distributions of the IPC measured at Atomki and reported in section 1.2).

Figure 5.24 shows the number of signal and background events simulated in 0.4 hours of data taking at 1 μA of proton current. Here the IPC is simulated using the photon spectrum measured at Atomki. Even after a short amount of time the signal starts to emerge from the background, even though with a significance lower than 2.5. The simulation of the distributions with a more significant signal bump can be found in the significance study in section 6.4, where the updated background model and the final design of the target region are used.

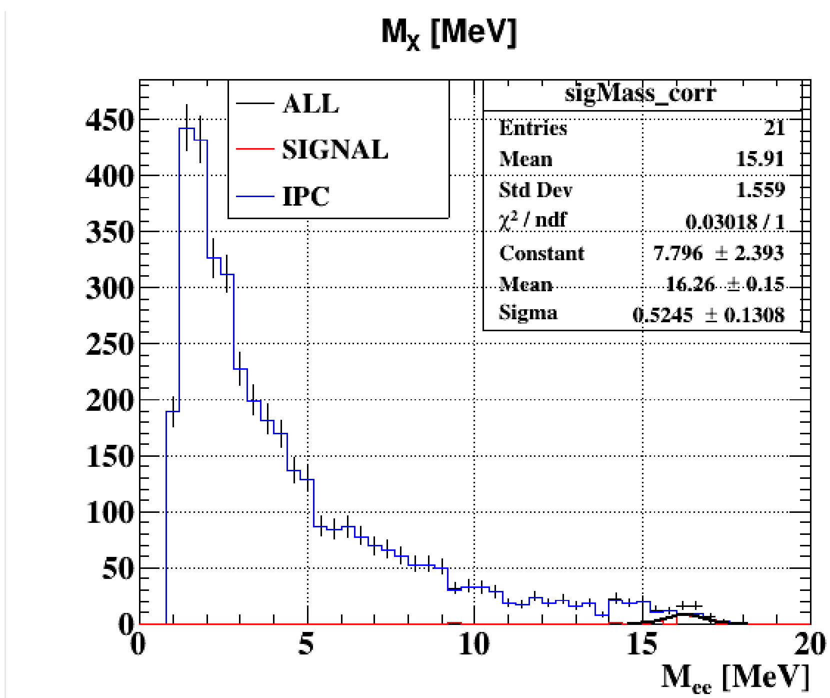

Figure 5.24: Signal and background distribution after 0.4 hours of data taking at 1 μA of proton current.

From the calculations in appendix A the rate of photons produced in the resonance is 1849 s^{-1} for a 1 μA proton beam. Using the whole photon spectrum and not only the

18.15 MeV resonance requires a normalization of the rate. The normalization factor is estimated as the ratio between the integral of the e^+e^- total energy spectrum and the integral of its peak around the resonance. The pair energy is used instead of the photon energy since in this way the IPC rate dependence on the photon energy is automatically taken into account. The resulting normalization factor in this configuration is $N = 10.1$, thus the expected photon rate from the calculations becomes, in this fraction of the spectrum, $R_\gamma = 18675\ s^{-1}$

Zhang-Miller model implementation

A further improvement with respect to the use of the photon spectrum measured at Atomki is the implementation of the model published by Zhang and Miller in [1]. This model provides a description both for the photon production and the e^+e^- pair cross sections. The photon cross section model has parameters that are obtained from a fit performed on old data. Thus, with a new measurement of the photon spectrum up to approximately 18.5 MeV (that can be done with the MEG II detector), it is possible to further improve the fit parameters estimate. This measurement can be carried out using the LXe detector or an auxiliary Lanthanum Bromide LaBr3 calorimeter used for MEG II calibrations. This detector can also be used to continuously monitor the photon spectrum during the X(17) measurement, allowing to know the status of the target degradation.

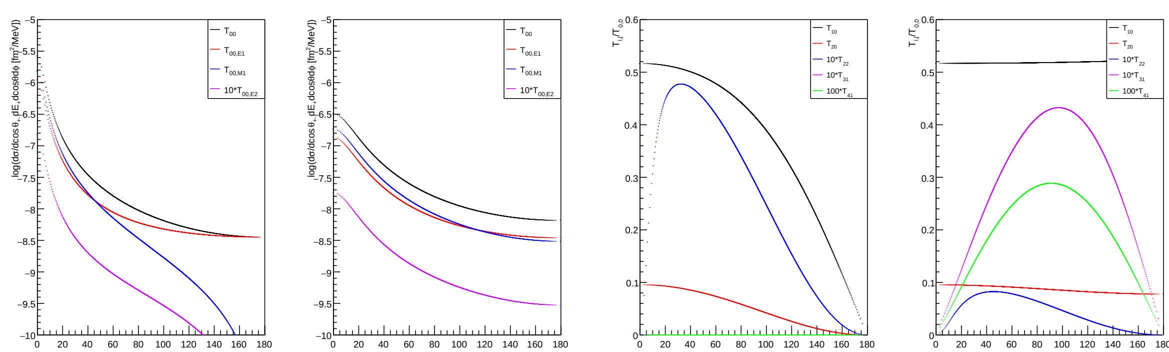

(a) (b)

Figure 5.25: Reproduction of the pair cross section coefficients obtained with the IPC generator implemented in the MEG II simulation (to be compared to figure 1.20 (a) and 1.20 (b)).

The electron-positron pair is simulated following the pair cross section provided by the model, which is a 4D quantity $\mathrm{d}\sigma/\mathrm{d}\cos\theta_{+-}\mathrm{d}\cos\theta\mathrm{d}E_+\mathrm{d}\phi$ (refer to figure 1.18 for the definition of the angles). A reproduction of the pair cross section obtained with the IPC model implemented in the MEG II simulation is reported in figure 5.25, and is in agreement with the model predictions. Figure 5.26 shows the shape of the 1D cross sections obtained by integrating out 3 of the 4 variables on which the 4D cross section depends.

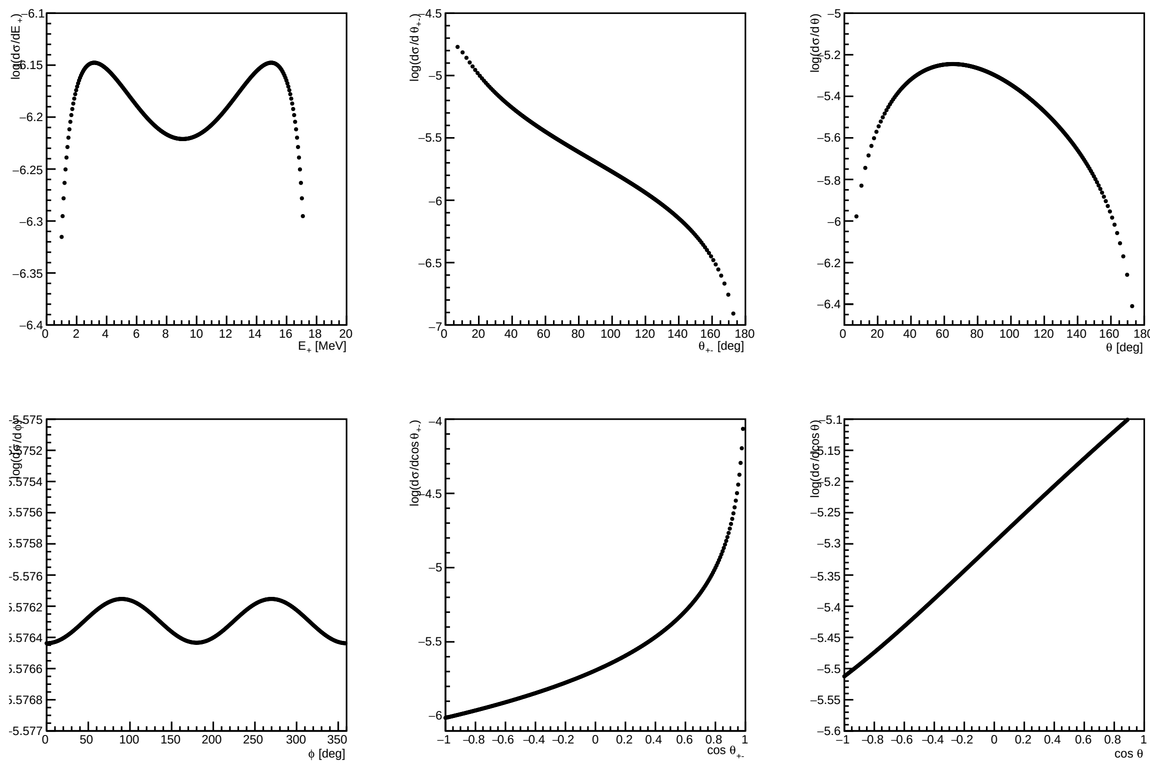

Figure 5.26: 1D cross sections obtained by integrating out 3 variables from the 4D cross section provided by the Zhang-Miller model.

The IPC generator implemented is based on the hit or miss algorithm. Running a simulation with this improved setup gives as a result the 4 generated variables distributions, in agreement with the ones from the model as figure 5.27 shows, proving the reliability of the generator. The only difference is in the ϕ distribution: this is due to the fact that in this case the proton energy is not fixed as it was in figure 5.26, but it is itself generated considering a variable energy loss that depends on the photon cross section given by this model. I will give more details about the proton generation in section 6.2 when I will show a refined estimate of the IPC rate. The angular and invariant mass distributions of a IPC MC production performed with the upgraded software are shown in figure 5.28.

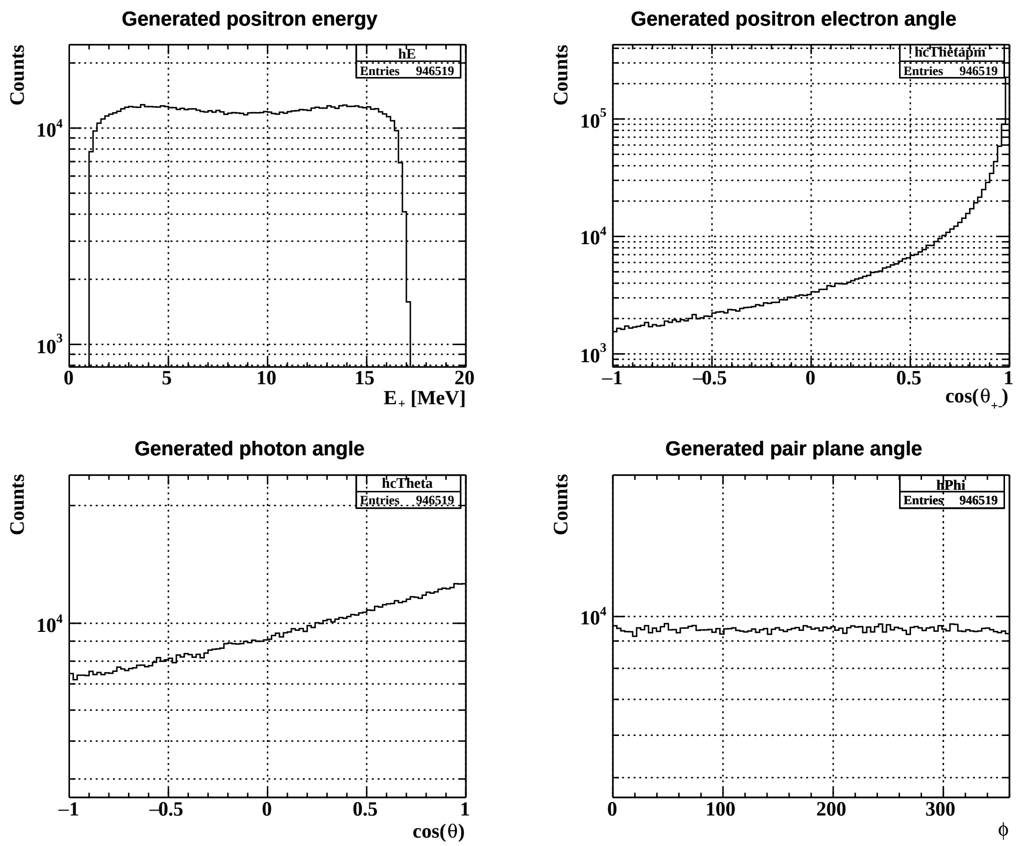

Figure 5.27: Pair energy and angles distributions from the IPC generator.

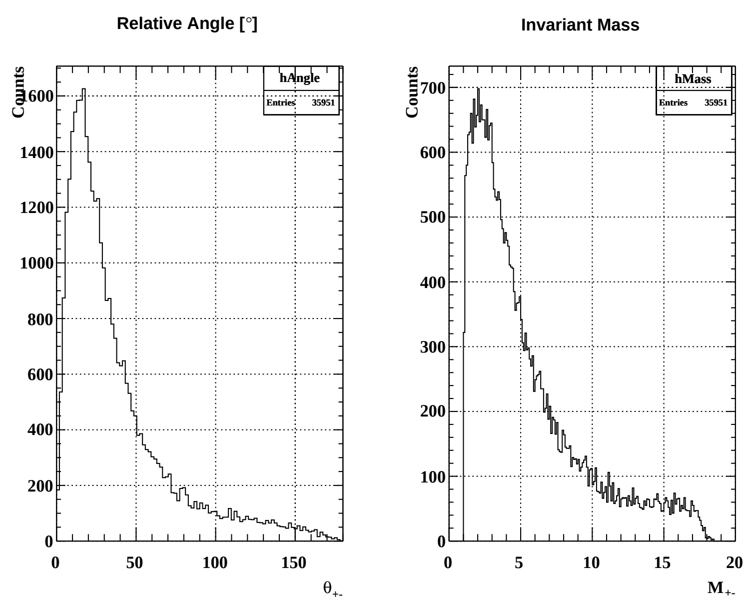

Figure 5.28: Angular and invariant mass distribution of reconstructed IPC pairs.

5.2.2 External Pair Creation

There is the possibility that a photon produced in the proton capture inside the Li_2O target converts into a e^+e^- pair interacting with the experimental apparatus nuclei. If that pair is in the detector acceptance and has an energy in the signal region it can be a source of background. An event of this kind is called External Pair Creation (EPC) and, even though its occurrence is dominant at small pair separation angles, there is a small chance to observe it at large angles. A generator for the EPC was then implemented in the simulation code: its first version generated only isotropically distributed photons in the 18.15 MeV resonance, while its final version generates photons following the Zhang-Miller cross section, that defines both the energy and the direction of the particle.

First estimate

The impact of EPC in the X(17) measurement at MEG II has been simulated at first only for 18.15 MeV photons, in agreement with the first IPC model. The number of photons to simulate in order to be able to compare the numbers between EPC and IPC background events can be calculated as follows:

$$N_\gamma = R_\gamma \cdot \mathrm{T}, \qquad N_{\mathrm{IPC}} = R_{\mathrm{IPC}} \cdot \mathrm{T} \tag{5.4}$$

where T is the DAQ time in which a fixed number N_{IPC}^{sig} of IPC events in the signal region are detected, R_γ and R_{IPC} are the rates of the photons and the IPC events respectively, N_γ is the number of photons that we want to simulate in order to have N_{IPC}^{sig} events in the signal region and N_{IPC} is the total number of IPC events generated in the same time T. The number of photons to simulate in order to have $N_{IPC}^{sig} = 10$, for example, is:

$$N_\gamma = \frac{N_{\mathrm{IPC}} \cdot R_\gamma}{R_{\mathrm{IPC}}} \sim 8 \times 10^6 \tag{5.5}$$

In this first estimate the numbers used for the rates are the ones quoted in appendix A, while the resolution and efficiency used to calculate N_{IPC} are the ones obtained from a simulation with the first target design using a 50 μm thick Al substrate (configuration 015 in table 5.2). None of these simulated photons produces a background event in the signal region, where we expect $N_{IPC}^{sig} = 10$ IPC events. It is then possible to conclude that this kind of background does not give a noticeable contribution if confronted with IPC, at least in the estimate given for the first target design and the first simplified IPC model.

EPC study refinement

A simulation with increased statistics and improved target region and background model is needed to have a more accurate estimate of the EPC contribution. In section 6.3 I will give an estimate of the photon and IPC rates based on the Zhang-Miller model for the ^{7}Li$(p,\gamma)^8$Be and ^{7}Li$(p,e^+e^-)^8$Be reactions, respectively $R_\gamma = 12150$ s^{-1} and $R_{\mathrm{IPC}} = 38.8$ s^{-1}. Also N_{IPC} has to be updated by using the latest simulations with the large CF chamber target region. This value, in fact, depends on the resolution and efficiency calculated in section 5.1.4. The expected number of EPC events is better estimated by raising the value of N_{IPC}^{sig} to 1000 (instead of 10 as in the previous estimate), so to see how many of them can happen each 1000 IPC events in the signal region. The number N_{IPC} needed to have $N_{IPC}^{sig} = 1000$ is $\sim 2.0 \times 10^6$ by looking at simulations in section 5.1.4 so, using this number and the improved values for the rates, equation 5.5 becomes:

$$\frac{N_{\mathrm{IPC}} \cdot R_\gamma}{R_{\mathrm{IPC}}} \sim 6 \times 10^7 \tag{5.6}$$

For a conservative result the final choice for N_γ is then:

$$N_\gamma = 1 \times 10^8 \tag{5.7}$$

Such a large number of events to simulate is a problem both from computational time and disk space point of view, so the simulation has been performed using a bias factor on the photon conversion cross section in GEANT4. This artificially increase the interaction probability of the photon, allowing to simulate less events and have the same result.
The simulation of 1×10^6 photons with a cross section bias factor of 100 is equivalent to 1×10^8 photons. As a consistency check the number of reconstructed hits in the CDCH was estimated for different values of the cross section bias factor: figure 5.29 shows how the number of hits increases with the bias factor. The result is the same of the previous study: none of the simulated photons creates a pair that has invariant mass in the signal region. Most of them have energy <5 MeV, and none of them exceeds 10 MeV, as shown in figure 5.30. This plot shows the reconstructed pairs invariant mass with none of the selection cuts previously used in the analysis.

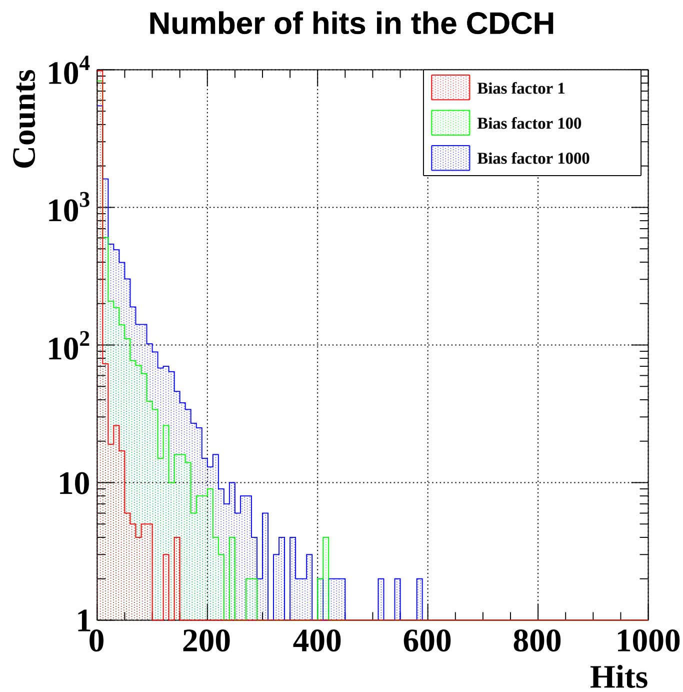

Figure 5.29: Number of CDCH reconstructed hits for three different cross section bias.

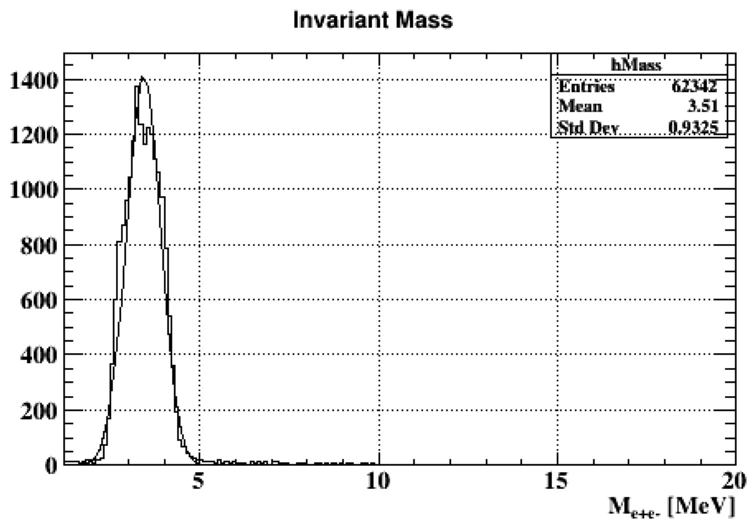

Figure 5.30: Invariant mass distribution of the EPC background. None of the usual analysis cuts is applied.

Chapter 6

Significance and DAQ time

After having defined the experimental setup and modeled the background it is possible to estimate the DAQ time needed for the measurement. This time is described in terms of significance, which is defined as the ratio between the number of signal events and the square root of the number of background events integrated around the expected signal region. The first estimate of the significance trend with the DAQ time was made for the first target design, using the simplified IPC model from the Rose theory and the rates estimated from the calculations. To improve this preliminary estimate the study was repeated with the final target design, the complete IPC background model and the rates calculated from a detailed simulation that takes into consideration both the photon cross section and the proton energy loss in the target.

In this chapter I will show the results of the study of the significance as a function of the DAQ time for both the first target design and for its definitive implementation.

My contribution in the work presented in this chapter consists in the development of the simulation for the proton energy loss in the target. I also calculated the significance trend with the DAQ time, based on the resolution and efficiency estimated from the signal and background simulations for both the first and the final target designs.

6.1 First target design

A preliminary estimate of the significance vs DAQ time was made by using the calculations in appendix A and the resolutions and efficiencies simulated in section 5.1.1 for the first target region design. The expected significance growth in time is extrapolated by scaling the number of signal and background events using the information given by the efficiency.

Figure 6.1 shows the significance as a function of the data taking time for the substrate thicknesses and materials studied in the first simulations. Here the proton current is assumed to be 5 μA. The study carried out in this section takes into account only the IPC resonant background for simplicity. The more detailed model of the background reported in section 5.2.1 will be taken into account for the studies on the final design, together with a more accurate estimate of the reaction rates.

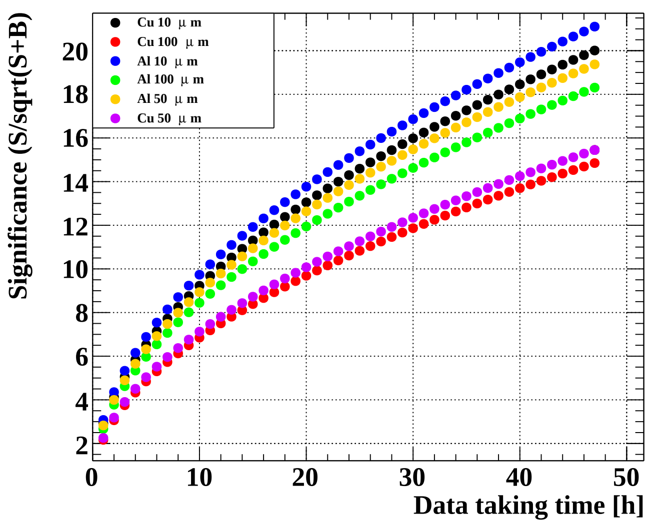

Figure 6.1: Significance vs data taking time from the simulations with a 10/50/100 μm Cu/Al target substrate and 5 μA current. The significance is calculated in a region of $\pm 2\ \sigma$ around the mean of the invariant mass distribution fit of the signal.

6.2 Proton energy loss and photon generation

From the Zhang-Miller photon cross section it is possible to generate the photon energy and the interaction depth of the proton. This needs the knowledge of the proton energy loss in Li_2O as a function of its position inside the target. This value was supposed constant in the previous calculations, but this is just an approximation, since the dependence on the proton energy is not negligible. The latest simulation developed for the X(17) measurement at MEG II includes a model that randomly generates the proton energy loss in the target from a Gaussian distribution. The μ and σ of this Gaussian are calculated from a GEANT4 simulation that consider the proton interactions in the Li_2O target and calculates its energy at every 0.5 μm step, as shown in figure 6.2. Here the average energy loss is 40.4 MeV/mm, in agreement with the average value used in the calculations in appendix A of 420 MeV/cm.

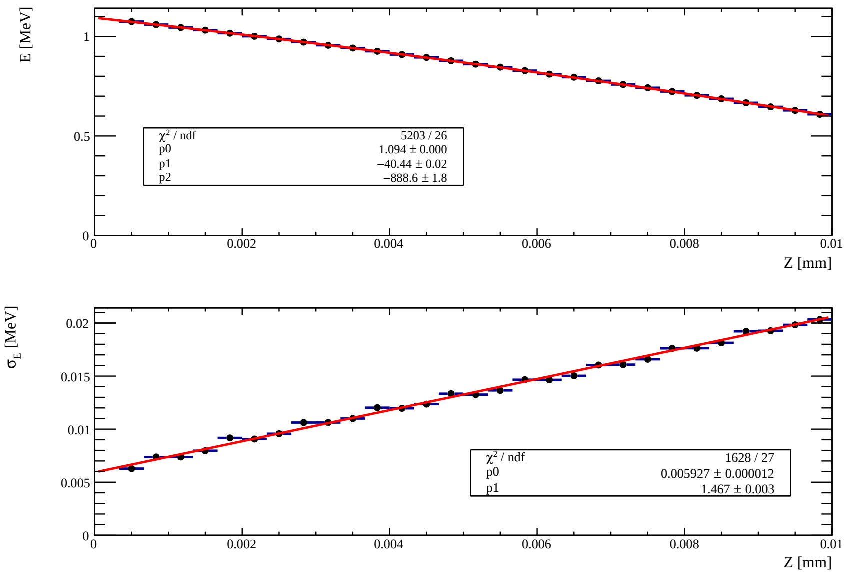

Figure 6.2: μ and σ of the Gaussian used to generate the proton energy loss in the target. These plots are obtained from a GEANT4 simulation.

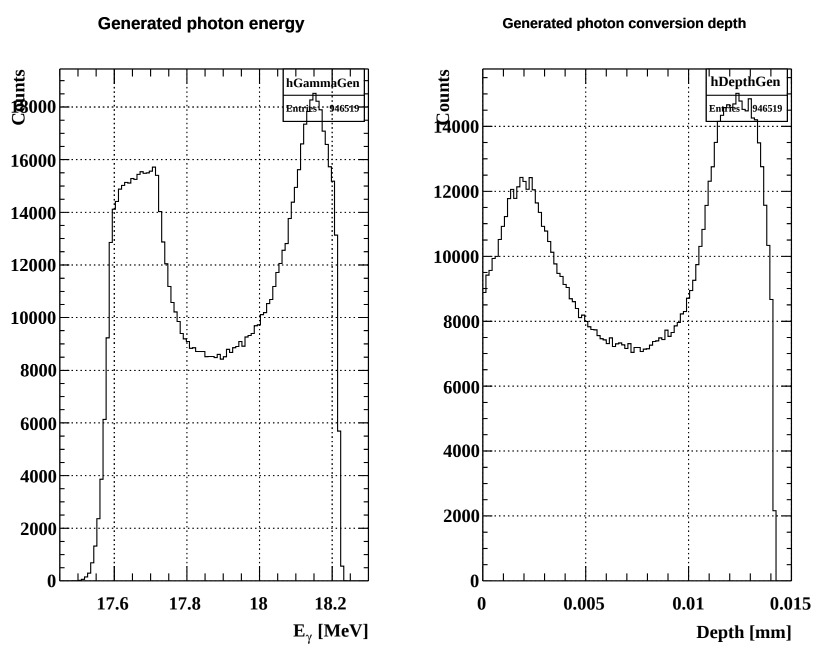

Figure 6.3: Left: generated photon (and proton) energy. Right: generated photon interaction depth.

The photon (and thus the proton) energy have been calculated from the randomly generated interaction depth using the randomly generated proton energy loss. The calculated value is then accepted or rejected with a probability determined by the photon cross section. Figure 6.3 shows the distribution of the photon energy and the conversion depth simulated with the IPC generator implemented in the MEG II simulation tool.

6.3 Production rates

With the IPC cross section described in section 5.2.1 it is possible to predict the rate of the reactions involved in the X(17) measurement. The first information needed is the photon production rate, which depends on the target thickness and the photon cross section. Figure 6.4 shows a simulation of the photon production rate as a function of the Li_2O thickness crossed by a 1.1 MeV proton. This rate increases when the thickness is more than 7μm: this happens because the proton enters the lower energy resonance at 17.6 MeV, as can be seen also in the excess on the right in the plot in figure 6.3. The target slant angle of 45° means that for the proton to cross 7 μm of Li_2O the target thickness has to be 5 μm. Nonetheless the following calculations will be carried out considering 10 μm of material crossed by the proton for immediate scalability.

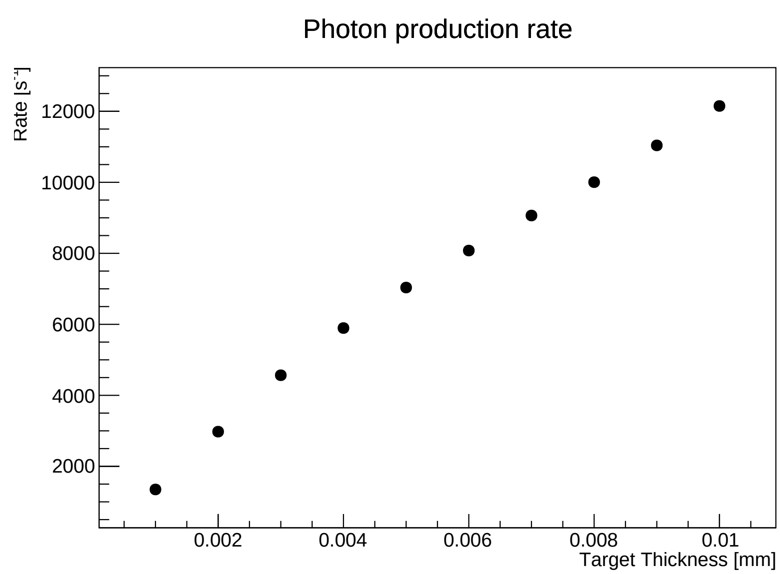

Figure 6.4: Photon production rate vs target size for 1 μA proton current impinging on a LiO target.

Assuming a 10 μm thickness the photon production rate is:

$$R_\gamma = 12150 \text{ s}^{-1} \tag{6.1}$$

This is higher than the value obtained from the calculations in equation 3.4 because in this case the simulation takes into account photons both from inside and outside the 18.15 MeV resonance. From the e^+e^- pair cross section provided by the Zhang-Miller model and the generated photon energy distribution in a 10 μm Li_2O target, the IPC production rate is:

$$R_{\text{IPC}} = 38.8 \text{ s}^{-1} \tag{6.2}$$

With these values it is then possible to estimate the IPC coefficient:

$$\text{IPC}_{\text{coeff}} = \frac{R_{\text{IPC}}}{R_\gamma} = 3.19 \times 10^{-3} \tag{6.3}$$

Taking into account the ratio $\frac{BR(^8\text{Be}^* \to ^8\text{Be}X)}{BR(^8\text{Be}^* \to ^8\text{Be}\gamma)}$, estimated to be 6×10^{-6} by the Atomki experiments, the estimated X(17) production rate is then:

$$R_X = R_\gamma \times \frac{BR(^8\text{Be}^* \to ^8 \text{Be}X)}{BR(^8\text{Be}^* \to ^8 \text{Be}\gamma)} = 7.29 \times 10^{-2} \text{ s}^{-1} \tag{6.4}$$

A summary of all the reaction rates is reported in table 6.1.

	Photon	**IPC**	**X(17)**
Rate	12150 s^{-1}	38.8 s^{-1}	$7.29 \times 10^{-2} \text{ s}^{-1}$

Table 6.1: Summary of the X(17) measurement reaction rates assuming a 10 μm thick LiO target. The values are estimated via GEANT4 simulations.

6.4 Significance study

Knowing the reaction rates, the resolution and the efficiency of the X(17) measurement it is possible to estimate the significance and thus the DAQ time needed to achieve a satisfactory result. The study of the significance as a function of the DAQ time has been preliminarily performed on the first target design, as briefly reported at the beginning of chapter 6, and then refined and repeated for the final target design and with the improved background model implementation.

Figure 6.5 shows the invariant mass distribution for both signal and IPC background in a range around the expected signal region. Here the signal region is considered as $\mu \pm 3\sigma$ with μ and σ parameters of the core of the double Gaussian fit to the invariant mass distribution of signal events. This distribution comes from the simulation with the final design of the target region reported in section 5.1.4. Based on the detection efficiency and on the branching ratio of the different reactions it was possible to extrapolate the expected number of signal and background events: the distribution shown in the figure corresponds to 40 h of data taking, and the excess has a significance of $s = 5$.

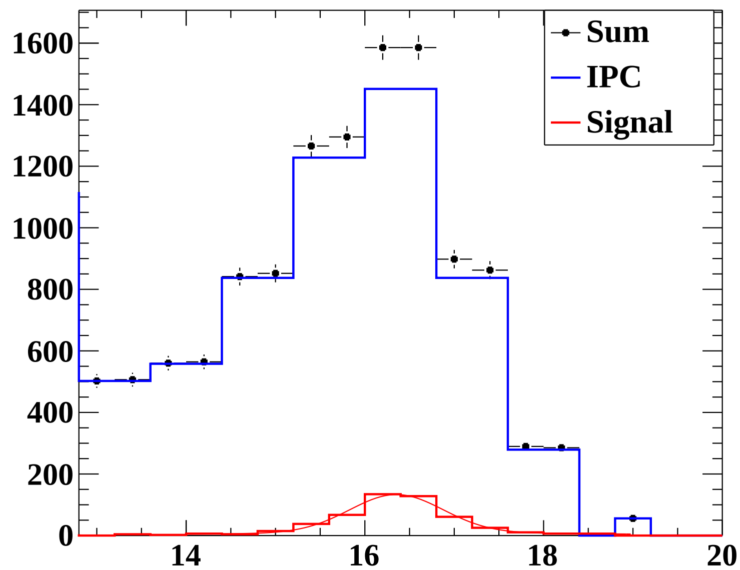

Figure 6.5: Invariant mass distribution of signal and IPC background from simulations. The "sum" distribution is also reported.

The quantities involved in the significance calculation are the total number of reconstructed events $N_{\text{tot}} = N_{\text{sig}} + N_{\text{IPC}}$, the number of signal events in the signal region N_{sig} and the number of IPC background events in the signal region N_{IPC}. The significance s can be estimated as:

$$s = \frac{N_{\text{sig}}}{\sqrt{N_{\text{sig}} + N_{\text{IPC}}}} = \frac{N_{\text{sig}}}{\sqrt{N_{\text{tot}}}} \tag{6.5}$$

Figure 6.6 shows the significance vs DAQ time calculated from the invariant mass distribution. The values of N_{sig} and N_{IPC} are extrapolated using the following efficiencies, BR and photon production rate:

$$\begin{aligned}
\mathrm{BR}_{\mathrm{IPC}} &= 3.19 \times 10^{-3} \\
\mathrm{BR}_{\mathrm{sig}} &= 6.0 \times 10^{-6} \\
\varepsilon_{\mathrm{IPC}} &= 2.5\% \\
\varepsilon_{\mathrm{sig}} &= 5.0\% \\
R_{\gamma} &= 12150\ \mathrm{s}^{-1}
\end{aligned} \tag{6.6}$$

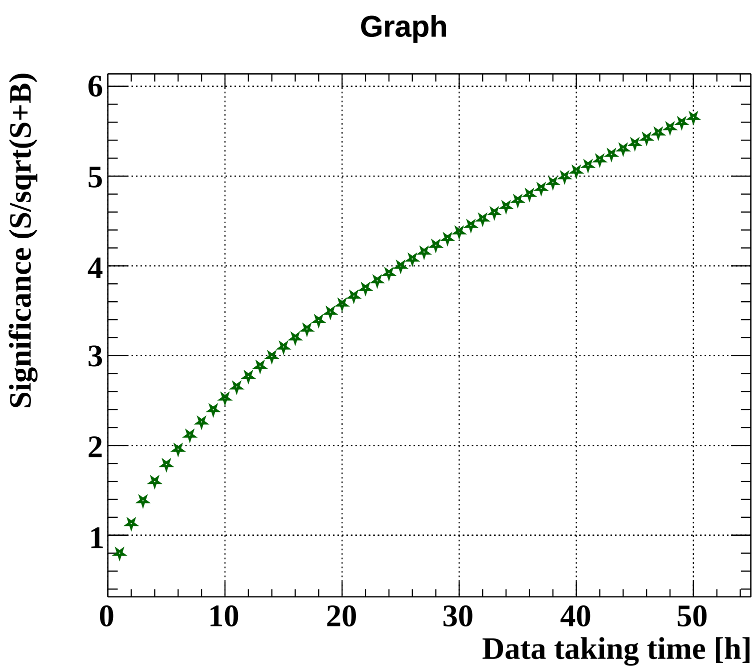

Figure 6.6: Significance vs DAQ time for invariant mass search at 1 μA proton current.

The number of signal and background events reconstructed in the signal region after a time T is calculated as follows:

$$\begin{aligned}
N_{\mathrm{IPC}} &= N_{\gamma}\mathrm{BR}_{\mathrm{IPC}}\varepsilon_{\mathrm{IPC}}\frac{N_{\mathrm{sig}}^{\mathrm{roi}}}{N_{\mathrm{sig}}^{\mathrm{tot}}} \\
N_{\mathrm{sig}} &= N_{\gamma}\mathrm{BR}_{\mathrm{sig}}\varepsilon_{\mathrm{roi}}\frac{N_{\mathrm{IPC}}^{\mathrm{roi}}}{N_{\mathrm{IPC}}^{\mathrm{tot}}}
\end{aligned} \tag{6.7}$$

where $N_{\gamma} = TR_{\gamma}$ is the number of photon produced in the time T, and the superscripts "roi" and "tot" refers to the integral of the simulated distributions respectively in the signal region and in the total range.

In conclusion a significant excess is expected to be visible in:

$$\mathrm{T_{DAQ}}(s=5) = 40 \text{ h} \qquad @1\ \mu\text{A proton current} \tag{6.8}$$

Including the estimated time for the preparation of the experiment, the expected time needed for this measurement is of the order of one week, and can be easily included in the MEG II activities programmed during the 4 months long shutdown of the PSI muon beam at the beginning of 2022.

6.5 Summary

Table 6.2 summarizes the results of the simulations of the X(17) measurement at MEG II.

Proton current	1 μA
Max temperature	55.92°C
Target deformation	0.082 mm
Target material	Li_2O
Target thickness	5 μm
Substrate material	Cu
Substrate thickness	25 μm
Resolution	504 keV
Efficiency	5.0%
Efficiency with pTC	2.0%
Photon rate	12150 Hz
IPC rate	38.8 Hz
X(17) rate	7.29×10^{-2} Hz
$\mathbf{T_{DAQ}}(s = 5)$	40 h

Table 6.2: Results of the simulations of the X(17) measurement at MEG II.

Chapter 7

First pair conversion data taking

In the second half of 2021 a first prototype of the new target region for the X(17) measurement was ready to be tested. The prototype is composed by a target support structure inside a small CF chamber compatible with the CW insertion system. It will not be used for the final measurement, nonetheless it was used during the MEG II 2021 engineering run to take some data with the first prototype of the Li target. This data taking was useful to test the stability of the setup, even though it was not the final one, and to look at some e^+e^- pair with the CDCH, mostly produced by EPC in the apparatus.

In this chapter I will describe the different configurations used to take data, together with a preliminary analysis. The first data were collected before the production of the CF chamber: the CW Al beam pipe was used, together with the $Li_2B_4O_7$ target used for the LXe calibration, that was placed at the center of the COBRA volume. This setup is far from ideal, but allows to study the behavior of the CDCH with e^+e^- pairs. After the production of the small CF chamber, the Cu target support and a first target prototype, a first test outside the COBRA volume allowed to prove the stability of this preliminary apparatus and to get a first measurement of the Li photon spectrum using the LaBr3 calorimeter. The CF chamber was then inserted at the center of the COBRA volume to measure again the photon spectrum and to take some preliminary data with the CDCH. The data were collected with the magnetic field both off and on (reduced at 15% with respect to the $\mu^+ \to e^+\gamma$ measurement), and using both a CDCH self trigger and a single pTC tile trigger, already available because developed for the MEG II commissioning.

My contribution in the work presented in this chapter consists in the participation in the data taking campaign at the end of 2021 with the first prototype of the target region and in the participation in the preliminary analysis of such data.

7.1 MEG II calibrations experimental setup

The first X(17) preliminary test dataset was collected before the production of the CF vacuum chamber and the Li target. The goal was to test the behavior of the CDCH in the 2021 configuration exposed to the CW proton beamline at $E_p = 500$ keV and $E_p = 1$ MeV up to 10 μA proton current, and to find the parameters of the CW for the operation under a magnetic field reduced at 15%. This was the first dataset with e^+e^- pairs detected by the CDCH, both with straight and curved tracks: the data were in fact collected both with the COBRA magnetic field off and on.

The e^+e^- pairs in this dataset were mostly produced in EPC processes, since the setup used was the one for the LXe calibrations, with a $Li_2B_4O_7$ target installed in an Al beam pipe. The target was placed at the center of the COBRA volume using the CW insertion system, thus the photons produced in the nuclear reactions had to cross a lot of material: at first the thick target, then the Al beam pipe and finally the bellows of the insertion system, resulting in a high EPC probability. Figure 7.1 shows a picture of the ending of the CW Al beam pipe in which the target is installed, together with a picture of the target itself. It also shows the first prototype of the small CF chambers that will be used in other tests.

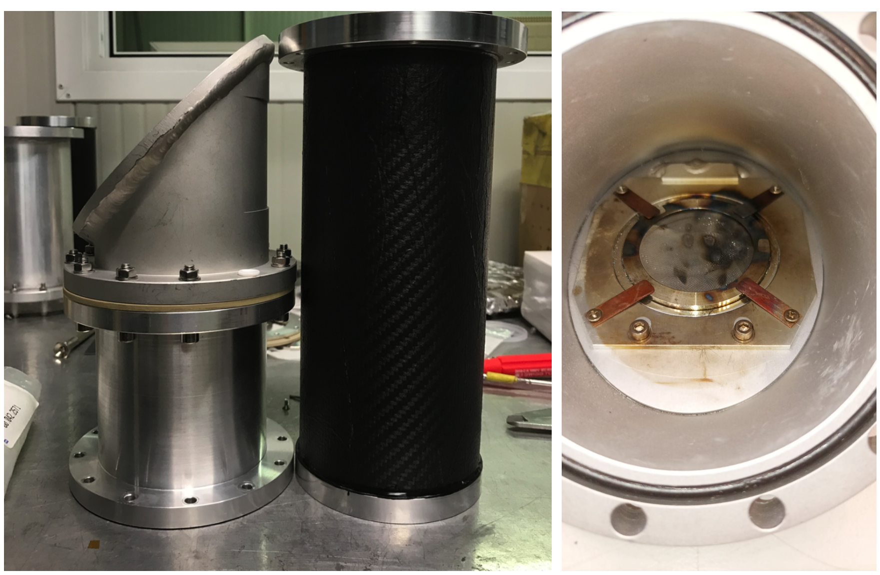

(a) (b)

Figure 7.1: (a) Picture of the end part of the CW Al beam pipe, where the $Li_2B_4O_7$ target is installed. The new CF vacuum chamber is also shown. (b) Picture of the $Li_2B_4O_7$ target.

7.2 Small CF chamber experimental setup

A first prototype of a CF vacuum chamber was produced during the second part of the 2021 engineering run. It is a small vacuum CF chamber which is compatible with the CW insertion system, so that it can be used during the $\mu^+ \to e^+\gamma$ run. This is in fact a replacement of the usual CW end part of the Al beamline with the same length and diameter, as shown in figure 7.1.

This setup was first installed outside the MEG II experimental apparatus for several tests. The insertion system was removed from the CW beamline, and the CF vacuum chamber was attached to the flange of such beamline just after the concrete wall that separates the CW experimental area from the πE5 experimental area where MEG II is hosted, as shown in figure 7.2. In this configuration it was possible to test the new setup with the proton beam at 500 keV and 1 MeV and have a first look at the photon spectra with the LaBr3 calorimeter.

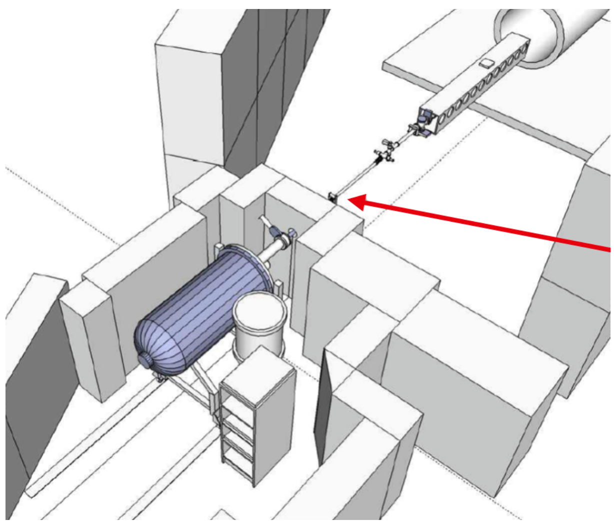

Figure 7.2: CW (bottom-left) and MEG II (top-right) experimental areas separated by a concrete wall. The red arrow indicates where the CF vacuum chamber was installed for the tests.

The new preliminary setup is composed of the small CF vacuum chamber with the Cu support structure on which the target is installed. Two targets were available for these tests: the $Li_2B_4O_7$ target used in the LXe calibrations and a Li target obtained by sputtering 1 μm of lithium phosphorus oxynitride (LiPON) on a 100 μm Cu foil. This second target was used to test the sputtering process and its durability under a long exposure to a proton beam, even though the characteristics are far from the design that will be used in the X(17) measurement.

This apparatus was also used to take some preliminary data with the CDCH. It was in fact installed in the insertion system as a replacement of the original Al end pipe of the CW line, and placed at the center of the COBRA volume for data taking. With this setup some data have been collected in different configurations: magnetic field on/off, pTC single tile/CDCH self trigger, 500/1000 keV proton energy. This gives the possibility to make the same preliminary tests described in section 7.1 but with the thin LiPON target, more similar to the definitive one. Moreover, with these data it is possible to extrapolate some indications for the trigger, since there is a set with different trigger configurations.

7.2.1 Copper support structure and target

Figure 7.3 shows a picture of the final version of the Li target support structure. It is a 3D printed system composed of 4 parts: a Cu arm, a Cu ring connected to one side of the arm, an Al flange connected to this ring and, on the other side of the arm, a set of two Cu rings with threaded holes, one connected to the structure and one free. These rings are used to keep the target and the substrate in position, and the Al flange is used to connect the apparatus for the X(17) measurement to the CW beamline.

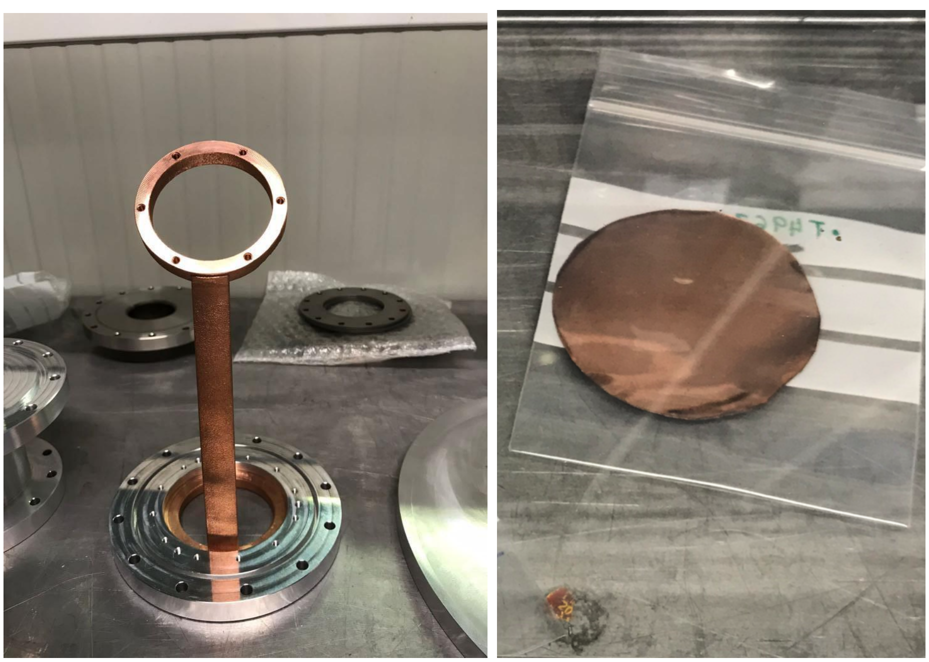

(a) (b)

Figure 7.3: Picture of the Cu support structure connected to an Al flange (a) and the test LiPON target on a Cu substrate (b).

The figure also shows an example of the test target used in the 2021 data taking. It is a 1 μm thick LiPON target sputtered on a 100 μm thick Cu substrate. This disc has to be placed between the two rings of the support, which is designed to keep the target at the center of the experiment and rotated by 45° around the x axis. Even though the Cu substrate is a factor 4 thicker with respect to its design for the final measurement, the whole setup (sputtered target, substrate, support arm) proved to be effective in dissipating up to $\sim$5 W, since no deterioration was observed on the thin LiPON film.

7.2.2 Carbon Fiber vacuum chamber

The Cu support structure, after the installation of the target, was placed inside the new small CF vacuum chamber. This chamber is a 13 cm diameter and 400 μm thick carbon fiber tube reinforced with a binding polymer which is, in this case, epoxy. The tube is terminated with an Al cap, glued to it with Stycast to prevent any gas leakage. The same glue is used to couple the chamber to the Al flange connected to the Cu support, which is itself connected to the CW beam line during data taking. The sturdiness and gas tightness of the CF chamber were tested by creating vacuum inside it with a vacuum pump. The result of this test demonstrated that this volume can bear a vacuum at least up to 8×10^{-6} mbar.

Figure 7.4 shows a picture of the vacuum chamber. Here the Al cap was not yet glued to it, but the tube was already installed on the Al flange coupled to the Cu support.

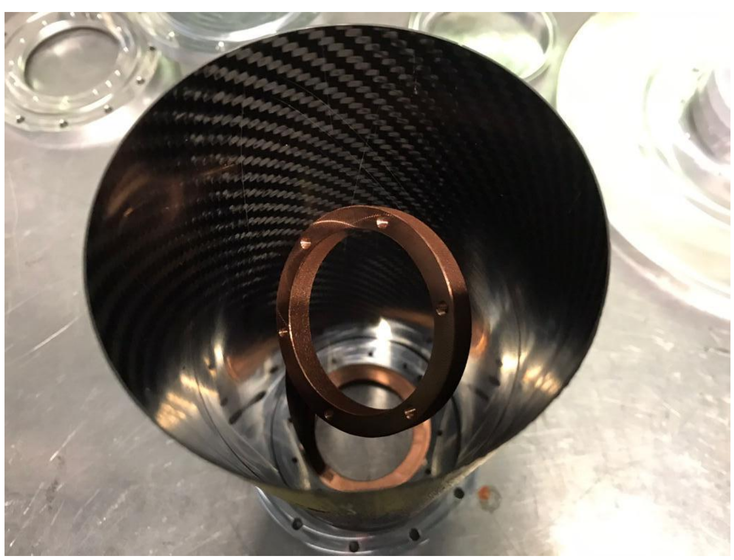

Figure 7.4: Picture of the small CF chamber with the Cu support inside.

7.2.3 Experimental setup at COBRA center

After the vacuum test and the first test under proton beam behind the concrete wall of the CW experimental area, the CF chamber with the Li target was mounted as the final part of the CW beam line, inside the insertion system. Figure 7.5 shows a picture of this setup before the insertion inside the COBRA volume, together with a picture of the position of the LaBr3 calorimeter, placed outside the CDCH volume, at $z = 0$. This setup is identical to the one described in section 7.1 except for the replacement of the target and its surroundings, now more similar to the configuration designed for the X(17) measurement. This solution allowed to take some preliminary e^+e^- data with the CDCH during the 2021 MEG II engineering run, during which it is not possible to dismount the insertion system, thus impeding the installation of the large CF chamber.

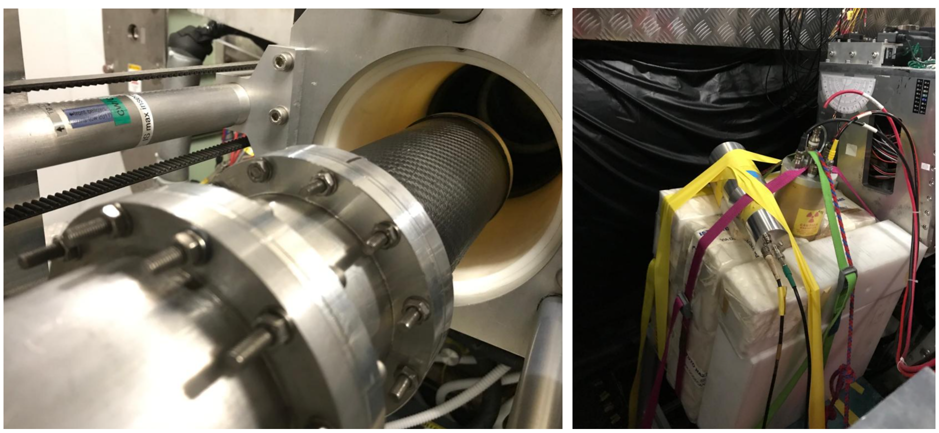

(a) (b)

Figure 7.5: Picture of the small CF chamber inside the insertion system before its installation inside the COBRA volume (a) and the LaBr3 calorimeter used to monitor the photon spectrum, placed outside the CDCH (covered by a black cloth) at $z = 0$ (b).

The data collected in this configuration involved not only the CDCH studies of the e^+e^- pairs. In fact, also the pTC was read out, unlike the dataset taken with the $Li_2B_4O_7$ target and the Al pipe. This way it is possible to see if the hits on the pTC tiles can improve the tracking performance. Moreover, the triggers used for such data were of two kinds: a multiplicity trigger on the CDCH, that requires at least two hits on one of the two ends of the detector, US or DS, and a single hit trigger on the pTC. This allows for a study of the optimal thresholds for these two trigger strategies, and for a comparison between them.

7.3 Photon spectra with test targets

The small CF chamber setup was first mounted outside the MEG II experimental apparatus for some tests, as described in section 7.2. The main goal was to measure the photon spectra of the targets used for the data taking with the CDCH using the LaBr3 crystal coupled to a PMT as photon detector. Figure 7.6 shows a picture of the setup for the photon spectra measurement. The beam pipe section that connects the insertion system to the CW accelerator was disconnected, so that it was possible to connect the CF chamber to the CW beamline right after the wall that separates the accelerator from the πE5 area. The LaBr3 detector was installed on a table sideways the CF chamber and with an inclination that made the crystal point towards the target region.

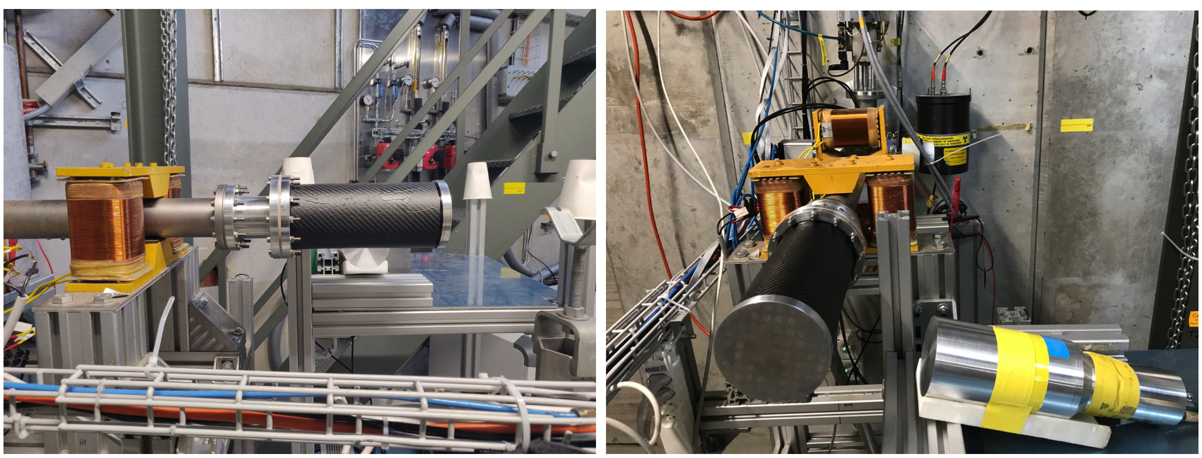

(a) (b)

Figure 7.6: Pictures of the experimental setup for the first test with the small CF vacuum chamber. In picture (b) the LaBr3 small calorimeter used to measure the photon spectrum is also visible.

$Li_2B_4O_7$

The first test was made using the $Li_2B_4O_7$ target used also for the measurements described in section 7.1. The measurement of the Li line with this target was possible thanks to the calibration lines produced by the self scintillation of the LaBr3 crystal and the photons produced in the $^{11}B(p,\gamma\gamma)^{12}C$ reaction.

Figure 7.7 shows the self scintillation spectrum of the LaBr3 crystal, in both the Ce and the Ce+Sr doped version. The one used for this detector is the LaBr3(Ce), and the calibration lines of interest are at $E_\gamma = 0.789$ MeV, $E_\gamma = 1.173$ MeV and $E_\gamma = 0.789 + 1.173 = 1.962$ MeV.

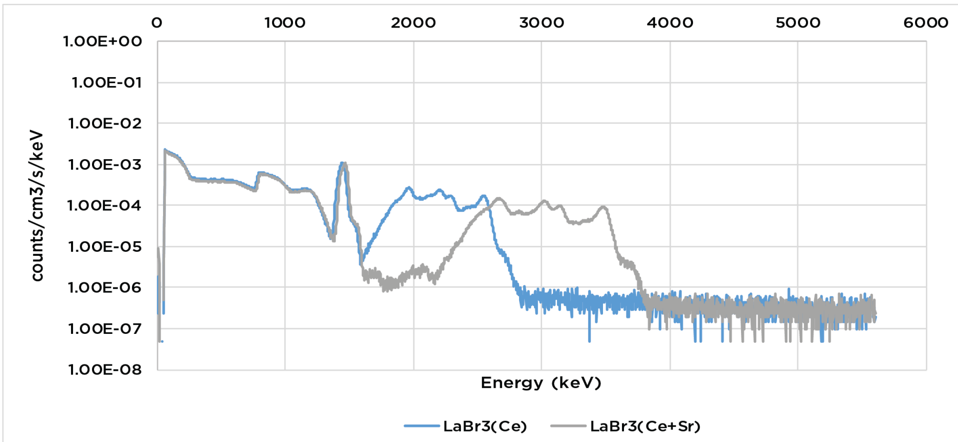

Figure 7.7: Photon energy spectrum of the self scintillation of the LaBr3 crystal, both in the Ce and Ce+Sr doped version. Figure from [144].

Figure 7.8 shows the proton cross section of the ^{11}B$(p,\gamma\gamma)^{12}$C reaction. Here the photon lines, visible in the spectrum that is also reported in figure, are at $E_\gamma = 4.44$ Mev, $E_\gamma = 11.7$ MeV and $E_\gamma = 4.44 + 11.7 = 16.1$ MeV, with the first two photons emitted simultaneously.

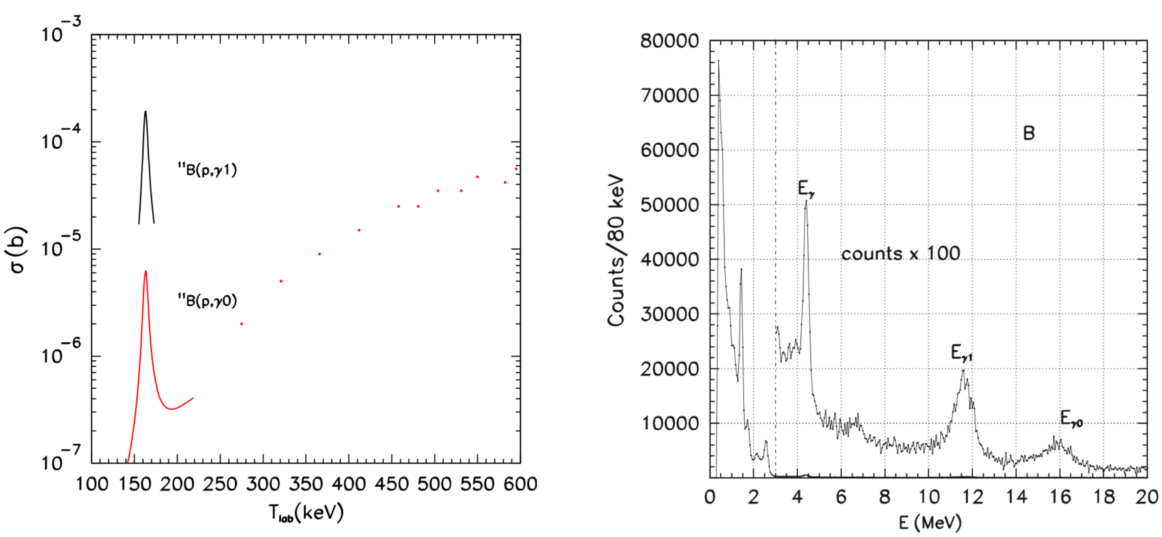

(a)

(b)

Figure 7.8: Proton cross section (a) and photon energy spectrum (b) of the ^{11}B$(p,\gamma\gamma)^{12}$C reaction. Pictures from [99].

After having established the calibration scale for the photon detector it was possible to proceed to the measurement of the Li lines in the photon spectrum. Figure 7.9 shows the energy spectra at $E_p = 500$ keV and $E_p = 1$ MeV, with the calibration lines highlighted. At $E_p = 500$ keV the 17.6 MeV Li line is visible, together with the other lower energy lines, obtained thanks to the fact that the target is thick enough to make the proton lose enough energy to excite the corresponding states. The $E_p = 1$ MeV energy spectrum shows a slight increase around the expected excited state at 18.15 MeV which is most likely smeared by the presence of too much material in the target. This may depend on some non optimal CW configuration, thus another measurement is needed to investigate this observation.

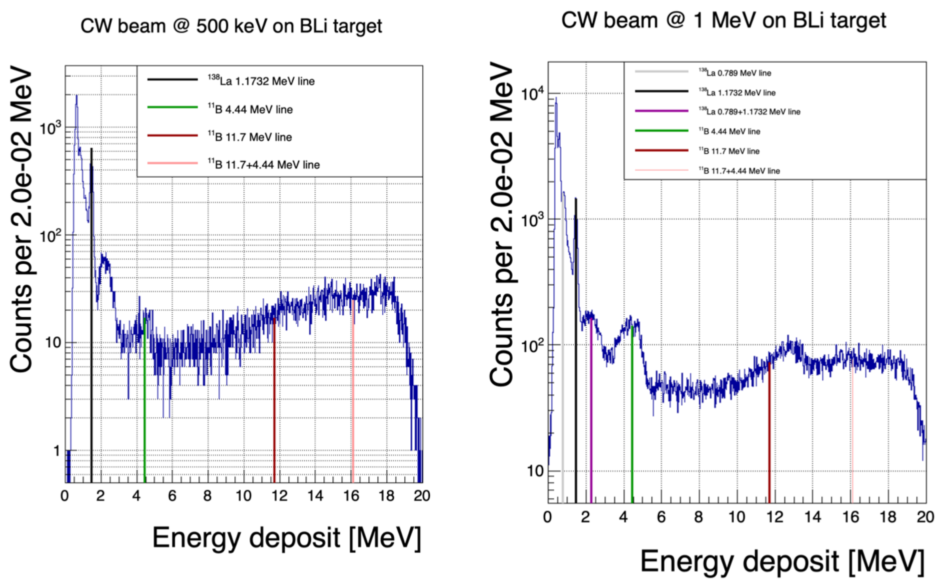

(a) (b)

Figure 7.9: Measured photon energy spectrum with the $Li_2B_4O_7$ target at (a) $E_p = 500$ keV and (b) $E_p = 1.0$ MeV. The colored lines are the ones used to calibrate the LaBr3 detector.

LiPON (1 μm) sputtered on copper substrate (100 μm)

The second photon spectrum measurement was performed using the test LiPON target. Here an external calibration source was tested as a different method, with respect to the LaBr3 self scintillation, to set the scale of the photon detector. The choice was a ^{60}Co source, which produces the following calibration lines: one at $E_\gamma = 1.173$ MeV, one at $E_\gamma = 1.332$ MeV and one at $E_\gamma = 1.173 + 1.332 = 2.505$ MeV. Figure 7.10 shows the photon energy spectrum up to 2 MeV from a ^{60}Co source.

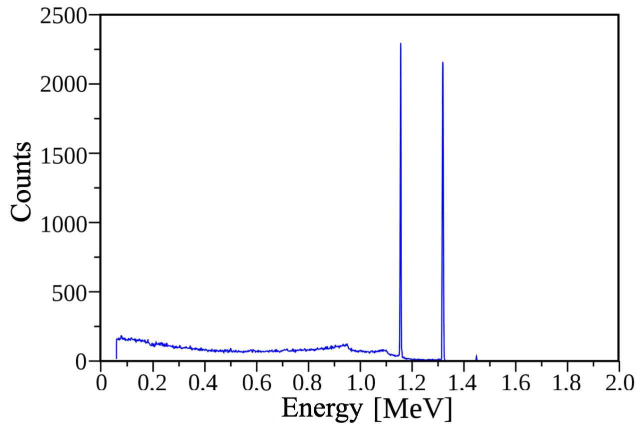

Figure 7.10: Photon energy spectrum up to 2 MeV from a ^{60}Co source.

Figure 7.11 shows the measured photon spectrum at $E_p = 500$ keV and $E_p = 1.0$ MeV. The only evident excess is in the $E_p = 500$ keV case and not in the $E_p = 1$ MeV case, so further measurements are needed to investigate this observation.

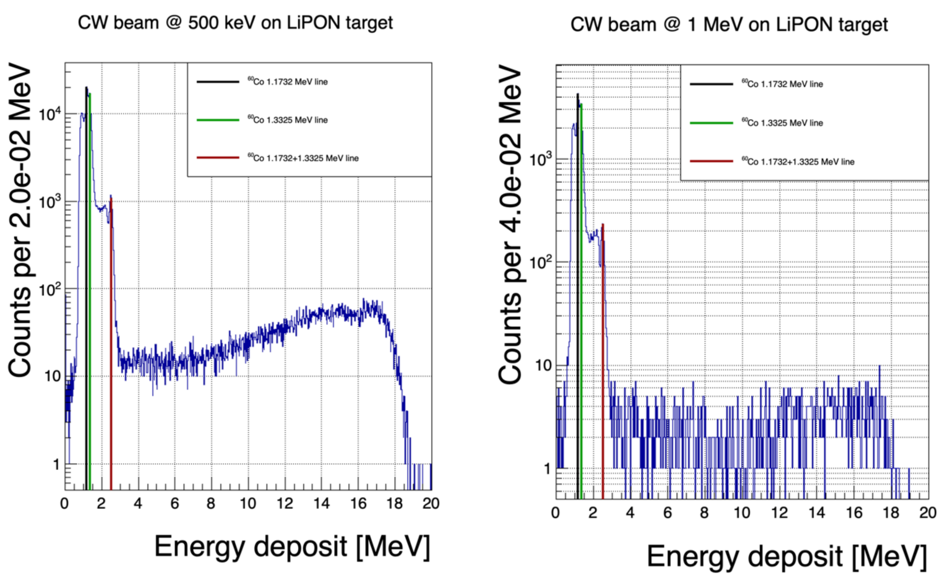

(a) (b)

Figure 7.11: Measured photon energy spectrum with the LiPON target at (a) $E_p = 500$ keV and (b) $E_p = 1.0$ MeV. The colored lines are the ones used to calibrate the LaBr3 detector.

The measurement has been repeated with the setup inside the experiment, during the data taking with the CDCH, as shown in figure 7.5. Here the results, reported in figure 7.12, show both Li lines at 17.6 MeV and 18.15 MeV. In this case the calibration was made using the LaBr3 self scintillation data measured in a different dataset.

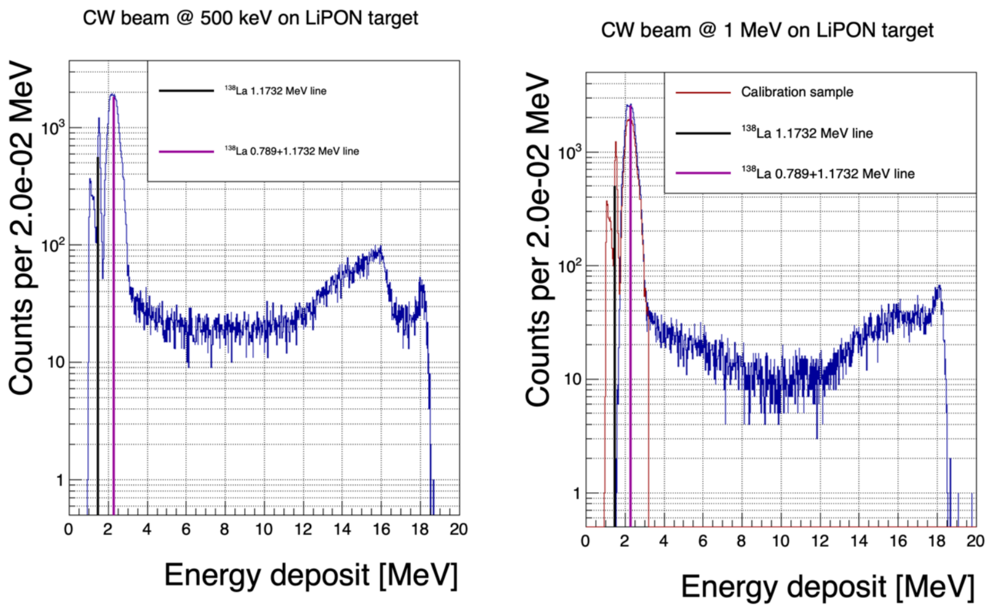

(a)

(b)

Figure 7.12: Measured photon energy spectrum with the LiPON target at COBRA center at (a) E_p = 500 keV and (b) E_p = 1.0 MeV. The colored lines are the ones used to calibrate the LaBr3 detector.

7.4 Data analysis

The data collected with the two Li targets can be used to adapt the analysis algorithm to X(17) events and to optimize the trigger type (CDCH or pTC) and parameters (thresholds, number of wires/tiles over threshold, etc.). Before analyzing these data, though, a modification to the MEG II tracking algorithm is needed, since the $\mu^+ \rightarrow e^+\gamma$ event topology is different from the X(17)$\rightarrow e^+e^-$ one. Nonetheless, even without a dedicated tracking, it is possible to look at the hit distributions of the EPC events to study the CDCH hit reconstruction performance.

7.4.1 Tracking algorithm

The CDCH tracking algorithm for $\mu^+ \rightarrow e^+\gamma$ has been developed to cope with a high rate environment, so a good Pattern Recognition (PR) is needed to select only the hits that belong to a track and discard the ones that are due to the pile-up. The tracking process happens in two phases: track finding and track fitting. In the first one the PR algorithm selects the hits that belong to a track and creates a track candidate, in the second one the hits selected in the track finding phase are fitted to extract the parameters of the particle track. In the X(17) measurement the situation is different: the occupancy of the detector is much smaller, but there is the need to track two particles instead of only one, so some modifications are needed. While the structure of the algorithm can remain unchanged, a new PR that is able to separate two tracks with opposite sign has to be developed.

GENFIT and Kalman Filter

The MEG II tracking algorithm is based on the Kalman Filter (KF) for the track fitting phase. The algorithm is implemented using the GENFIT (GENeric track-FItting Toolkit) tool. The KF is a progressive fitting algorithm commonly used to fit tracks in particle spectrometers. It provides better performance with respect to global minimization algorithms in presence of materials and non-homogeneous magnetic fields. GENFIT is independent on the event topology and has a completely modular design, that makes it a versatile toolkit for track fitting.

The first inputs of the KF are the raw detector measurement, indicated with $\vec{m}_k$, and the covariance matrix V_k. The k hits in the detector are defined in the so called detector planes, that can be either virtual or physical. GENFIT assumes that the hits are already sorted, hence the need for the track finding step before the track fitting. No assumption is made on the hit dimensionality, since there are predefined measurement classes for various detector types. Each detector is in fact best described in one, two or three dimensions.

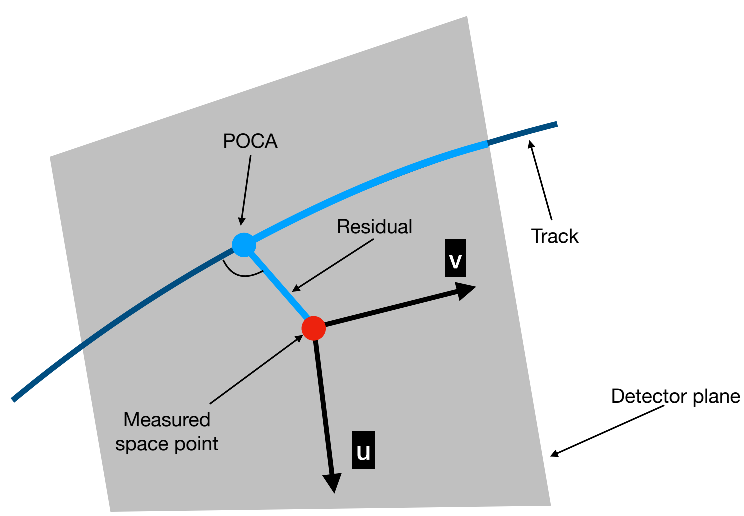

Figure 7.13: Virtual detector plane for a space point hit.

Non-planar detectors like the CDCH are sliced into virtual detector planes orthogonal to the track in the Point Of Closest Approach (POCA). Each plane is associated to a two dimensional coordinate calculated from the measured drift time. Figure 7.13 shows a drawing of the virtual plane concept in case of a space point hit. GENFIT offers the possibility to give different representations to a track, allowing to consider more particle hypothesis in the fitting procedure and try different track parametrizations to select the one that gives the best result.

The KF is a recursive algorithm that looks for the best estimate of the state vectors of a track from hit position measurements. A step of this algorithm updates the state vector and covariance matrix of a track representation, adding the information from a detector hit. The hit processing goes through the following steps:

- calculation of the virtual detector plane;
- extrapolation of the track to the detector plane and prediction of the state vector and covariance matrix;
- calculation of the hit covariance;
- calculation of the H_k matrix, that allows to change coordinate system from x_k (state vectors) to v_k (hit coordinates);
- calculation of the Kalman gain K_k, which determines how much a hit can attract the track towards itself;
- calculation of the residual vector;
- update of the state vector, covariance matrix and reference plane;
- increment of the χ^2.

The track is then obtained by repeating the step of the algorithm for all the hits in the detector planes.

Performance for X(17) events

The first simulations described in section 5.1.4 are preformed using an ideal PR that uses the MC truth to assign hits to a track. If one tries to use the standard MEG II PR out of the box the results are unsatisfactory, because this algorithm is tuned for positrons only and assumes a harsh environment in terms of pile-up, which is not expected in the X(17) measurement.

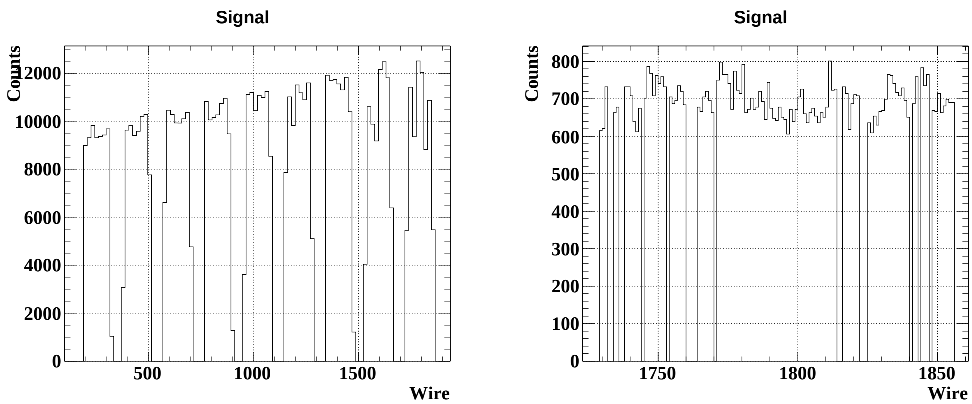

(a) (b)

Figure 7.14: (a) CDCH hit occupancy for 5k simulated signal events. (b) Zoom on layer 9. The wires with 0 events are missing from the CDCH or have hardware problems, and thus are excluded from the analysis.

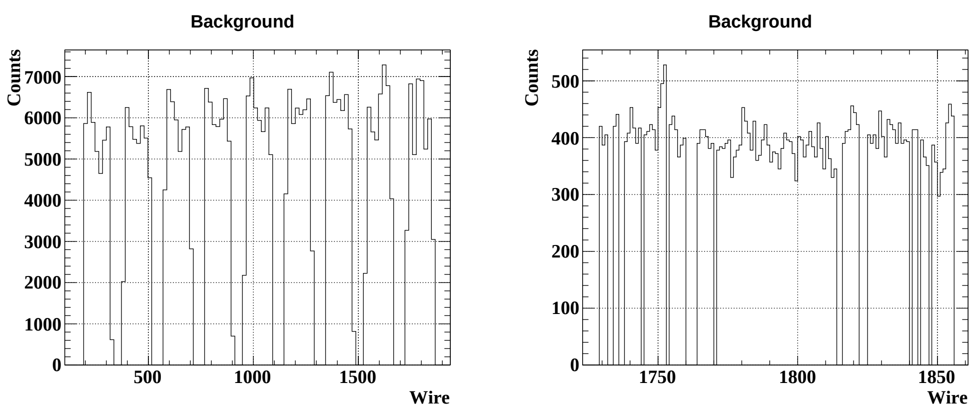

(a) (b)

Figure 7.15: (a) CDCH hit occupancy for 10k simulated background events. (b) Zoom on layer 9. The wires with 0 events are missing from the CDCH or have hardware problems, and thus are excluded from the analysis.

The expected occupancy of the CDCH has been estimated from simulations: figures 7.14 and 7.15 show the number of hits per wire for signal and background events respectively. The resulting occupancy is expected to be less than 0.05 hits per wire per event for background and less than 0.1 hits per wire per event for signal, allowing for a simpler track finding algorithm with respect to the MEG II one.

New pattern recognition for X(17) events

Since the standard MEG II PR algorithm cannot be used in the X(17) measurement, a new one is under development. It is based on a Graph Neural Network (GNN), which is a deep learning method based on graphs. The GNN takes the list of hits in a event as input and assigns them to a track belonging to one of four mutually exclusive classes: primary e^+, primary e^- (the ones from IPC events), secondary $e^\pm$ (can be for example δ rays or other kind of particles), and noise hits. Since the network works with a fixed number of hits, the strategy is to create an array of hits with a fixed length, which has to be always higher than the actual number of hits in a event (600 in this case). The input array will then have real hits and fake empty hits that add up to 600, and the fake hits are categorized into a new class, which is dubbed "unphysical". The hits are passed to the network by means of their coordinates x, y, z, calculated as follows: the z is calculated with the charge division of the signal from the two wire ends, and the x and y are calculated from the wire position at that z in the global coordinate system.

The network was tested on a sample of 100k IPC events from the simulations described in section 5.2.1. The events used for testing are actually 80k, while 20k are used to train the algorithm. Three efficiencies describe this GNN:

- Positron efficiency: number of reconstructed positron tracks with nhits>6 and purity≥90%;
- electron efficiency: same as positron efficiency but for electrons;
- pair efficiency: number of events with both particles with nhits>6 and purity≥90%.

Figure 7.16 shows how the efficiencies of this algorithm vary as the purity and number of good hits thresholds changes. The numerical values are summarized in table 7.1 both for simulations that use MC hits and reconstructed hits.

	MC hits	**Reconstructed hits**
Electron efficiency	92%	85%
Positron efficiency	91%	83%
Pair efficiency	79%	57%

Table 7.1: Efficiencies of the tracking GNN.

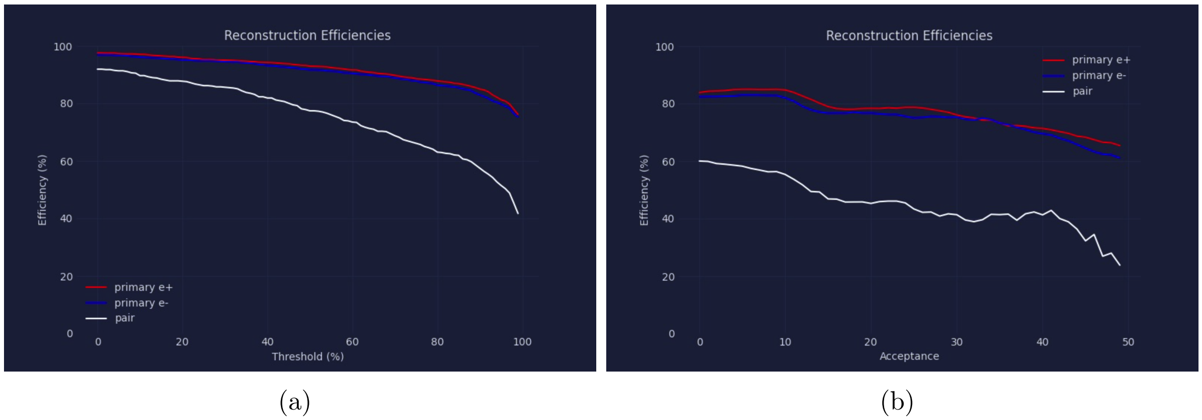

Figure 7.16: Track efficiencies as a function of purity (a) and number of hits (b) threshold. Here the reconstructed hits are used as input.

Dedicated tracking for pairs without magnetic field

In absence of the magnetic field it is possible to observe straight tracks from the e^+e^- pairs in the CDCH. For such tracks it is possible to use an extension of the standard MEG II tracking algorithm for straight tracks, usually used for cosmic rays. The track finder here combines all the hits to a single track candidate for the fit. By adding a simple histogramming method it is possible to merge hits in some ϕ angle window, allowing to separate different tracks with a sufficient separation angle. Figure 7.17 shows an example of two tracks coming from an EPC event collected during the data taking described in section 7.1.

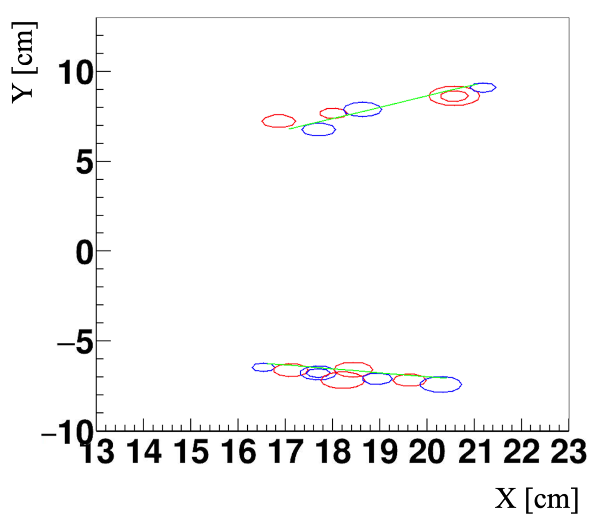

Figure 7.17: Example of tracking of EPC event without magnetic field.

7.4.2 Data with MEG II calibration setup

The first data were collected at the beginning of the 2021 engineering run, before the construction of the CF vacuum chamber. The experimental setup is described in section 7.1, and with it two different set of data were taken: one with the magnetic field off and one with the magnetic field reduced to 15%. The actual magnetic field reduction factor for the final measurement should be 17.4% from simulations (see results from section 3.6.3), but for these preliminary measurements it has been set to 15% for simplicity. Only the dataset with straight tracks has been analyzed with this setup, since a better dataset with magnetic field on was available with the small CF chamber setup, as will be shown in section 7.4.3.

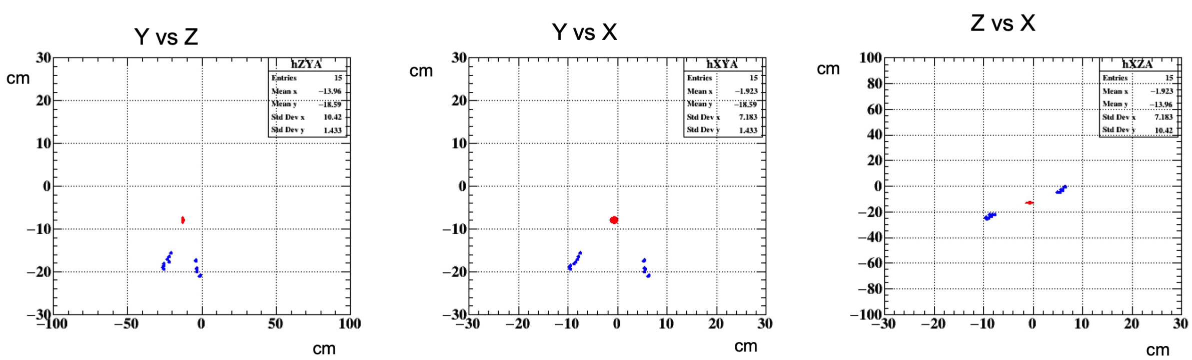

Figure 7.18: Event display of two e^+e^- tracks. The blue dots are the hits detected by the CDCH, the red dots are the DOCA of the two tracks.

The dataset with the magnetic field off offers a quick way to look at straight tracks in the CDCH even without the final version of the tracking algorithm for curved tracks, only using an extension of the existing one for cosmic rays tracks described at the end of section 7.4.1. Figure 7.18 shows an example of e^+e^- pair event detected by the CDCH viewed in the XY, ZY and XZ planes.

The position of the track vertexes for all the events shows how the EPC interaction points are distributed. Here the vertex is calculated as the middle point of the Distance Of Closest Approach (DOCA) line, which connects the two closest points, one on each track. Figure 7.19(a) shows the DOCA distribution: by cutting for events with a DOCA<10 cm $\sim$ 53% of the events survives. The distribution of their vertexes in the XY plane is reported in figure 7.19(b): here the shape seems to match the dimensions of the target and beam pipe at the center, and the bellows and CDCH internal wall around it.

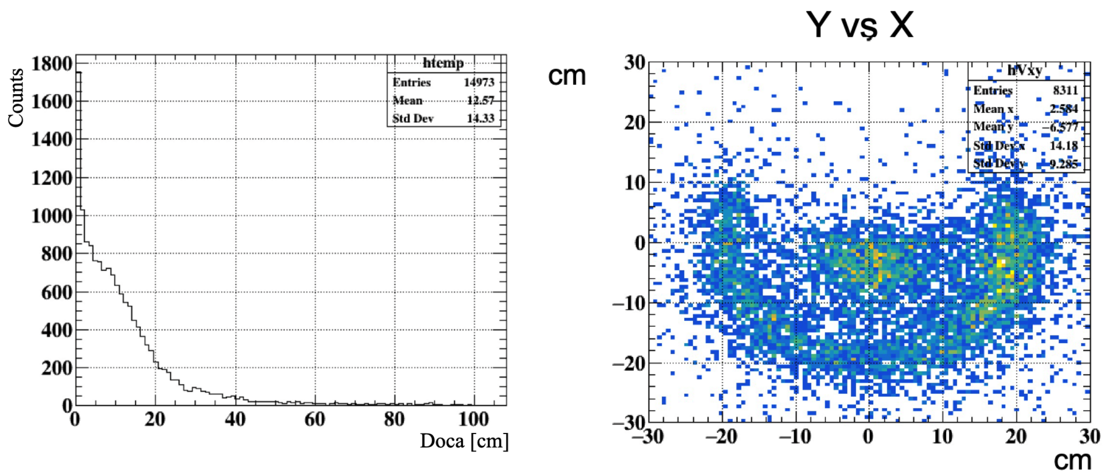

(a) (b)

Figure 7.19: (a) DOCA distribution. (b) Projection on the XY plane of the vertexes of the two tracks from EPC pair. Only events with two tracks with a DOCA<10 cm are selected.

The indication that comes from these data is that the CDCH is able to reconstruct some straight pair coming from the target. The efficiency in doing this is limited by the non optimal experimental setup, affected by multiple scattering and energy loss, nonetheless it was possible to look at some tracks and reconstruct their vertexes. Further software development is on the way to allow a deeper analysis of future datasets with an improved experimental setup.

7.4.3 Data with small CF chamber setup

In the second part of the 2021 run the small CF chamber was installed at COBRA center to take data with the CDCH and the pTC.

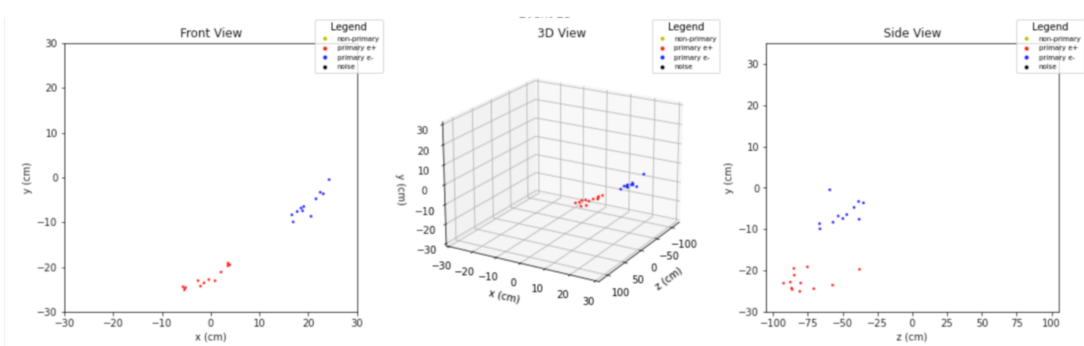

Figure 7.20: Example of event display from data with magnetic field on.

Also in this case the data have been taken with magnetic field on and off, but this preliminary analysis focuses only on the case with magnetic field on, since the other case has been addressed already with the Al pipe setup. Figure 7.20 shows an example of e^+e^- pair event with the tracks curved by the presence of the magnetic field.

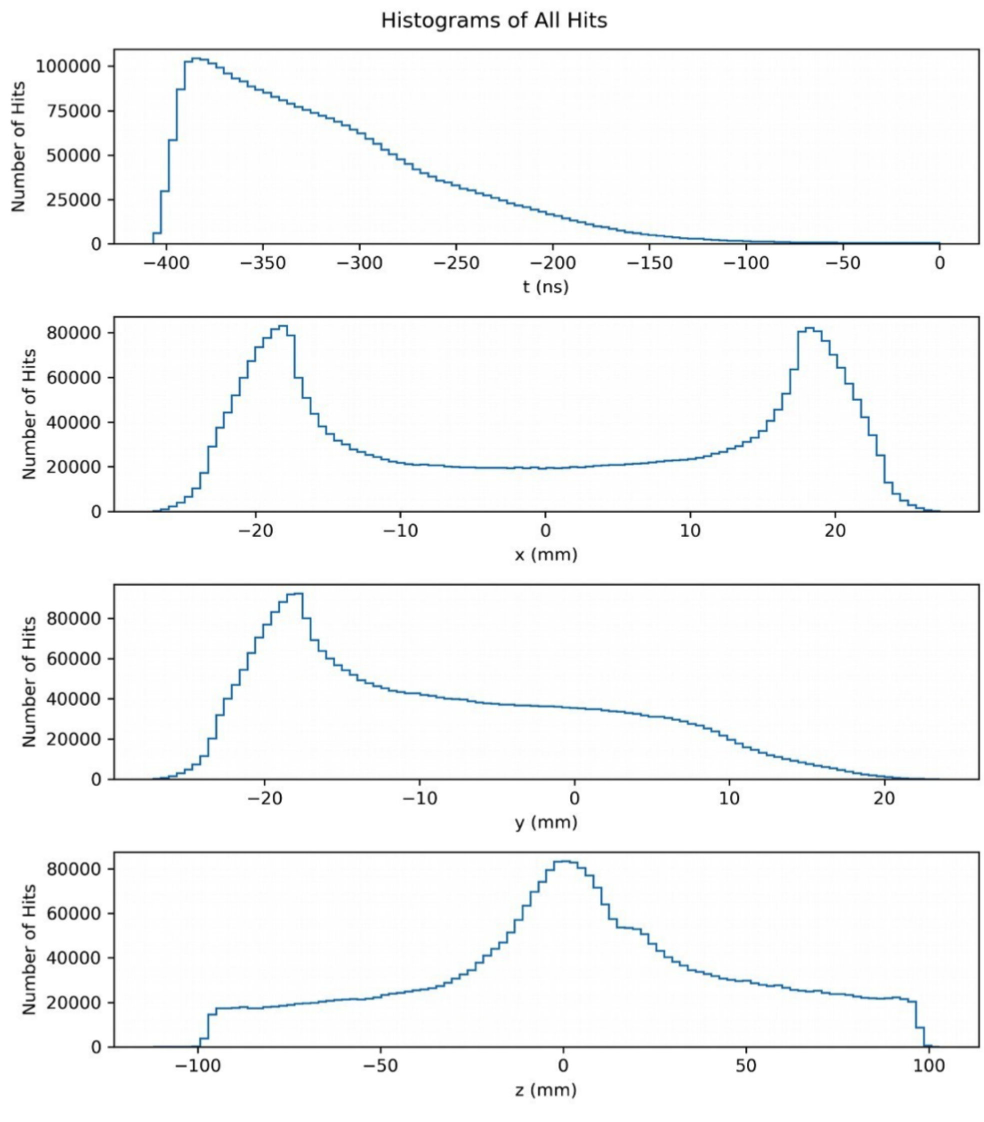

Figure 7.21: From top to bottom: hit time, hit x, y, z distributions from IPC simulation.

The new PR algorithm described in section 7.4.1 is under development, thus the information on the tracks are still unavailable. Nonetheless it is possible to look at the hit distributions and compare them to the IPC simulations. Figure 7.21 shows as a reference the distribution of the hit time and the hit coordinates from the MC simulations, where the z is calculated from the charge division of the hits on both ends of the wire.

Figure 7.22 shows the hit coordinate distributions from the dataset took with the CF setup inside the CDCH. The CW settings for this specific case were $I_p = 1$ μA and $E_p = 1030$ keV, and the trigger used is a coincidence between 2 CDCH hits on one of the two ends (CDCH 2|2 multiplicity trigger). The distributions look similar to the ones obtained from the simulation, the main differences being the two excesses at $z \sim \pm 70$ cm and the smaller peak at negative x, which is even more evident in the other datasets collected with this setup, at $I_p = 2.5$ μA and $E_p = 500$ keV.

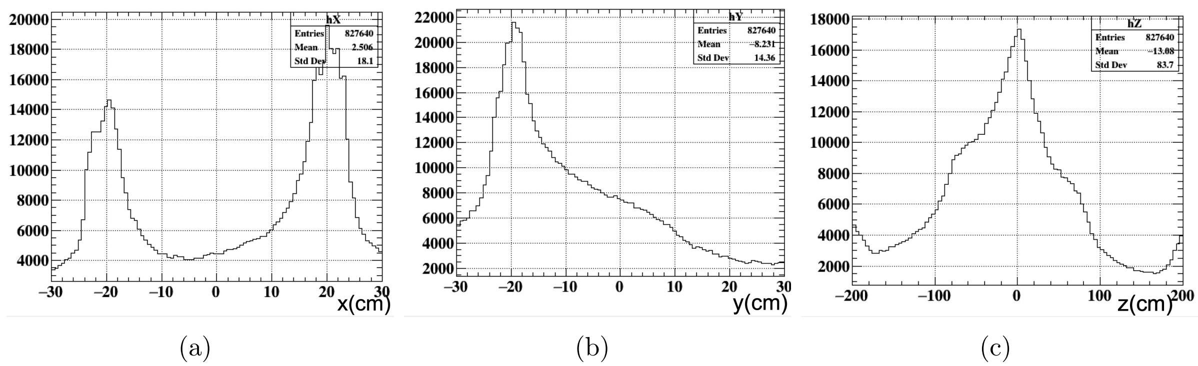

Figure 7.22: Hit coordinates distributions from data collected with the small CF chamber setup.

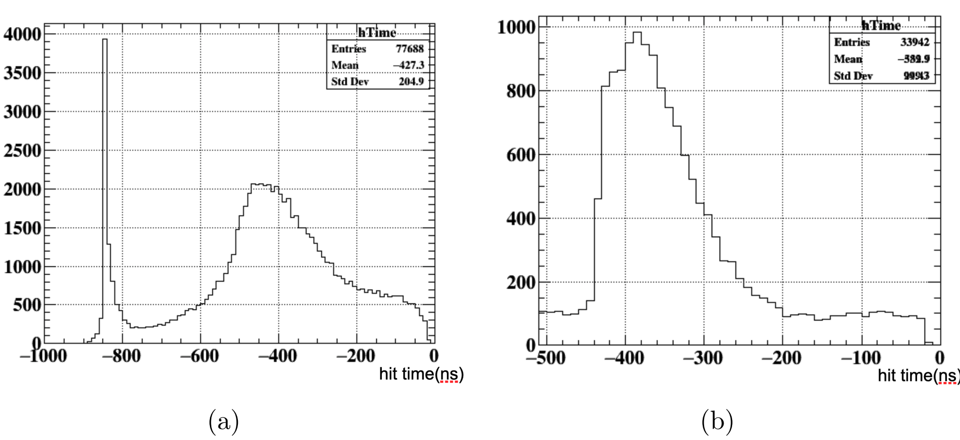

Figure 7.23: Time distribution for the datasets collected with CDCH multiplicity trigger (a) and pTC single tile trigger (b).

Figure 7.23 shows the time distribution for both datasets with CDCH multiplicity trigger and pTC single tile trigger. The CW settings here are $I_p = 2.5$ μA and $E_p = 1030$ keV. The peak at ~ -850 ns in the first plot, which is present also in the distribution with the pTC trigger but is out of the range shown, is due to noise events easily recognizable by their time, amplitude and waveform shape.

After the application of a software threshold of 26 mV in the CDCH waveform analysis the ratio between signal hits and fake hits is ~ 2.5 for both triggers. This value can be further improved by optimizing the CDCH trigger threshold, that was set to 65 mV: a 100 mV threshold would in fact help to remove fake triggers, while not skipping events with both reconstructed tracks. The simulations show in fact that all the reconstructed events have waveforms above 100 mV. The same is true also for the multiplicity, which can be raised from 2 to 4. These plots show also that the presence of the pTC is beneficial, since the rise time of the distribution in the pTC trigger case is much steeper than in the CDCH self trigger case.

The indication that comes from these data is that, even though with a selection that discards a lot of fake hits, the events collected are comparable to simulations, at least for what concerns the hits coordinates. The CDCH trigger can be further tuned to increase the efficiency on real hits, and the pTC information improves the hit time reconstruction, that will be crucial in the tracking process. With these improvements it will be possible to take higher quality data that will be fully analyzed when the tracking algorithm will be optimized.

Conclusion

The observation of the ^{8}Be anomaly raised the interest of the scientific community. Many interpretations have been attempted, both in the nuclear and particle physics field, but currently there is no unanimous consensus on the origin of such phenomenon. The improvement of the nuclear physics theoretical model of the reaction showed that a small excess is expected around the region of the angular distribution in which it was observed. However this does not fully explain the anomaly, but only decrease its significance. Moreover it was shown that there is a possibility that the observed peak is partly due to the limited geometrical acceptance of the experimental apparatus. Also the particle physics interpretation of the anomaly as the creation of a X(17) boson needs more evidence. The nature of such particle, in fact, depends on its quantum numbers, and can be verified only by further IPC measurements in different nuclear reactions.

Several experiments around the world are planning to deepen the knowledge on the X(17) boson characteristics. The MEG II experiment, even though built with another purpose, has all the ingredients to repeat the Atomki measurement with a better invariant mass resolution and angular acceptance. Such measurement can be not only an independent confirmation of the observation, but also a way to confirm or disprove the hypothesis of the anomaly being the result of a limited solid angle coverage of the Atomki apparatus. The IPC can in fact be studied not only on the plane perpendicular to the proton beam, but also at different angles.

This measurement is possible only through a redesign of the target region of the CW accelerator used for MEG II calibrations. It has in fact too much material, and this would spoil the tracker resolution because of the multiple scattering. The new target region design was carefully selected after thermomechanical and physics simulations. Through them it was possible to find a solution to balance the heat dissipation capability of this experimental setup and its performance in terms of invariant mass resolution and efficiency. The signal and background simulations, modeled on the state of the art knowledge of the IPC theory, showed that the MEG II experiment can perform the ^{7}Li$(p, e^+e^-)^8$Be measurement with a resolution on the invariant mass of $\sigma_{m_{ee}} = 504$ keV and an efficiency of 5%, reaching a sensitivity of 5 in few days of data acquisition. This is true only if the trigger has high purity and efficiency: a low efficiency will in fact reduce the number of good events detected, while a low purity will increase the number of fake hits. Having a lot of fake hits will increase the trigger rate and, if a prescaling factor p (which means that only 1 out of p triggered events is written to disk) is needed to limit the disk usage, there is the possibility to lose good events because of it. Moreover, the efficiency drops by a factor 2.5 when a hit on the pTC, needed for time reference and background rejection, is required. The most favorable trigger strategy is based on the combination of CDCH and pTC and it is under development: once its purity and efficiency will be optimized it will be possible to have a precise estimate of the overall efficiency of the measurement and of the DAQ time needed, that should not exceed ~ 1 week anyway.

The final design of the new target region is incompatible with the $\mu^+ \to e^+\gamma$ data taking. The new experimental setup is in fact composed by a large vacuum CF chamber in which the Li target and its support structure are installed, and it is incompatible with the insertion system of the CW accelerator that is used to insert/remove the CW beamline for the calibrations whenever needed. However a prototype of this experimental setup was built to not interfere with the insertion system. This prototype is different from the final design, but was nonetheless useful to take some preliminary data during the 2021 MEG II engineering run. Even though it is not possible to extract information about the IPC from these data, they can be used to test the CDCH reconstruction algorithms and to find the optimal trigger strategy for the final measurement.

The construction of the definitive target region is underway. The target support structure will be the same used for the test in 2021, and the sputtering procedure of a 1 μm thin LiPON film has been tested. The first step will be the production of a thinner Cu substrate, possibly 25 μm. Then the sputtering procedure will be tested for a 5 μm thick target, if possible with a Li_2O film instead of the LiPON used for the test. In parallel, the construction of the large CF chamber is ongoing. The small CF chamber proved to be suitable for the vacuum needed for the measurement, but the same may not be true for a larger chamber. For this reason several chambers with different thicknesses will be tested to see which is the minimum thickness reachable.

When the final design of the modified target region will be realized and proved to be working the X(17) measurement can start. It is programmed for the first months of 2022, during the annual shutdown period of the PSI muon beam, so to avoid conflicts with the $\mu^+ \to e^+\gamma$ measurement. The software development will go on in parallel to the hardware procurement, and will be ready for a complete and efficient analysis of the data.

Appendix A

X(17) boson calculations

Let's consider the ${}^7\text{Li}(p,\gamma){}^8\text{Be}$ reaction:

$$p + {}^7\text{Li} \rightarrow {}^8\text{Be}^* \rightarrow {}^8\text{Be X}, \qquad \text{X} \rightarrow e^+e^- \tag{A.1}$$

In order to populate the 18.15 MeV ^{8}Be excited state the proton kinetic energy has to be $K_i = 1.1$ MeV, including the energy loss in a thin Lithium Oxide (Li_2O) target. In the following calculations I will use these numerical values:

$$\begin{aligned}
&u = 931.494 \text{ MeV}, && m_{\text{Li}} = 7.0160 \text{ u}, && m_{\text{Be}} = 8.0053 \text{ u} \\
&\Delta E_{\text{Be}^*} = 18.15 \text{ MeV}, && \Gamma_{\text{res}} = 138 \text{ keV}, && m_e = 0.511 \text{ MeV} \\
&\rho_{\text{LiO}} = 2.01 \text{ g/cm}^3, && A_{\text{LiO}} = 29.88 \text{ g/mol}, && X_{0,\text{LiO}} = 23.38 \text{ cm}
\end{aligned} \tag{A.2}$$

where u is the atomic mass unit, m_{Li} and m_{Be} are the Li and Be masses respectively, ΔE_{Be^*} is the energy of the ^{8}Be excited state, Γ_{res} is the resonance width and ρ_{LiO}, A_{LiO} and $X_{0,\text{LiO}}$ are the density, molar mass and radiation length of the Li_2O. I will also assume $M_X = 17.01$ MeV/c^2 and BR(X(17))=6.0×10^{-6} relative to the photon production. The masses of the nuclei are calculated from the masses of the isotopes by subtracting m_e:

$$\begin{aligned}
&m_{\text{Be}} = 7454.85 \text{ MeV}, && m_{\text{Be}^*} = m_{\text{Be}} + \Delta E_{\text{Be}^*} = 7473.00 \text{ MeV} \\
&m_{\text{Li}} = 6533.83 \text{ MeV}
\end{aligned} \tag{A.3}$$

A.1 Kinematics

The first step in the X(17) production kinematics calculation is to determine the proton kinetic energy K_0 at the peak of the resonance. The 4-momenta of the proton p_p and the Li nucleus p_{Li} can be written as:

$$p_p = \left(K + m_p, \sqrt{\left(K + m_p\right)^2 - m_p^2}\, \hat{\mathbf{x}} \right), \qquad p_{\text{Li}} = (m_{\text{Li}}, \mathbf{0}) \tag{A.4}$$

The invariant mass $\sqrt{s}$ is then:

$$\begin{aligned} \sqrt{s} &= \sqrt{(K + m_p + m_{\text{Li}})^2 - (K^2 + 2m_p K)} \\ &= \sqrt{K^2 + m_p^2 + m_{\text{Li}}^2 + 2Km_p + 2Km_{\text{Li}} + 2m_p m_{\text{Li}} - K^2 - 2m_p K} \\ &= \sqrt{2Km_{\text{Li}} + (m_p + m_{\text{Li}})^2} \end{aligned} \tag{A.5}$$

By requiring $\sqrt{s} = m_{\text{Be}^*}$ we get the peak kinetic energy:

$$K_0 = \frac{m_{\text{Be}^*}^2 - (m_p + m_{\text{Li}})^2}{2m_{\text{Li}}} = 1.024 \text{ MeV} \tag{A.6}$$

The velocity β_{Be^*} of the Be* in the laboratory frame is:

$$\beta_{\text{Be}^*} = \frac{p_{\text{Be}^*}}{E_{\text{Be}^*}} = \frac{|\vec{p}_p|}{E_p + m_{\text{Li}}} = \frac{\sqrt{\left(K_0 + m_p\right)^2 - m_p^2}}{K_0 + m_p + m_{\text{Li}}} = 0.006 \tag{A.7}$$

Let's now switch to the X(17) related quantities. The energy, momentum and velocity of the X(17) in the Be* rest frame are:

$$
\begin{aligned}
E_X &= \frac{m^2_{\mathrm{Be}^*} + m^2_X - m^2_{\mathrm{Be}}}{2m_{\mathrm{Be}^*}} = 18.15 \text{ MeV} \\
|\vec{p}_X| &= \sqrt{E^2_X - m^2_X} = 6.3 \text{ MeV} \\
\beta_X &= \frac{p_X}{E_x} = 0.35 \\
\gamma_X &= \frac{E_X}{m_x} = 1.067
\end{aligned}
\tag{A.8}
$$

In the laboratory frame the X(17) can be considered as a product of the decay at rest of a ^{8}Be*. The e^+ and e^- will have the same energy E_e and momentum p_e in the X(17) rest frame, labeled with the $*$ superscript:

$$
E^*_e = M_X/2 = 8.50 \text{ MeV}, \qquad |\vec{p}^*_e| = \sqrt{E^{*2}_e - m^2_e} = 8.49 \text{ MeV} \tag{A.9}
$$

In the lab frame, the maximum (minimum) energy corresponds to the electron or the positron emitted in the same (opposite) direction of the X(17):

$$
\begin{aligned}
E^{\text{max,min}}_e &= \gamma_X(E^*_e \pm \beta_X|\vec{p}^*_e|) \\
E^{\text{max}}_e &= 12.2 \text{ MeV} \\
E^{\text{min}}_e &= 5.9 \text{ MeV}
\end{aligned}
\tag{A.10}
$$

The sum of the energies must be $E_{e^+} + E_{e^-} = E_X$. Since $\beta^*_e \sim 1 > \beta_X$, the maximum angle between the electron and the positron in the laboratory rest frame is 180°. The minimum angle is obtained when the positron and the electron are emitted at $\theta^* = \pm 90°$ in the X(17) rest frame with respect to its line of flight. The corresponding angle in the laboratory frame is:

$$
\begin{aligned}
\tan\theta &= \frac{1}{\gamma_X}\frac{\beta^*_e \sin\theta^*}{\beta^*_e \cos\theta^* + \beta_X} \sim \frac{1}{\gamma_X}\frac{\pm 1}{\beta_X} = \pm 2.68 \Longrightarrow \theta = \pm 70° \\
\theta_{ee} &= 2|\theta| = 140°
\end{aligned}
\tag{A.11}
$$

The expected energy asymmetry $y = (E_+ - E_-)/(E_+ + E_-)$ at this opening angle is around 0, as shown in figure A.1.

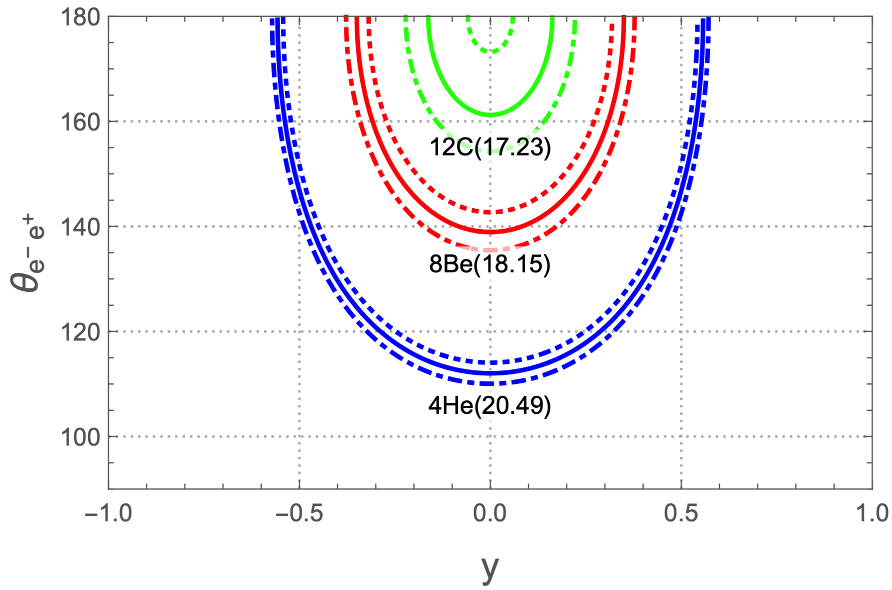

Figure A.1: Pair opening angle vs energy asymmetry for 12C, ^{8}Be and ^{4}He for three different values of m_X: 16.8 MeV (dot-dashed line), 17 MeV (continuous line) and 17.2 MeV (dotted line). Figure from [145].

A.2 Production rate

Assuming a non-relativistic Breit-Wigner distribution for the cross section of the resonant production of ^{8}Be*, for $^8\text{Be}^* \to {}^8\text{Be}\gamma$ we can write:

$$\sigma_\gamma = \sigma_\gamma^0 \frac{\Gamma_{\text{res}}^2/4}{(K-K_0)^2 + \Gamma_{\text{res}}^2/4} \tag{A.12}$$

where $\sigma_\gamma^0 \sim 10^{-2}$ mb is the peak cross section. The expected width of the resonance is:

$$\begin{aligned}\Gamma(^8\text{Be}^* \to ^8\text{Be}X) &= \frac{BR(^8\text{Be}^* \to ^8\text{Be}X)}{BR(^8\text{Be}^* \to ^8\text{Be}\gamma)}\Gamma(^8\text{Be}^* \to ^8\text{Be}\gamma) \\ &= (6 \pm 1) \times 10^{-6}\Gamma(^8\text{Be}^* \to ^8\text{Be}\gamma) = (1.2 \pm 0.2) \times 10^{-5}\ \text{eV}\end{aligned} \tag{A.13}$$

The proton flux integrated over the whole area Σ of the beam profile is, considering 10 μA of proton current:

$$\Sigma\Phi = \frac{I_p}{e} = 6.25 \times 10^{13}\ \mathrm{s}^{-1} \tag{A.14}$$

The numerical density of the target nuclei is:

$$n_b = 2 \cdot 0.95 \cdot \frac{N_A \rho_{\mathrm{LiO}}}{A_{\mathrm{LiO}}} = 7.70 \times 10^{22}\ \mathrm{cm}^{-3} \tag{A.15}$$

where the factor 2 comes from the two Li nuclei per molecule and 0.95 is the relative abundance of ^{7}Li in natural Li. The resonant γ production rate in a slice of target of thickness dx is:

$$\mathrm{d}R_\gamma = \sigma_\gamma \Phi N_b = \sigma_\gamma \cdot \Phi \cdot n_b \Sigma \mathrm{d}x = \sigma_\gamma^0 \frac{\Gamma_{\mathrm{res}}^2/4}{(K-K_0)^2 + \Gamma_{\mathrm{res}}^2/4} \cdot \frac{I_p}{e} \cdot n_b \cdot \mathrm{d}x \tag{A.16}$$

This has to be integrated over the target thickness d, taking into account the proton energy loss and the proton range $\overline{x}$:

$$R_\gamma = \sigma_\gamma^0 \cdot \frac{I_p}{e} \cdot n_b \cdot \frac{\Gamma_{\mathrm{res}}^2}{4} \int_0^{\overline{x}} \frac{1}{(K(x)-K_0)^2 + \Gamma_{\mathrm{res}}^2/4} dx \tag{A.17}$$

If we assume a constant energy loss rate k, we can write $K(x) = K_i - k \cdot x$. With the substitution $t = K(x) - K_0$, the integral becomes:

$$-\frac{1}{k} \int_{K_i-K_0}^{-K_0} \frac{1}{t^2 + \Gamma_{\mathrm{res}}^2/4} dt = -\frac{1}{k} \frac{2}{\Gamma_{\mathrm{res}}} \left[\mathrm{atan} \frac{2t}{\Gamma_{\mathrm{res}}} \right]_{K_i-K_0}^{-K_0} \tag{A.18}$$

and hence:

$$R_\gamma = \sigma_\gamma^0 \cdot \frac{I_p}{e} \cdot n_b \cdot \frac{\Gamma_{\mathrm{res}}}{2} \cdot \frac{1}{k} \left[\mathrm{atan} \frac{2K_0}{\Gamma_{\mathrm{res}}} + \mathrm{atan} \frac{2(K_i - K_0)}{\Gamma_{\mathrm{res}}} \right] \tag{A.19}$$

An estimate of the average proton energy loss k in Li_2O from simulations is 420 MeV/cm.

The resulting rate at 1 μA is:

$$R_\gamma = 1849\ s^{-1} \tag{A.20}$$

The production rate of X(17) particles decaying to e^+e^- is then:

$$R_X = R_\gamma \times \frac{BR(^8\mathrm{Be}^* \to {}^8\mathrm{Be}X)}{BR(^8\mathrm{Be}^* \to {}^8\mathrm{Be}\gamma)} = 1.11 \times 10^{-2}\ \mathrm{s}^{-1} \tag{A.21}$$

A.3 Multiple Scattering inside the target

The multiple scattering (MS) inside the target affects the angular resolution. For example, if a target of width t_0 is slanted by 45° with respect to the beam axis, the thickness seen by the protons is $t_p = t_0/\sin(45°) \sim 14\ \mu$m. The thickness seen by electrons or positrons emitted at the center of the target and at 90° with respect to the beam axis is $t_e = t_p/2\tan(45°) = 7\ \mu$m. The corresponding contribution to the MS is:

$$\langle\theta_{\mathrm{MS}}\rangle = \frac{21\ \mathrm{MeV}}{p}\sqrt{\frac{t_e}{X_0}} = \frac{0.115\ \mathrm{MeV}}{p} \in [9.5, 19.6]\ \mathrm{mrad} \tag{A.22}$$

The contribution to the resolution on the relative angle, considering that $p \sim E$ and $E_{e^+} + E_{e^-} = E_X$, will be:

$$\begin{gathered}\sqrt{12.6^2 + 12.6^2} < \sigma_{\theta,\mathrm{MS}} < \sqrt{9.5^2 + 19.6^2} \\ 20.5\ \mathrm{mrad} < \sigma_{\theta,\mathrm{MS}} < 21.8\ \mathrm{mrad}\end{gathered} \tag{A.23}$$

This is a dominant contribution to the angular resolution, since the contribution from the tracking is few mrad. The corresponding contribution to the mass resolution is:

$$\begin{aligned}\sigma_{M^2,\mathrm{MS}} &= \left|\frac{d}{d\theta_{ee}}(2E_{e^+}E_{e^-}(1-\cos\theta_{ee}))\right| \cdot \sigma_{\theta,\mathrm{MS}} = |2E_{e^+}E_{e^-}\sin\theta_{ee}| \cdot \sigma_{\theta,\mathrm{MS}} \\ \sigma_{M,\mathrm{MS}} &= \frac{1}{2M}\sigma_{M^2,\mathrm{MS}} = \frac{1}{2M_X}\,|2E_{e^+}E_{e^-}\sin\theta_{ee}| \cdot \sigma_{\theta,\mathrm{MS}}\end{aligned} \tag{A.24}$$

Considering the average of $\sigma_{\theta,\mathrm{MS}} = 21.15$ mrad, and considering for simplicity $\sin\theta_{ee} \sim 1$ and $E_{e^+} = E_{e^-} = 9.1$ MeV, we get $\sigma_{M,\mathrm{MS}} \sim 102$ keV.

Bibliography

[1] X. Zhang and G. A. Miller. Can nuclear Physics explain the anomaly observed in the Internal Pair Production in the Beryllium-8 nucleus? *Physics Letters B*, 773:159–165, 2017.

[2] J. L. Feng et al. Particle physics models for the 17 MeV anomaly in beryllium nuclear decays. *Physical Review D*, 95(3):035017, 2017.

[3] J.M. Blatt and V.F. Weisskopf. *Theoretical nuclear physics*. Courier Corporation, 1991.

[4] M. E. Rose. Internal Pair Formation. *Phys. Rev.*, 76:678–681, Sep 1949.

[5] M.E. Rose et al. The internal conversion coefficients. I: The K-shell. *Physical Review*, 83(1):79, 1951.

[6] J. C. Jaeger and H. R. Hulme. The internal conversion of γ-rays with the production of electrons and positrons. *Proceedings of the Royal Society of London. Series A-Mathematical and Physical Sciences*, 148(865):708–728, 1935.

[7] G. A. Fisher, P. Paul, F. Riess, and S. S. Hanna. Giant E1 resonances in ^{8}Be from the reaction ^{7}Li(p, γ)^{8}Be. *Physical Review C*, 14(1):28, 1976.

[8] G. Goldring. Internal Pairs in Anisotropic Emission. *Proceedings of the Physical Society. Section A*, 66(4):341, 1953.

[9] F.W.N. De Boer et al. A deviation in internal pair conversion. *Physics Letters B*, 388(2):235–240, 1996.

[10] F.W.N. De Boer et al. Excess in nuclear pairs near 9 MeV/invariant mass. *Journal of Physics G: Nuclear and Particle Physics*, 23(11):L85, 1997.

[11] F.W.N. De Boer et al. Further search for a neutral boson with a mass around 9 MeV/c2. *Journal of Physics G: Nuclear and Particle Physics*, 27(4):L29, 2001.

[12] A. Vitéz et al. Anomalous internal pair creation in 8Be as a signature of the decay of a new particle. *Acta Physica Polonica B*, 39(2), 2008.

[13] A.J. Krasznahorkay et al. "". *Frascati Physics Series*, 56(86), 2013.

[14] D.R. Tilley et al. Energy levels of light nuclei A= 8, 9, 10. *Nuclear Physics A*, 745(3-4):155–362, 2004.

[15] J. Gulyás et al. A pair spectrometer for measuring multipolarities of energetic nuclear transitions. *Nuclear Instruments and Methods in Physics Research Section A: Accelerators, Spectrometers, Detectors and Associated Equipment*, 808:21–28, 2016.

[16] A.J. Krasznahorkay et al. Observation of anomalous internal pair creation in ^{8}Be: a possible indication of a light, neutral boson. *Physical Review Letters*, 116(4):042501, 2016.

[17] A.J. Krasznahorkay et al. On the creation of the 17 MeV X boson in the 17.6 MeV M1 transition of ^{8}Be. In *EPJ Web of Conferences*, volume 142, page 01019. EDP Sciences, 2017.

[18] A. Krasznahorkay et al. New results on the ^{8}Be anomaly. *Journal of Physics: Conference Series*, 1056:012028, 07 2018.

[19] A. J. Krasznahorkay et al. A new anomaly observed in 4He supporting the existence of the hypothetical X17 particle. *Journal of Physics: Conference Series*, 1643:012001, dec 2020.

[20] K. E. Stiebing et al. A multi-detector array for high energy nuclear $e^{+}e^{-}$ pair spectroscopy. *Journal of Physics G: Nuclear and Particle Physics*, 30(2):165, 2004.

[21] J.L. Feng et al. Protophobic Fifth-Force Interpretation of the Observed Anomaly in ^{8}Be Nuclear Transitions. *Phys. Rev. Lett.*, 117:071803, Aug 2016.

[22] A. J. Krasznahorkay et al. New evidence supporting the existence of the hypothetic X17 particle, 2019.

[23] A. Aleksejevs et al. A Standard Model explanation for the "ATOMKI anomaly". *arXiv preprint arXiv:2102.01127*, 2021.

[24] J. L. Feng et al. Dynamical Evidence For a Fifth Force Explanation of the ATOMKI Nuclear Anomalies. *arXiv preprint arXiv:2006.01151*, 2020.

[25] L. Delle Rose et al. New Physics Suggested by Atomki Anomaly. *Frontiers in Physics*, 7:73, 2019.

[26] P. Kálmán and T. Keszthelyi. Anomalous internal pair creation. *The European Physical Journal A*, 56(8):1–5, 2020.

[27] B. Koch. X17: A new force, or evidence for a hard $\gamma+\gamma$ process? *Nuclear Physics A*, 1008:122143, 2021.

[28] J. R. Batley et al. Search for the dark photon in $\pi 0$ decays. *Physics Letters B*, 746:178–185, 2015.

[29] Xilin Zhang and Gerald A Miller. Can a protophobic vector boson explain the ATOMKI anomaly? *Physics Letters B*, 813:136061, 2021.

[30] Y. Kahn et al. Light weakly coupled axial forces: models, constraints, and projections. *Journal of High Energy Physics*, 2017(5):1–34, 2017.

[31] Ulrich Ellwanger and Stefano Moretti. Possible explanation of the electron positron anomaly at 17 MeV in 8Be transitions through a light pseudoscalar. *Journal of High Energy Physics*, 2016(11):1–13, 2016.

[32] H. W. Hammer, C. Ji, and D. R. Phillips. Effective field theory description of halo nuclei. *Journal of Physics G: Nuclear and Particle Physics*, 44(10):103002, 2017.

[33] D. Zahnow et al. The S(E) factor of ^{7}Li(p,γ)^{8}Be and consequences for S(E) extrapolation in ^{7}Be(p,γ0)^{8}B. *Zeitschrift für Physik A Hadrons and Nuclei*, 351(2):229–236, 1995.

[34] D. J. Schlueter, R. W. Krone, and F. W. Prosser Jr. Measurements and analysis of angular distribution interference effects in the ^{7}Li(p,γ)^{8}Be reaction. *Nuclear Physics*, 58:254–272, 1964.

[35] B. Mainsbridge. The angular distributions of the gamma radiation from the ^{7}Li(p,γ)^{8}Be reaction from E_p=200 keV. *Nuclear Physics*, 21:1–14, 1960.

[36] P.H. Gu and X.G. He. Realistic model for a fifth force explaining anomaly in 8Be*→8Be e+e- decay. *Nuclear Physics B*, 919:209–217, 2017.

[37] C.S. Chen et al. The 17 MeV anomaly in beryllium decays and U (1)portal to dark matter. *International Journal of Modern Physics A*, 32(31):1750178, 2017.

[38] Y. Liang et al. X(16.7) as the solution of the NuTeV anomaly. *Chinese Physics C*, 41(6):063105, 2017.

[39] L.B. Jia and X.Q. Li. The new interaction suggested by the anomalous 8Be transition sets a rigorous constraint on the mass range of dark matter. *The European Physical Journal C*, 76(12):1–7, 2016.

[40] T. Kitahara and Y. Yamamoto. Protophobic light vector boson as a mediator to the dark sector. *Physical Review D*, 95(1):015008, 2017.

[41] O. Seto and T. Shimomura. Atomki anomaly and dark matter in a radiative seesaw model with gauged B-L symmetry. *Physical review D*, 95(9):095032, 2017.

[42] M.J. Neves and J.A. Helayël-Neto. A unified hidden-sector-electroweak model, paraphotons and the X-boson. *arXiv preprint arXiv:1611.07974*, 2016.

[43] C.W. Chiang and P.Y. Tseng. Probing a dark photon using rare leptonic kaon and pion decays. *Physics Letters B*, 767:289–294, 2017.

[44] J. Kozaczuk et al. Light axial vector bosons, nuclear transitions, and the 8Be anomaly. *Physical Review D*, 95(11):115024, 2017.

[45] M. Raggi. NA48/2 studies of rare decays. *arXiv preprint arXiv:1508.01307*, 2015.

[46] D. Banerjee et al. Search for a hypothetical 16.7 MeV gauge boson and dark photons in the NA64 experiment at CERN. *Physical review letters*, 120(23):231802, 2018.

[47] A. Anastasi et al. Limit on the production of a low-mass vector boson in $e^+e^- \to U\gamma$, $U \to e^+e^-$ with the KLOE experiment. *Physics Letters B*, 750:633–637, 2015.

[48] G.W. Bennett et al. Final report of the Muon E821 anomalous magnetic moment measurement at BNL. *Phys. Rev. D*, 73, 2006.

[49] T. Blum et al. The muon (g-2) theory value: Present and future. *arXiv preprint arXiv:1311.2198*, 2013.

[50] M. Lindner et al. A call for new physics: the muon anomalous magnetic moment and lepton flavor violation, 2018.

[51] B. Abi et al. Measurement of the positive muon anomalous magnetic moment to 0.46 ppm. *Physical Review Letters*, 126(14):141801, 2021.

[52] M. Veselsky, V. Petousis, and J. Leja. Anomaly in decay of ^{8}Be and ^{4}He - can a chirally symmetric light boson be able to mediate the low energy nucleon-nucleon interaction? *arXiv preprint arXiv:2004.09758*, 2020.

[53] Thomas Schäfer and Edward V Shuryak. Instantons in QCD. *Reviews of Modern Physics*, 70(2):323, 1998.

[54] D.S.M. Alves and N. Weiner. A viable QCD axion in the MeV mass range. *Journal of High Energy Physics*, 2018(7):1–49, 2018.

[55] D.S.M. Alves. Signals of the QCD axion with mass of 17 MeV/c 2: Nuclear transitions and light meson decays. *Physical Review D*, 103(5):055018, 2021.

[56] D. Banerjee. Search for Dark Sector Physics at the NA64 experiment in the context of the Physics Beyond Colliders Project. *arXiv preprint arXiv:1909.04363*, 2019.

[57] D. Banerjee et al. Improved limits on a hypothetical X(16.7) boson and a dark photon decaying into e^+e^- pairs. *Phys. Rev. D*, 101:071101, Apr 2020.

[58] M. Kirsanov. Recent results of the NA64 experiment at the CERN SPS. In *EPJ Web of Conferences*, volume 212, page 06005. EDP Sciences, 2019.

[59] Y. M. Andreev et al. Search for pseudoscalar bosons decaying into e^+e^- pairs. *arXiv preprint arXiv:2104.13342*, 2021.

[60] E. Depero et al. Hunting down the X17 boson at the CERN SPS. *arXiv preprint arXiv:2009.02756*, 2020.

[61] V. Fanti et al. The beam and detector for the NA48 neutral kaon CP violation experiment at CERN. *Nuclear Instruments and Methods in Physics Research Section A: Accelerators, Spectrometers, Detectors and Associated Equipment*, 574(3):433–471, 2007.

[62] E.C. Gil et al. Search for π 0 decays to invisible particles. *Journal of High Energy Physics*, 2021(2):1–27, 2021.

[63] G. L. Castro and N. Quintero. Tests of the Atomki anomaly in lepton pair decays of heavy mesons. *arXiv preprint arXiv:2101.01865*, 2021.

[64] D. Matvienko. The Belle II experiment: status and physics program. In *EPJ Web of Conferences*, volume 191, page 02010. EDP Sciences, 2018.

[65] BESIII experiment website. http://bes3.ihep.ac.cn/index.html.

[66] K. Ban et al. Search for new light vector boson using J/Ψ at BESIII and Belle II. *arXiv preprint arXiv:2012.04190*, 2020.

[67] J. Jiang et al. X(16.7) production in electron-positron collision. *The European Physical Journal C*, 78(6):1–9, 2018.

[68] J. Jiang, H. Yang, and C. F. Qiao. Exploring bosonic mediator of interaction at BESIII. *The European Physical Journal C*, 79(5):404, 2019.

[69] A. Ariga et al. FASER's physics reach for long-lived particles. *Physical Review D*, 99(9):095011, 2019.

[70] M. Raggi et al. The PADME experiment at LNF. In *EPJ Web of Conferences*, volume 96, page 01025. EDP Sciences, 2015.

[71] E. Nardi et al. Resonant production of dark photons in positron beam dump experiments. *Physical Review D*, 97(9):095004, 2018.

[72] D. Domenici. The PADME experiment at LNF. *Journal of Instrumentation*, 15(10):C10015, 2020.

[73] C. D. R. Carvajal. Dark photon production in e^+ beam dump experiments via resonant $e^+ - e^-$ annihilation. *Frascati Physics Series*, 67, 2018.

[74] V. Kozhuharov. Searching for dark sector with missing mass technique in fixed target experiments. In *EPJ Web of Conferences*, volume 212, page 06001. EDP Sciences, 2019.

[75] S. Spagnolo et al. Status of the PADME experiment. In *Journal of Physics: Conference Series*, volume 1137, page 012043. IOP Publishing, 2018.

[76] J. Balewski et al. The DarkLight experiment: a precision search for new physics at low energies. *arXiv preprint arXiv:1412.4717*, 2014.

[77] R. Corliss et al. Searching for a dark photon with DarkLight. *Nuclear Instruments and Methods in Physics Research Section A: Accelerators, Spectrometers, Detectors and Associated Equipment*, 865:125–127, 2017.

[78] B. Echenard et al. Projections for dark photon searches at Mu3e. *Journal of High Energy Physics*, 2015(1):113, 2015.

[79] A. Papa. Charged lepton flavour violation searches at the Paul Scherrer Institut: Status of the MEGII and Mu3e experiments. In *EPJ Web of Conferences*, volume 179, page 01018. EDP Sciences, 2018.

[80] P. Ilten et al. Dark photons from charm mesons at LHCb. *Physical Review D*, 92(11):115017, 2015.

[81] LHCb collaboration. LHCb detector performance. *International Journal of Modern Physics A*, 30(07):1530022, Mar 2015.

[82] B. Wojtsekhowski et al. Searching for a dark photon: Project of the experiment at VEPP-3. *Journal of Instrumentation*, 13(02):P02021, 2018.

[83] L. Doria et al. Search for light dark matter with the MESA accelerator, 2018.

[84] O. Moreno. The heavy photon search experiment at Jefferson Lab. *arXiv preprint arXiv:1310.2060*, 2013.

[85] A. Celentano et al. The heavy photon search experiment at Jefferson laboratory. In *Journal of Physics: Conference Series*, volume 556, page 012064. IOP Publishing, 2014.

[86] P.H. Adrian et al. Search for a dark photon in electroproduced e+ e- pairs with the Heavy Photon Search experiment at JLab. *Physical Review D*, 98(9):091101, 2018.

[87] A. Ahmidouch et al. A Direct Detection Search for Hidden Sector New Particles in the 3-60 MeV Mass Range. *arXiv preprint arXiv:2108.13276*, 2021.

[88] R. Bolzonella. An experimental setup for the detection of e+ e-pairs in the decay of 8Be. Master's thesis, Università di Padova, 2021.

[89] M. Viviani et al. The X17 boson and the $^3\mathrm{H}(p, e^+e^-)^4\mathrm{He}$ and $^3\mathrm{He}(n, e^+e^-)^4\mathrm{He}$ processes: a theoretical analysis. *arXiv preprint arXiv:2104.07808*, 2021.

[90] J. Adam et al. The MEG detector for $\mu^+ \to e^+\gamma$ decay search. *The European Physical Journal C*, 73(4):2365, 2013.

[91] J. Adam et al. New limit on the lepton-flavor-violating decay $\mu^+ \to e^+\gamma$. *Physical review letters*, 107(17):171801, 2011.

[92] J. Adam et al. New constraint on the existence of the $\mu^+ \to e^+\gamma$ decay. *Physical Review Letters*, 110(20):201801, 2013.

[93] A. M. Baldini et al. Search for the lepton flavour violating decay $\mu^+ \to e^+\gamma$ with the full dataset of the MEG experiment. *The European Physical Journal C*, 76(8):434, 2016.

[94] A. M. Baldini et al. MEG upgrade proposal. *arXiv preprint arXiv:1301.7225*, 2013.

[95] A.M. Baldini et al. The design of the MEG II experiment. *The European Physical Journal C*, 78(5):380, 2018.

[96] A.M. Baldini et al. Search for lepton flavour violating muon decay mediated by a new light particle in the MEG experiment. *The European Physical Journal C*, 80(9):1–21, 2020.

[97] Y. Fujii. Development of Radiative Decay Counter to reduce the background in the MEG experiment. In *2013 IEEE Nuclear Science Symposium and Medical Imaging Conference (2013 NSS/MIC)*, pages 1–6. IEEE, 2013.

[98] R. Iwai, K. Ieki, and R. Sawada. Radiative decay counter for active background identification in MEG II experiment. In *International conference on Technology and Instrumentation in Particle Physics*, pages 82–86. Springer, 2017.

[99] J. Adam et al. Calibration and monitoring of the MEG experiment by a proton beam from a Cockcroft–Walton accelerator. *Nuclear Instruments and Methods in Physics Research Section A: Accelerators, Spectrometers, Detectors and Associated Equipment*, 641(1):19–32, 2011.

[100] W. Ootani et al. Development of a thin-wall superconducting magnet for the positron spectrometer in the MEG experiment. *IEEE transactions on applied superconductivity*, 14(2):568–571, 2004.

[101] M. De Gerone et al. Design and test of an extremely high resolution timing counter for the MEG II experiment: preliminary results. *Journal of Instrumentation*, 9(02):C02035, 2014.

[102] M. De Gerone et al. A high resolution Timing Counter for the MEG II experiment. *Nuclear Instruments and Methods in Physics Research Section A: Accelerators, Spectrometers, Detectors and Associated Equipment*, 824:92–95, 2016.

[103] G. Boca et al. The laser-based time calibration system for the MEG II pixelated Timing Counter. *Nuclear Instruments and Methods in Physics Research Section A: Accelerators, Spectrometers, Detectors and Associated Equipment*, 947:162672, 2019.

[104] G. Boca et al. Timing resolution of a plastic scintillator counter read out by radiation damaged SiPMs connected in series. *Nuclear Instruments and Methods in Physics Research Section A: Accelerators, Spectrometers, Detectors and Associated Equipment*, 999:165173, 2021.

[105] R.A. Lerche and D.W. Phillon. Rise time of BC-422 plastic scintillator$<$ 20 ps. In *Conference Record of the 1991 IEEE Nuclear Science Symposium and Medical Imaging Conference*, pages 167–170. IEEE, 1991.

[106] P.W. Cattaneo et al. Development and commissioning of the 30 ps time resolution MEG II pixelated Timing Detector. *Nuclear Instruments and Methods in Physics Research Section A: Accelerators, Spectrometers, Detectors and Associated Equipment*, 936:660–662, 2019.

[107] A.M. Baldini et al. The ultra light Drift Chamber of the MEG II experiment. *Nuclear Instruments and Methods in Physics Research Section A: Accelerators, Spectrometers, Detectors and Associated Equipment*, 958:162152, 2020.

[108] S. Ogawa et al. Liquid xenon calorimeter for MEG II experiment with VUV-sensitive MPPCs. *Nuclear Instruments and Methods in Physics Research Section A: Accelerators, Spectrometers, Detectors and Associated Equipment*, 845:528–532, 2017.

[109] K. Ieki et al. Large-area MPPC with enhanced VUV sensitivity for liquid xenon scintillation detector. *Nuclear Instruments and Methods in Physics Research Section A: Accelerators, Spectrometers, Detectors and Associated Equipment*, 925:148–155, 2019.

[110] A.M. Baldini et al. The Search for $\mu^+ \to e^+\gamma$ with 10^{-14} Sensitivity: The Upgrade of the MEG Experiment. *Symmetry*, 13(9):1591, 2021.

[111] L. Galli et al. A new generation of integrated trigger and read out system for the MEG II experiment. In *2014 IEEE Nuclear Science Symposium and Medical Imaging Conference (NSS/MIC)*, pages 1–3. IEEE, 2014.

[112] M. Francesconi et al. The WaveDAQ integrated Trigger and Data Acquisition System for the MEG II experiment. *arXiv preprint arXiv:1806.09218*, 2018.

[113] L. Galli et al. WaveDAQ: An highly integrated trigger and data acquisition system. *Nuclear Instruments and Methods in Physics Research Section A: Accelerators, Spectrometers, Detectors and Associated Equipment*, 936:399–400, 2019.

[114] S. Ritt. The DRS chip: cheap waveform digitizing in the GHz range. *Nuclear Instruments and Methods in Physics Research Section A: Accelerators, Spectrometers, Detectors and Associated Equipment*, 518(1-2):470–471, 2004.

[115] Maximum Integration Data Acquisition System. https://midas.psi.ch/.

[116] GEANT4 - A simulation toolkit. https://geant4.web.cern.ch/.

[117] A.M. Baldini et al. Single-hit resolution measurement with MEG II drift chamber prototypes.

[118] B. Aubert et al. The BABAR detector. *Nuclear Instruments and Methods in Physics Research Section A: Accelerators, Spectrometers, Detectors and Associated Equipment*, 479(1):1–116, 2002.

[119] M. Chiappini et al. The new drift chamber of the MEG II experiment. *Nuclear Instruments and Methods in Physics Research Section A: Accelerators, Spectrometers, Detectors and Associated Equipment*, 936:501–502, 2019.

[120] G.F. Tassielli et al. The drift chamber of the MEG II experiment. *Journal of Instrumentation*, 15(09):C09051, 2020.

[121] ThreeBond 1530. https://threebond-europe.com/it/products/tb1530/.

[122] Stycast 2850. https://www.henkel-adhesives.com/it/en/product/potting-compounds/loctite_stycast_2850ft.html.

[123] California Fine Wires - Al (5056) alloy. https://calfinewire.com/datasheets/100024-aluminum5056/.

[124] G. Chiarello et al. The construction technique of the high granularity and high transparency drift chamber of MEG II. *Journal of Instrumentation*, 12(07):C07022, 2017.

[125] G. Chiarello et al. The construction technique of the new MEG II tracker. *Nuclear Instruments and Methods in Physics Research Section A: Accelerators, Spectrometers, Detectors and Associated Equipment*, 936:495–496, 2019.

[126] G. Chiarello et al. An automatic system for the wiring of Drift Chambers for modern high intensity and high precision particle physics experiments. *Journal of Instrumentation*, 15(07):C07034, 2020.

[127] M. Panareo et al. The front end electronics for the drift chamber readout in MEG experiment upgrade. *Journal of Instrumentation*, 15(07):C07009, 2020.

[128] G. Chiarello et al. Improving spatial and PID performance of the high transparency Drift Chamber by using the Cluster Counting and Timing techniques. *Nuclear Instruments and Methods in Physics Research Section A: Accelerators, Spectrometers, Detectors and Associated Equipment*, 936:464–465, 2019.

[129] Analog Device ADA4927. https://www.analog.com/media/en/technical-documentation/data-sheets/ADA4927-1_4927-2.pdf.

[130] Texas Instruments THS4509. https://www.ti.com/product/THS4509.

[131] ISEG EHS F430p. https://iseg-hv.com/en/products/detail/EHS.

[132] CAEN A648. https://www.caen.it/products/a648/.

[133] Draka. https://www.drakauk.com/.

[134] A.M. Baldini et al. Gas distribution and monitoring for the drift chamber of the MEG II experiment. *Journal of Instrumentation*, 13(06):P06018, 2018.

[135] M. Meucci. Performance study of a gas monitoring drift chamber for the MEG II experiment. Master's thesis, Università di Roma La Sapienza, 2017.

[136] A.M. Baldini et al. Detailed analysis of chemical corrosion of ultra-thin wires used in drift chamber detectors. *Journal of Instrumentation*, 16(12):T12003, 2021.

[137] M. Chiappini et al. Commissioning of the MEG II tracker system. *Journal of Instrumentation*, 15(06):C06056, 2020.

[138] M. Chiappini et al. Towards a New $\mu^+ \to e^+\gamma$ Search with the MEG II Experiment: From Design to Commissioning. *Universe*, 7(12):466, 2021.

[139] Garfield++ - simulation of tracking detectors. http://garfieldpp.web.cern.ch/garfieldpp/.

[140] ANSYS - Engineering Simulation Software. https://www.ansys.com/.

[141] Li_2O properties. http://www-ferp.ucsd.edu/LIB/PROPS/PANOS/li2o.html.

[142] Li_2O elastic limit. http://www-ferp.ucsd.edu/LIB/PROPS/PANOS/li2o.html.

[143] Li_2O yield stress. http://www.hrc.u-toyama.ac.jp/action/workshop/figure/fig4_8.html,
http://www.hrc.u-toyama.ac.jp/action/workshop/figure/fig4_9.html.

[144] LaBr3 Crystal Scintillator. https://www.crystals.saint-gobain.com/radiation-detection-scintillators/crystal-scintillators/lanthanum-bromide-labr3#.

[145] C. Toni. Emission of a new particle from ^{8}Be and ^{4}He excited nuclei. Master's thesis, Università di Roma La Sapienza, 2020.